Systematic Synthesis and Properties of Coordination Cluster Using β-Diketone-Based Ligand

都地，恭拡

KYUSHU UNIVERSITY

Systematic Synthesis and Properties of Coordination Cluster Using β-Diketone-Based Ligand

Yasuhiro Tsuji

March 2018
Department of Chemistry
Graduate School of Science
Kyushu University

Contents

General Introduction

Coordination Clusters

High-nuclearity complexes have recently attracted significant attention because of their unique properties, topology, magnetism, and reactivities, including multi-electron transfer.[1] Structures where a number of metal ions are bridged by N, O, or S are called "coordination clusters" (CCs), and this definition differentiates them from those with direct metal-metal bonds.[2,3] CCs have attracted particular interest in the general field of bioinorganic chemistry, and more specifically, in molecule-based magnetic materials. Several metalloenzymes possess metal-assembled structures similar to those of CCs. The Mn_4CaO_5 cluster, which is an oxygen-evolving center in Photosystem II, has a cubane structure consisting of 3 Mn, 1 Ca, and 4 bridging oxygen atoms with an additional dangling manganese ion (**Figure 1a**).[4] The FeMo cofactor also has a cluster structure consisting of 9 Fe ions and 1 Mo ion bridged by several sulfur atoms and a carbon atom (**Figure 1b**).[5,6] The FeMo cofactor is the active site of the nitrogenase enzyme and is able to reduce dinitrogen to yield bioavailable ammonium. Several coordination clusters show single-molecule magnetic (SMM) behavior and are expected to be applied in molecule-based nanoscale magnetic materials. Therefore, the development of rational synthetic strategies for and systematic syntheses of coordination clusters is expected to help realize novel useful SMMs and effective catalysts mimicking the active sites of enzymes.
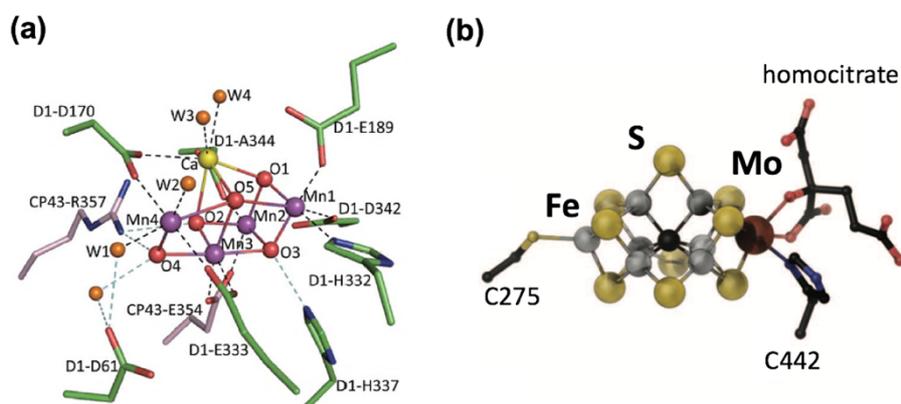

Figure 1. (a) Structure of the Mn_4CaO_5 cluster of Photosystem II [4] and (b) FeMo cofactor of nitrogenase and its ligand environment.[5,6]

β-diketone-based Coordination Clusters

An effective way to construct CCs is through the use of β-diketone-based ligands, because they can be prepared in a one-step reaction (e.g. Claisen condensation between acetone and ethyl acetate, **Figure 2a**) from commercially or readily available reactants.[7-9] The simplest β-diketone is acetylacetone (Hacac), which can be used to form very stable metal acetyl acetonates, $[M^{n+}(acac)_n]$, often used as catalyst precursors. In addition, poly β-diketone ligands are typically used in the field of supramolecular chemistry. To date, a number of poly β-diketone complexes have been reported, including homo- and heterometallic linear arrays, metallocycles, metallacoronates, triple-stranded helicates, and cage clusters (**Figure 2b**).
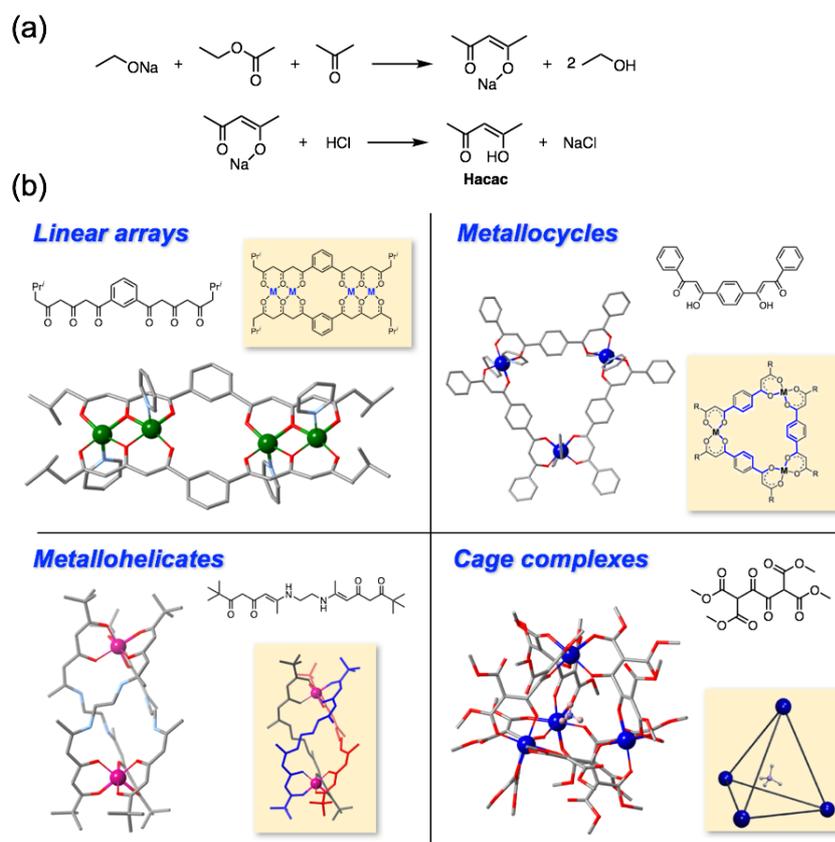

Figure 2. (a) Synthetic scheme of β-diketone via Claisen condensation and (b) oligonuclear complexes based on poly-β-diketone complexes.[7-9]

Our group has reported the synthesis and magnetic properties of 18 trinuclear $Ni^{II}_2Ln^{III}$ complexes (Ln = La–Lu except for Pm), which are heterometallic linear arrays.[9] They were prepared via the one-pot reaction of a β-diketone-based ligand (2,6-di(acetoacetyl)pyridine) and metals, where 4f metal ions are specifically included in the central cavity constructed by two nickel ions and ligands.
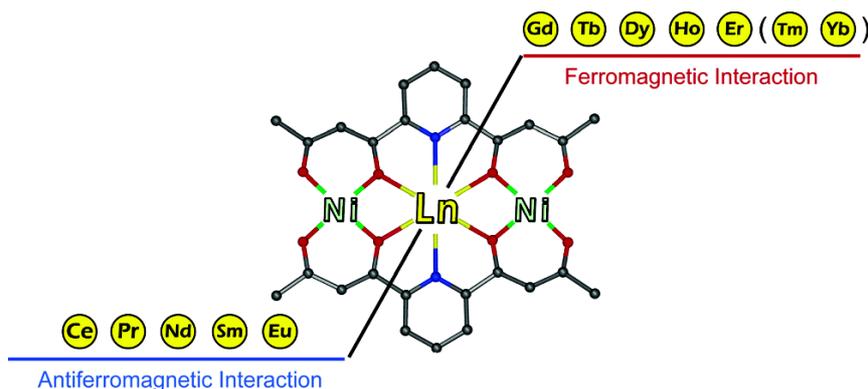
Figure 3. Trinuclear Ni_2Ln complexes of 2, 6-di(acetoacetyl)pyridine.[9]

Triple-stranded metallohelicates also adopt unique structures constructed by poly β-diketone ligands. Although they always form racemic mixtures, they possess absolute chirality attributed to their helical character. Several metallohelicates can incorporate another metal, including alkali metals, alkaline-earth metals, and lanthanides, in their cavity to form linear heterometallic clusters. Saalfrank *et al.* reported the synthesis of the metallacryptate, $[K \subset (Fe_2L^{tBu}_3)]PF_6$, where the β-diketone ligand sites coordinated to Fe and formed triple-stranded helicates, and the pyridine dicarbonyl sites trapped a potassium ion.[8]

Redox and Catalytic Properties of Oxygen-bridged CCs

Oxygen- (oxo- or hydroxyl-) bridged metal-assembled structures are another class of CCs, and their unique properties and functions have been extensively studied. The CC structure is found in several compounds, which are efficient water oxidation catalysts. As described above, the Mn_4CaO_5 cluster of Photosystem II has a cubane structure consisting of 3 manganese ions, 1 calcium ion, and 4 bridging oxygen atoms with an additional dangling manganese ion.[4]   As artificial water oxidation catalysts, metal oxide materials, such as cobalt oxides and layered double hydroxides (LDHs), possess an oxygen-bridged cluster structure (**Figure 4**).[10-15]   For example, **Co-Pi** is a cobalt oxide material that has attracted significant attention because of its high catalytic activity under mild conditions for water oxidation reactions (neutral pH in aqueous solution) and self-healing properties.[16,17]   The complex is generated by electrodeposition from aqueous solutions containing phosphate and Co^{2+}, and consists of several cobalt ions bridged by hydroxyl and oxo-bridges and phosphate ions.   However, structural characterization and mechanistic studies of this material are inherently difficult because of their heterogeneous nature.   Thus, many researchers have attempted to elucidate their properties by computational calculations.   The cobalt ions are coordinated by six oxygen atoms, forming octahedral CoO_6 units.   In addition, the assembled structure of two CoO_6 units was suggested by Fourier transform EXAFS spectra.   One unit is complete, but adopts an incomplete vertex-sharing (corner-sharing) cobalt-oxo cubane motif, and the other adopts a layered edge-sharing CoO_6 octahedra (**Figure 5**).[18,19]
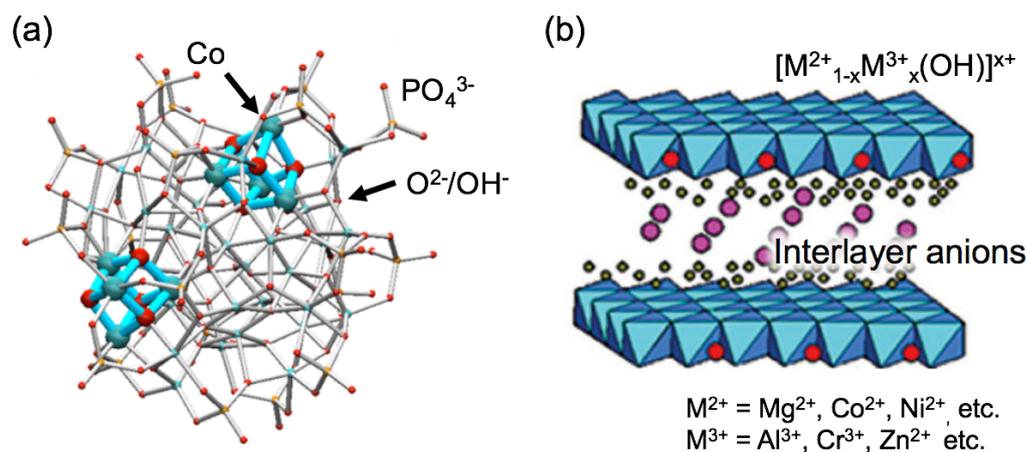

Figure 4. (a) The estimated structure of **Co-Pi**[16,17] and (b) structure of **LDH**.[10-15]
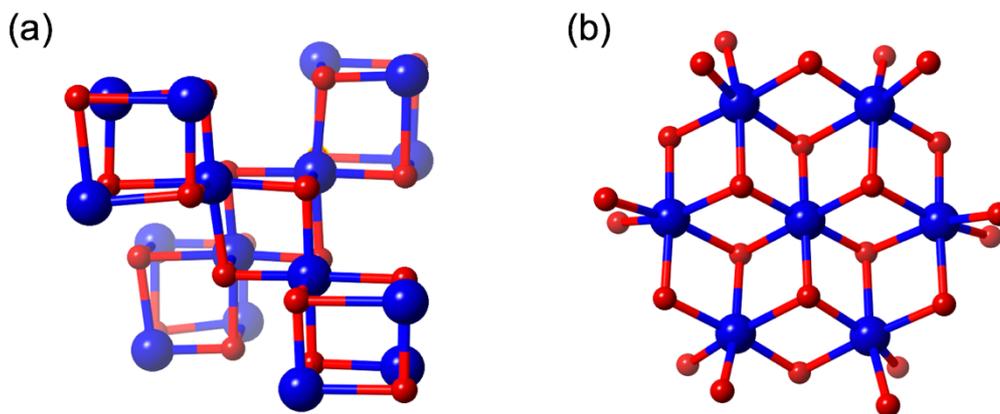
Figure 5. Structural models of **Co-Pi**. (a) Corner-sharing cubane model and (b) edge-sharing model.[18,19] Cobalt; blue, oxo/hydroxyl anion; red.

Layered double hydroxides (LDHs) also form compounds featuring an oxygen-bridged cluster structure. LDHs are anion clays consisting of cationic layers and interlayer anions. LDHs have attracted much attention in the fields of catalysis and adsorption.[20] The assembled structure of the cationic layer is an edge-sharing MO_6 octahedral structure consisting of two kinds of metal ions bridged by hydroxyl anions. These compounds act as catalysts for various reactions depending on their constituent metal ions and interlayer anions. Particularly, LDHs with Co and Zn show efficient catalytic performance for water and alcohol oxidation.[21] With respect to water electrooxidation, the turnover frequency (TOF) per Co atom is much higher than that of other Co counterparts (e.g., Co_3O_4 and $Co(OH)_2$). However, the specific structure and reaction mechanism of the active sites is unknown for the Co-based LDHs. Thus, model compounds of these heterogeneous catalysts are needed to elucidate their reaction mechanism and active sites structures in detail.

Nocera and co-workers reported a heptanuclear cobalt cluster $[Co^{II}_7(OH)_6L_6](OTf)_2$ and its oxidized form, $[Co^{III}Co^{II}_6(OH)_6L_6](OTf)_3$, as soluble model of **Co-Pi** (**Figure 6a**).[22] These complexes showed an anomalously slow self-exchange electron transfer accelerated by the dissociation of the OTf$^-$ anion from the oxidized cluster. This result sheds light on the self-repair mechanism of **Co-Pi**. Mimicking the cubane motif of **Co-Pi**, a number of cobalt cubane complexes have been reported as soluble models. In particular, the cobalt cubane complexes $[Co^{III}_4O_4(OAc)_4py_4]$ and $[Co^{II}_4(hmp)_4(\mu\text{-}OAc)_2(\mu_2\text{-}OAc)_2(H_2O)_2]$ (hmp = 2-(hydroxymethyl)pyridine), were

reported to catalyze water oxidation under electrochemical and photochemical conditions.[23-25] Thus, these complexes can act as structural as well as functional models for cobalt oxide materials. The oxygen-bridged CCs in the unit structure of these catalysts are expected to underlie the function and reveal the relationship between structure and function upon further study.
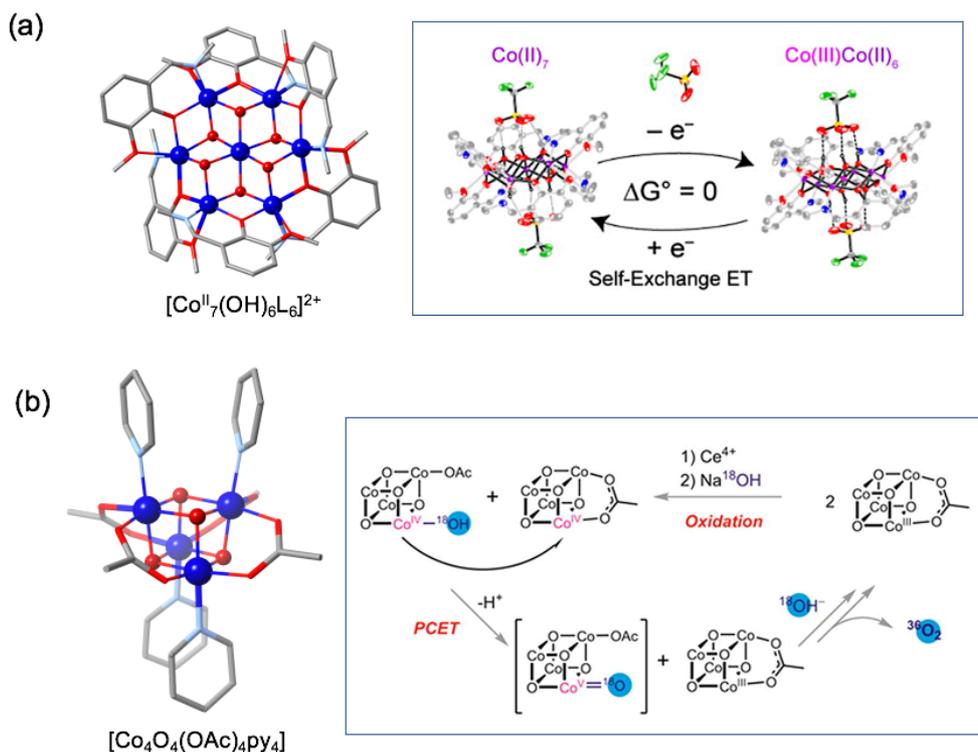
Figure 6. (a) Structure of the heptanuclear cobalt cluster and self-exchange electron transfer.[22] (b) Cobalt cubane cluster and its reaction mechanism for the water oxidation reaction by Ce^{4+}.[23-25]

By constructing a model compound with a discrete complex, it is possible to monitor a reaction by measurement in solution, which simplifies the identification of its molecular structure by single-crystal structural analysis. In addition, the redox potentials of its metal ions are finely controllable by several methods including the introduction of ligand substituents, doping metal ions, and changing bridging agents. Several oxygen-bridged clusters reported to date have been synthesized by spontaneous self-assembly simple pyridine- and acetate-based ligands and metal ions. However, it is difficult to obtain certain target structures with this method because there are many possible structures that can form in the self-assembly process. Using rigid and

multidentate ligands is an effective method that helps minimize structural variations. Moreover, it is useful to construct oxygen-bridged cluster structures by triple-stranded helicate with rigid multidentate ligands.   As described above, several metallohelicates can incorporate large metal ions in their cavities.   As a large metal ion complex, oxo-bridged metal clusters can also be enclosed by the cavity.   Ohio and co-workers reported the synthesis and magnetic properties of the oxo-bridged pentanuclear complex, $[Fe^{II}_2Fe^{III}_3L_3(\mu_3\text{-}O)(\mu_2\text{-}OMe)(OAc)_2]Cl_2$, coordinated by (poly)pyridine ligands (**Figure 7**).[26]   The structure includes an oxygen-bridged trinuclear core, $[Fe^{III}_3(\mu_3\text{-}O)]^{7+}$ as a dinuclear triple stranded unit, and $[M^{II}_2L_3]^{2-}$ units.   Saalfrank *et al*. were reported the oxo-bridged octanuclear bis(triple-helical) complex $[Co_8(\mu_3\text{-}O)_2L_6]$ (M = Cd^{2+}, Mn^{2+}, Co^{2+}) coordinate by (poly)β-diketone ligands (H_2L = 1,1'-(pyridine-2,6-diyl)bis(1-hydroxy-4,4-dimethylpent-1-en-3-one).[8]   In these complexes, terminal mononuclear triple stranded helicate units $[M^{II}L_3]^{4-}$ and two oxygen-bridged trinuclear cores, $[M_3(\mu_3\text{-}O)]^{4+}$, flanked by helicates constitute the heptanuclear structure.

(a)   (b)
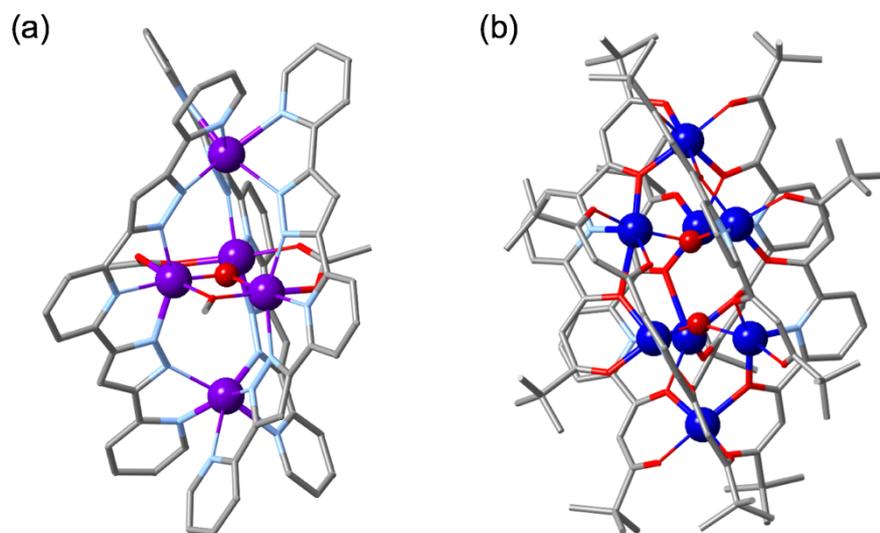
Figure 7. Oxygen-bridged cluster complexes coordinated by triple-stranded helicates with rigid multidentate ligands. (a) $[Fe^{II}_2Fe^{III}_3L_3(\mu_3\text{-}O)(\mu_2\text{-}OMe)(OAc)_2]^{2+}$, (b) $[Co_8(\mu_3\text{-}O)_2L_6]$.[8,26]

In this study, we attempted to synthesize novel oxygen-bridged CCs with β-diketone based ligands (H_2L1; 6-acetoacetyl-2-pyridinecarboxylic acid, HL5; 2-acetoacetyl pyridine).   The reaction of H_2L1 and HL5 with 3d metal ions resulted in two types of novel hydroxyl-bridged cluster complexes, $[M^{II}_9(L1)_6(OH)_6(sol.)_6]$ (**M$_9$L1,** M =

Co, Ni) and $[Fe^{III}Fe^{II}_6(L5)_6(OH)_6](PF_6)_3$ (**Fe$_7$L5**).   **M$_9$L1** formed a nonanuclear structure with a unique corner-sharing tetrahedra-type hydroxyl-bridged heptad core, $[M_7(\mu_3\text{-}OH)_6]^{8+}$ with terminal mononuclear units.   **M$_7$L5** had an edge-sharing octahedra cluster composed of 7 metal ions on the same plane and 6 hydroxyl ions, which is the same composition as the heptad core of **M$_9$L1**.

The assembled structures of these complexes are unique and similar to the incomplete corner-sharing (vertex-sharing) cobalt-oxo cubane motif and the layered edge sharing CoO_6 octahedra, respectively (**Figure 8**).   Thus, we focused on these hydroxyl-bridged clusters and studied their electrochemical properties.   In Chapter 1, the electrochemical properties of nonanuclear complexes (**M$_9$L1**) are investigated, and attempts were made to regulate their redox potentials by introducing substituents to the ligands.   In Chapter 2, the electrochemical properties of the heptanuclear complexes (**Fe$_7$L5**) were evaluated and regulated by constructing hetero-metal complexes.

corner-sharing tetrahedra cluster

edge-sharing octahedra cluster

Figure 8. Structure of **M$_9$L1** and **Fe$_7$L5**.
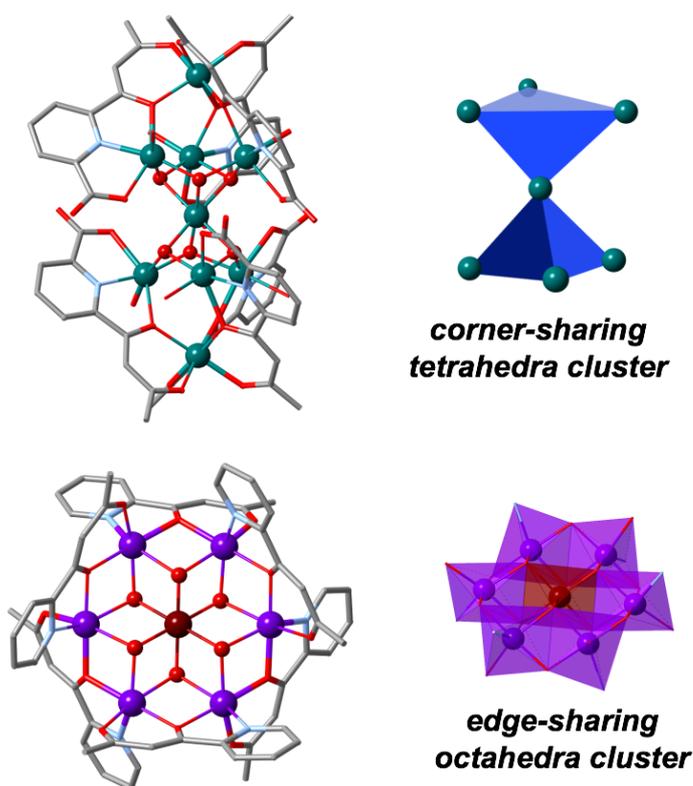
Magnetic Properties of CCs

Several CCs are expected to be applied in molecule-based nanoscale magnetic materials, which are generally described as SMMs. The first report of a single-molecule magnet was the oxo-bridged dodecanuclear manganese cluster, $[Mn_{12}O_{12}(OAc)_{16}(H_2O)_4]$ (**Figure 9**). [27,28] This manganese cluster contains a central oxo-bridged cubane $Mn^{IV}_4O_4$ core surrounded by 8 outer Mn^{III} ions with 8 μ_3-O^{2-} bridges. This cluster showed hysteresis loops with steps at constant magnetic field intervals and a long magnetization relaxation time below 4 K. This was primarily due to the large spin grand state of $S = 10$ derived from magnetic coupling of the 8 Mn^{III} and 4 Mn^{IV} ions and a negative axial anisotropy. Since the discovery of SMM behavior of the dodecanuclear manganese cluster, the magnetic properties of novel multinuclear clusters have been actively studied. The disk-shaped cobalt heptanuclear cluster is the most magnetically studied structural type of Co^{II}-based SMMs.[29-32] These molecules have a disk-shaped structure with a central cobalt ion and 6 surrounding cobalt ions bridged by 6 μ_3-X anions. The first Co_7 disks, $[Co_7(bzp)_6(N_3)_9(CH_3O)_3][ClO_4]_2$ (bzp = 2-benzoyl pyridine), to display slow magnetic relaxation was reported by Gao *et. al.* and are shown in **Figure 10**.[29] These disk-shaped cobalt clusters were synthesized with a variety of ligands, bridging agents (e.g. OH^-, OMe^-, N_3^-), and oxidation states. Slow magnetic relaxation is observed depending on the overall composition, structure, and symmetry of the cluster. Therefore, the development of rational synthetic strategies and systematic syntheses of coordination clusters and elucidation of their magnetism/structure relationships could lead to novel SMMs which can be used higher temperatures.

In Chapter 3, the correlation between magnetism and structure of the hydroxyl-bridged nonanuclear cluster, $[M^{II}_9(L1)_6(OH)_6(sol.)_6]$ (**M₉L1,** M = Co, Ni) and disk-shaped edge-sharing heptanucler nickel clusters $[Ni_7(L5)_6(X)_6](ClO_4)_2$ (**Ni₇L5_X**, X = OH^-, OMe^-, N_3^-) was investigated.
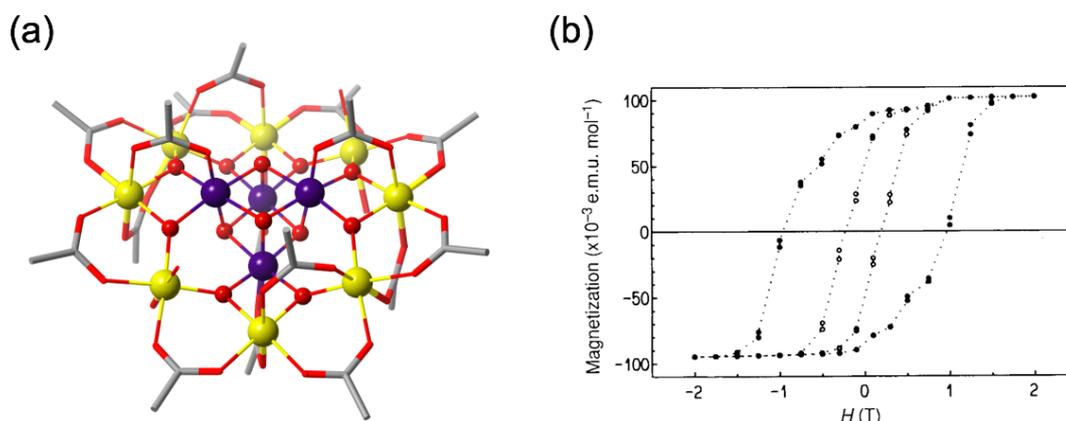
Figure 9. (a) Structure of the dodecanuclear manganese cluster, $[Mn_{12}O_{12}(OAc)_{16}(H_2O)_4]$. (b) Hysteresis loops of $[Mn_{12}O_{12}(OAc)_{16}(H_2O)_4]$ recorded parallel to the c axis with a SQUID magnetometer at 2.2 K (filled circle) and 2.8 K (open circle).[27,28]
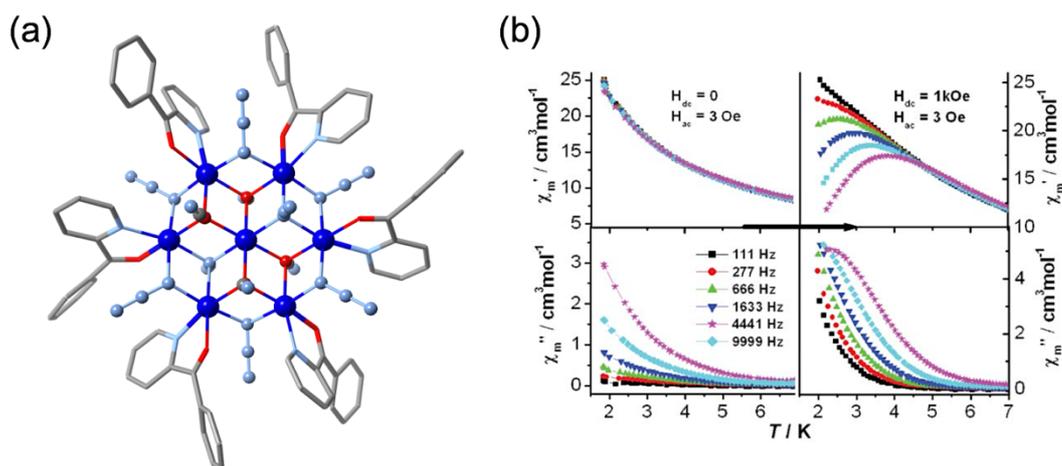
Figure 10. (a) Structure of the disk-shaped cobalt heptanuclear cluster, $[Co_7(bzp)_6(N_3)_9(CH_3O)_3]^{2+}$. (b) Temperature dependence of the real (top) and imaginary (bottom) components of the AC susceptibility. (with zero applied static field (left) and 1 kOe (right) with an oscillating field) [29]

References

1   G. E. Kostakis and A. K. Powell, *Coord. Chem. Rev.*, 2009, **253**, 2686–2697.

2   G. E. Kostakis, A. M. Ako and A. K. Powell, *Chem. Soc. Rev.*, 2010, **39**, 2238.

3   G. E. Kostakis, S. P. Perlepes, V. A. Blatov, D. M. Proserpio and A. K. Powell, *Coord. Chem. Rev.*, 2012, **256**, 1246–1278.

4   Y. Umena, K. Kawakami, J.-R. Shen and N. Kamiya, *Nature*, 2011, **473**, 55–60.

5   T. Spatzal, M. Aksoyoglu, L. Zhang, S. L. A. Andrade, E. Schleicher, S. Weber, D. C. Rees and O. Einsle, *Science*, 2011, **334**, 940–940.

6   M. W. Ribbe, Y. Hu, K. O. Hodgson and B. Hedman, *Chem. Rev.*, 2014, **114**, 4063–4080.

7   R. L. Lintvedt and J. K. Zehetmair, *Inorg. Chem.*, 1990, **29**, 2204–2209.

8   R. W. Saalfrank, V. Seitz, F. W. Heinemann, C. Göbel and R. Herbst-Irmer, *J. Chem. Soc., Dalton Trans.*, 2001, 599–603.

9   T. Shiga, N. Ito, A. Hidaka, H. Ōkawa, S. Kitagawa and M. Ohba, *Inorg. Chem.*, 2007, **46**, 3492–3501.

10   J. O. Bockris and T. Otagwa, *Journal of the Electrochemical Society*, 1984, **131**, 290–302.

11   D. K. Bediako, B. Lassalle-Kaiser, Y. Surendranath, J. Yano, V. K. Yachandra and D. G. Nocera, *J. Am. Chem. Soc.*, 2012, **134**, 6801–6809.

12   R. Subbaraman, D. Tripkovic, K.-C. Chang, D. Strmcnik, A. P. Paulikas, P. Hirunsit, M. Chan, J. Greeley, V. Stamenkovic and N. M. Markovic, *Nature Materials*, 2012, **11**, 550–557.

13   L. Trotochaud, J. K. Ranney, K. N. Williams and S. W. Boettcher, *J. Am. Chem. Soc.*, 2012, **134**, 17253–17261.

14   M. D. Struble, M. T. Scerba, M. Siegler and T. Lectka, *Science*, 2013, **340**, 57–60.

15   A. Grimaud, C. E. Carlton, M. Risch, W. T. Hong, K. J. May and Y. Shao-Horn, *The Journal of Physical Chemistry C*, 2013, **117**, 25926–25932.

16   M. W. Kanan and D. G. Nocera, *Science*, 2008, **321**, 1072–1075.

17   D. A. Lutterman, Y. Surendranath and D. G. Nocera, *J. Am. Chem. Soc.*, 2009, **131**, 3838–3839.

18   M. Risch, V. Khare, I. Zaharieva, L. Gerencser, P. Chernev and H. Dau, *J. Am. Chem. Soc.*, 2009, **131**, 6936–6937.

19   M. W. Kanan, J. Yano, Y. Surendranath, M. Dincă, V. K. Yachandra and D. G. Nocera, *J. Am. Chem. Soc.*, 2010, **132**, 13692–13701.

20   C. Li, M. Wei, D. G. Evans and X. Duan, *Small*, 2014, **10**, 4469–4486.

21   X. Zou, A. Goswami and T. Asefa, *J. Am. Chem. Soc.*, 2013, **135**, 17242–17245.

22   A. M. Ullman and D. G. Nocera, *J. Am. Chem. Soc.*, 2013, **135**, 15053–15061.

23   N. S. McCool, D. M. Robinson, J. E. Sheats and G. C. Dismukes, *J. Am. Chem. Soc.*, 2011, **133**, 11446–11449.

24   S. Berardi, G. La Ganga, M. Natali, I. Bazzan, F. Puntoriero, A. Sartorel, F. Scandola, S. Campagna and M. Bonchio, *J. Am. Chem. Soc.*, 2012, **134**, 11104–11107.

25   F. Evangelisti, R. Güttinger, R. Moré, S. Luber and G. R. Patzke, *J. Am. Chem. Soc.*, 2013, **135**, 18734–18737.

26   T. Shiga, M. Noguchi, H. Sato, T. Matsumoto, G. N. Newton and H. Oshio, *Dalton Trans.*, 2013, **42**, 16185–16193.

27   R. Sessoli, H. L. Tsai, A. R. Schake, S. Wang, J. B. Vincent, K. Folting, D. Gatteschi, G. Christou and D. N. Hendrickson, *J. Am. Chem. Soc.*, 1993, **115**, 1804–1816.

28   R. Sessoli, D. Gatteschi, A. Caneschi and M. A. Novak, *Nature*, 1993, **365**, 141–143.

29   Y.-Z. Zhang, F. Pan, Z.-M. Wang and S. Gao, *Chem. Commun.*, 2006, 3302.

30   X.-T. Wang, B.-W. Wang, Z.-M. Wang, W. Zhang and S. Gao, *Inorg. Chim. Acta*, 2008, **361**, 3895–3902.

31   Y.-L. Zhou, M.-H. Zeng, L.-Q. Wei, B.-W. Li and M. Kurmoo, *Chemistry of Materials*, 2010, **22**, 4295–4303.

32   A. A. Kitos, C. G. Efthymiou, C. Papatriantafyllopoulou, V. Nastopoulos, A. J. Tasiopoulos, M. J. Manos, W. Wernsdorfer, G. Christou and S. P. Perlepes, *Polyhedron*, 2011, **30**, 2987–2996.

Chapter 1

Electrochemical Properties of

Corner-Sharing Tetrahedra Cluster

Based on Asymmetric Multidentate Ligand

Abstract

Novel nonanuclear complexes $[M_9(Ln)_6(OH)_6(sol.)_6]$ (**M_9Ln**, M = Ni, Co, n = 1–4; H_2Ln = 6-actoacetyl-2-pyridinecarboxylic acid derivatives, sol. = MeOH, H_2O), were prepared by a self-assembling reaction. **M_9Ln** formed a unique corner-sharing tetrahedra-type structure with a central hydroxyl-bridged heptanuclear core, $[M_7(\mu_3\text{-}OH)_6]^{8+}$, and terminal mononuclear units, $[M^{II}(L1)_3]^{4-}$, constitute the nonanuclear structure in a [1-7-1] formation. In cyclic voltammetry, **Ni_9Ln** showed quasi-reversible redox waves at 0.48 V and 0.59 V ($vs.$ Fc^+/Fc) attributed to the Ni(III)/Ni(III) of central Ni(II) ion in the heptad core. In the case of **Co_9L1**, two oxidation waves (0.39 V and 0.85 V) and a reduction wave (–0.08 V) were observed. These redox waves are attributed to the Co(III)/Co(II) of central Co(II) ion in the heptad core (0.39 V, –0.08 V) and terminal two Co(II) ions out of the heptad core (0.85 V). This result is confirmed by structural characterization of oxidized species, $[Co^{II}_8Co^{III}(L1)_6(OH)_6(H_2O)_6](ClO_4)$ (**$Co_9L1^+\_ClO_4$**), $[Co^{II}_6Co^{III}_3(L1)_6(OH)_6(H_2O)_6]\text{-}[Ce(NO_3)_6]$ (**$Co_9L1^{3+}\_Ce$**) prepared by chemical oxidation. These electrochemical properties were regulated by introduction of substituents such as *tert*-butyl group and methoxy group in H_2Ln.

Introduction

Oxygen- (oxo- or hydroxyl-) bridged metal-assembled structure is found in metalloenzymes such as Mn_4CaO_5 cluster at oxygen-evolving center in Photosystem II.[1] In the field of artificial water oxidation reaction, metal oxides or hydroxides materials of first-row transition-metal have been attracted much attention, because they are cheap, abundant and efficient catalyst.[2-5] Therefore, oxygen-bridged CCs quarried the unit structure of such catalysts are expected to extract the essence of function and reveal relation between structure and functions.

For these reasons, several oxo-bridged cobalt clusters are reported as a model complex for metal oxide material. $[Co_4O_4(OAc)(py)_4]$ have Co4O4 cubane structure supported by bridging acetate ions and capping pyridine ligands.[6-10,11] These complexes showed catalytic ability for water oxidation reaction in both photochemical and electrochemical condition, and the mechanism of these reaction were investigated in detail. In these systems, efficient charge delocalization in the Co4O4 cluster and open-metal site generated by dissociation of acetate are important for efficient water oxidation reaction.[8] Moreover, Birinchi K. Das et al, reported that redox potential of this cubane cluster could be finely controlled by introduction of substituent to the para position of pyridine ligand (**Figure 1**).[12,13] $[Co^{III}_4(\mu_3\text{-}O)_4(O_2CC_6H_4\text{-}X)_4(py)_4]$ (X = H, Me, OMe, Cl, NO$_2$) showed one-electron oxidation wave at potentials (~0.7 - 1.0 V) that linearly depend on the electronic influence of substituent (X). This means that the redox potentials can be finely controlled by introducing an appropriate substituent.
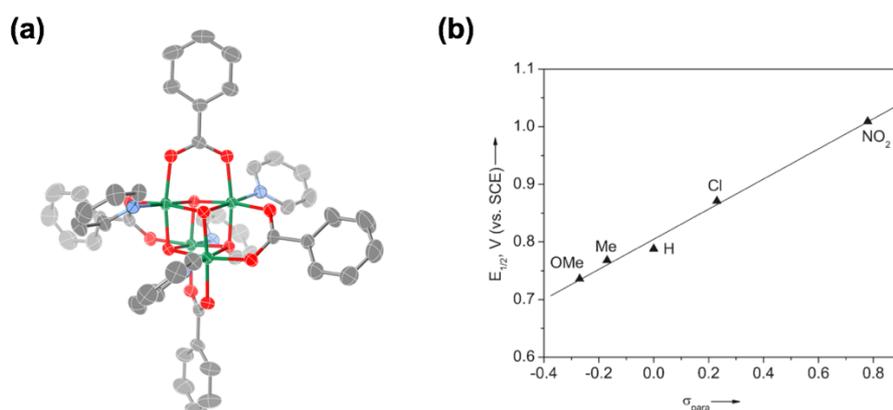
Figure 1. (a) Crystal structure of $[Co^{III}_4(\mu_3\text{-}O)_4(O_2CC_6H_5)_4(py)_4]$. ($Co^{III}$: green; C: gray; O: red; N: light blue) (b) Correlation of Hammett constants σ_{para} for the para substituents on the aryl carboxylates with midpoint potentials ($E_{1/2}$) in $[Co^{III}_4(\mu_3\text{-}O)_4(O_2CC_6H_4\text{-}X)_4(py)_4]$ (X = H, Me, OMe, Cl, NO$_2$).[12,13]

Several oxygen-bridged clusters reported so far is synthesized by a spontaneous self-assembling reaction of metal ions and simple ligand such as acetate-based ligands and pyridine based ligands described above. However, it is difficult to obtain the target structure with such method, because there are so many possible structures in the self-assembly process. Using a rigidity and multidentate ligands such as poly pyridine or poly β-diketonate ligand is effective way to minimize the variability of structures. Moreover, it's useful to construct oxygen-bridged cluster structure by triple-stranded helicate with such ligand. Oxygen-bridged cluster structures can be created by wrapping it with two triplicated mononuclear units constructed by coordination of bidentate site of liner multidentate ligand (**Figure 2a**). This method is more rational than using self-assembling reaction of simple ligands described above and easier than making complicated huge multidentate ligands by complicated organic synthesis. K. Yoneda, M. Okamura and coworkers reported the pentanuclear iron complex $[Fe^{II}_4Fe^{III}(\mu_3\text{-}O)L_6]^{3+}$ (HL = 3,5-bis(2-pyridyl)pyrazole) including oxygen-bridged trinuclear core, $[Fe_3(\mu_3\text{-}O)]$ wrapped by two helicate units, $[FeL_3]$, in a [1-3-1] formation (**Figure 2b**).[14,15] This complex possesses high redox flexibility and catalyzes water oxidation reaction with extraordinary high efficiency (turnover frequency of 1,900 per second). In this reaction, all five Fe ions are redox active and involving the reaction, and adjacent active site of two Fe ions in the oxo-bridged trinuclear core, $[Fe_3(\mu_3\text{-}O)]$ facilitate O-O bond formation. Rolf W. Saalfrank and co-workers were reported the [1-3-3-1] type octanuclear bis(triple-helical) complexes $[M_8O_2L_6]$ (H_2L = 1,1'-(pyridine-2,6-diyl)bis(1-hydroxy-4,4-dimethylpent-1-en-3-one), M = Cd^{2+}, Mn^{2+}, Co^{2+}) (**Figure 2b**).[16,17] In these complexes, two oxygen-bridged trinuclear core $[M_3O]^{4+}$ was flanked by helicate unit, $[ML_3]^{4-}$ based on β-diketonate sites of the ligands. Several other oxygen-bridged CCs with same topology that M_3O core is flanked by helicate unit also have been reported so far.[18,19]
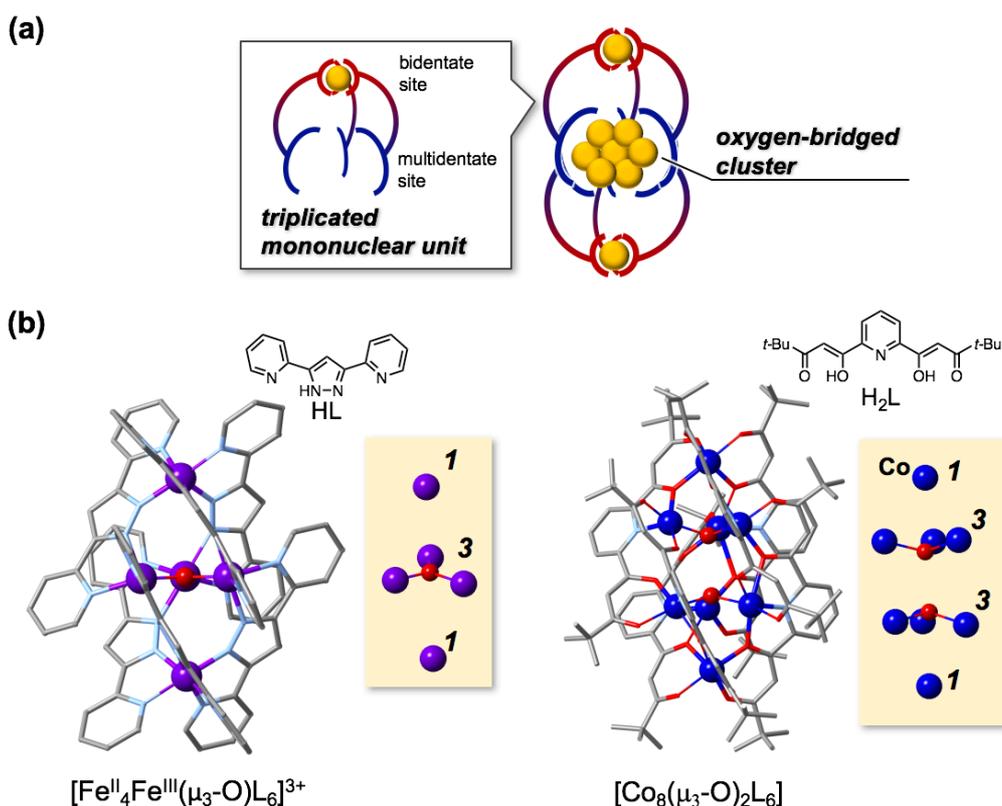
Figure 2. (a) Construction of oxygen-bridged cluster by multidentate ligands. (b) Reported oxo-bridged multinuclear complexes with multidentate ligands.

As described above, oxygen-bridged metal-assembled structure not only gives us an insight into the Mn_4CaO cluster and metal oxide materials, but also can catalyze the reactions such as the water oxidation. For these reasons, we also have synthesized the 3d-metal [1-3-3-1] type octanuclear bis(triple-helical) complex $[M_8O_2L_6]$ (**M_8L**, M = Mn^{II}, Co^{II}, Zn; H_2L = 2,6-diacetoacetyl-pyridine) which have the same topology as octanuclear complexes reported by Rolf W. Saalfrank described above. Although **M_8L** have oxo-bridged trinuclear core, they have no open-metal site, it is necessary to act as catalyst, and they are redox inactive. One of the reasons for this redox inactivity is lack of structural flexibility of entire complex because metal ions in trinuclear core are coordinated rigidly by both 1,6-substituted pyridine site and β-diketone site.

Based on previous studies, we attempted to synthesize a novel oxygen-bridged CCs based on the [1-3] type tetranuclear cluster structure which is the half structure of an octanuclear complexes, $[M_8O_2L_6]$, by using new linear multidentate ligand H_2L1 (6-acetoacetyl-2-pyridinecarboxylic acid), with less coordination site than H_2L. The reaction of H_2L1 and Ni(II) or Co(II) ions derived a novel hydroxyl-bridged nonanuclear complexes $[M_9(L1)_6(OH)_6(H_2O)_6]$ (**M_9L1**: **Figure 3**). **M_9L1** formed a

[1-3-1-3-1] type cluster structure, in which two [1-3] tetranuclear units were connected via a central Ni ion by hydroxyl-bridges. The cluster structure consists of a central hydroxyl-bridged heptad core, $[M_7(\mu_3\text{-}OH)_6]^{8+}$, with a corner-sharing tetrahedra-type structure and two terminal mononuclear M(II) units, $[M(Ln)_3]^{4-}$, in a [1-7-1] formation. Therefore, we investigated the electrochemical and magnetic properties of **M₉L1**. In addition, we examined substituent effects of ligands (H₂L*n*) on the structure, electrochemical and magnetic properties of the resulting complexes.
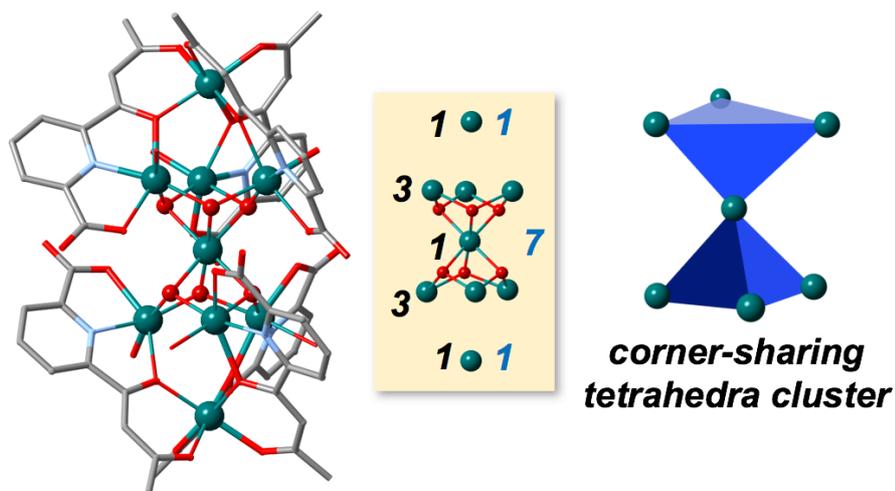
Figure 3. Entire and core structure of $[M_9(L1)_6(OH)_6(H_2O)_6]$ (**M₉L1**).

Experimental Section

Physical measurements

Elemental analyses of carbon, hydrogen and nitrogen were carried out by the staff of technical support division graduate school of science, Kyushu University. UV-Vis absorption was measured by JASCO V-630. Infrared spectra were measured with a JASCO FT/IR-4200 using ATR method. ^{1}H NMR spectra were acquired on a JEOL JNM-ESA 600 spectrometer. Cyclic voltammogram was recorded on an ALS 612D electrochemical analyzer in a degassed acetonitrile solution containing 0.1 M tetra(*n*-butyl)ammonium hexafluorophosphate (TBAPF$_6$) which was purified by recrystallization from ethanol. All electrodes used was purchased from BAS. Platinum electrode was used as counter electrode and glassy carbon electrode was used as working with electrode which was polished with 0.05 μm polishing alumina. As the reference electrode, RE-7 nonaqueous reference electrode (Ag$^+$/Ag) was used. Bulk electrolysis was carried on the platinum electrode as counter electrode, RE-7 nonaqueous electrode (Ag$^+$/Ag) as reference electrode (Ag$^+$/Ag) and porous carbon electrode as the working electrode.

Preparations

All chemicals were purchased from commercial sources and used without further purification.   Dimethyl pyridine 2,6-carboxylate (**a**) and dimethyl 4-methoxypyridine-2,6-dicarboxylate (**b**) were prepared according to literature procedures.[20,21]   The preparation of the 6-acetoacetyl-2-pyridinecarboxylic acid (H_2L1) and its derivatives were carried out in three steps including a Claisen condensation with reference to the literature method.[22]   Synthetic scheme of the ligand is shown in **scheme 1**.
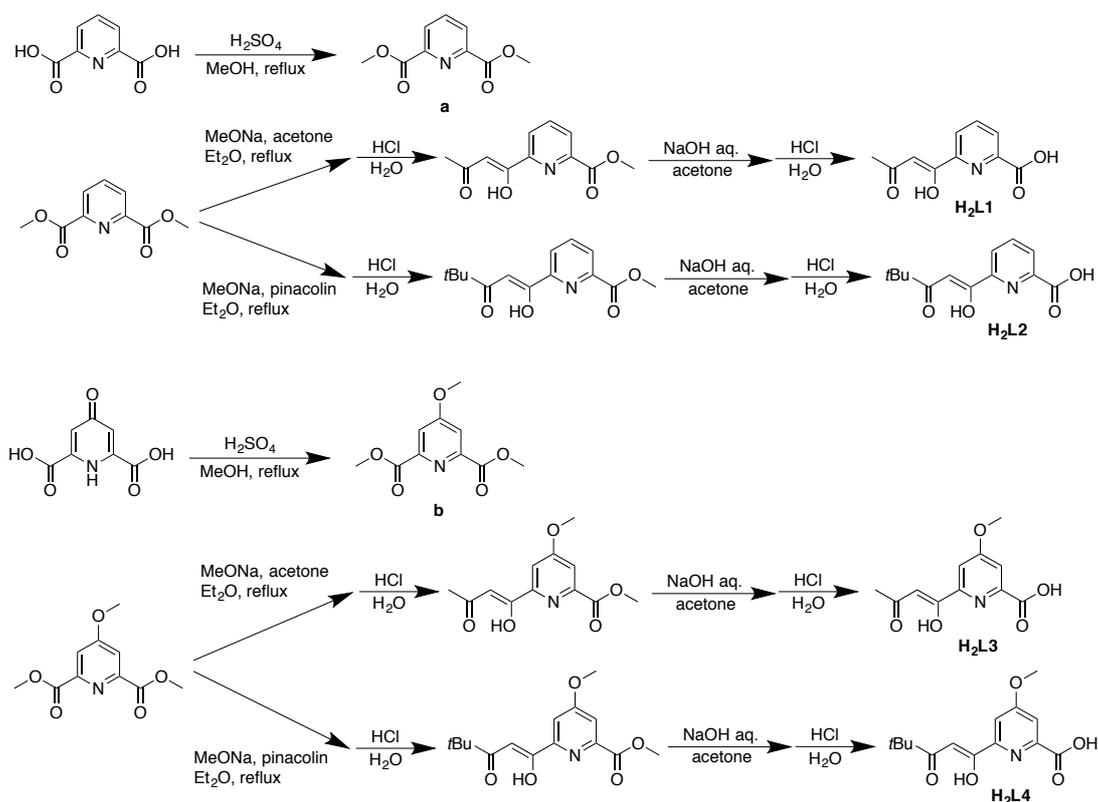
Scheme 1.   Synthetic scheme of 6-acetoacetyl-2-pyridinecarboxylic acid and its derivatives

Dimethyl pyridine-2, 6-dicarboxylate (a) [20]

Pyridine-2, 6-dicarboxylic acid (33.42 g, 0.20 mol) and concentrated sulfuric acid (6.0 g) was added to MeOH (100 ml).   The mixture was refluxed for 3 h, and then cooled to room temperature with stirring.   The white crystals of dimethyl pyridine-2, 6-dicarboxylate was filtrated and washed with MeOH and dried *in vacuo*.
Yield 35.70 g (91.5 %) ^{1}H NMR (600 MHz, CDCl$_3$ δ in ppm): 8.30 (d, 2H, J=7.8 Hz, py), 8.01 (dd, 1H, J=8.1Hz, py), 4.01 (s, 1H, OMe).   Elemental analysis (%); Calcd.

for $C_9H_9NO_4$: C 55.39, H 4.65, N 7.18; found: C 55.31, H 4.60, N 7.16.   FT-IR (cm^{-1}); 1739, 1290, 1163, 996, 755, 694

Dimethyl 4-methoxypyridine-2,6-dicarboxylate (b) [21]

Chelidamic acid monohydrate (16.09 g, 80 mmol) was refluxed in methanol (800 mL) in presence of sulfuric acid (16 mL) for 10 days.   The solvent was concentrated to dryness, and the crude product dissolved in water and neutralized by saturated NaHCO$_3$ solution. It was extracted by dichloromethane, the organic phase dried over Na$_2$SO$_4$ and was evaporated to dryness.   White solid of crude product was purified by column chromatography on silica gel with CHCl$_3$ / MeOH (20:1), and the solvent evaporated to give Dimethyl 4-methoxypyridine-2,6-dicarboxylate.

Yield 12.070 g, (67.0 %). ^{1}H NMR (600 MHz, CDCl$_3$ δ in ppm): 7.80 (s, 2H, py), 4.00 (s, 6H, CO$_2$Me), 3.97 (s, 3H, OMe).   Elemental analysis (%); Calcd. for $C_{10}H_{11}NO_5$: C 53.33, H 4.92, N 6.22; found: C 53.28, H 4.93, N 6.18.   FT-IR (cm^{-1}); 1716, 1604, 1431, 1362, 1268, 1107, 1048, 993, 887, 786

6-acetoacetyl-2-pyridinecarboxylic acid (H$_2$L1)

Compound **a** (9.76 g, 0.05 mol) and 28 % sodium methoxide methanol solution (9.65 g, 0.05 mol) was added to diethyl ether (150 ml).   Acetone (4.36 g, 0.075 mol) in 30 ml of diethyl ether was added dropwise to the mixture.   The yellow precipitate formed after refluxed 4 hours was filtered and washed with diethyl ether and dried *in vacuo*.   After that, yellow powder was dissolved in 100 ml of water and pH was adjusted to 1 by 5M HCl.   Stirring 12 h and yellowish white powder of methyl ester was filtrate and wash with water and dried *in vacuo*.   30 % aqueous NaOH (15 ml) was added to a solution of methyl ester in acetone (150 ml) under stirring at room temperature for 12 h.   The yellow solid was collected by filtration and washed with acetone and dried *in vacuo*.   After that, yellow powder was dissolved in 100 ml of water and pH was adjusted to 1 by 5M HCl.   Yellowish white powder of crude product formed after several hours was collected by filtration and wash with water and dried *in vacuo*.   Crude product was purified by recrystallization from hot EtOH.   Yield 7.701 g (54.43 %). ^{1}H NMR (600 MHz, CDCl$_3$ δ in ppm): 15.64 (s, H, C=C−OH), 8.33-8.35 (m, 2H, py) 8.12 (d, 1H, J=7.8 Hz, py), 6.74 (s, 1H, −CH=), 2.29 (s, 3H, −CH$_3$). Elemental analysis (%); Calcd. for $C_{10}H_9NO_4$: C 57.97, H 4.38, N 6.76; found: C 57.83, H 4.31, N 6.72.   FT-IR (cm^{-1}); 1706, 1617, 1580, 1460, 1422, 1327, 1300, 1249, 942, 779

6-(4,4-dimethyl-3-oxopentanoyl)picolinic acid (H₂L2)

Compound **a** (9.76 g, 0.05 mol) and 28 % sodium methoxide methanol solution (9.65 g, 0.05 mol) was added to diethyl ether (150 ml). Pinacolin (7.51 g, 0.075 mol) in 30 ml of diethyl ether was added dropwise to the mixture. The yellow precipitate formed after refluxed 4 hours was filtered and washed with diethyl ether and dried *in vacuo*. After that, yellow powder was dissolved in 100 ml of water and pH was adjusted to 1 by 5M HCl. Stirring 12 h and yellowish white powder of methyl ester was filtrate and wash with water and dried *in vacuo*. 30 % aqueous NaOH (15 ml) was added to a solution of methyl ester in acetone (150 ml) under stirring at room temperature for 12 h. The yellow solid was collected by filtration and washed with acetone and dried *in vacuo*. After that, yellow powder was dissolved in 100 ml of water and pH was adjusted to 1 by 5M HCl. Yellowish white powder of crude product formed after several hours was collected by filtration and wash with water and dried *in vacuo*. Crude product was purified by recrystallization from hot EtOH. Yield 7.519 g (56.3 %). ^{1}H NMR (600 MHz, CDCl₃ δ in ppm): 16.05 (s, H, C=C−OH), 8.35-8.33 (m, 2H, py) 8.12 (dd, 1H, J=7.8 Hz, py), 6.84 (s, 1H, −CH=), 1.28 (s, 9H, −*t*Bu). Elemental analysis (%); Calcd. for $C_{13}H_{17}NO_5$ (monohydrated): C 58.42, H 6.41, N 5.24; found: C 58.52, H 6.34, N 5.24. FT-IR (cm^{-1}); 1685, 1576, 1317, 1263, 1237, 785, 755, 687

4-methoxy-6-(3-oxobutanoyl)picolinic acid (H₂L3)

Compound **b** (11.26 g, 0.05 mol) and 28 % sodium methoxide methanol solution (9.65 g, 0.05 mol) was added to diethyl ether (150 ml). Acetone (4.36 g, 0.075 mol) in 30 ml of diethyl ether was added dropwise to the mixture. The yellow precipitate formed after refluxed 4 hours was filtered and washed with diethyl ether and dried *in vacuo*. After that, yellow powder was dissolved in 100 ml of water and pH was adjusted to 1 by 5M HCl. Stirring 12 h and yellowish white powder of methyl ester was filtrate and wash with water and dried *in vacuo*. 30 % aqueous NaOH (15 ml) was added to a solution of methyl ester in acetone (150 ml) under stirring at room temperature for 12 h. The yellow solid was collected by filtration and washed with acetone and dried *in vacuo*. After that, yellow powder was dissolved in 100 ml of water and pH was adjusted to 1 by 5M HCl. Yellowish white powder of crude product formed after several hours was collected by filtration and wash with water and dried *in vacuo*. Crude product was purified by recrystallization from hot EtOH. Yield 9.220 g (77.74 %). ^{1}H NMR (600 MHz, CDCl₃ δ in ppm): 15.61 (s, H, C=C−OH), 7.81 (s, 2H, py), 6.71 (s, 1H, −CH=), 4.00 (s, 3H, −OMe), 2.28 (s, 3H, CH₃). Elemental

analysis (%); Calcd. for $C_{11}H_{11}NO_5$: C 55.70, H 4.67, N 5.90; found: C 55.80, H 4.82, N 5.42.　FT-IR (cm^{-1}); 1702, 1583, 1236, 1042, 704

6-(4,4-dimethyl-3-oxopentanoyl)-4-methoxypicolinic acid (H₂L4)

　　　Compound **b** (11.26 g, 0.05 mol) and 28 % sodium methoxide methanol solution (9.65 g, 0.05 mol) was added to diethyl ether (150 ml).　Pinacolin (7.51 g, 0.075 mol) in 30 ml of diethyl ether was added dropwise to the mixture.　The yellow precipitate formed after refluxed 4 hours was filtered and washed with diethyl ether and dried *in vacuo*.　After that, yellow powder was dissolved in 100 ml of water and pH was adjusted to 1 by 5M HCl.　Stirring 12 h and yellowish white powder of methyl ester was filtrate and wash with water and dried *in vacuo*.　30 % aqueous NaOH (15 ml) was added to a solution of methyl ester in acetone (150 ml) under stirring at room temperature for 12 h.　The yellow solid was collected by filtration and washed with acetone and dried *in vacuo*.　After that, yellow powder was dissolved in 100 ml of water and pH was adjusted to 1 by 5M HCl.　Yellowish white powder of crude product formed after several hours was collected by filtration and wash with water and dried *in vacuo*.　Crude product was purified by recrystallization from hot EtOH.　Yield 6.436 g (51.7 %).　^{1}H NMR (600 MHz, CDCl₃ δ in ppm): 16.02 (s, H, C=C−OH), 7.81 (s, 2H, py), 6.81 (s, 1H, −CH=), 4.00 (s, 3H, −OMe), 1.27 (s, 9H, *t*Bu).　Elemental analysis (%); Calcd. for $C_{14}H_{17}NO_5$: C 60.21, H 6.14, N 5.02; found: C 59.62, H 6.13, N 4.94. FT-IR (cm^{-1}); 1694, 1585, 1464, 1334, 1044, 932, 738

[Ni₉(L1)₆(OH)₆(H₂O)₆] (Ni₉L1)

　　　H₂L1 (207 mg, 1.0 mmol) and Et₃N (416 μl) were dissolved in 15 ml of MeOH. Then, NiSO₄·6H₂O (526 mg, 2.0 mmol) in water (5 ml) was added in the methanol solution and stirred for 12 hours. Green solution was concentrated under ambient condition. Green crystals formed within 2 weeks ware collected by filtration and washed with MeOH/H₂O and diethyl ether and dried *in vacuo*.　Yield 110 mg (33.8 %), Elemental analysis (%); Calcd. for $C_{60}H_{60}Ni_9N_6O_{36}$ [Ni₉(L1)₆(OH)₆(H₂O)₆]: C 36.59, H 3.07, N 4.27; found: C 36.67, H 2.66, N 4.37. Formula weight 1969.39　FT-IR (cm^{-1}); 1621, 1591, 1515, 1469, 1410, 1370, 1291, 1145

[Ni₉(L2)₆(OH)₆(H₂O)₆]·2H₂O (Ni₉L2)

　　　H₂L2 (498 mg, 2.0 mmol) and Et₃N (831 μl) were dissolved in 20 ml of MeOH. Then, NiSO₄·6H₂O (1.052 g, 4.0 mmol) in water (5 ml) was added in the methanol solution and stirred for 12 hours.　Green solution was concentrated under ambient

condition.   Green crystals formed within two weeks were collected by filtration and recrystallized from 25 ml of MeOH/H_2O ($v : v$ = 4 : 1).   Green crystals formed were collected and washed with H_2O and dried *in vacuo.*   Yield 110.2 mg (14.6 %), Elemental analysis (%); Calcd. for $C_{78}H_{100}Ni_9N_6O_{38}$ {[$Ni_9(L2)_6(OH)_6(H_2O)_6$]·$2H_2O$}: C 41.49, H 4.46, N 3.72; found: C 41.05, H 4.09, N 3.82.   Formula weight 2257.90. FT-IR (cm^{-1}); 1623, 1594, 1510, 1468, 1413, 1372, 1293, 1116

[Ni$_9$(L3)$_6$(OH)$_6$(H$_2$O)$_6$] (Ni$_9$L3)

H_2L3 (237 mg, 1.0 mmol) and Et_3N (416 μl) were dissolved in 18 ml of MeOH. Then, $NiSO_4$·$6H_2O$ (526 mg, 2.0 mmol) in water (2 ml) was added in the methanol solution and reflux for 24 hours.   Green solution was concentrated under ambient condition.   Green crystals formed within three weeks ware collected by filtration and washed with H_2O and dried *in vacuo.*   Yield 115.0 mg (32.1 %), Elemental analysis (%); Calcd. for $C_{66}H_{72}N_6Ni_9O_{42}$ {[$Ni_9(L3)_6(OH)_6(H_2O)_6$]: C 36.88, H 3.38, N 3.91; found: C 37.38, H 3.20, N 4.01.   Formula weight 2149.54.   FT-IR (cm^{-1}); 1601, 1512, 1469, 1416, 1363, 1231, 1170, 1061

[Ni$_9$(L4)$_6$(OH)$_6$(MeOH)$_2$(H$_2$O)$_4$] (Ni$_9$L4)

H_2L4 (279 mg, 1.0 mmol) and Et_3N (416 μl) were dissolved in 40 ml of MeOH. Then, $NiSO_4$·$6H_2O$ (526 mg, 2.0 mmol) in water (10 ml) was added in the methanol solution and stirred for 12 hours. Green solution was concentrated under ambient condition. Green crystals formed within 7 days ware collected by filtration and washed with MeOH and diethyl ether and dried *in vacuo.*   Yield 242 mg (89.6 %), Elemental analysis (%); Calcd. for $C_{60}H_{92}Ni_9N_6O_{52}$ {[$Ni_9(L4)_6(OH)_6(MeOH)_2(H_2O)_4$]: C 42.51, H 4.65, N 3.46; found: C 42.54, H 4.45, N 3.50.   Formula weight 2430.083.   FT-IR (cm^{-1}); 1598, 1512, 1469, 1416, 1366, 1146, 1106, 1060

[Co$^{II}_9$(L1)$_6$(OH)$_6$(H$_2$O)$_6$]·13H$_2$O (Co$_9$L1)

$CoCl_2$·$6H_2O$ (1.43 g, 6.0 mmol) and H_2L1 (0.83 g, 4 mmol) were mixed in MeOH (8 ml), and pH was adjusted by 1.6 ml of triethylamine.   The mixture was evaporated ambient temperature for a day, and the red crystals were formed.   Crystals were collected by filtration and wash with MeOH and diethyl ether and dried *in vacuo.* Yield 1.029 g (72.3 %) Elemental analysis (%); Calcd. for $C_{60}H_{86}Co_9N_6O_{49}$ {[$Co_9(L1)_6(OH)_6(H_2O)_6$]·$13H_2O$}: C 32.67, H 3.93, N 3.81; found: C 32.76, H 4.12, N 3.81.   Formula weight: 2205.740.   FT-IR (cm^{-1}); 1617, 1588, 1513, 1467, 1407, 1368

[Co^{II}$_9$(L2)$_6$(OH)$_6$(H$_2$O)$_6$]·10H$_2$O (Co$_9$L2)

CoCl$_2$·6H$_2$O (713 mg, 3.0 mmol) and H$_2$L2 (498 mg, 2 mmol) were mixed in MeOH (10 ml), and pH was adjusted by 1.1 ml of triethylamine. The mixture was standing ambient temperature. Red crystals formed within 2 days were collected by filtration and wash with MeOH and diethyl ether and dried *in vacuo*. Yield 580 mg (77.8 %). Elemental analysis (%); Calcd. for C$_{78}$H$_{98}$Co$_9$N$_6$O$_{37}$ {[Co$_9$(L2)$_6$(OH)$_6$(H$_2$O)$_6$]·H$_2$O}: C 41.79, H 4.41, N 3.75; found: C 42.08, H 4.61, N 3.71. Formula weight: 2242.05. FT-IR (cm^{-1}); 1620, 1591, 1516, 1467, 1410, 1368

[Co^{II}$_9$(L3)$_6$(OH)$_6$(H$_2$O)$_6$]·14H$_2$O (Co$_9$L3) (under anaerobic condition)

CoCl$_2$·6H$_2$O (713 mg, 3.0 mmol) and H$_2$L3 (474 mg, 2 mmol) were mixed in MeOH (15 ml), and pH was adjusted by 1.1 ml of triethylamine. The mixture was standing ambient temperature. Red crystals formed within a day were collected by filtration and wash with MeOH and diethyl ether and dried *in vacuo*. Yield 536 mg (64.7 %). Elemental analysis (%); Calcd. for C$_{72}$H$_{112}$Co$_9$N$_6$O$_{56}$ {[Co$_9$(L3)$_6$(OH)$_6$(H$_2$O)$_6$]·14H$_2$O}: C 34.76, H 4.54, N 3.38; found: C 34.47, H 4.34, N 3.66. Formula weight: 2488.07. FT-IR (cm^{-1}); 1596, 1512, 1467, 1420, 1367

[Co^{II}$_9$(L4)$_6$(OH)$_6$(H$_2$O)$_6$]·3H$_2$O (Co$_9$L4)

CoCl$_2$·6H$_2$O (713 mg, 3.0 mmol) and H$_2$L4 (558 mg, 2 mmol) were mixed in MeOH (15 ml), and pH was adjusted by 1.1 ml of triethylamine. The mixture was standing ambient temperature. Red crystals formed within a week were collected by filtration and wash with MeOH and diethyl ether and dried *in vacuo*. Yield 326 mg (35.7 %). Elemental analysis (%); Calcd. for C$_{84}$H$_{114}$Co$_9$N$_6$O$_{45}$ {[Co$_9$(L4)$_6$(OH)$_6$(H$_2$O)$_6$]·3H$_2$O}: C 41.04, H 4.67, N 3.42; found: C 41.06, H 4.77, N 3.41. Formula weight: 2458.23. FT-IR (cm^{-1}); 1598, 1515, 1469, 1420, 1363

[Co^{II}$_8$Co^{III}(L1)$_6$(OH)$_6$(H$_2$O)$_6$](ClO$_4$) (Co$_9$L1$^+$_ClO$_4$)

Co$_9$L1 (1.1 g, 0.5 mmol) and 70 % *tert*-butyl hydroperoxide aqueous solution (1 ml) were mixed in 50 ml of MeOH for a day. tetrabutylammonium perchlorate (171 mg 0.5 mmol) was added to the mixture. Red crystals formed within a week days were collected by filtration and wash with diethyl ether and dried *in vacuo*. Yield 289 mg (27.9 %). Elemental analysis (%); Calcd. for C$_{60}$H$_{60}$ClCo$_9$N$_6$O$_{40}$ {[Co$_9$(L1)$_6$(OH)$_6$(H$_2$O)$_6$](ClO$_4$)}: C 34.80, H 2.92, N 4.06; found: C 34.63, H 3.13, N 3.95. Formula weight: 2070.99. FT-IR (cm^{-1}); 1628, 1592, 1516, 1468, 1411, 1365

[Co$^{II}_6$Co$^{III}_3$(L1)$_6$(OH)$_6$(H$_2$O)$_6$]{Ce(NO$_3$)$_6$}·16H$_2$O (Co$_9$L1^{3+}_Ce)

(NH$_4$)$_2$[Ce(NO$_3$)$_6$] (466 mg, 0.85 mmol) in MeOH (5 ml) was added to the **Co$_9$L1** (200 mg, 0.09 mmol) in MeOH (20 ml), and dark green crystals were formed after a day. Crystals were collected by filtration and wash with diethyl ether and dried *in vacuo*. Yield 196.9 mg (78.9 %). Elemental analysis (%) Calcd. for C$_{60}$H$_{92}$CeCo$_9$N$_{12}$O$_{70}$ {[Co$_9$(L1)$_6$(OH)$_6$(H$_2$O)$_6$]{Ce(NO$_3$)$_6$}·16H$_2$O}: C 26.00, H 3.35, N 6.06; found: C 26.00, H 3.26, N 6.07. Formula weight 2771.93. FT-IR (cm^{-1}); 1629, 1587, 1509, 1462, 1363

[Co$^{II}_6$Co$^{III}_3$(L1)$_6$(OH)$_6$(H$_2$O)$_6$](ClO$_4$)$_3$·10H$_2$O (Co$_9$L1^{3+}_ClO$_4$)

NaClO$_4$ (734 mg, 6.0 mmol) was added to the **Co$_9$L1^{3+}_Ce** (568.1 mg, 0.2 mmol) in H$_2$O (30 ml), and green crystals were formed after a day. Crystals were collected by filtration and wash with diethyl ether and dried *in vacuo*. Yield 272.6 mg (54.3 %). Elemental analysis (%); Calcd. for C$_{60}$H$_{80}$Cl$_3$Co$_9$N$_6$O$_{58}$ {[Co$_9$(L1)$_6$(OH)$_6$(H$_2$O)$_6$](ClO$_4$)$_3$·10H$_2$O}: C 29.41, H 3.29, N 3.43; found: C 29.23, H 3.17, N 3.51. Formula weight: 2450.03. FT-IR (cm^{-1}); 1621, 1589, 1510, 1462, 1363

X-ray Crystallography

All Single-crystal X-ray diffraction data were collected on a Bulker SMART APEX II ULTRA CCD-detector Diffractometer, a rotating-anode (Bruker Tourbo X-ray source) with graphite-monochromated $Mo_{K\alpha}$ radiation (λ = 0.71073 Å) was used. Computations were carried out on a APEX2 crystallographic software package and OLEX2 software. [23]   A single crystal was mounted on a polymer film with liquid paraffin and the temperature kept –173 ℃ under flowing N_2 gas.   All of the structures were solved by direct method or intrinsic method.   All the structures were expanded using Fourier techniques.   Fullmatrixleast-squares refinements were carried out with anisotropic thermal parameters for all non-disordered and non-hydrogen atoms.   The hydrogen atoms were attached based on the difference Fourier map and calculation geometrically.   The SQUEEZE program was used to remove the contribution of the highly disordered solvent molecules from the structural calculations.   Crystal parameters are summarized in **Table 1-5**.

Table 1. Crystallographic parameters of **Ni$_9$L1** and **Ni$_9$L2**

Complex	**Ni$_9$L1**	**Ni$_9$L2**
Formula	C$_{60.19}$H$_{60.18}$N$_6$Ni$_9$O$_{36}$	C$_{81}$H$_{102}$N$_6$Ni$_9$O$_{36}$
Formula weight	1971.90	2264.09
Temperature / K	100	100
Crystal size / mm	0.341 × 0.077 × 0.054	0.238 × 0.085 × 0.084
Crystal system	Monoclinic	Cubic
Space group	$P2_1/n$	$Pa\bar{3}$
a / Å	17.738(2)	28.0844(16)
b / Å	26.380(3)	28.0844(16)
c / Å	21.689(2)	28.0844(16)
α / °	90	90
β / °	95.9356(13)	90
γ / °	90	90
Volume / Å^3	10094.5(19)	22151.(4)
Z value	4	8
D (calcd.) / gcm^{-3}	1.298	1.358
R1	0.0294	0.0805
wR2	0.0800	0.1998
Goodness of Fit	1.074	1.073

Table 2.   Crystallographic parameters of **Ni₉L3** and **Ni₉L4**

Complex	Ni₉L3	Ni₉L4
Formula	$C_{102}H_{99}N_9Ni_{13.5}O_{63}$	$C_{88.39}H_{99.67}N_6Ni_9O_{42.86}$
Formula weight	3251.48	2457.62
Temperature / K	100	100
Crystal size / mm	$0.296 \times 0.08 \times 0.06$	$0.232 \times 0.56 \times 0.052$
Crystal system	monoclinic	Monoclinic
Space group	$C2/c$	$C2/c$
a / Å	43.678(5)	22.931(2)
b / Å	35.508(4)	24.553(3)
c / Å	28.756(3)	21.426(2)
α / °	90	90
β / °	126.189(10)	106.2012(12)
γ / °	90	90
Volume / Å³	35993(7)	11584.(2)
Z value	8	4
D (calcd.) / gcm^{-3}	1.200	1.409
$R1$	0.0803	0.0489
$wR2$	0.2361	0.1461
Goodness of Fit	1.059	1.065

Table 3. Crystallographic parameters of **Co₉L1** and **Co₉L2**

Complex	Co₉L1	Co₉L2
Formula	$C_{60}H_{48}Co_9N_6O_{36}$	$C_{84}H_{107}Co_9N_6O_{36}$
Formula weight	1959.41	2307.12
Temperature / K	100	100
Crystal size / mm	$0.261 \times 0.207 \times 0.136$	$0.22 \times 0.176 \times 0.081$
Crystal system	Monoclinic	Monoclinic
Space group	$P2_1$/n	$P2_1$/n
a / Å	17.909(7)	14.707(2)
b / Å	26.490(11)	45.997(6)
c / Å	21.658(9)	17.916(2)
α / °	90	90
β / °	95.652(5)	98.930(2)
γ / °	90	90
Volume / Å^3	10225(7)	11973(3)
Z value	4	4
D (calcd.) / gcm^{-3}	1.273	1.280
$R1$	0.0390	0.0795
$wR2$	0.0981	0.1690
Goodness of Fit	1.034	1.138

Table 4. Crystallographic parameters of **Co₉L3** and **Co₉L4**

Complex	Co₉L3	Co₉L4
Formula	$C_{72}H_{78}Co_9N_6O_{44}$	$C_{60}H_{120}Co_9N_6O_{42}$
Formula weight	2261.76	2488.28
Temperature / K	100	100
Crystal size / mm	0.144× 0.046 × 0.035	0.164 × 0.072 × 0.046
Crystal system	Monoclinic	Monoclinic
Space group	$C2$/c	$C2$/c
a / Å	33.767(5)	22.842(3)
b / Å	17.372(2)	24.759(3)
c / Å	25.904(4)	21.533(2)
α / °	90	90
β / °	123.8840(10)	106.2280(10)
γ / °	90	90
Volume / Å³	12614(3)	11692(2)
Z value	4	4
D (calcd.) / gcm⁻³	1.191	1.414
R1	0.0629	0.0517
wR2	0.2153	0.1418
Goodness of Fit	1.097	1.025

Table 5. Crystallographic parameters of **Co₉L1⁺_ClO₄** and **Co₉L1³⁺_Ce**

Complex	$\mathbf{Co_9L1^+\_ClO_4}$	$\mathbf{Co_9L1^{3+}\_Ce}$
Formula	$C_{66}H_{66}ClCo_9N_6O_{40}$	$C_{66}H_{66}CeCo_9N_{12}O_{54}$
Formula weight	2149.06	2561.79
Temperature / K	100	100
Crystal size / mm	$0.339 \times 0.124 \times 0.041$	$0.217 \times 0.189 \times 0.076$
Crystal system	Triclinic	Trigonal
Space group	$P\bar{1}$	$R\bar{3}$
a / Å	14.167(4)	14.814(2)
b / Å	26.388(7)	14.814(2)
c / Å	28.704(8)	90.897(14)
α / °	96.514(3)	90
β / °	101.987(4)	90
γ / °	94.669(4)	120
Volume / Å³	10368(5)	17275(6)
Z value	4	6
D (calcd.) / gcm⁻³	1.377	1.477
$R1$	0.0643	0.0432
$wR2$	0.1786	0.1375
Goodness of Fit	1.070	1.085

Results and Discussion

Crystal Structures of Nickel Nonanuclear Complex

The molecular structure of **Ni₉L*n*** is shown in **Figure 4-11**. All nickel complexes, **Ni₉L*n***, has a unique nonanuclear structure with central heptad core and terminal mononuclear units in a [1-7-1] formation that a hydroxyl-bridged heptanuclear Ni(II) core, $[Ni_7(\mu_3\text{-OH})_6]^{8+}$, was flanked by mononuclear Ni(II) units, $[Ni(Ln)_3]^{4-}$. The heptad core of **Ni₉L*n*** is [3M-M-3M] type structure that two trinuclear core is combined with a central Ni(II) by six hydroxyl anions. This is quite different structure form oxygen-bridged cluster sandwiched between triplicated mononuclear unit reported so far which include $[Ni_3(\mu_3\text{-O})]$ or $[Ni_3(\mu_3\text{-OH})]$ type and it can be described $[3M]^{[14,15,18,19]}$ and $[3M\text{-}3M]^{[17,18]}$ type cluster structure respectively. This assembled structure is corner-sharing tetrahedra-type and similar to a "double-cubane structure" which can be vied as two M_4O_4 cubane cores sharing the one metal corner. Cluster complexes having such structures are reported by Mohamedally K. *et al.* and Dominique, L. *et al.* with Cobalt and Nickel ions respectively.[24,25] In the terminal mononuclear units, Ni(II) ion (Ni1, Ni9 for **Ni₉L1**) was in an O6 octahedral coordination geometry with three β-diketonate sites of Ln^{2-}. In the heptad core, six Ni(II) ions (Ni2-Ni4, Ni6-Ni8) were in an O5N1 octahedral coordination environment with a tridentate site of Ln^{2-}, two hydroxyl ions and solvent. The central Ni(II) ion (Ni5) was octahedrally surrounded by six hydroxyl ions and linked with six Ni(II) ions of triad by μ_3-hydroxyl bridges. The average bond distances of Ni-L that are in the range 2.0-2.2 Å, which is typical for Ni(II) ion. The valence of Ni is also supported by bond valence sum (BVS) calculation (**Table 14**).[26]
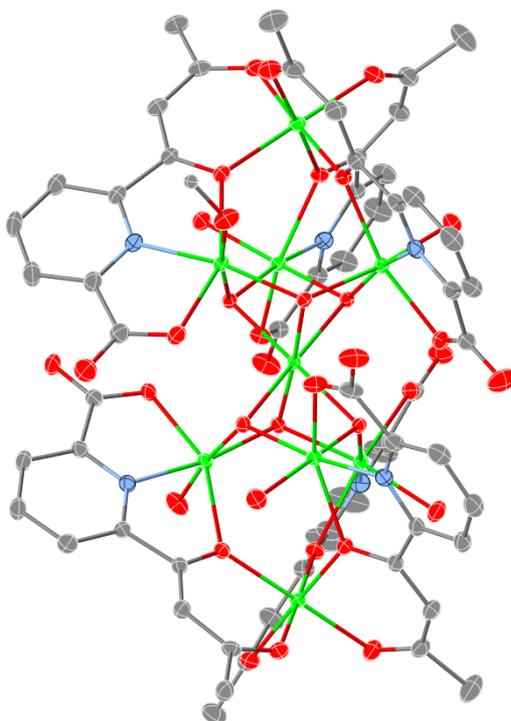
Figure 4.   An ORTEP view of **Ni₉L1**.   H atoms and solvent molecules are omitted for clarity (Ni: light green; C: gray; O: red; and N: light blue).
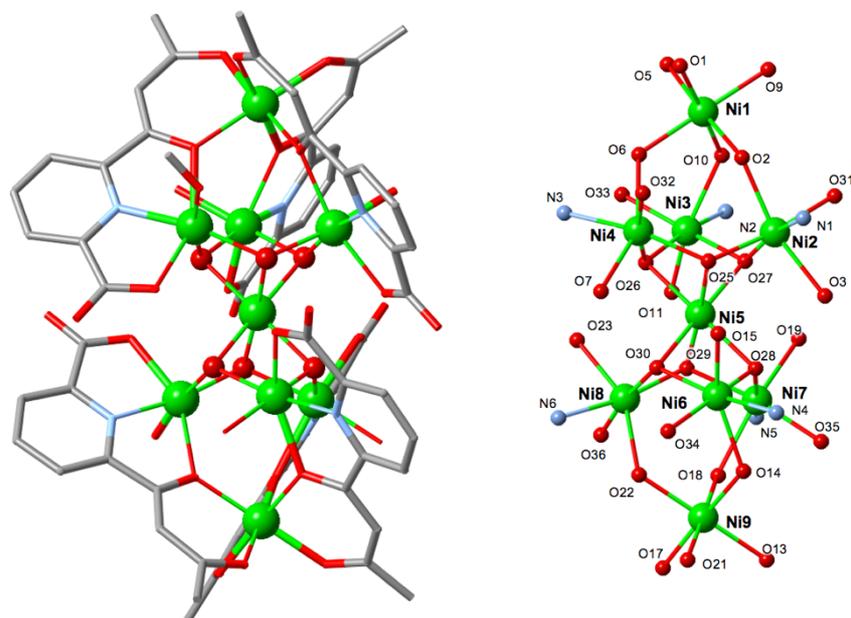

Figure 5.   Molecular structure of **Ni₉L1** (left), and the core (right).   H atoms and solvent molecules are omitted for clarity.

Table 6. Selected bond distances of **Ni₉L1** (Å).

Ni1–O1	2.0312(14)	Ni1–O2	2.0340(13)	Ni1–O5	2.0390(13)
Ni1–O6	2.0383(12)	Ni1–O9	2.0258(13)	Ni1–O10	2.0361(13)
Ni2–N1	2.0105(15)	Ni2–O2	2.2411(13)	Ni2–O3	2.1484(13)
Ni2–O25	2.0272(12)	Ni2–O27	2.0349(12)	Ni2–O31	2.0676(13)
Ni3–N2	2.0033(15)	Ni3–O6	2.2465(13)	Ni3–O7	2.0948(13)
Ni3–O25	2.0340(12)	Ni3–O26	2.0245(12)	Ni3–O32	2.0887(13)
Ni4–N3	2.0126(15)	Ni4–O10	2.2345(13)	Ni4–O11	2.1313(13)
Ni4–O26	2.0157(12)	Ni4–O27	2.0264(12)	Ni4–O33	2.0674(14)
Ni5–O25	2.0762(12)	Ni5–O26	2.0620(12)	Ni5–O27	2.0627(12)
Ni5–O28	2.0794(12)	Ni5–O29	2.0675(12)	Ni5–O30	2.0781(12)
Ni6–N4	2.0078(15)	Ni6–O14	2.2224(13)	Ni6–O15	2.1392(13)
Ni6–O28	2.0235(12)	Ni6–O30	2.0212(12)	Ni6–O34	2.1060(13)
Ni7–N5	2.0160(16)	Ni7–O18	2.2448(13)	Ni7–O19	2.1291(13)
Ni7–O28	2.0292(12)	Ni7–O29	2.0213(12)	Ni7–O35	2.0421(14)
Ni8–N6	2.0053(15)	Ni8–O22	2.2792(13)	Ni8–O23	2.1005(13)
Ni8–O29	2.0085(12)	Ni8–O30	2.0164(12)	Ni8–O36	2.1271(14)
Ni9–O13	2.0355(14)	Ni9–O14	2.0256(13)	Ni9–O17	2.0280(13)
Ni9–O18	2.0374(13)	Ni9–O21	2.0402(13)	Ni9–O22	2.0440(13)

Table 7. Selected bond angles of **Ni₉L1** (°).

O1–Ni1–O2	91.72(5)	O1–Ni1–O5	89.49(6)	O1–Ni1–O6	175.51(5)
O1–Ni1–O10	89.86(5)	O2–Ni1–O5	87.72(5)	O2–Ni1–O6	92.65(5)
O2–Ni1–O10	90.66(5)	O6–Ni1–O5	91.71(5)	O9–Ni1–O1	88.16(6)
O9–Ni1–O2	176.77(5)	O9–Ni1–O5	89.05(6)	O9–Ni1–O6	87.54(5)
O9–Ni1–O10	92.57(5)	O10–Ni1–O5	178.23(5)	O10–Ni1–O6	89.06(5)
N1–Ni2–O2	74.94(5)	N1–Ni2–O3	77.59(6)	N1–Ni2–O25	168.21(6)
N1–Ni2–O27	93.02(5)	N1–Ni2–O31	93.45(6)	O3–Ni2–O2	152.35(5)
O25–Ni2–O2	114.21(5)	O25–Ni2–O3	93.43(5)	O25–Ni2–O27	80.83(5)
O25–Ni2–O31	93.91(5)	O27–Ni2–O2	84.97(5)	O27–Ni2–O3	99.65(5)
O27–Ni2–O31	170.66(5)	O31–Ni2–O2	90.23(5)	O31–Ni2–O3	88.32(5)
N2–Ni3–O6	74.89(5)	N2–Ni3–O7	78.29(6)	N2–Ni3–O25	98.87(5)
N2–Ni3–O26	169.84(6)	N2–Ni3–O32	89.98(6)	O7–Ni3–O6	153.17(5)
O25–Ni3–O6	86.03(5)	O25–Ni3–O7	98.82(5)	O25–Ni3–O32	169.07(5)
O26–Ni3–O6	115.18(5)	O26–Ni3–O7	91.64(5)	O26–Ni3–O25	81.18(5)
O26–Ni3–O32	91.24(5)	O32–Ni3–O6	90.14(5)	O32–Ni3–O7	89.20(5)

N3–Ni4–O10	74.94(6)	N3–Ni4–O11	77.83(6)	N3–Ni4–O26	93.80(6)
N3–Ni4–O27	169.49(6)	N3–Ni4–O33	93.46(6)	O11–Ni4–O10	152.27(5)
O26–Ni4–O10	88.61(5)	O26–Ni4–O11	98.39(5)	O26–Ni4–O27	80.94(5)
O26–Ni4–O33	170.56(6)	O27–Ni4–O10	113.78(5)	O27–Ni4–O11	93.86(5)
O27–Ni4–O33	92.81(5)	O33–Ni4–O10	87.46(5)	O33–Ni4–O11	89.03(6)
O25–Ni5–O28	100.13(5)	O25–Ni5–O30	177.30(5)	O26–Ni5–O25	79.30(5)
O26–Ni5–O27	79.00(5)	O26–Ni5–O28	177.68(5)	O26–Ni5–O29	98.83(5)
O26–Ni5–O30	101.98(5)	O27–Ni5–O25	79.04(5)	O27–Ni5–O28	103.14(5)
O27–Ni5–O29	176.41(5)	O27–Ni5–O30	98.82(5)	O29–Ni5–O25	103.46(5)
O29–Ni5–O28	79.08(5)	O29–Ni5–O30	78.76(5)	O30–Ni5–O28	78.68(5)
N4–Ni6–O14	75.09(6)	N4–Ni6–O15	77.63(6)	N4–Ni6–O28	99.70(5)
N4–Ni6–O30	170.49(6)	N4–Ni6–O34	88.97(6)	O15–Ni6–O14	152.43(5)
O28–Ni6–O14	85.41(5)	O28–Ni6–O15	103.12(5)	O28–Ni6–O34	168.50(5)
O30–Ni6–O14	114.41(5)	O30–Ni6–O15	92.92(5)	O30–Ni6–O28	81.33(5)
O30–Ni6–O34	91.37(5)	O34–Ni6–O14	89.58(5)	O34–Ni6–O15	86.03(5)
N5–Ni7–O18	74.66(6)	N5–Ni7–O19	77.98(6)	N5–Ni7–O28	169.13(6)
N5–Ni7–O29	92.60(6)	N5–Ni7–O35	93.18(6)	O19–Ni7–O18	152.32(5)
O28–Ni7–O18	113.79(5)	O28–Ni7–O19	93.88(5)	O28–Ni7–O35	94.44(6)
O29–Ni7–O18	87.15(5)	O29–Ni7–O19	98.29(5)	O29–Ni7–O28	81.35(5)
O29–Ni7–O35	168.21(5)	O35–Ni7–O18	84.48(5)	O35–Ni7–O19	92.96(5)
N6–Ni8–O22	73.95(5)	N6–Ni8–O23	78.71(6)	N6–Ni8–O29	170.62(6)
N6–Ni8–O30	96.10(5)	N6–Ni8–O36	90.24(6)	O23–Ni8–O22	152.27(5)
O23–Ni8–O36	84.08(6)	O29–Ni8–O22	114.81(5)	O29–Ni8–O23	92.78(5)
O29–Ni8–O30	81.61(5)	O29–Ni8–O36	92.80(5)	O30–Ni8–O22	86.22(5)
O30–Ni8–O23	101.30(5)	O30–Ni8–O36	172.37(5)	O36–Ni8–O22	91.47(5)
O13–Ni9–O18	88.97(6)	O13–Ni9–O21	91.60(6)	O13–Ni9–O22	175.84(5)
O14–Ni9–O13	91.83(5)	O14–Ni9–O17	174.88(5)	O14–Ni9–O18	94.14(5)
O14–Ni9–O21	86.83(5)	O14–Ni9–O22	91.00(5)	O17–Ni9–O13	87.28(6)
O17–Ni9–O18	90.88(5)	O17–Ni9–O21	88.15(5)	O17–Ni9–O22	90.16(5)
O18–Ni9–O21	178.86(5)	O18–Ni9–O22	87.79(5)	O21–Ni9–O22	91.60(5)

Figure 6.   An ORTEP view of **Ni₉L2**.   H atoms and solvent molecules are omitted for clarity (Ni: light green; C: gray; O: red; and N: light blue).

Figure 7.   Molecular structure of **Ni₉L2** (left), and the core (right).   H atoms and solvent molecules are omitted for clarity

Table 8. Selected bond distances of **Ni₉L2** (Å).

Ni1–O1$^{#1}$	2.033(6)	Ni1–O1$^{#2}$	2.033(6)	Ni1–O1	2.033(6)
Ni1–O2	2.022(5)	Ni1–O2$^{#1}$	2.022(5)	Ni1–O2$^{#2}$	2.022(5)
Ni2–N1	2.016(6)	Ni2–O2	2.230(5)	Ni2–O3	2.108(5)
Ni2–O9$^{#2}$	2.029(4)	Ni2–O9	2.005(4)	Ni2–O11	2.096(5)
Ni3–O9	2.059(4)	Ni3–O9$^{#2}$	2.059(4)	Ni3–O9$^{#1}$	2.059(4)
Ni3–O10$^{#1}$	2.071(4)	Ni3–O10	2.071(4)	Ni3–O10$^{#2}$	2.071(4)
Ni4–N2	2.009(5)	Ni4–O6	2.219(4)	Ni4–O7	2.143(5)
Ni4–O10	2.024(4)	Ni4–O10$^{#2}$	2.014(4)	Ni4–O12	2.095(5)
Ni5–O5$^{#2}$	2.028(5)	Ni5–O5	2.028(5)	Ni5–O5$^{#1}$	2.028(5)
Ni5–O6	2.041(4)	Ni5–O6$^{#1}$	2.041(4)	Ni5–O6$^{#2}$	2.041(4)

Symmetry operation (#1) 1/2+Z, 3/2-X, 1-Y; (#2) 3/2-Y, 1-Z, -1/2+X

Table 9. Selected bond angles of **Ni₉L2** (°).

O2$^{#2}$–Ni1–O2$^{#1}$	92.12(18)	O2–Ni1–O2$^{#2}$	92.12(18)	O2–Ni1–O2$^{#1}$	92.12(18)
N1–Ni2–O2	75.4(2)	N1–Ni2–O3	77.4(2)	N1–Ni2–O9$^{#2}$	169.6(2)
N1–Ni2–O11	90.0(2)	O3–Ni2–O2	152.60(18)	O9–Ni2–N1	97.8(2)
O9$^{#2}$–Ni2–O2	114.65(18)	O9–Ni2–O2	86.88(17)	O9–Ni2–O3	100.24(17)
O9$^{#2}$–Ni2–O3	92.67(18)	O9–Ni2–O9$^{#2}$	80.8(2)	O9–Ni2–O11	168.23(19)
O9$^{#2}$–Ni2–O11	93.03(19)	O11–Ni2–O2	86.6(2)	O11–Ni2–O3	90.0(2)
O9$^{#2}$–Ni3–O9$^{#1}$	78.85(18)	O9$^{#2}$–Ni3–O9	78.85(18)	O9$^{#1}$–Ni3–O9	78.85(18)
O9$^{#2}$–Ni3–O10$^{#2}$	99.84(16)	O9$^{#1}$–Ni3–O10$^{#2}$	177.78(16)	O9–Ni3–O10	99.84(16)
O9$^{#1}$–Ni3–O10$^{#1}$	99.84(16)	O9$^{#2}$–Ni3–O10$^{#1}$	102.71(16)	O9–Ni3–O10$^{#1}$	177.77(16)
O9$^{#1}$–Ni3–O10	102.71(16)	O9#2–Ni3–O10	177.78(16)	O9–Ni3–O10$^{#2}$	102.71(16)
O10–Ni3–O10$^{#2}$	78.65(17)	O10–Ni3–O10$^{#1}$	78.66(17)	O10$^{#1}$–Ni3–O10$^{#2}$	78.65(17)
N2–Ni4–O6	75.2(2)	N2–Ni4–O7	77.2(2)	N2–Ni4–O10	170.5(2)
N2–Ni4–O10$^{#2}$	99.33(19)	N2–Ni4–O12	92.4(2)	O7–Ni4–O6	152.29(18)
O10–Ni4–O6	114.33(16)	O10$^{#2}$–Ni4–O6	88.33(16)	O10$^{#2}$–Ni4–O7	98.56(17)
O10–Ni4–O7	93.29(18)	O10$^{#2}$–Ni4–O10	81.1(2)	O10$^{#2}$–Ni4–O12	167.78(19)
O10–Ni4–O12	87.87(18)	O12–Ni4–O6	91.46(18)	O12–Ni4–O7	87.3(2)
O5$^{#1}$–Ni5–O5$^{#2}$	86.8(2)	O5$^{#1}$–Ni5–O5	86.8(2)	O5$^{#2}$–Ni5–O5	86.8(2)
O5$^{#1}$–Ni5–O6$^{#1}$	175.9(2)	O5$^{#2}$–Ni5–O6$^{#1}$	90.95(19)	O5$^{#1}$–Ni5–O6$^{#2}$	89.74(19)
O5$^{#2}$–Ni5–O6$^{#2}$	175.9(2)	O5$^{#1}$–Ni5–O6	90.95(19)	O5–Ni5–O6$^{#2}$	90.95(19)
O5$^{#2}$–Ni5–O6	89.74(19)	O5–Ni5–O6	175.9(2)	O5–Ni5–O6$^{#1}$	89.74(19)
O6$^{#1}$–Ni5–O6$^{#2}$	92.42(17)	O6–Ni5–O6$^{#1}$	92.42(17)	O6–Ni5–O6$^{#2}$	92.42(16)

Symmetry operation (#1) 1/2+Z, 3/2-X, 1-Y; (#2) 3/2-Y, 1-Z, -1/2+X
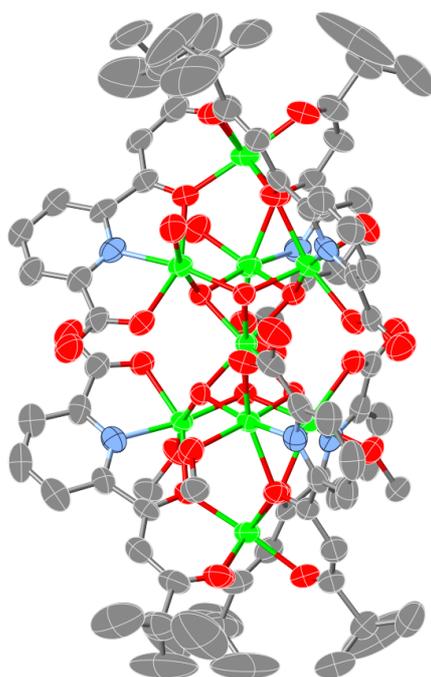
Figure 8.　An ORTEP view of **Ni₉L3**.　H atoms and solvent molecules are omitted for clarity (Ni: light green; C: gray; O: red; and N: light blue).
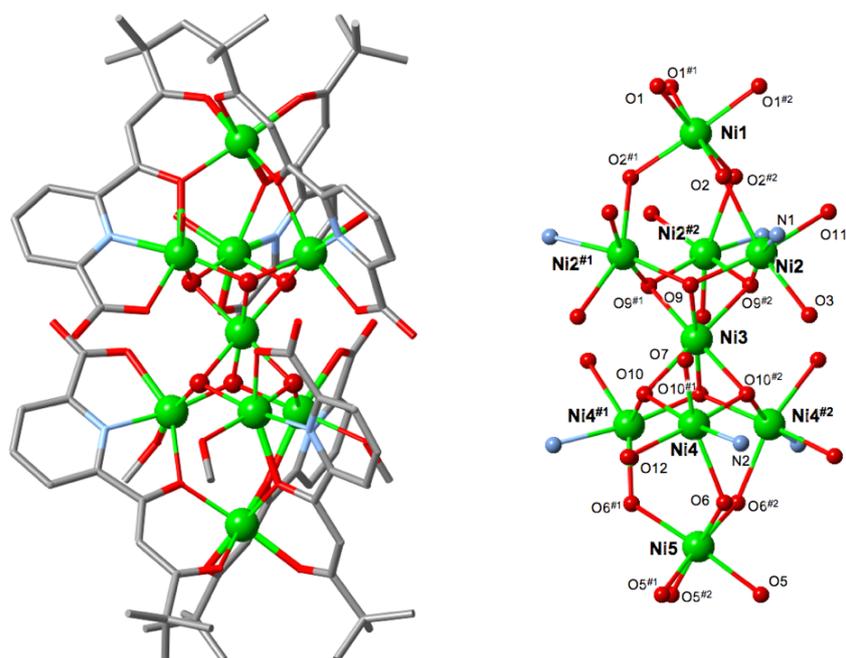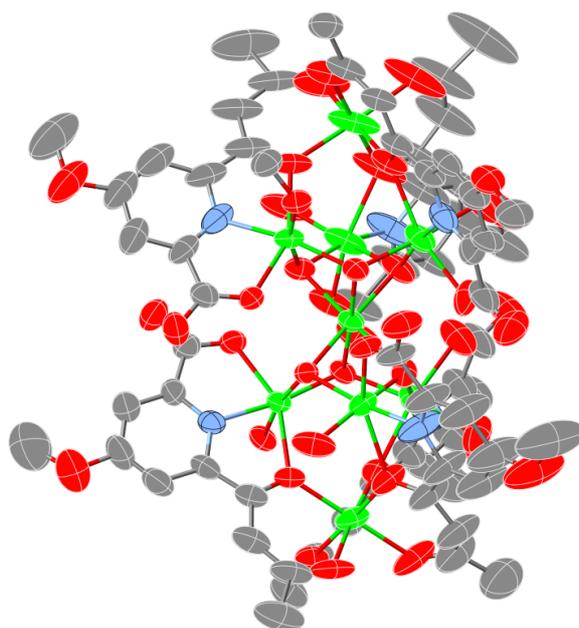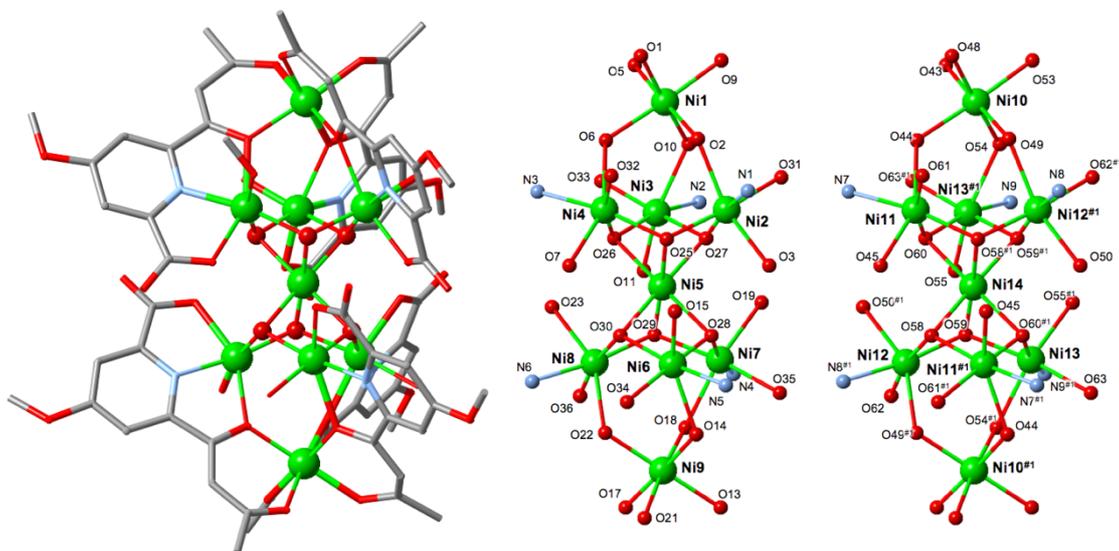

Figure 9.　Molecular structure of **Ni₉L3** (left), and the core (right).　H atoms and solvent molecules are omitted for clarity.

Table 10. Selected bond distances of **Ni₉L3** (Å).

Ni1–O1	2.019(8)	Ni1–O2	2.028(8)	Ni1–O6	2.034(10)
Ni1–O7	2.032(9)	Ni1–O11	2.006(11)	Ni1–O12	2.062(9)
Ni2–N1	2.010(9)	Ni2–O2	2.242(7)	Ni2–O3	2.103(9)
Ni2–O31	2.020(6)	Ni2–O33	2.022(6)	Ni2–O37	2.078(7)
Ni3–N2	1.986(11)	Ni3–O7	2.229(7)	Ni3–O8	2.167(7)
Ni3–O31	2.022(8)	Ni3–O32	2.039(6)	Ni3–O38	2.075(10)
Ni4–N3	2.008(9)	Ni4–O12	2.280(7)	Ni4–O13	2.123(6)
Ni4–O32	2.013(6)	Ni4–O33	2.001(6)	Ni4–O39	2.093(6)
Ni5–O31	2.076(6)	Ni5–O32	2.073(6)	Ni5–O33	2.056(5)
Ni5–O34	2.073(6)	Ni5–O35	2.059(5)	Ni5–O36	2.061(6)
Ni6–N4	2.031(9)	Ni6–O17	2.292(6)	Ni6–O18	2.100(6)
Ni6–O34	2.003(7)	Ni6–O36	2.018(6)	Ni6–O40	2.079(8)
Ni7–N5	2.023(8)	Ni7–O22	2.240(6)	Ni7–O23	2.148(9)
Ni7–O34	2.019(6)	Ni7–O35	2.026(6)	Ni7–O41	2.056(8)
Ni8–N6	2.004(8)	Ni8–O27	2.222(6)	Ni8–O28	2.128(6)
Ni8–O35	2.037(6)	Ni8–O36	2.007(6)	Ni8–O42	2.068(6)
Ni9–O16	2.029(8)	Ni9–O17	2.049(6)	Ni9–O21	2.014(7)
Ni9–O22	2.017(7)	Ni9–O26	2.033(9)	Ni9–O27	2.033(7)
Ni10–O43	2.017(7)	Ni10–O44	2.047(6)	Ni10–O48	2.032(6)
Ni10–O49	2.049(6)	Ni10–O53	2.012(6)	Ni10–O54	2.035(5)
Ni11–N–	1.998(7)	Ni11–O44	2.195(6)	Ni11–O45	2.151(6)
Ni11–O58[#1]	2.036(5)	Ni11–O60	2.020(5)	Ni11–O61	2.104(6)
Ni12[#1]–N8	2.004(7)	Ni12–O49[#1]	2.277(5)	Ni12–O50[#1]	2.139(6)
Ni12–O58	2.017(5)	Ni12–O59	2.014(5)	Ni12–O62	2.064(6)
Ni13[#1]–N9	2.019(6)	Ni13–O54[#1]	2.273(5)	Ni13–O55[#1]	2.111(5)
Ni13–O59	2.014(5)	Ni13–O60[#1]	2.027(5)	Ni13–O63	2.085(6)
Ni14–O58	2.074(5)	Ni14–O58[#1]	2.075(5)	Ni14–O59[#1]	2.061(5)
Ni14–O59	2.061(5)	Ni14–O60[#1]	2.064(5)	Ni14–O60	2.063(5)

Symmetry operation (#1) 1-X, +Y, -1/2-Z

Table 11. Selected bond angles of **Ni₉L3** (°).

O1–Ni1–O2	92.1(3)	O1–Ni1–O6	86.4(4)	O1–Ni1–O7	175.5(3)
O1–Ni1–O12	88.8(3)	O2–Ni1–O6	89.6(4)	O2–Ni1–O7	91.8(4)
O2–Ni1–O12	89.6(3)	O6–Ni1–O12	175.1(4)	O7–Ni1–O6	91.5(4)
O7–Ni1–O12	93.4(3)	O11–Ni1–O1	89.2(4)	O11–Ni1–O2	177.5(5)
O11–Ni1–O6	88.5(6)	O11–Ni1–O7	86.7(5)	O11–Ni1–O12	92.4(5)
N1–Ni2–O2	74.0(3)	N1–Ni2–O3	78.1(4)	N1–Ni2–O31	172.0(4)
N1–Ni2–O33	96.2(3)	N1–Ni2–O37	92.9(3)	O3–Ni2–O2	151.7(3)
O31–Ni2–O2	113.4(3)	O31–Ni2–O3	94.8(3)	O31–Ni2–O33	80.7(2)
O31–Ni2–O37	90.9(3)	O33–Ni2–O2	91.5(2)	O33–Ni2–O3	95.6(3)
O33–Ni2–O37	169.4(4)	O37–Ni2–O2	85.9(3)	O37–Ni2–O3	91.5(4)
N2–Ni3–O7	75.6(4)	N2–Ni3–O8	76.3(3)	N2–Ni3–O31	95.6(4)
N2–Ni3–O32	168.0(4)	N2–Ni3–O38	92.9(5)	O8–Ni3–O7	151.5(3)
O31–Ni3–O7	85.3(3)	O31–Ni3–O8	102.7(3)	O31–Ni3–O32	81.2(3)
O31–Ni3–O38	169.1(3)	O32–Ni3–O7	115.5(3)	O32–Ni3–O8	92.9(3)
O32–Ni3–O38	91.7(3)	O38–Ni3–O7	90.4(4)	O38–Ni3–O8	85.8(3)
N3–Ni4–O12	74.6(4)	N3–Ni4–O13	77.8(3)	N3–Ni4–O32	98.8(3)
N3–Ni4–O39	93.3(3)	O13–Ni4–O12	152.4(3)	O32–Ni4–O12	86.6(3)
O32–Ni4–O13	98.9(2)	O32–Ni4–O39	165.3(3)	O33–Ni4–N3	169.6(3)
O33–Ni4–O12	115.7(3)	O33–Ni4–O13	91.9(2)	O33–Ni4–O32	81.7(2)
O33–Ni4–O39	87.9(2)	O39–Ni4–O12	88.7(3)	O39–Ni4–O13	91.6(2)
O32–Ni5–O31	79.1(3)	O33–Ni5–O31	78.6(2)	O33–Ni5–O32	78.9(2)
O33–Ni5–O34	103.5(2)	O33–Ni5–O35	177.3(2)	O33–Ni5–O36	99.8(2)
O34–Ni5–O31	98.7(3)	O34–Ni5–O32	176.4(2)	O35–Ni5–O31	102.9(2)
O35–Ni5–O32	99.1(2)	O35–Ni5–O34	78.6(2)	O35–Ni5–O36	78.8(2)
O36–Ni5–O31	177.4(3)	O36–Ni5–O32	102.7(2)	O36–Ni5–O34	79.6(2)
N4–Ni6–O17	73.5(3)	N4–Ni6–O18	78.5(3)	N4–Ni6–O40	89.3(5)
O18–Ni6–O17	151.8(2)	O34–Ni6–N4	97.2(4)	O34–Ni6–O17	87.4(3)
O34–Ni6–O18	99.1(3)	O34–Ni6–O36	82.3(2)	O34–Ni6–O40	168.8(3)
O36–Ni6–N4	172.1(3)	O36–Ni6–O17	114.3(2)	O36–Ni6–O18	93.8(2)
O36–Ni6–O40	92.5(3)	O40–Ni6–O17	85.8(3)	O40–Ni6–O18	91.1(3)
N5–Ni7–O22	74.6(3)	N5–Ni7–O23	77.4(3)	N5–Ni7–O35	100.5(3)
N5–Ni7–O41	90.7(4)	O23–Ni7–O22	151.9(3)	O34–Ni7–N5	169.9(3)
O34–Ni7–O22	115.6(3)	O34–Ni7–O23	92.5(3)	O34–Ni7–O35	80.6(2)
O34–Ni7–O41	89.9(3)	O35–Ni7–O22	84.2(2)	O35–Ni7–O23	102.7(3)
O35–Ni7–O41	165.9(4)	O41–Ni7–O22	90.6(3)	O41–Ni7–O23	88.0(4)

|					
N6–Ni8–O27	74.9(3)	N6–Ni8–O28	77.8(3)	N6–Ni8–O35	172.1(3)
N6–Ni8–O36	98.8(3)	N6–Ni8–O42	88.8(3)	O28–Ni8–O27	152.2(3)
O35–Ni8–O27	112.9(3)	O35–Ni8–O28	94.5(3)	O35–Ni8–O42	93.0(2)
O36–Ni8–O27	89.9(2)	O36–Ni8–O28	99.3(2)	O36–Ni8–O35	80.5(2)
O36–Ni8–O42	169.4(3)	O42–Ni8–O27	84.9(2)	O42–Ni8–O28	89.5(3)
O16–Ni9–O17	92.4(3)	O16–Ni9–O26	90.1(4)	O16–Ni9–O27	177.8(3)
O21–Ni9–O16	90.6(3)	O21–Ni9–O17	174.6(3)	O21–Ni9–O22	91.9(3)
O21–Ni9–O26	86.5(3)	O21–Ni9–O27	88.1(3)	O22–Ni9–O16	84.5(4)
O22–Ni9–O17	92.8(3)	O22–Ni9–O26	174.4(3)	O22–Ni9–O27	93.7(3)
O26–Ni9–O17	89.0(3)	O27–Ni9–O17	89.0(3)	O27–Ni9–O26	91.6(3)
O43–Ni10–O44	91.6(3)	O43–Ni10–O48	89.6(3)	O43–Ni10–O49	175.8(3)
O43–Ni10–O54	88.4(2)	O44–Ni10–O49	92.3(2)	O48–Ni10–O44	87.7(2)
O48–Ni10–O49	92.0(2)	O48–Ni10–O54	177.9(2)	O53–Ni10–O43	88.1(3)
O53–Ni10–O44	176.4(3)	O53–Ni10–O48	88.7(3)	O53–Ni10–O49	88.1(2)
O53–Ni10–O54	92.1(2)	O54–Ni10–O44	91.5(2)	O54–Ni10–O49	89.9(2)
N7–Ni11–O44	75.0(3)	N7–Ni11–O45	77.8(3)	N7–Ni11–O58#1	170.3(3)
N7–Ni11–O60	99.3(3)	N7–Ni11–O61	89.2(3)	O45–Ni11–O44	152.2(2)
O58#1–Ni11–O44	114.7(2)	O58#1–Ni11–O45	92.6(2)	O58#1–Ni11–O61	91.9(2)
O60–Ni11–O44	88.8(2)	O60–Ni11–O45	101.3(2)	O60–Ni11–O58#1	80.9(2)
O60–Ni11–O61	169.3(2)	O61–Ni11–O44	87.1(2)	O61–Ni11–O45	86.8(2)
N8#1–Ni12–O49#1	73.1(3)	N8#1–Ni12–O50#1	78.0(3)	N8#1–Ni12–O58	98.3(3)
N8#1–Ni12–O59	170.6(3)	N8#1–Ni12–O62	94.1(3)	O50#1–Ni12–O49#1	151.0(2)
O58–Ni12–O49#1	84.5(2)	O58–Ni12–O50#1	101.5(2)	O58–Ni12–O62	164.6(3)
O59–Ni12–O49#1	116.1(2)	O59–Ni12–O50#1	92.9(2)	O59–Ni12–O58	81.3(2)
O59–Ni12–O62	88.0(2)	O62–Ni12–O49#1	90.4(2)	O62–Ni12–O50#1	89.9(2)
N9#1–Ni13–O54#1	73.9(2)	N9#1–Ni13–O55#1	78.3(2)	N9#1–Ni13–O60#1	172.5(2)
N9#1–Ni13–O63	90.5(3)	O55#1–Ni13–O54#1	152.2(2)	O59–Ni13–N9#1	99.2(2)
O59–Ni13–O54#1	89.3(2)	O59–Ni13–O55#1	95.4(2)	O59–Ni13–O60#1	81.2(2)
O59–Ni13–O63	169.3(2)	O60#1–Ni13–O54#1	113.5(2)	O60#1–Ni13–O55#1	94.3(2)
O60#1–Ni13–O63	89.9(2)	O63–Ni13–O54#1	89.0(2)	O63–Ni13–O55#1	91.0(2)
O58–Ni14–O58#1	98.4(3)	O59#1–Ni14–O58#1	78.8(2)	O59–Ni14–O58	78.8(2)
O59#1–Ni14–O58	176.5(2)	O59–Ni14–O58#1	176.5(2)	O59#1–Ni14–O59	104.0(3)
O59#1–Ni14–O60#1	99.4(2)	O59–Ni14–O60	99.4(2)	O59–Ni14–O60#1	79.2(2)
O59#1–Ni14–O60	79.2(2)	O60–Ni14–O58	102.5(2)	O60–Ni14–O58#1	79.0(2)
O60#1–Ni14–O58	79.0(2)	O60#1–Ni14–O58#1	102.5(2)	O60–Ni14–O60#1	177.7(3)

Symmetry operation (#1) 1-X, +Y, -1/2-Z
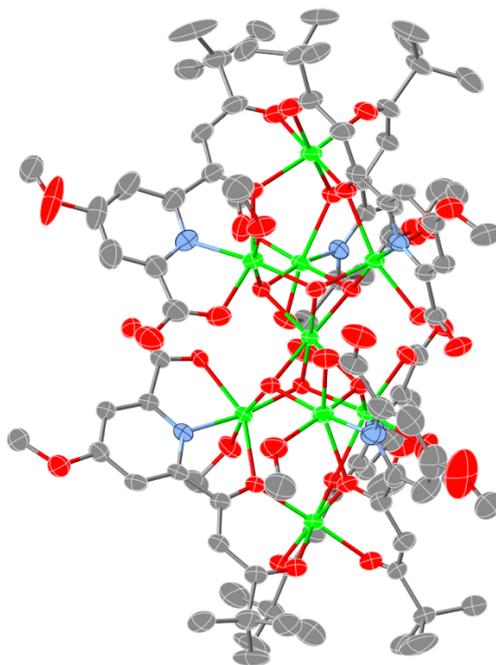
Figure 10. An ORTEP view of **Ni₉L4**. H atoms and solvent molecules are omitted for clarity (Ni: light green; C: gray; O: red; and N: light blue).
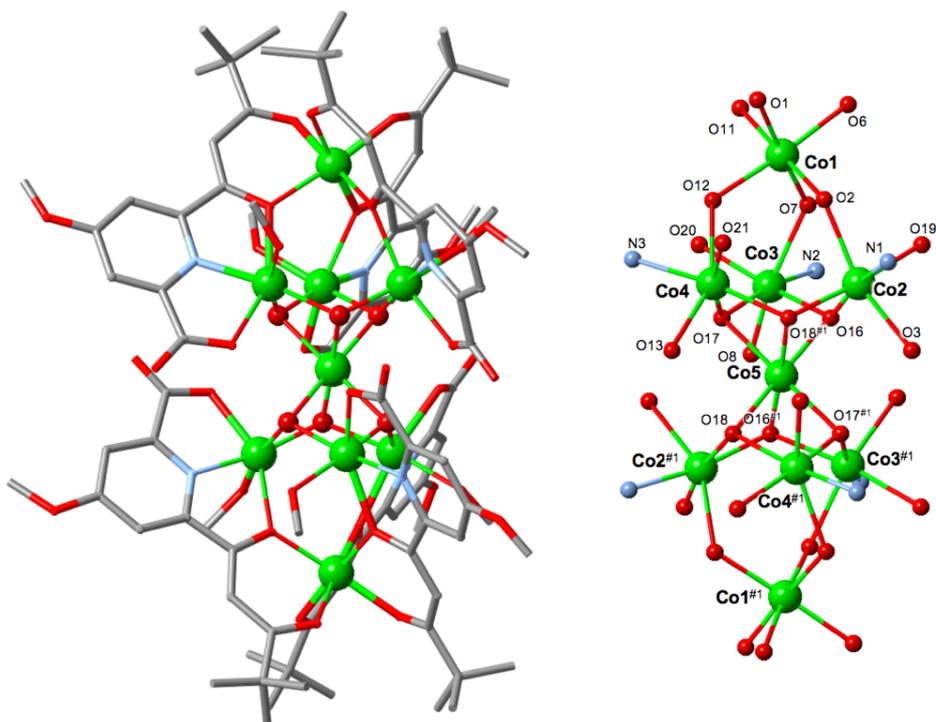

Figure 11. Molecular structure of **Ni₉L4** (left), and the core (right). H atoms and solvent molecules are omitted for clarity.

Table 12. Selected bond distances of **Ni₉L4** (Å).

Ni1–O1	2.021(3)	Ni1–O2	2.029(2)	Ni1–O6	2.024(3)
Ni1–O7	2.033(3)	Ni1–O11	2.032(3)	Ni1–O12	2.042(3)
Ni2–N1	2.010(3)	Ni2–O2	2.239(2)	Ni2–O3	2.128(2)
Ni2–O16	2.024(2)	Ni2–O18$^{\#1}$	2.016(2)	Ni2–O19	2.075(3)
Ni3–N2	2.006(3)	Ni3–O7	2.225(2)	Ni3–O8	2.119(2)
Ni3–O16	2.028(2)	Ni3–O17	2.025(2)	Ni3–O20	2.107(3)
Ni4–N3	2.010(3)	Ni4–O12	2.280(2)	Ni4–O13	2.119(3)
Ni4–O17	2.013(2)	Ni4–O18$^{\#1}$	2.024(2)	Ni4–O21	2.085(3)
Ni5–O16$^{\#1}$	2.067(2)	Ni5–O16	2.067(2)	Ni5–O17$^{\#1}$	2.081(2)
Ni5–O17	2.081(2)	Ni5–O18$^{\#1}$	2.063(2)	Ni5–O18	2.063(2)

Symmetry operation (#1) 1-X, +Y, 1/2-Z

Table 13. Selected bond angles of **Ni₉L4** (°).

O1–Ni1–O2	91.56(10)	O1–Ni1–O6	85.81(12)	O1–Ni1–O7	174.33(11)
O1–Ni1–O11	85.83(11)	O1–Ni1–O12	89.87(11)	O2–Ni1–O7	93.10(9)
O2–Ni1–O11	177.37(10)	O2–Ni1–O12	90.07(10)	O6–Ni1–O2	92.24(10)
O6–Ni1–O7	90.77(11)	O6–Ni1–O11	87.29(12)	O6–Ni1–O12	175.15(11)
O7–Ni1–O12	93.36(10)	O11–Ni1–O7	89.50(10)	O11–Ni1–O12	90.21(11)
N1–Ni2–O2	74.25(10)	N1–Ni2–O3	77.80(10)	N1–Ni2–O16	170.76(11)
N1–Ni2–O18$^{\#1}$	95.15(11)	N1–Ni2–O19	94.72(12)	O3–Ni2–O2	151.71(9)
O16–Ni2–O2	113.97(9)	O16–Ni2–O3	94.23(9)	O16–Ni2–O19	90.03(10)
O18$^{\#1}$–Ni2–O2	90.29(9)	O18$^{\#1}$–Ni2–O3	96.50(9)	O18$^{\#1}$–Ni2–O16	80.98(10)
O18$^{\#1}$–Ni2–O19	168.75(10)	O19–Ni2–O2	87.20(10)	O19–Ni2–O3	90.85(11)
N2–Ni3–O7	74.78(11)	N2–Ni3–O8	77.58(11)	N2–Ni3–O16	98.19(10)
N2–Ni3–O17	168.83(11)	N2–Ni3–O20	93.81(11)	O8–Ni3–O7	152.03(9)
O16–Ni3–O7	86.42(9)	O16–Ni3–O8	101.80(9)	O16–Ni3–O20	164.71(11)
O17–Ni3–O7	116.13(10)	O17–Ni3–O8	91.68(9)	O17–Ni3–O16	80.81(9)
O17–Ni3–O20	89.22(10)	O20–Ni3–O7	87.63(11)	O20–Ni3–O8	89.99(12)
N3–Ni4–O12	74.03(11)	N3–Ni4–O13	78.07(12)	N3–Ni4–O17	101.75(12)
N3–Ni4–O18$^{\#1}$	170.33(12)	N3–Ni4–O21	90.14(13)	O13–Ni4–O12	152.09(10)
O17–Ni4–O12	87.21(9)	O17–Ni4–O13	97.97(10)	O17–Ni4–O18$^{\#1}$	81.31(9)
O17–Ni4–O21	166.00(11)	O18$^{\#1}$–Ni4–O12	115.44(9)	O18$^{\#1}$–Ni4–O13	92.46(10)
O18$^{\#1}$–Ni4–O21	88.17(10)	O21–Ni4–O12	89.01(10)	O21–Ni4–O13	91.66(12)
O16$^{\#1}$–Ni5–O16	102.66(12)	O16$^{\#1}$–Ni5–O17	99.89(9)	O16–Ni5–O17	78.58(9)
O16$^{\#1}$–Ni5–O17$^{\#1}$	78.58(9)	O16–Ni5–O17$^{\#1}$	99.89(9)	O17–Ni5–O17$^{\#1}$	177.60(12)

O18–Ni5–O16$^{\#1}$	78.88(9)	O18$^{\#1}$–Ni5–O16	78.88(9)	O18–Ni5–O16	177.79(8)
O18$^{\#1}$–Ni5–O16$^{\#1}$	177.79(8)	O18$^{\#1}$–Ni5–O17	78.81(9)	O18–Ni5–O17	102.78(9)
O18–Ni5–O17$^{\#1}$	78.81(9)	O18$^{\#1}$–Ni5–O17$^{\#1}$	102.78(9)	O18–Ni5–O18$^{\#1}$	99.62(13)

Symmetry operation (#1) 1-X, +Y, 1/2-Z

Table 14.　Calculated value of valence (V_i)

Complex	Ni1	Ni2	Ni3	Ni4	Ni5	Ni6	Ni7	Ni8	Ni9
Ni$_9$L1	2.15	2.01	2.04	2.04	1.94	2.02	2.05	2.02	2.14
Ni$_9$L2	2.19	2.04	1.98	2.03	2.15				
Ni$_9$L3	2.17	2.06	2.03	2.04	1.97	2.02	2.02	2.06	2.18
Ni$_9$L4	2.17	2.04	2.02	2.02	1.95				
	Ni11	**Ni12**	**Ni13**	**Ni14**	**Ni15**				
Ni$_9$L3	2.16	2.03	2.04	1.91	1.97				

Crystal Structures of Cobalt Nonanuclear Complex

Co₉L*n* also formed the same [1-7-1] structure as **Ni₉L*n*** that a hydroxyl-bridged heptanuclear Co(II) core, $[Co_7(\mu_3\text{-}OH)_6]^{8+}$, was flanked by mononuclear Co(II) units, $[Co(Ln)_3]^{4-}$ (**Figure 12-23**).   The heptad core of **Co₉L*n*** is a corner-sharing tetrahedra-type structure that two trinuclear core is combined with a central Co(II) by six hydroxyl anions and this structure is similar to the one of the proposed structure of cobalt oxide materials (corner-sharing cubane model).[27]   The average bond distances of Co-L that are in the range 2.0-2.3 Å, which is typical for Co(II) ion.   The valence of Co is also supported by bond valence sum (BVS) calculation (**Table 27**).

Co₉L1⁺_ClO₄ which synthesized by oxidation of **Co₉L1** with *t*-butyl hydroperoxide, formed almost the same as **Co₉L1** (**Figure 20, 21**) and included a counter anion (ClO_4^-) in the crystal structure.   Only the average bond distance of central Co ions (Co5, Co14) to O is in the range of 1.9 Å - 2.0 Å which is typical for Co(III) ion.   The valence of Co is also supported by BVS calculation (**Table 27**).   **Co₉L1³⁺_Ce** which synthesized by oxidation of **Co₉L1** with strong oxidant $(NH_3)_2[Ce^{IV}(NO)_6]$ also formed almost the same structure as **Co₉L1** and included $[Ce(NO_3)_6]^{3-}$ as counter anion in the crystal structure (**Figure 22, 23**).   Average bond distance of terminal (Co1) and central (Co3) Co ion to O is in the range of 1.85 Å-1.95 Å and 1.8 Å-1.9 Å respectively, which is typical for Co(III) ion.   This result is supported by BVS calculation (**Table 27**). Therefore, three Co ions with O6 coordination by β-diketonate site and bridging hydroxyl anion was oxidized.   There is a trigonal axis passes through the three Co ions (Co1, Co3, Co1$^{\#8}$) and C_2 axis passes though the Co3.   This highly symmetric structure is attributed to high symmetric d electron configuration (t_{2g}^6) of trivalent cobalt ion and three-fold symmetry of $[Ce(NO_3)_6]^{3-}$.
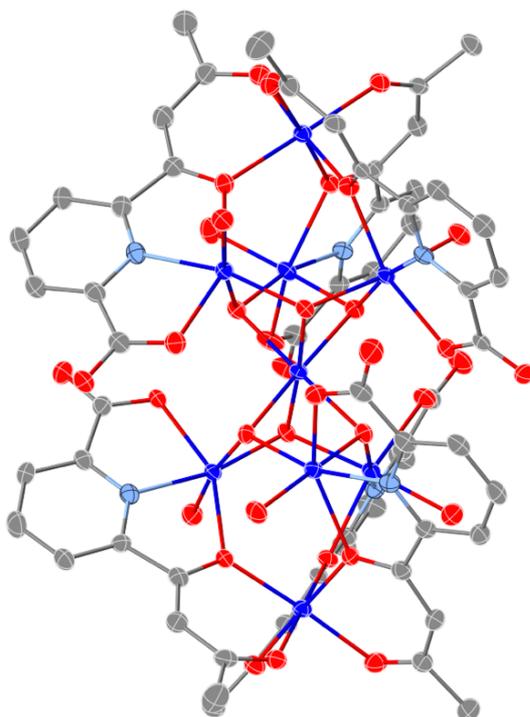
Figure 12. An OETEP view of **Co₉L1**. H atoms and solvent molecules are omitted for clarity (Co: blue; C: gray; O: red; and N: light blue).
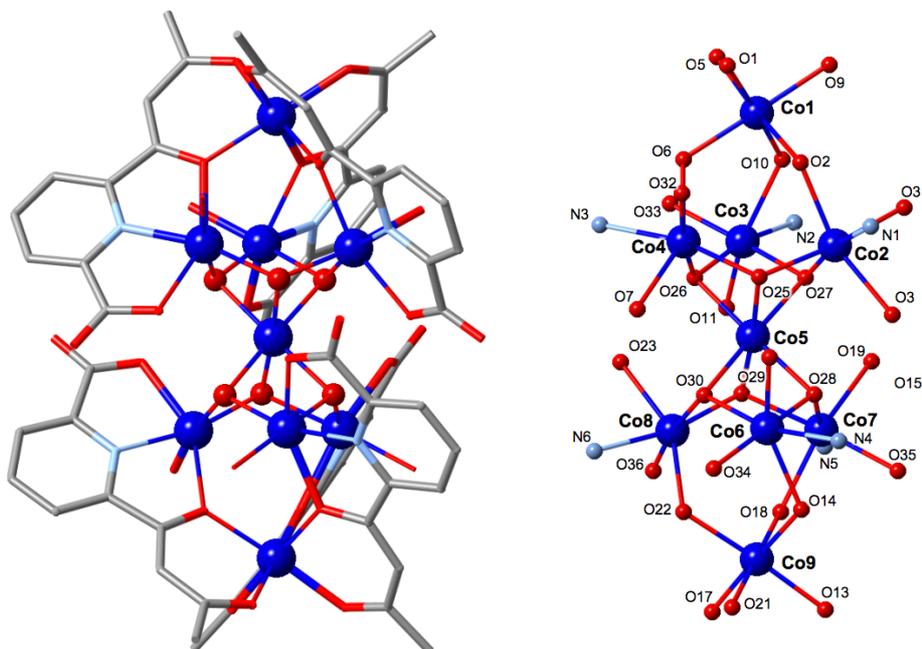

Figure 13. Molecular structure of **Co₉L1** (left), and the core (right). H atoms and solvent molecules are omitted for clarity.

Table 15. Selected bond distances of **Co₉L1** (Å).

Co1–O1	2.052(2)	Co1–O2	2.062(2)	Co1–O5	2.063(2)
Co1–O6	2.081(2)	Co1–O9	2.079(2)	Co1–O10	2.086(2)
Co2–N1	2.059(3)	Co2–O2	2.239(2)	Co2–O3	2.176(2)
Co2–O25	2.078(2)	Co2–O27	2.017(2)	Co2–O31	2.134(2)
Co3–N2	2.066(3)	Co3–O6	2.242(2)	Co3–O7	2.178(3)
Co3–O25	2.021(2)	Co3–O26	2.084(2)	Co3–O32	2.094(2)
Co4–N3	2.060(3)	Co4–O10	2.255(2)	Co4–O11	2.154(2)
Co4–O26	1.992(2)	Co4–O27	2.087(2)	Co4–O33	2.182(2)
Co5–O25	2.089(2)	Co5–O26	2.076(2)	Co5–O27	2.085(2)
Co5–O28	2.074(2)	Co5–O29	2.073(2)	Co5–O30	2.084(2)
Co6–N4	2.061(3)	Co6–O14	2.221(2)	Co6–O15	2.193(2)
Co6–O28	2.115(2)	Co6–O30	2.015(2)	Co6–O34	2.124(2)
Co7–N5	2.070(3)	Co7–O18	2.215(2)	Co7–O19	2.205(2)
Co7–O28	2.018(2)	Co7–O29	2.091(2)	Co7–O35	2.108(3)
Co8–N6	2.062(3)	Co8–O22	2.231(2)	Co8–O23	2.146(2)
Co8–O29	2.018(2)	Co8–O30	2.104(2)	Co8–O36	2.132(3)
Co9–O21	2.084(2)	Co9–O13	2.056(3)	Co9–O14	2.070(2)
Co9–O17	2.053(2)	Co9–O18	2.093(2)	Co9–O22	2.078(2)

Table 16. Selected bond angles of **Co₉L1** (°).

O1–Co1–O2	90.21(10)	O1–Co1–O5	87.43(10)	O1–Co1–O6	89.79(10)
O1–Co1–O9	92.24(10)	O1–Co1–O10	176.60(9)	O2–Co1–O5	175.33(10)
O2–Co1–O6	95.55(9)	O2–Co1–O9	87.27(10)	O2–Co1–O10	92.69(9)
O5–Co1–O6	88.47(10)	O5–Co1–O9	88.79(10)	O5–Co1–O10	89.80(10)
O6–Co1–O10	88.16(9)	O9–Co1–O6	176.52(9)	O9–Co1–O10	89.68(9)
N1–Co2–O2	73.91(10)	N1–Co2–O3	75.51(10)	N1–Co2–O25	98.04(10)
N1–Co2–O31	90.36(10)	O3–Co2–O2	149.29(8)	O25–Co2–O2	85.28(9)
O25–Co2–O3	101.75(9)	O25–Co2–O31	169.65(9)	O27–Co2–N1	169.85(10)
O27–Co2–O2	116.00(9)	O27–Co2–O3	94.68(9)	O27–Co2–O25	81.23(9)
O27–Co2–O31	91.55(9)	O31–Co2–O2	91.31(9)	O31–Co2–O3	86.15(10)
N2–Co3–O6	73.96(10)	N2–Co3–O7	76.07(11)	N2–Co3–O26	90.45(10)
N2–Co3–O32	93.57(11)	O7–Co3–O6	149.73(9)	O25–Co3–N2	165.55(10)
O25–Co3–O6	116.63(9)	O25–Co3–O7	93.62(9)	O25–Co3–O26	80.88(9)
O25–Co3–O32	96.95(9)	O26–Co3–O6	86.38(9)	O26–Co3–O7	98.04(9)
O26–Co3–O32	169.70(9)	O32–Co3–O6	85.63(9)	O32–Co3–O7	92.13(10)

|					
N3–Co4–O10	73.54(10)	N3–Co4–O11	76.15(10)	N3–Co4–O27	94.36(10)
N3–Co4–O33	91.83(10)	O11–Co4–O10	149.36(9)	O11–Co4–O33	82.57(10)
O26–Co4–N3	167.04(10)	O26–Co4–O10	117.81(9)	O26–Co4–O11	92.82(9)
O26–Co4–O27	80.86(9)	O26–Co4–O33	93.47(10)	O27–Co4–O10	86.09(9)
O27–Co4–O11	100.73(10)	O27–Co4–O33	173.53(9)	O33–Co4–O10	93.88(9)
O26–Co5–O25	79.51(9)	O26–Co5–O27	78.98(9)	O26–Co5–O30	103.48(9)
O27–Co5–O25	79.41(9)	O28–Co5–O25	103.51(9)	O28–Co5–O26	175.12(9)
O28–Co5–O27	97.70(9)	O28–Co5–O29	79.74(9)	O28–Co5–O30	80.00(9)
O29–Co5–O25	176.32(9)	O29–Co5–O26	97.38(9)	O29–Co5–O27	101.99(9)
O29–Co5–O30	80.19(9)	O30–Co5–O25	98.57(9)	O30–Co5–O27	176.55(9)
N4–Co6–O14	74.58(10)	N4–Co6–O15	75.42(10)	N4–Co6–O28	91.17(10)
N4–Co6–O34	94.18(11)	O15–Co6–O14	149.83(9)	O28–Co6–O14	84.85(9)
O28–Co6–O15	98.99(9)	O28–Co6–O34	172.78(9)	O30–Co6–N4	164.48(10)
O30–Co6–O14	117.32(9)	O30–Co6–O15	92.78(9)	O30–Co6–O28	80.60(9)
O30–Co6–O34	95.26(10)	O34–Co6–O14	91.88(10)	O34–Co6–O15	87.07(9)
N5–Co7–O18	74.60(10)	N5–Co7–O19	75.13(10)	N5–Co7–O29	91.24(10)
N5–Co7–O35	95.38(11)	O19–Co7–O18	149.21(9)	O28–Co7–N5	165.76(10)
O28–Co7–O18	116.40(9)	O28–Co7–O19	94.38(9)	O28–Co7–O29	80.59(9)
O28–Co7–O35	93.85(10)	O29–Co7–O18	88.00(9)	O29–Co7–O19	98.13(9)
O29–Co7–O35	171.87(10)	O35–Co7–O18	89.21(10)	O35–Co7–O19	88.15(10)
N6–Co8–O22	74.41(10)	N6–Co8–O23	75.95(10)	N6–Co8–O30	97.30(10)
N6–Co8–O36	89.92(10)	O23–Co8–O22	150.32(9)	O29–Co8–N6	167.16(11)
O29–Co8–O22	117.93(9)	O29–Co8–O23	91.56(9)	O29–Co8–O30	81.00(9)
O29–Co8–O36	92.92(9)	O30–Co8–O22	85.44(9)	O30–Co8–O23	96.74(9)
O30–Co8–O36	171.56(9)	O36–Co8–O22	92.34(9)	O36–Co8–O23	89.23(10)
O21–Co9–O18	179.13(9)	O13–Co9–O21	89.14(10)	O13–Co9–O14	89.52(9)
O13–Co9–O18	90.72(10)	O13–Co9–O22	176.56(9)	O14–Co9–O21	88.14(9)
O14–Co9–O18	92.72(9)	O14–Co9–O22	93.68(9)	O17–Co9–O21	89.07(10)
O17–Co9–O13	88.99(10)	O17–Co9–O14	176.86(10)	O17–Co9–O18	90.07(9)
O17–Co9–O22	87.75(9)	O22–Co9–O21	89.72(10)	O22–Co9–O18	90.36(9)
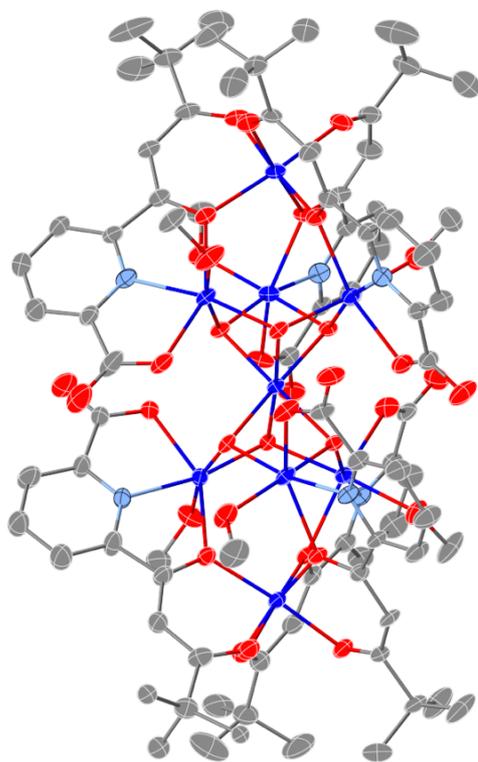
Figure 14. An OETEP view of **Co₉L2**. H atoms and solvent molecules are omitted for clarity (Co: blue; C: gray; O: red; and N: light blue).
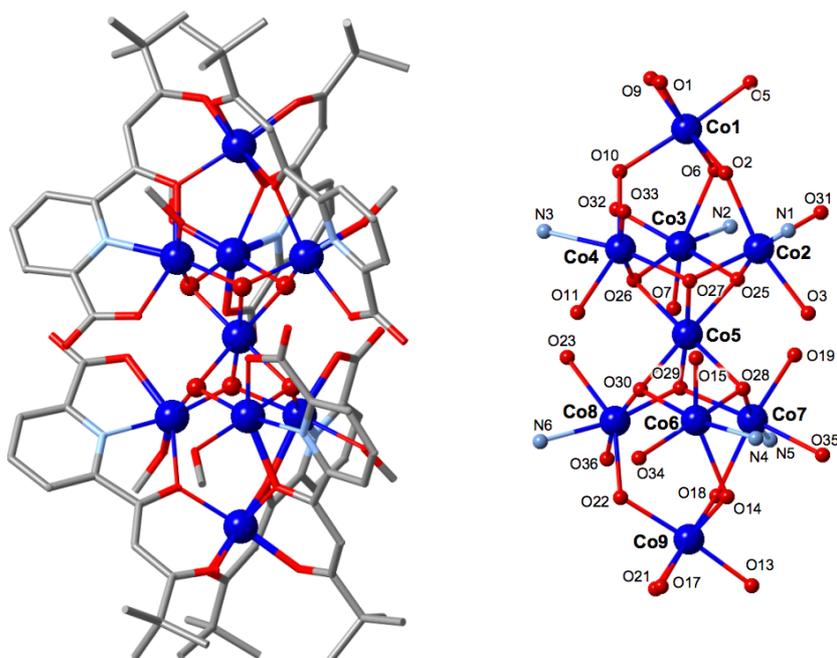

Figure 15. Molecular structure of **Co₉L2** (left), and the core (right). H atoms and solvent molecules are omitted for clarity.

Table 17. Selected bond distances of **Co₉L2** (Å).

Co1–O1	2.051(3)	Co1–O2	2.078(3)	Co1–O5	2.052(4)
Co1–O6	2.068(3)	Co1–O9	2.057(4)	Co1–O10	2.065(4)
Co2–N1	2.084(4)	Co2–O2	2.228(3)	Co2–O3	2.191(4)
Co2–O25	2.025(3)	Co2–O27	2.075(3)	Co2–O31	2.114(4)
Co3–N2	2.078(4)	Co3–O6	2.230(3)	Co3–O7	2.165(3)
Co3–O25	2.091(3)	Co3–O26	2.004(3)	Co3–O32	2.119(4)
Co4–N3	2.078(4)	Co4–O10	2.258(3)	Co4–O11	2.157(4)
Co4–O26	2.081(3)	Co4–O27	2.022(3)	Co4–O33	2.101(4)
Co5–O25	2.099(3)	Co5–O26	2.099(3)	Co5–O27	2.109(3)
Co5–O28	2.106(3)	Co5–O29	2.105(3)	Co5–O30	2.090(3)
Co6–N4	2.078(4)	Co6–O14	2.238(3)	Co6–O15	2.154(4)
Co6–O28	2.084(3)	Co6–O30	2.013(3)	Co6–O34	2.108(4)
Co7–N5	2.068(4)	Co7–O18	2.237(3)	Co7–O19	2.156(4)
Co7–O28	2.025(3)	Co7–O29	2.086(3)	Co7–O35	2.130(4)
Co8–N6	2.069(4)	Co8–O22	2.230(3)	Co8–O23	2.177(3)
Co8–O29	2.013(3)	Co8–O30	2.091(3)	Co8–O36	2.116(4)
Co9–O13	2.039(3)	Co9–O14	2.077(3)	Co9–O17	2.056(4)
Co9–O18	2.080(3)	Co9–O21	2.061(4)	Co9–O22	2.074(3)

Table 18. Selected bond angles of **Co₉L2** (°).

O1–Co1–O2	89.25(14)	O1–Co1–O5	87.31(15)	O1–Co1–O6	174.95(14)
O1–Co1–O9	85.16(14)	O1–Co1–O10	91.26(14)	O5–Co1–O2	88.84(15)
O5–Co1–O6	89.15(14)	O5–Co1–O9	86.73(16)	O5–Co1–O10	175.86(15)
O6–Co1–O2	94.29(13)	O9–Co1–O2	173.02(14)	O9–Co1–O6	91.03(14)
O9–Co1–O10	89.28(14)	O10–Co1–O2	95.03(13)	O10–Co1–O6	92.02(13)
N1–Co2–O2	73.52(14)	N1–Co2–O3	75.28(15)	N1–Co2–O31	91.98(16)
O3–Co2–O2	148.80(13)	O25–Co2–N1	168.55(15)	O25–Co2–O2	117.88(12)
O25–Co2–O3	93.31(13)	O25–Co2–O27	81.27(13)	O25–Co2–O31	89.00(15)
O27–Co2–N1	98.92(15)	O27–Co2–O2	87.76(12)	O27–Co2–O3	96.63(13)
O27–Co2–O31	168.08(15)	O31–Co2–O2	90.74(14)	O31–Co2–O3	90.77(15)
N2–Co3–O6	73.30(14)	N2–Co3–O7	75.76(15)	N2–Co3–O25	96.78(15)
N2–Co3–O32	93.86(16)	O7–Co3–O6	149.03(13)	O25–Co3–O6	88.26(13)
O25–Co3–O7	96.79(13)	O25–Co3–O32	168.16(14)	O26–Co3–N2	167.06(15)
O26–Co3–O6	119.42(13)	O26–Co3–O7	91.55(13)	O26–Co3–O25	81.97(13)
O26–Co3–O32	88.82(14)	O32–Co3–O6	89.82(14)	O32–Co3–O7	90.86(15)

| N3–Co4–O10	72.87(15)	N3–Co4–O11	76.56(16)	N3–Co4–O26	93.42(15)
N3–Co4–O33	97.23(17)	O11–Co4–O10	149.29(13)	O26–Co4–O10	87.32(12)
O26–Co4–O11	97.43(14)	O26–Co4–O33	167.07(17)	O27–Co4–N3	168.35(16)
O27–Co4–O10	117.24(13)	O27–Co4–O11	93.47(14)	O27–Co4–O26	81.77(12)
O27–Co4–O33	89.06(14)	O33–Co4–O10	88.81(14)	O33–Co4–O11	92.19(17)
O25–Co5–O27	78.75(12)	O25–Co5–O28	98.02(13)	O25–Co5–O29	103.65(12)
O26–Co5–O25	79.55(13)	O26–Co5–O27	79.33(12)	O26–Co5–O28	176.06(12)
O26–Co5–O29	98.18(12)	O28–Co5–O27	103.32(12)	O29–Co5–O27	176.25(12)
O29–Co5–O28	79.32(12)	O30–Co5–O25	176.12(13)	O30–Co5–O26	102.97(12)
O30–Co5–O27	98.72(13)	O30–Co5–O28	79.62(12)	O30–Co5–O29	79.03(12)
N4–Co6–O14	73.22(14)	N4–Co6–O15	75.86(15)	N4–Co6–O28	95.74(15)
N4–Co6–O34	95.14(16)	O15–Co6–O14	148.95(13)	O28–Co6–O14	86.86(12)
O28–Co6–O15	99.09(14)	O28–Co6–O34	166.84(16)	O30–Co6–N4	168.82(15)
O30–Co6–O14	117.40(13)	O30–Co6–O15	93.64(13)	O30–Co6–O28	81.94(13)
O30–Co6–O34	88.75(14)	O34–Co6–O14	89.21(15)	O34–Co6–O15	90.73(17)
N5–Co7–O18	73.71(14)	N5–Co7–O19	75.67(15)	N5–Co7–O29	99.68(14)
N5–Co7–O35	90.12(15)	O19–Co7–O18	149.29(13)	O28–Co7–N5	170.08(15)
O28–Co7–O18	116.20(13)	O28–Co7–O19	94.43(13)	O28–Co7–O29	81.63(12)
O28–Co7–O35	89.57(13)	O29–Co7–O18	87.47(12)	O29–Co7–O19	95.32(14)
O29–Co7–O35	169.03(14)	O35–Co7–O18	90.59(14)	O35–Co7–O19	91.86(16)
N6–Co8–O22	73.90(14)	N6–Co8–O23	75.09(15)	N6–Co8–O30	99.97(16)
N6–Co8–O36	91.23(17)	O23–Co8–O22	148.97(13)	O29–Co8–N6	167.71(15)
O29–Co8–O22	118.38(12)	O29–Co8–O23	92.62(13)	O29–Co8–O30	81.14(13)
O29–Co8–O36	89.38(14)	O30–Co8–O22	87.00(13)	O30–Co8–O23	97.14(13)
O30–Co8–O36	166.87(15)	O36–Co8–O22	89.56(15)	O36–Co8–O23	92.33(16)
O13–Co9–O14	88.83(13)	O13–Co9–O17	84.92(14)	O13–Co9–O18	89.16(14)
O13–Co9–O21	88.36(15)	O13–Co9–O22	175.51(15)	O14–Co9–O18	93.99(14)
O17–Co9–O14	172.91(14)	O17–Co9–O18	89.26(15)	O17–Co9–O21	87.19(16)
O17–Co9–O22	91.43(14)	O21–Co9–O14	89.30(15)	O21–Co9–O18	175.84(14)
O21–Co9–O22	88.87(14)	O22–Co9–O14	94.66(14)	O22–Co9–O18	93.40(13)
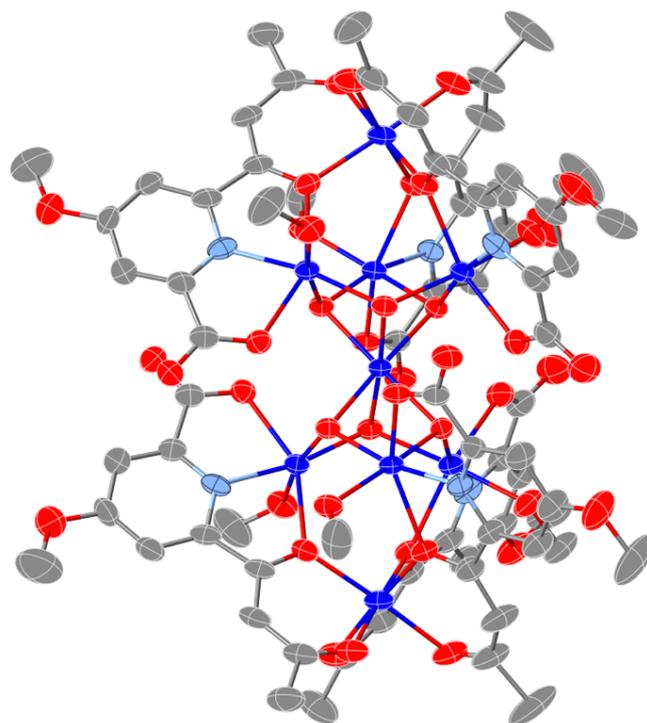
Figure 16. An OETEP view of **Co₉L3**. H atoms and solvent molecules are omitted for clarity (Co: blue; C: gray; O: red; and N: light blue).
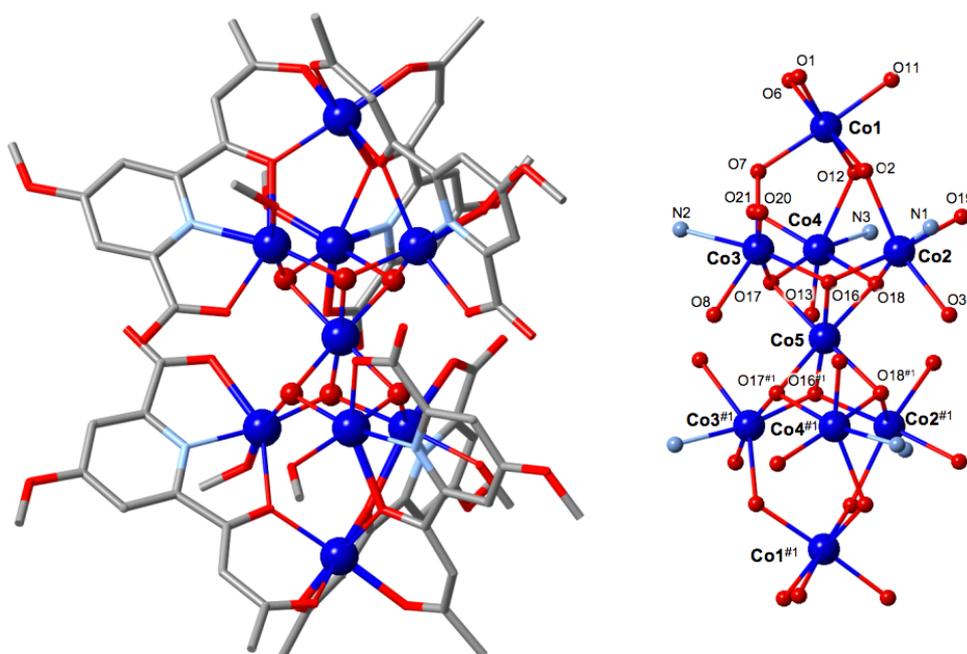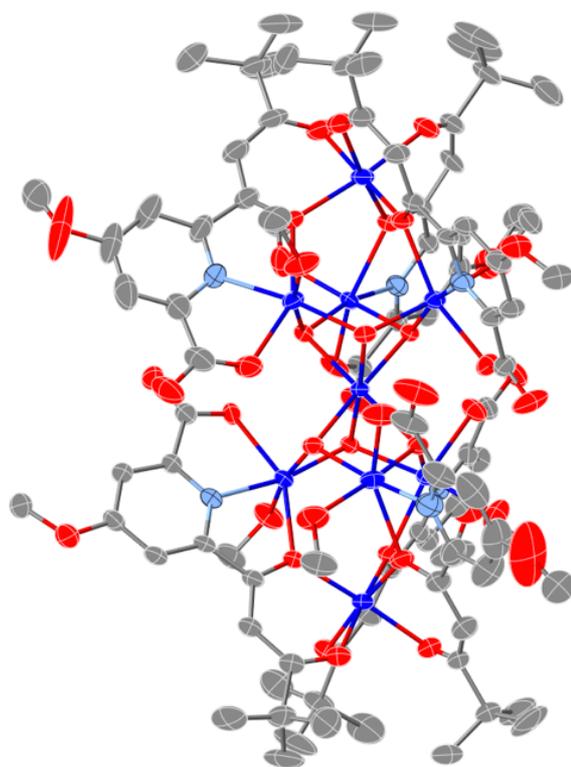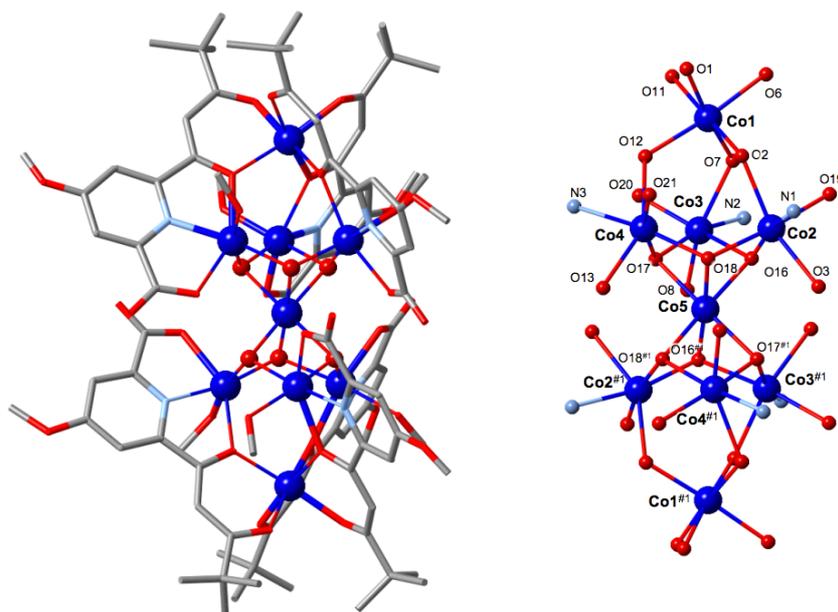

Figure 17. Molecular structure of **Co₉L3** (left), and the core. H atoms and solvent molecules are omitted for clarity.

Table 19.   Selected bond distances of **Co₉L3** (Å).

Co1–O1	2.073(3)	Co1–O2	2.064(3)	Co1–O6	2.048(3)
Co1–O7	2.076(3)	Co1–O11	2.066(3)	Co1–O12	2.064(3)
Co2–N1	2.075(4)	Co2–O2	2.284(3)	Co2–O3	2.159(3)
Co2–O16	2.076(3)	Co2–O18	2.022(3)	Co2–O19	2.119(3)
Co3–N2	2.055(4)	Co3–O7	2.261(3)	Co3–O8	2.176(3)
Co3–O16	2.012(3)	Co3–O17	2.085(3)	Co3–O20	2.124(3)
Co4–N3	2.074(3)	Co4–O12	2.252(3)	Co4–O13	2.149(3)
Co4–O17	2.018(3)	Co4–O18	2.078(3)	Co4–O21	2.111(3)
Co5–O16[#1]	2.118(3)	Co5–O16	2.118(3)	Co5–O17	2.093(3)
Co5–O17[#1]	2.092(3)	Co5–O18[#1]	2.089(3)	Co5–O18	2.089(3)

Symmetry operation: (#1) 1-X, +Y, 3/2-Z

Table 20.   Selected bond angles of **Co₉L3** (°).

O1–Co1–O7	89.83(13)	O2–Co1–O1	90.95(12)	O2–Co1–O7	92.11(11)
O2–Co1–O11	88.94(13)	O2–Co1–O12	91.42(11)	O6–Co1–O1	88.08(13)
O6–Co1–O2	177.16(12)	O6–Co1–O7	90.56(12)	O6–Co1–O11	88.34(14)
O6–Co1–O12	89.41(12)	O11–Co1–O1	87.30(14)	O11–Co1–O7	176.97(13)
O12–Co1–O1	176.08(12)	O12–Co1–O7	93.20(11)	O12–Co1–O11	89.62(12)
N1–Co2–O2	72.45(13)	N1–Co2–O3	75.99(13)	N1–Co2–O16	99.80(12)
N1–Co2–O19	91.63(13)	O3–Co2–O2	148.42(11)	O16–Co2–O2	87.16(10)
O16–Co2–O3	97.39(11)	O16–Co2–O19	167.27(12)	O18–Co2–N1	171.35(13)
O18–Co2–O2	116.20(10)	O18–Co2–O3	95.37(11)	O18–Co2–O16	81.44(11)
O18–Co2–O19	88.10(12)	O19–Co2–O2	91.00(12)	O19–Co2–O3	90.76(13)
N2–Co3–O7	73.53(12)	N2–Co3–O8	75.46(12)	N2–Co3–O17	97.18(12)
N2–Co3–O20	92.58(13)	O8–Co3–O7	148.98(11)	O16–Co3–N2	169.36(12)
O16–Co3–O7	116.78(11)	O16–Co3–O8	94.16(11)	O16–Co3–O17	81.38(11)
O16–Co3–O20	90.00(11)	O17–Co3–O7	87.02(10)	O17–Co3–O8	95.91(10)
O17–Co3–O20	168.87(12)	O20–Co3–O7	90.65(11)	O20–Co3–O8	91.69(12)
N3–Co4–O12	73.23(12)	N3–Co4–O13	75.95(12)	N3–Co4–O18	95.20(12)
N3–Co4–O21	95.09(13)	O13–Co4–O12	149.17(10)	O17–Co4–N3	168.22(12)
O17–Co4–O12	117.66(10)	O17–Co4–O13	93.13(10)	O17–Co4–O18	81.36(11)
O17–Co4–O21	89.66(11)	O18–Co4–O12	87.67(10)	O18–Co4–O13	95.88(10)
O18–Co4–O21	168.19(12)	O21–Co4–O12	89.76(11)	O21–Co4–O13	92.22(11)

O16$^{#1}$–Co5–O16	176.37(14)	O17–Co5–O16	78.76(10)	O17$^{#1}$–Co5–O16$^{#1}$	78.76(10)
O17–Co5–O16$^{#1}$	98.96(10)	O17$^{#1}$–Co5–O16	98.96(10)	O17$^{#1}$–Co5–O17	103.77(15)
O18–Co5–O16	78.90(10)	O18$^{#1}$–Co5–O16$^{#1}$	78.90(10)	O18–Co5–O16$^{#1}$	103.55(10)
O18$^{#1}$–Co5–O16	103.55(10)	O18$^{#1}$–Co5–O17$^{#1}$	79.36(11)	O18–Co5–O17$^{#1}$	175.87(10)
O18–Co5–O17	79.36(11)	O18$^{#1}$–Co5–O17	175.87(10)	O18$^{#1}$–Co5–O18	97.64(15)

Symmetry operation: (#1) 1-X, +Y, 3/2-Z

Figure 18. An OETEP view of **Co₉L4**. H atoms and solvent molecules are omitted for clarity (Co: blue; C: gray; O: red; and N: light blue).

Figure 19. Molecular structure of **Co₉L4** (left), and the core (right). H atoms and solvent molecules are omitted for clarity.

Table 21.   Selected bond distances of **Co₉L4** (Å).

Co1–O1	2.055(3)	Co1–O2	2.063(2)	Co1–O6	2.054(3)
Co1–O7	2.077(2)	Co1–O11	2.046(3)	Co1–O12	2.088(3)
Co2–N1	2.064(3)	Co2–O2	2.233(2)	Co2–O3	2.172(2)
Co2–O16	2.012(2)	Co2–O18	2.081(2)	Co2–O19	2.119(3)
Co3–N2	2.070(3)	Co3–O7	2.221(2)	Co3–O8	2.168(2)
Co3–O16	2.088(2)	Co3–O17	2.016(2)	Co3–O20	2.110(3)
Co4–N3	2.056(3)	Co4–O12	2.277(2)	Co4–O13	2.166(3)
Co4–O17	2.076(2)	Co4–O18	2.012(2)	Co4–O21	2.127(3)
Co5–O16	2.095(2)	Co5–O16#1	2.095(2)	Co5–O17	2.099(2)
Co5–O17#1	2.099(2)	Co5–O18	2.087(2)	Co5–O18#1	2.087(2)

Symmetry operation: (#1) 1-X, +Y, 1/2-Z

Table 22.   Selected bond distances of **Co₉L4** (°).

O1–Co1–O2	89.55(10)	O1–Co1–O7	172.89(10)	O1–Co1–O12	90.36(11)
O2–Co1–O7	94.89(9)	O2–Co1–O12	91.10(10)	O6–Co1–O1	85.55(12)
O6–Co1–O2	92.74(10)	O6–Co1–O7	88.68(11)	O6–Co1–O12	174.37(11)
O7–Co1–O12	95.10(10)	O11–Co1–O1	85.91(11)	O11–Co1–O2	175.45(10)
O11–Co1–O6	87.16(12)	O11–Co1–O7	89.66(11)	O11–Co1–O12	88.69(11)
N1–Co2–O2	73.72(10)	N1–Co2–O3	75.45(10)	N1–Co2–O18	93.56(11)
N1–Co2–O19	95.59(12)	O3–Co2–O2	148.82(9)	O16–Co2–N1	168.29(10)
O16–Co2–O2	116.65(9)	O16–Co2–O3	94.50(9)	O16–Co2–O18	81.48(9)
O16–Co2–O19	90.43(10)	O18–Co2–O2	89.78(9)	O18–Co2–O3	96.70(10)
O18–Co2–O19	169.52(11)	O19–Co2–O2	87.90(10)	O19–Co2–O3	90.55(12)
N2–Co3–O7	73.84(10)	N2–Co3–O8	75.22(10)	N2–Co3–O16	96.12(10)
N2–Co3–O20	95.35(12)	O8–Co3–O7	148.88(9)	O16–Co3–O7	86.17(9)
O16–Co3–O8	100.42(10)	O16–Co3–O20	166.41(12)	O17–Co3–N2	166.01(10)
O17–Co3–O7	119.43(9)	O17–Co3–O8	91.67(9)	O17–Co3–O16	81.23(9)
O17–Co3–O20	89.33(10)	O20–Co3–O7	90.03(11)	O20–Co3–O8	89.56(13)
N3–Co4–O12	73.21(12)	N3–Co4–O13	75.82(13)	N3–Co4–O17	102.39(12)
N3–Co4–O21	89.67(14)	O13–Co4–O12	148.74(11)	O17–Co4–O12	87.28(9)
O17–Co4–O13	95.30(10)	O17–Co4–O21	166.54(12)	O18–Co4–N3	169.81(12)
O18–Co4–O12	116.65(9)	O18–Co4–O13	94.50(10)	O18–Co4–O17	81.41(9)
O18–Co4–O21	87.72(11)	O21–Co4–O12	90.56(11)	O21–Co4–O13	93.43(13)

O16–Co5–O16$^{\#1}$	102.81(12)	O16$^{\#1}$–Co5–O17	98.72(9)	O16$^{\#1}$–Co5–O17$^{\#1}$	79.13(9)
O16–Co5–O17$^{\#1}$	98.72(9)	O16–Co5–O17	79.14(9)	O17–Co5–O17$^{\#1}$	176.61(12)
O18$^{\#1}$–Co5–O16	176.63(9)	O18–Co5–O16$^{\#1}$	176.63(9)	O18$^{\#1}$–Co5–O16$^{\#1}$	79.42(9)
O18–Co5–O16	79.42(9)	O18$^{\#1}$–Co5–O17	103.12(9)	O18–Co5–O17$^{\#1}$	103.13(9)
O18$^{\#1}$–Co5–O17$^{\#1}$	79.14(9)	O18–Co5–O17	79.14(9)	O18$^{\#1}$–Co5–O18	98.48(13)

Symmetry operation: (#1) 1-X, +Y, 1/2-Z
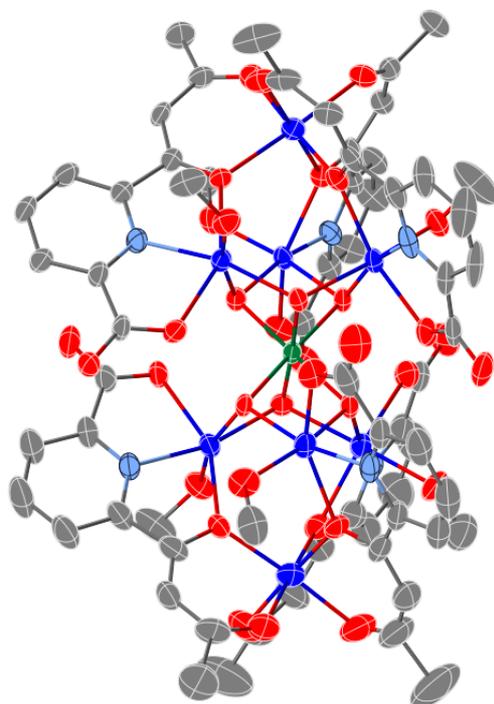
Figure 20. An OETEP view of **Co₉L1⁺_ClO₄**. H atoms, solvent molecules and counter anions are omitted for clarity (Co^{II}: blue; Co^{III}: green; C: gray; O: red; and N: light blue)
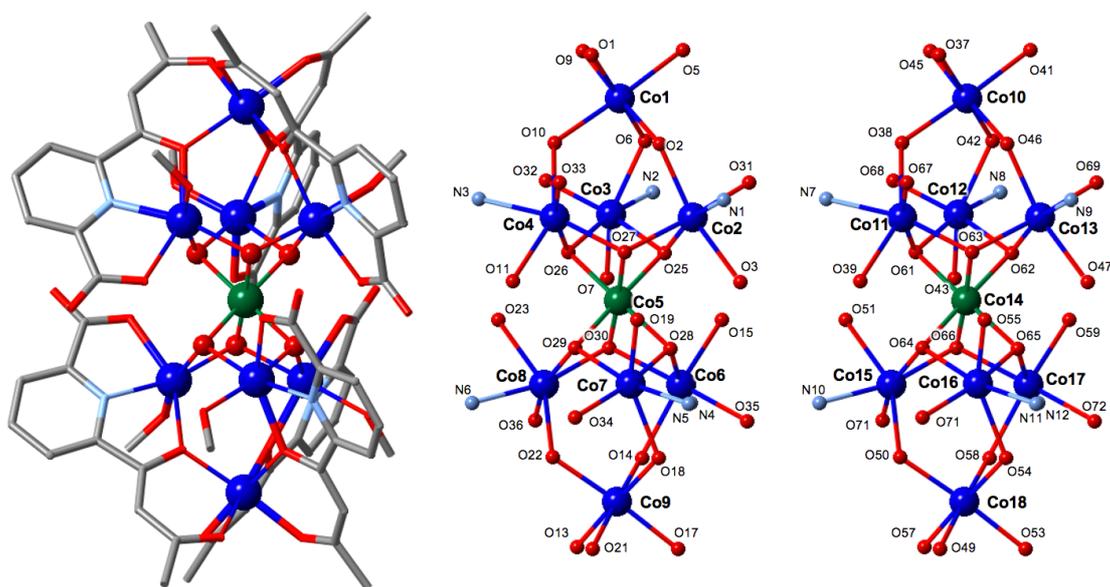
Figure 21. Molecular structure of **Co₉L1⁺_ClO₄** (left), and the core (right). H atoms, solvent molecules and counter anions are omitted for clarity.

Table 23. Selected bond distances of **Co₉L1⁺_ClO₄** (Å).

Co1–O1	2.043(4)	Co1–O2	2.065(4)	Co1–O5	2.066(4)
Co1–O6	2.045(4)	Co1–O9	2.052(4)	Co1–O10	2.065(4)
Co2–N1	2.056(5)	Co2–O2	2.188(4)	Co2–O3	2.134(4)
Co2–O25	2.042(4)	Co2–O27	2.093(3)	Co2–O31	2.058(4)
Co3–N2	2.059(5)	Co3–O6	2.199(4)	Co3–O7	2.097(4)
Co3–O25	2.098(3)	Co3–O26	2.068(4)	Co3–O32	2.062(4)
Co4–N3	2.049(5)	Co4–O10	2.184(4)	Co4–O11	2.157(4)
Co4–O26	2.079(4)	Co4–O27	2.034(4)	Co4–O33	2.068(4)
Co5–O25	1.910(3)	Co5–O26	1.914(4)	Co5–O27	1.914(4)
Co5–O28	1.914(4)	Co5–O29	1.909(3)	Co5–O30	1.906(4)
Co6–N4	2.052(5)	Co6–O14	2.187(4)	Co6–O15	2.140(4)
Co6–O28	2.056(4)	Co6–O30	2.097(4)	Co6–O34	2.063(4)
Co7–N5	2.059(5)	Co7–O18	2.191(4)	Co7–O19	2.140(4)
Co7–O28	2.089(4)	Co7–O29	2.067(3)	Co7–O35	2.049(4)
Co8–N6	2.045(5)	Co8–O22	2.181(4)	Co8–O23	2.136(4)
Co8–O29	2.105(4)	Co8–O30	2.050(4)	Co8–O36	2.064(4)
Co9–O13	2.052(6)	Co9–O14	2.071(5)	Co9–O17	2.024(6)
Co9–O18	2.063(5)	Co9–O21	2.049(5)	Co9–O22	2.042(4)

Table 24. Selected bond angles of **Co₉L1⁺_ClO₄** (°).

O1–Co1–O2	89.89(16)	O1–Co1–O5	89.81(17)	O1–Co1–O6	178.02(17)
O1–Co1–O9	89.73(17)	O1–Co1–O10	88.19(17)	O2–Co1–O5	89.75(15)
O2–Co1–O10	92.20(15)	O6–Co1–O2	92.06(14)	O6–Co1–O5	90.55(15)
O6–Co1–O9	88.34(15)	O6–Co1–O10	91.39(15)	O9–Co1–O2	177.38(16)
O9–Co1–O5	87.66(16)	O9–Co1–O10	90.37(16)	O10–Co1–O5	177.20(16)
N1–Co2–O2	74.31(18)	N1–Co2–O3	75.54(19)	N1–Co2–O27	99.31(16)
N1–Co2–O31	96.50(17)	O3–Co2–O2	149.79(15)	O25–Co2–N1	165.46(18)
O25–Co2–O2	118.18(14)	O25–Co2–O3	91.50(15)	O25–Co2–O27	74.79(14)
O25–Co2–O31	90.59(15)	O27–Co2–O2	88.50(14)	O27–Co2–O3	94.52(15)
O31–Co2–O2	92.51(15)	O31–Co2–O3	92.70(17)	O31–Co2–O27	163.83(15)
N2–Co3–O6	73.63(16)	N2–Co3–O7	76.36(17)	N2–Co3–O25	103.74(16)
N2–Co3–O26	168.16(17)	N2–Co3–O32	90.75(17)	O7–Co3–O6	149.26(15)
O7–Co3–O25	90.27(15)	O25–Co3–O6	90.41(13)	O26–Co3–O6	117.65(14)

O26–Co3–O7	91.98(15)	O26–Co3–O25	73.84(14)	O32–Co3–O6	92.72(15)
O32–Co3–O7	94.23(17)	O32–Co3–O25	165.48(15)	O32–Co3–O26	92.19(15)
N3–Co4–Co5	130.11(14)	N3–Co4–O10	74.42(16)	N3–Co4–O11	74.84(17)
N3–Co4–O26	98.46(17)	N3–Co4–O33	94.33(18)	O10–Co4–Co5	116.84(11)
O11–Co4–Co5	82.64(11)	O11–Co4–O10	149.23(15)	O26–Co4–Co5	39.27(10)
O26–Co4–O10	88.56(14)	O26–Co4–O11	94.52(15)	O27–Co4–Co5	39.10(10)
O27–Co4–N3	165.97(17)	O27–Co4–O10	117.24(14)	O27–Co4–O11	93.03(14)
O27–Co4–O26	75.10(14)	O27–Co4–O33	93.01(16)	O33–Co4–Co5	130.72(12)
O33–Co4–O10	92.11(15)	O33–Co4–O11	91.60(16)	O33–Co4–O26	166.88(16)
O25–Co5–Co4	93.00(12)	O25–Co5–O26	81.75(15)	O25–Co5–O27	82.12(15)
O25–Co5–O28	96.43(15)	O26–Co5–Co4	43.45(11)	O27–Co5–Co4	42.08(11)
O27–Co5–O26	81.83(15)	O28–Co5–Co4	138.70(12)	O28–Co5–O26	177.45(15)
O28–Co5–O27	99.73(16)	O29–Co5–Co4	87.13(11)	O29–Co5–O25	177.25(14)
O29–Co5–O26	100.18(15)	O29–Co5–O27	96.18(15)	O29–Co5–O28	81.70(15)
O30–Co5–Co4	135.10(11)	O30–Co5–O25	99.47(16)	O30–Co5–O26	95.88(16)
O30–Co5–O27	177.02(16)	O30–Co5–O28	82.63(16)	O30–Co5–O29	82.32(16)
N4–Co6–O14	73.8(2)	N4–Co6–O15	76.36(19)	N4–Co6–O28	166.06(18)
N4–Co6–O30	98.47(18)	N4–Co6–O34	94.7(2)	O15–Co6–O14	150.07(18)
O28–Co6–O14	117.58(16)	O28–Co6–O15	91.66(16)	O28–Co6–O30	74.77(14)
O28–Co6–O34	93.05(18)	O30–Co6–O14	89.00(15)	O30–Co6–O15	93.11(15)
O34–Co6–O14	91.55(18)	O34–Co6–O15	93.15(18)	O34–Co6–O30	166.45(18)
N5–Co7–O18	74.4(2)	N5–Co7–O19	75.8(2)	N5–Co7–O28	102.10(17)
N5–Co7–O29	167.7(2)	O19–Co7–O18	149.98(17)	O28–Co7–O18	88.63(15)
O28–Co7–O19	93.77(15)	O29–Co7–O18	116.68(16)	O29–Co7–O19	92.62(15)
O29–Co7–O28	73.98(14)	O35–Co7–N5	92.54(18)	O35–Co7–O18	92.44(18)
O35–Co7–O19	92.74(19)	O35–Co7–O28	165.05(16)	O35–Co7–O29	92.29(15)
N6–Co8–O22	74.25(18)	N6–Co8–O23	75.95(18)	N6–Co8–O29	101.58(17)
N6–Co8–O30	165.77(18)	N6–Co8–O36	93.72(19)	O23–Co8–O22	149.97(16)
O29–Co8–O22	88.51(15)	O29–Co8–O23	93.88(15)	O30–Co8–O22	118.73(15)
O30–Co8–O23	90.59(15)	O30–Co8–O29	74.35(14)	O30–Co8–O36	91.75(16)
O36–Co8–O22	91.67(16)	O36–Co8–O23	93.87(17)	O36–Co8–O29	164.14(16)
O13–Co9–O14	89.1(2)	O13–Co9–O18	177.7(2)	O17–Co9–O13	88.0(3)
O17–Co9–O14	90.7(2)	O17–Co9–O18	90.3(2)	O17–Co9–O21	87.2(2)

O17–Co9–O22	176.1(2)	O18–Co9–O14	92.37(17)	O21–Co9–O13	87.8(2)
O21–Co9–O14	176.4(2)	O21–Co9–O18	90.6(2)	O22–Co9–O13	89.1(2)
O22–Co9–O14	91.78(16)	O22–Co9–O18	92.66(17)	O22–Co9–O21	90.12(19)
O37–Co10–O38	88.16(16)	O37–Co10–O42	90.41(16)	O37–Co10–O46	176.06(15)
O38–Co10–O42	90.24(15)	O38–Co10–O46	95.67(14)	O41–Co10–O37	87.56(16)
O41–Co10–O38	175.70(16)	O41–Co10–O42	90.18(15)	O41–Co10–O45	88.20(16)
O41–Co10–O46	88.60(15)	O45–Co10–O37	88.99(16)	O45–Co10–O38	91.33(16)
O45–Co10–O42	178.29(16)	O45–Co10–O46	90.03(16)	O46–Co10–O42	90.46(15)
N7–Co11–O38	74.31(18)	N7–Co11–O39	75.92(18)	N7–Co11–O61	94.78(18)
O39–Co11–O38	150.06(15)	O61–Co11–O38	88.09(14)	O61–Co11–O39	97.49(14)
O63–Co11–N7	161.45(17)	O63–Co11–O38	119.30(14)	O63–Co11–O39	90.43(15)
O63–Co11–O61	74.31(14)	O67–Co11–N7	98.0(2)	O67–Co11–O38	89.78(16)
O67–Co11–O39	91.25(16)	O67–Co11–O61	165.97(16)	O67–Co11–O63	94.76(16)
N8–Co12–O42	74.52(16)	N8–Co12–O43	76.16(17)	N8–Co12–O62	98.05(16)
N8–Co12–O68	94.40(19)	O43–Co12–O42	150.64(16)	O61–Co12–N8	166.17(16)
O61–Co12–O42	116.53(15)	O61–Co12–O43	92.30(16)	O61–Co12–O62	74.82(14)
O61–Co12–O68	93.23(17)	O62–Co12–O42	88.92(14)	O62–Co12–O43	93.74(15)
O68–Co12–O42	93.30(15)	O68–Co12–O43	90.34(17)	O68–Co12–O62	167.50(18)
N9–Co13–O46	74.92(16)	N9–Co13–O47	75.70(17)	N9–Co13–O62	164.64(16)
N9–Co13–O63	100.15(17)	N9–Co13–O69	94.08(18)	O47–Co13–O46	150.48(14)
O62–Co13–O46	118.30(14)	O62–Co13–O47	90.49(14)	O62–Co13–O63	74.14(14)
O62–Co13–O69	93.05(15)	O63–Co13–O46	87.06(13)	O63–Co13–O47	95.46(14)
O69–Co13–O46	92.76(15)	O69–Co13–O47	91.97(16)	O69–Co13–O63	165.20(15)
O61–Co14–O62	82.29(15)	O63–Co14–O61	82.47(15)	O63–Co14–O62	82.15(15)
O63–Co14–O64	95.91(15)	O63–Co14–O65	100.21(15)	O64–Co14–O61	99.03(15)
O64–Co14–O62	177.52(15)	O64–Co14–O65	82.66(15)	O65–Co14–O61	176.70(16)
O65–Co14–O62	96.13(15)	O66–Co14–O61	94.99(15)	O66–Co14–O62	99.38(15)
O66–Co14–O63	176.86(15)	O66–Co14–O64	82.64(16)	O66–Co14–O65	82.38(15)
N10–Co15–O50	74.84(18)	N10–Co15–O51	75.65(19)	N10–Co15–O64	98.41(17)
N10–Co15–O70	98.15(18)	O51–Co15–O50	150.49(16)	O64–Co15–O50	86.26(14)
O64–Co15–O51	98.09(15)	O66–Co15–N10	163.77(17)	O66–Co15–O50	118.33(15)
O66–Co15–O51	90.79(15)	O66–Co15–O64	74.36(14)	O66–Co15–O70	90.90(15)

O70–Co15–O50	92.88(15)	O70–Co15–O51	91.21(17)	O70–Co15–O64	162.58(15)
N11–Co16–O54	74.32(17)	N11–Co16–O55	75.82(18)	N11–Co16–O64	165.42(17)
N11–Co16–O65	98.52(17)	N11–Co16–O71	94.97(19)	O55–Co16–O54	150.05(15)
O64–Co16–O54	117.40(15)	O64–Co16–O55	91.82(14)	O64–Co16–O65	74.30(14)
O64–Co16–O71	92.90(15)	O65–Co16–O54	88.31(15)	O65–Co16–O55	93.93(14)
O71–Co16–O54	93.75(16)	O71–Co16–O55	90.98(15)	O71–Co16–O65	166.40(15)
N12–Co17–O58	74.36(19)	N12–Co17–O59	76.16(19)	N12–Co17–O65	163.80(18)
N12–Co17–O66	97.19(17)	N12–Co17–O72	96.10(18)	O59–Co17–O58	150.49(16)
O65–Co17–O58	118.37(15)	O65–Co17–O59	90.44(15)	O65–Co17–O66	74.27(14)
O65–Co17–O72	93.56(16)	O66–Co17–O58	88.71(14)	O66–Co17–O59	93.60(15)
O72–Co17–O58	91.75(16)	O72–Co17–O59	92.73(17)	O72–Co17–O66	166.31(16)
O49–Co18–O50	89.59(18)	O49–Co18–O53	89.0(2)	O49–Co18–O54	90.69(17)
O49–Co18–O57	86.82(19)	O49–Co18–O58	176.75(16)	O53–Co18–O50	177.43(18)
O53–Co18–O54	90.08(18)	O53–Co18–O57	87.41(19)	O53–Co18–O58	88.82(18)
O54–Co18–O50	92.10(15)	O57–Co18–O50	90.36(17)	O57–Co18–O54	176.49(17)
O57–Co18–O58	90.65(18)	O58–Co18–O50	92.47(16)	O58–Co18–O54	91.74(16)
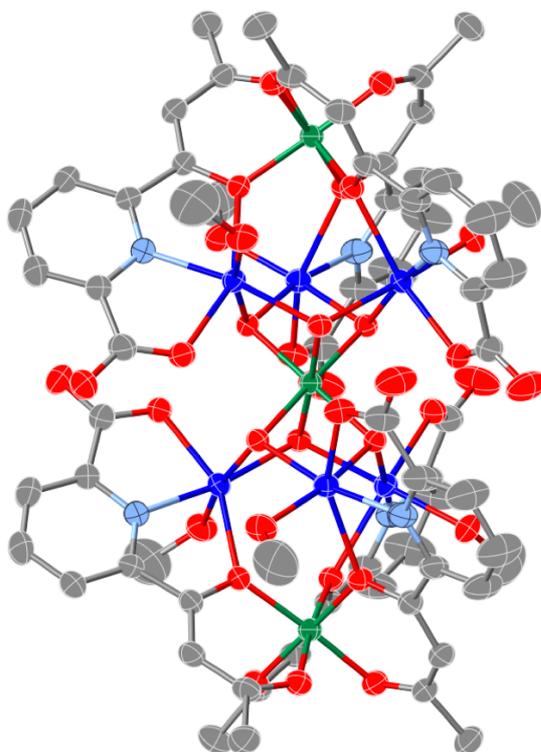
Figure 22. An ORTEP view of **Co₉L1³⁺_Ce**. H atoms, solvent molecules and counter anions are omitted for clarity (Co^II: blue; Co^III: green; C: gray; O: red; and N: light blue)
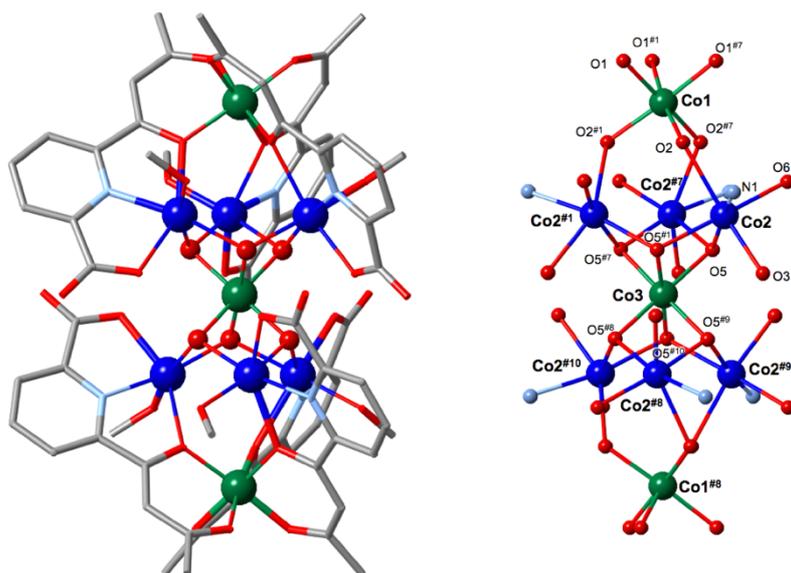
Figure 23. Molecular structure of **Co₉L1³⁺_Ce** (left) and the core (right). H atoms, solvent molecules and counter anions are omitted for clarity.

Table 25. Selected bond distances of **Co₉L1³⁺_Ce** (Å).

Co1–O1	1.876(2)	Co1–O1$^{\#1}$	1.876(2)	Co1–O1$^{\#7}$	1.876(2)
Co1–O2	1.903(2)	Co1–O2$^{\#1}$	1.903(2)	Co1–O2$^{\#7}$	1.903(2)
Co2–N1	2.057(3)	Co2–O2	2.317(2)	Co2–O3	2.088(2)
Co2–O5	2.068(2)	Co2–O5$^{\#1}$	2.091(2)	Co2–O6	2.054(2)
Co3–O5$^{\#7}$	1.912(2)	Co3–O5	1.912(2)	Co3–O5$^{\#8}$	1.912(2)
Co3–O5$^{\#9}$	1.912(2)	Co3–O5$^{\#10}$	1.912(2)	Co3–O5$^{\#1}$	1.912(2)

Symmetry Operation: (#1) +Y-X, 1-X, +Z; (#2) 1-Y, +X-Y, +Z; (#3) 4/3-X, 2/3-Y, 5/3-Z; (#4) 1+Y-X, 1-X, +Z; (#5) 1/3+Y, 2/3-X+Y, 5/3-Z; (#6) 1/3-Y+X, -1/3+X, 5/3-Z; (#7) 1-Y, 1+X-Y, +Z; (#8) -1/3+Y, 1/3+X, 11/6-Z; (#9) 2/3-X, 1/3-X+Y, 11/6-Z; (#10) 2/3-Y+X, 4/3-Y, 11/6-Z

Table 26. Selected bond distances of **Co₉L1³⁺_Ce** (°).

O1$^{\#1}$–Co1–O1$^{\#7}$	86.89(10)	O1$^{\#1}$–Co1–O1	86.88(10)	O1$^{\#7}$–Co1–O1	86.88(10)
O1$^{\#1}$–Co1–O2	173.52(10)	O1–Co1–O2	95.83(9)	O1$^{\#1}$–Co1–O2$^{\#7}$	173.52(10)
O1$^{\#7}$–Co1–O2$^{\#1}$	173.51(10)	O1$^{\#1}$–Co1–O2$^{\#7}$	87.37(9)	O1–Co1–O2$^{\#1}$	87.39(9)
O1$^{\#7}$–Co1–O2$^{\#7}$	95.81(9)	O1$^{\#7}$–Co1–O2	87.38(9)	O1$^{\#1}$–Co1–O2$^{\#1}$	95.82(9)
O2–Co1–O2$^{\#1}$	90.20(9)	O2–Co1–O2$^{\#7}$	90.20(9)	O2$^{\#7}$–Co1–O2$^{\#1}$	90.20(9)
N1–Co2–O2	72.25(9)	N1–Co2–O3	78.14(10)	N1–Co2–O5	169.58(10)
N1–Co2–O5$^{\#1}$	97.88(10)	O3–Co2–O2	150.06(8)	O3–Co2–O5$^{\#1}$	92.68(8)
O5$^{\#1}$–Co2–O2	87.13(8)	O5–Co2–O2	114.28(8)	O5–Co2–O3	94.44(8)
O5–Co2–O5#1	74.96(11)	O6–Co2–N1	94.65(12)	O6–Co2–O2	93.34(9)
O6–Co2–O3	93.35(10)	O6–Co2–O5	93.07(9)	O6–Co2–O5$^{\#1}$	166.98(9)
O5$^{\#1}$–Co3–O5$^{\#10}$	98.53(12)	O5–Co3–O5$^{\#10}$	95.74(12)	O5–Co3–O5$^{\#1}$	82.89(9)
O5–Co3–O5$^{\#8}$	98.53(12)	O5$^{\#1}$–Co3–O5$^{\#8}$	177.91(11)	O5$^{\#1}$–Co3–O5$^{\#7}$	82.88(9)
O5$^{\#7}$–Co3–O5	82.88(9)	O5$^{\#10}$–Co3–O5$^{\#8}$	82.89(9)	O5–Co3–O5$^{\#9}$	177.91(11)
O5$^{\#10}$–Co3–O5$^{\#9}$	82.89(9)	O5$^{\#7}$–Co3–O5$^{\#9}$	98.53(12)	O5$^{\#8}$–Co3–O5$^{\#9}$	82.88(9)
O5$^{\#1}$–Co3–O5$^{\#9}$	95.74(12)	O5$^{\#7}$–Co3–O5$^{\#10}$	177.91(11)	O5$^{\#7}$–Co3–O5$^{\#8}$	95.74(12)

Symmetry Operation: (#1) +Y-X, 1-X, +Z; (#2) 1-Y, 1+X-Y, +Z; (#3) 4/3-X, 2/3-Y, 5/3-Z; (#4) 1/3+Y, 2/3-X+Y, 5/3-Z; (#5) 1+Y-X, 1-X, +Z; (#6) 1-Y, +X-Y, +Z; (#7) 1/3-Y+X, -1/3+X, 5/3-Z; (#8) 2/3-Y+X, 4/3-Y, 11/6-Z; (#9) 2/3-X, 1/3-X+Y, 11/6-Z; (#10) -1/3+Y, 1/3+X, 11/6-Z

Table 27. Calculated value of valence (V_i)

Complex	Co1	Co2	Co3	Co4	Co5	Co6	Co7	Co8	Co9
Co$_9$L1	2.16	2.12	2.13	2.11	2.10	2.10	2.11	2.12	2.15
Co$_9$L2	2.21	2.09	2.12	2.12	1.98	2.13	2.11	2.12	2.19
Co$_9$L3	2.19	2.09	2.12	2.13	1.99				
Co$_9$L4	2.20	2.14	2.14	2.13	2.03				
Co$_9$L1$^+$_ClO$_4$	2.24	2.22	2.21	2.23	3.32	2.20	2.20	2.22	2.28
Co$_9$L1^{3+}_Ce	3.60	2.16	3.38						
	Co10	**Co11**	**Co12**	**Co13**	**Co14**	**Co15**	**Co16**	**Co17**	**Co18**
Co$_9$L1$^+$_ClO$_4$	2.27	2.23	2.28	2.23	3.49	2.25	2.23	2.23	2.31

UV-vis Spectra

All UV-vis spectra for **Ni₉L*n*** showed one intense band around 350 nm which could be attributed to the ligand origin.   The intensity of this band overlap of the charge transfer bands of Ni–μ-OH.   The d-d transition absorption band was observed around 660 nm in both spectra.   This band supposed to be involved with $^3A_2 \rightarrow {}^3T_1$ for the octahedral Ni(II) center.   In the case of cobalt complex, the bands at 330-400 nm attributed to the ligand origin were also observed, and charge transfer bands of Co−μ-OH probably overlap with these bands.   Two peaks from d-d transition absorption observed at 500, 550 nm in **Co₉L*n*** and **Co₉L1⁺_ClO₄** shifted to 619 nm in **Co₉L1³⁺_ClO₄**.   Absorption band at 500 nm is involved with $^4T_1 \rightarrow {}^4T_1(P)$ for the octahedral Co(II) centers and the 605 nm peak is involved with $^1A_1 \rightarrow {}^1T_1$, or $^1A_1 \rightarrow {}^1T_2$ for the octahedral Co(III) centers.[13]   In the case of **Co₉L1³⁺_ClO₄**, ligand-origin band shifts to 291 nm, and the band at 367 nm assigned to be charge transfer bands of Co−μ-OH was observed.

Table 28.   Numerical data of UV vis spectra of nickel complexes.

Complex	λ_{max} / nm (ε / 10^3 M^{-1} cm^{-1})	
Ni₉L1	351 (58.8)	663.5 (0.06)
Ni₉L2	353 (62.1)	657 (0.06)
Ni₉L3	349 (53.2)	668 (0.05)
Ni₉L4	351 (56.7)	656 (0.06)

Table 29.   Numerical data of UV-vis spectra of cobalt complexes.

Complex	λ_{max} / nm (ε / 10^3 M^{-1} cm^{-1})		
Co₉L1		337 (68.5)	500, 550 (shoulder)
Co₉L2		337 (64.5)	500, 550 (shoulder)
Co₉L3		335 (62.7)	495, 545 (shoulder)
Co₉L4		335 (69.1)	495, 545 (shoulder)
Co₉L1⁺_ClO₄		331 (80.9)	500, 550 (shoulder)
Co₉L1³⁺_ClO₄	291 (71.2)	367 (41.9)	605 (0.48)
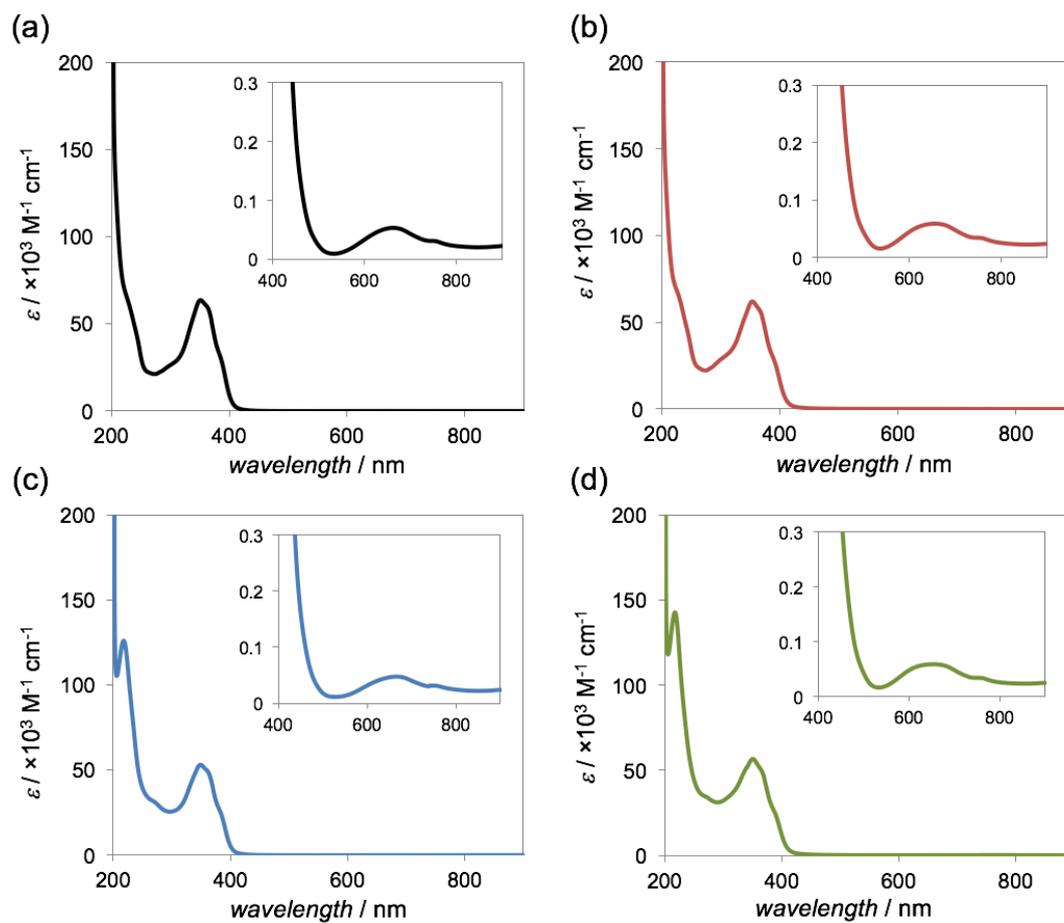
Figure 24. UV-vis spectra of **Ni₉L1** (a), **Ni₉L2** (b), **Ni₉L3** (c), **Ni₉L4** (d) in AN/MeOH
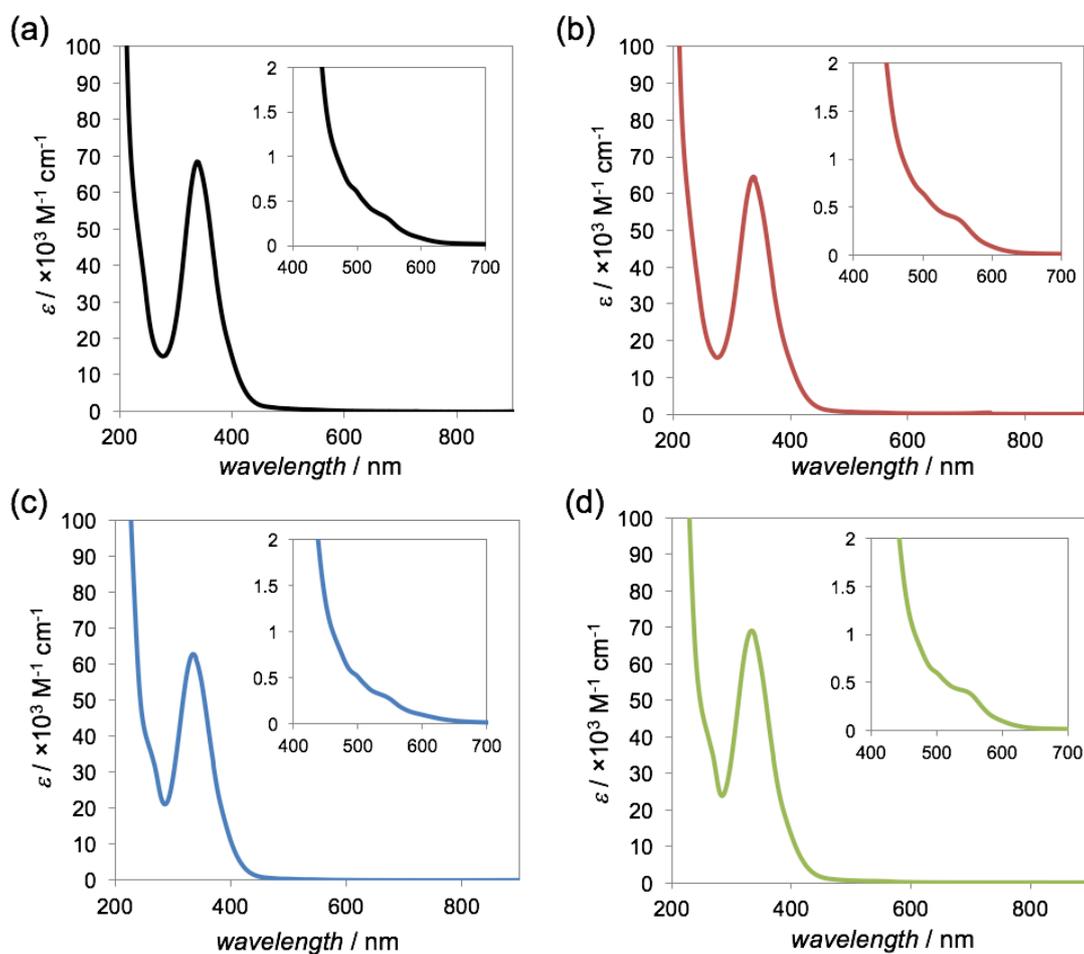
Figure 25. UV-vis spectra of **Co₉L1** (a), **Co₉L2** (b), **Co₉L3** (c), **Co₉L4** (d) in MeOH
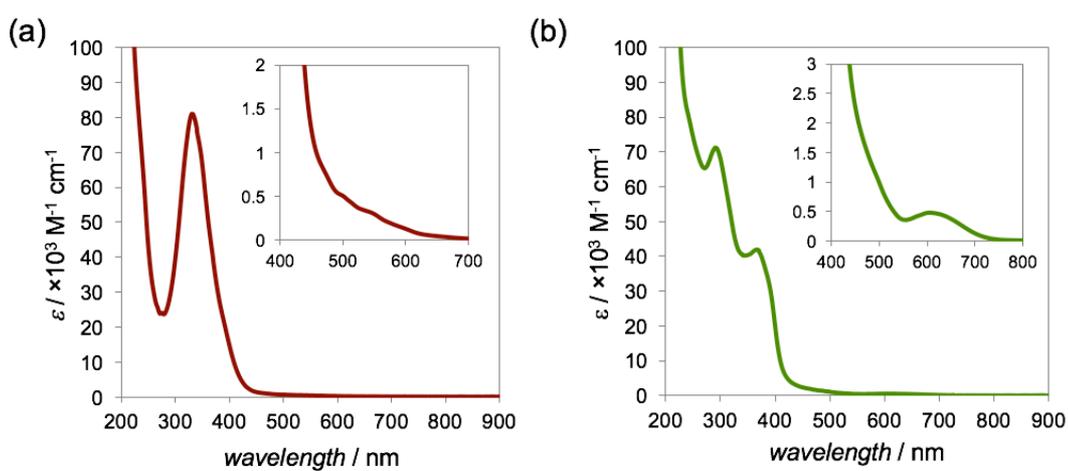
Figure 26. UV-vis spectra of **Co₉L1⁺_ClO₄** (a) and **Co₉L1³⁺_ClO₄** (b) in AN.

Electrochemical Property of Nickel Complexes

The cyclic voltammogram of **Ni$_9$Ln** is shown in **Figure 27** and numeric data are summarized in **Table 30**.   **Ni$_9$L1** showed one redox wave at 0.59 V and 0.48 V (*vs.* Fc$^+$/Fc).   Bulk electrolysis experiments confirm that the redox process correspond to the exchange of one electron.   This wave is assigned to Ni(III)/Ni(II) of the central Ni(II) ion in the heptad core, and this assignment is consistent with the first redox step of cobalt complexes (**Co$_9$Ln**) described later.   This Ni(III)/Ni(II) redox process is quasi-reversible, which means Ni(III) is stable in **Ni$_9$L1**, although usually Ni(III) is unstable and undergoes rapid decomposition.[28]   This results is consistent with a reported heptanuclear complex including stable Ni(III) which has the same coordination environment as central Ni(II) ion of **Ni$_9$L1**.[29]

The other complexes also showed one-electron redox behavior same as **Ni$_9$L1**. Because Ln^{2-} do not coordinate to the redox-active central Ni(II) ion directly, expected shift of the redox potential due to the methoxy group that introduced in the pyridine ring was not observed.   On the other hand, *t*-butyl group at the β-diketone site far from central Ni(II) ion, contributed to shift the redox potential slightly.   In **Ni$_9$L2** and **Ni$_9$L4**, which have *t*-butyl groups, O-Ni-O angle of central Ni(II) ion and bridging hydroxyl anions on the same triad side are smaller than the other complexes' ones (**Figure 28**, **Table 31**).   These slight structural changes, not electric contribution, by t-butyl group may affect the redox potential.

Table 30.   Redox Potential of **Ni$_9$Ln.** (V *vs.* Fc$^+$/Fc)

Complex	substituent	E_{pa} / V	E_{pc} / V	$E_{1/2}$ / V	ΔE / V
Ni$_9$L1	none	0.59	0.48	0.54	0.11
Ni$_9$L2	t-butyl	0.53	0.42	0.47	0.11
Ni$_9$L3	methoxy	0.61	0.45	0.53	0.16
Ni$_9$L4	t-butyl, methoxy	0.51	0.38	0.45	0.13
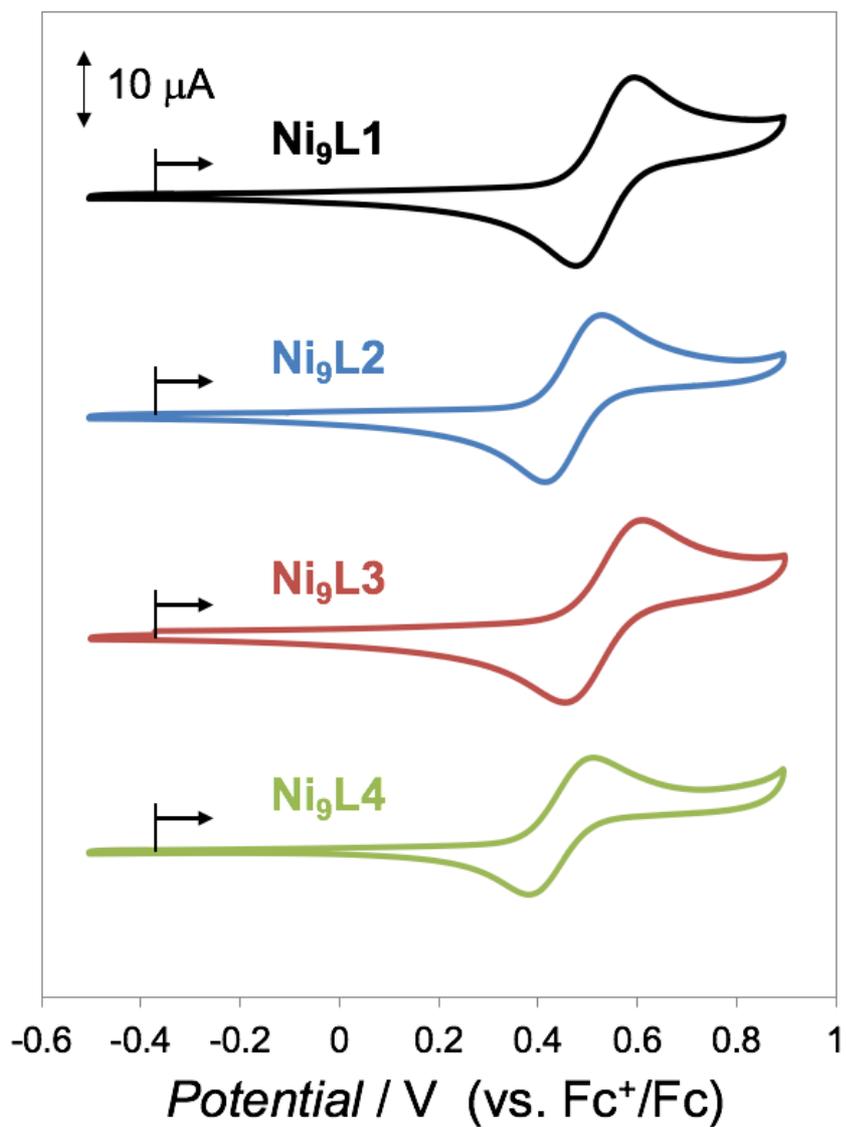
Figure 27. Cyclic voltammograms of **Ni₉L1-Ni₉L4** in MeOH/AN (v:v = 1:1). (1 mM, TBAP 0.1 M, scan rate 0.1V/s).
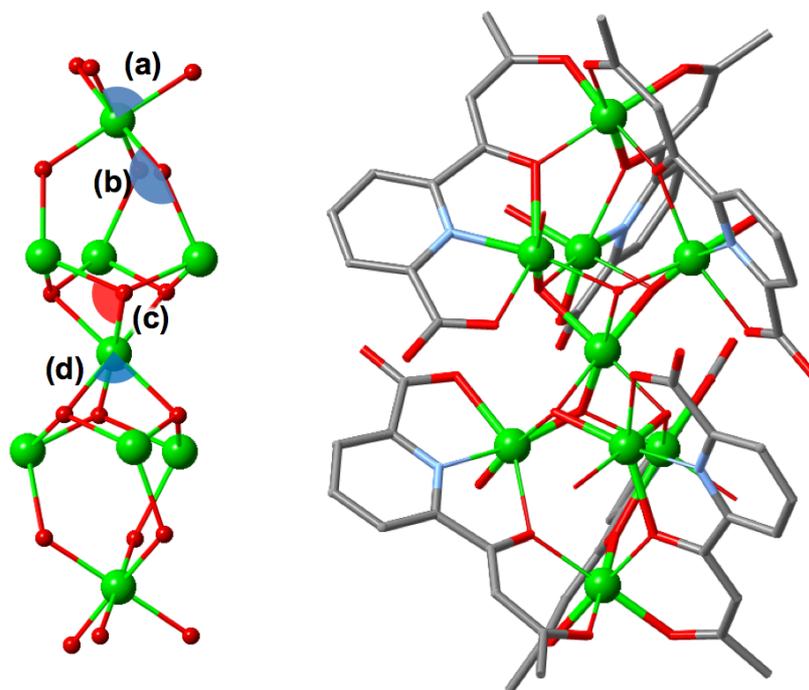
Figure 28. Ni-O-Ni or O-Ni-O angles changed by introduction of *t*-butyl group. (red and blue represent expanded angle and contracted angle respectively.   Numeric data were summarized in Table 31)

Table 31.   Electrochemical and structural data for **Ni$_9$Ln**.

	Ni$_9$L1	**Ni$_9$L2**	**Ni$_9$L3**	**Ni$_9$L4**
$E_{1/2}$ / V	0.54	0.47	0.53	0.45
(a)$_{(ave.)}$ / °	88.95	87.55	88.67	86.30
(b)$_{(ave.)}$ / °	123.62	123.35	123.58	123.06
(c)$_{(ave.)}$ / °	95.29	95.44	95.33	95.56
(d)$_{(ave.)}$ / °	78.98	78.85	78.98	78.86
Ni$_{(central)}$-O $_{(ave.)}$ / Å	2.071	2.065	2.066	2.070

Electrochemical Property of Cobalt Complexes

The **Co₉L1** showed two oxidation waves at 0.39 V and 0.85 V *vs* Fc⁺/Fc, and one reduction wave at –0.08 V *vs* Fc⁺/Fc (**Figure 29**).　When the first sweep was reversed at 0.5 V, reduction wave at –0.08 V were not observed.　This result indicates that reduction wave at –0.08 V is derived from Co ions oxidized at 0.39 V.　We tried to perform bulk electrolysis, it was difficult to reveal the number of reaction electron of these oxidation waves.　Instead of bulk electrolysis, we prepared oxidized species by chemical oxidation of **Co₉L1**, and revealed that which Co(II) ions are oxidized at two oxidation potentials respectively from their structural information.
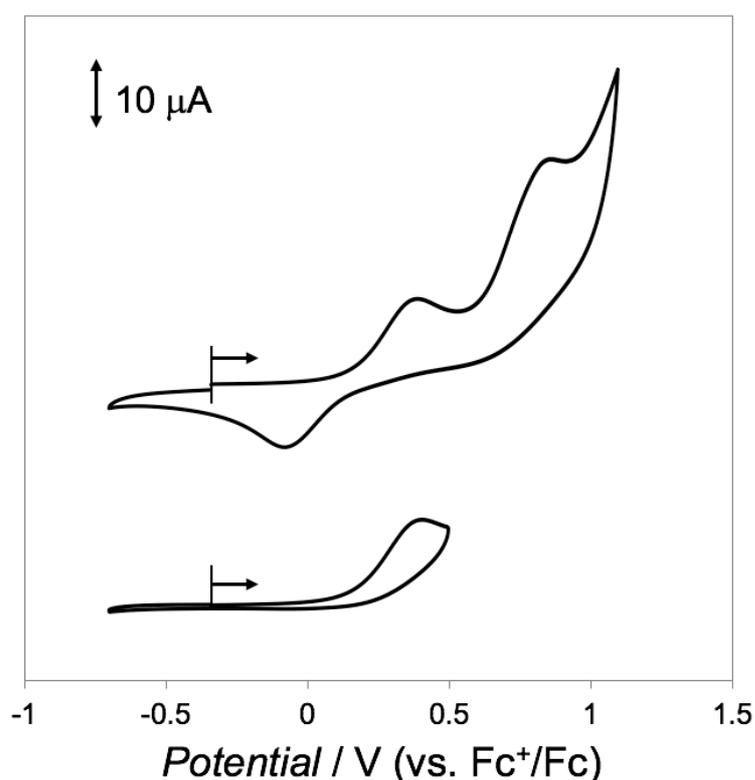
Figure 29.　Cyclic voltammograms of **Co₉L1** in MeOH/AN (*v:v* = 1:1) (1 mM, TBAP 0.1 M, scan rate 0.1V/s).

We used the two kinds of oxidants, *tert*-butyl hydroperoxide (TBHP) as weak oxidant and cerium(IV) diammonium nitrate (CAN) as strong oxidant, for chemical oxidation. As described above, when TBHP was used as the oxidant, the central Co(II) ion in heptad core was oxidized and **Co₉L1⁺_ClO₄** formed. In the case of CAN, addition to the central Co(II) ion, two terminal Co(II) ions coordinated to β-diketone were oxidized and **Co₉L1³⁺_Ce** formed. Considering the cyclic voltammetry based on these results, first oxidation wave (at 0.39 V) is one-electron oxidation derived from the central cobalt ion in hydroxyl-bridged heptanuclear core, and second wave (at 0.85 V) is two-electron oxidation derived two cobalt ions coordinated to β-diketone. Proposed redox process is shown in **Figure 30**.
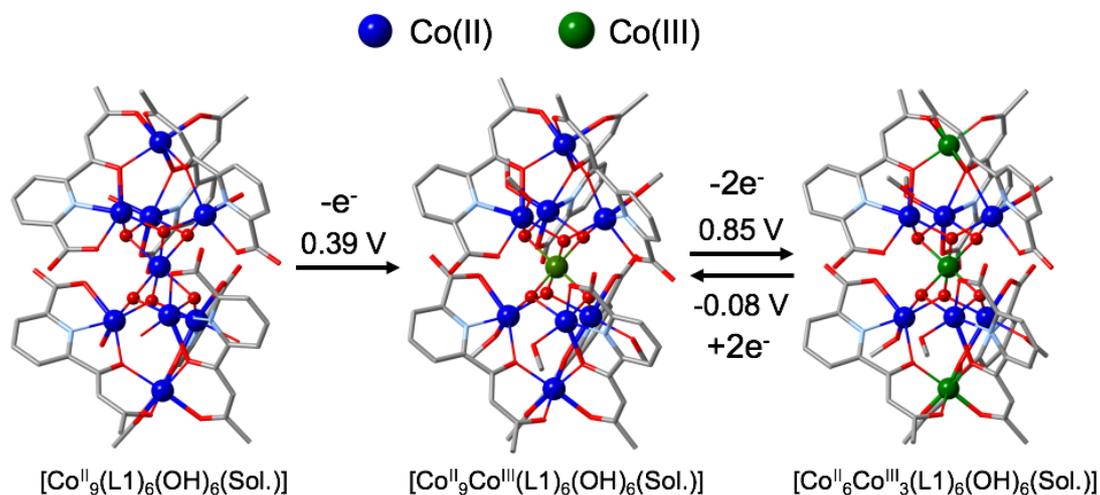
Figure 30. Proposed redox process of **Co₉L1** (Co^{II}, blue; Co^{III}, green).

The cyclic voltammograms of oxidized species are shown in **Figure 31**. **Co₉L⁺_ClO₄** showed an oxidation wave (0.85 V *vs* Fc⁺/Fc) and a reduction waves (−0.05 V *vs* Fc⁺/Fc) derived from two Co ions coordinated to β-diketone site. On the other hand, **Co₉L³⁺_ClO₄** showed no oxidation wave and one reduction waves derived from two Co(III) ions coordinated to β-diketone site. This results consistent with proposed redox process shown in **Figure 30**.
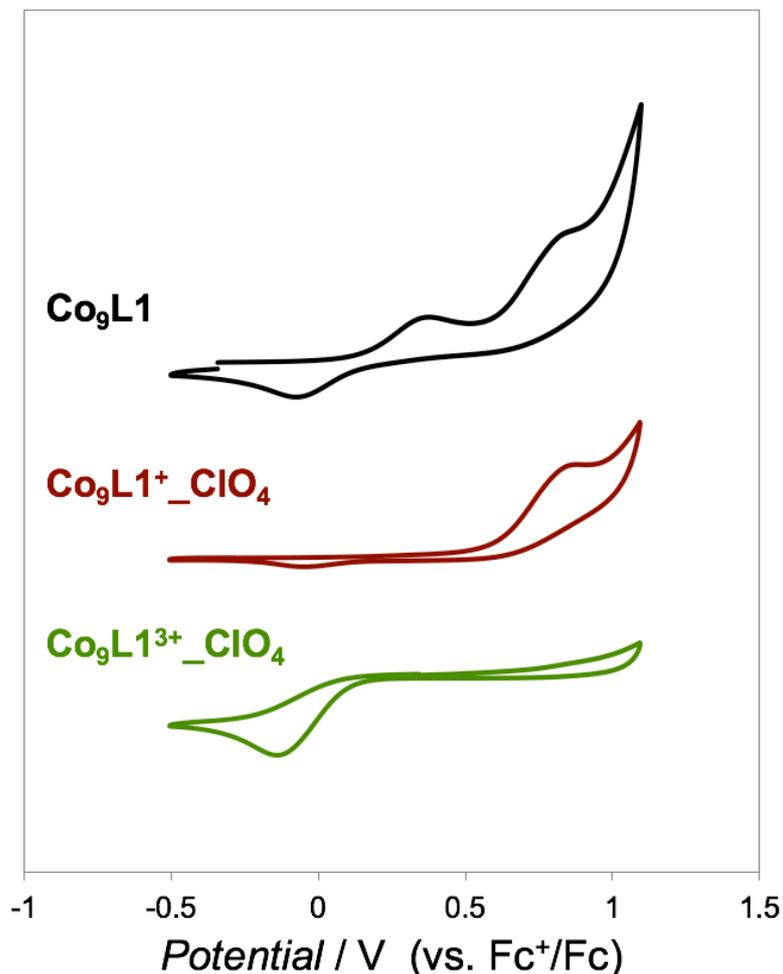
Figure 31. Cyclic voltammograms of oxidized species of **Co₉L1**. in MeOH/AN ($v{:}v$ = 1:1) (1 mM, TBAP 0.1 M, scan rate 0.1 V/s).

From the result of cyclic voltammetry and chemical oxidation, it is revealed that three Co ions in **Co₉L1** are redox active. The central Co(II) ion in hydroxyl-bridged heptanuclear core is oxidized at lower potential than cobalt ion coordinated to β-diketone site because center cobalt ion is surrounded by six hydroxyl ions and under the electron-rich environment. The Co ions coordinated to tridentate site, 1,6-subsitituted pyridine site, are redox inactive or have higher redox potential than the range of CV reported here. One of the reasons of this is that bond length of these cobalt ions and ligands are slightly longer (Co-O$_{diketone}$ = 2.233 Å, Co-O$_{carboxy}$ = 2.174 Å), so oxidation to the Co(III) which has small ion radius (0.55 Å) would be difficult.

Co₉L*n* (n = 2-4) showed almost the same CV curves as **Co₉L1** (**Figure 32**, **Table 32**). E_{pa2}, which are derived from terminal Co(II), are observed at more negative potential region compare to **Co₉L1** due to the electron donation of *t*-butyl group. Because L*n*$^{2-}$ do not coordinate to the redox-active Co(II) ion directly, expected shift of the redox potential due to the methoxy group was not observed.   On the other hand, *t*-butyl group at the β-diketone site far from central Co(II) ion, also contributed to a slight shift in the redox potential of central Co(II) (E_{pa1}).   These shifts of redox potentials may due to the slight structural changes induced by introduction of *t*-butyl group (**Figure 33**, **Table 33**).   The Co ions coordinated to tridentate site, 1,6-subsutituted pyridine site, are redox inactive or have higher redox potential than the range of CV reported here.
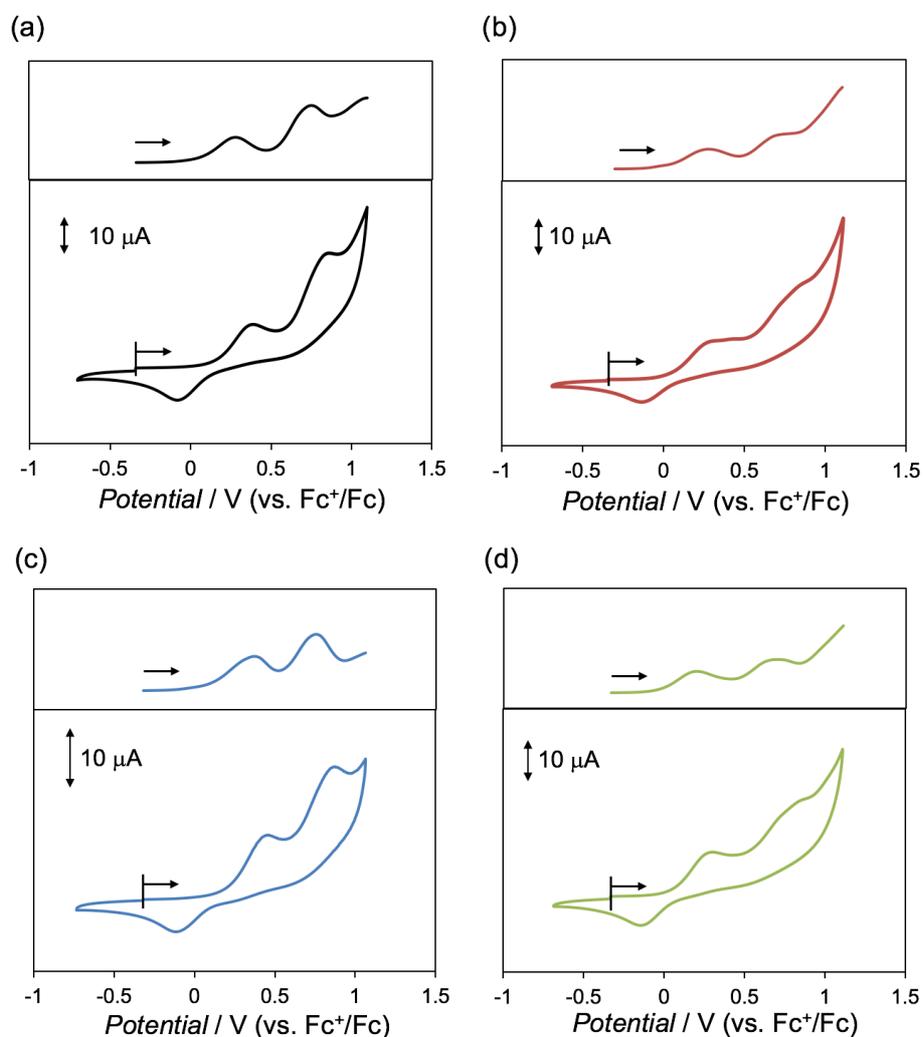
Figure 32.   Cyclic voltammograms and differential pulse voltammograms of **Co₉L1** (a), **Co₉L2** (b), **Co₉L3** (c), and **Co₉L4** (d) in MeOH/AN (*v:v* = 1:1) (1 mM, TBAP 0.1 M, scan rate 0.1 V/s)

Table 32. Redox potential of $\mathbf{Co_9L}\textit{n}$ (V vs. Fc$^+$/Fc)

complex	substituent	E_{pa1}[a]	E_{pa2}[a]	E_{pc}
$\mathbf{Co_9L1}$	none	0.28	0.75	−0.08
$\mathbf{Co_9L2}$	t-butyl	0.27	0.70	−0.13
$\mathbf{Co_9L3}$	methoxy	0.37	0.75	−0.12
$\mathbf{Co_9L4}$	t-butyl, methoxy	0.20	0.68	−0.14

[a] E_{pa1} and E_{pa2} were determined by differential pulse voltammetry.
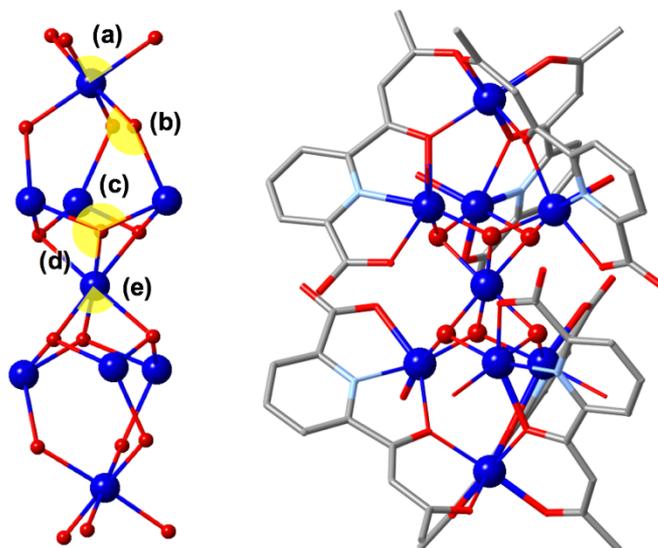
Figure 33. Co-O-Co or O-Co-O angles changed by introduction of substituent. (Numeric data were summarized in Table 33)

Table 33. Electrochemical and structural data of $\mathbf{Co_9L}\textit{n}$.

	$\mathbf{Co_9L1}$	$\mathbf{Co_9L2}$	$\mathbf{Co_9L3}$	$\mathbf{Co_9L4}$
E_{pa1} / V	0.28	0.27	0.37	0.20
(a)$_{(ave.)}$ / °	89.26	86.62	87.90	86.23
(b)$_{(ave.)}$ / °	120.98	120.30	121.83	120.67
(c)$_{(ave.)}$ / °	123.11	122.73	123.03	123.03
(d)$_{(ave.)}$ / °	95.61	95.43	95.57	95.51
(e)$_{(ave.)}$ / °	79.64	79.25	79.03	79.23
$Co_{(central)}$-O $_{(ave.)}$ / Å	2.080	2.102	2.100	2.094

Conclusion

We prepared novel nonanuclear complexes, **M₉L*n***, by a self-assembling reaction. **M₉L*n*** formed a unique corner-sharing tetrahedra-type structure with a central hydroxyl-bridged heptanuclear core, $[M_7(\mu_3\text{-}OH)_6]^{8+}$, and terminal mononuclear units, $[M^{II}(L1)_3]^{4-}$, constitute the nonanuclear structure in a [1-7-1] formation. **Ni₉L*n*** showed one quasi-reversible oxidation wave derived from Ni(III)/Ni(II) of central Ni(II) ion in heptad core. And **Co₉L*n*** showed two oxidation waves from Co(III)/Co(II) of central Co(II) ion in heptad core and both end of the Co(II) ions out of the heptad core. These results were confirmed by synthesis and structural characterization of oxidized species for **Co₉L1**. Although the number of electrons did not change in these complexes, a slight negative shift of redox potentials for central metal ions were observed by introduction of *t*-butyl group due to the structural effect.

The structure of the heptad core (corner-sharing tetrahedra) is similar to the proposed assembled structure of cobalt oxide materials (corner-sharing cubane model) known as an efficient water oxidation catalyst. However, even in the cobalt complexes with electron-donating substituent, six cobalt ions coordinated with 1,6-substituted pyridine site remained redox-inactive. It is because its coordination environment is small and unsuitable for Co(III) which has small ionic radius. Furthermore, it is considered that structural flexibility of entire complex is also needed for reversible multi-electron transfer called "redox-flexibility". To catalyze water oxidation, more than four electron transfer and high oxidation state such as Co(IV) are needed. So, we have to synthesize nonanuclear complexes by manganese and iron ions which are more redox active than cobalt ions. And we have to modify the ligand design to construct structural- and redox- flexible cluster complex to stabilize create high oxidation state, e.g. Co(IV), Fe(IV) and Mn(IV). In addition, introducing the second metal ions such as Ca⁺ like Mn_5CaO_4 cluster or construction of heterometallic cluster for tuning the redox potential of cluster is also one of the targets that we should try. Development of rational synthetic strategy for oxygen-bridged multinuclear complexes would lead to new effective catalysts inherited unique properties from the metal-oxides and metal-hydroxides.

References

1   Y. Umena, K. Kawakami, J.-R. Shen and N. Kamiya, *Nature*, 2011, **473**, 55–60.

2   L. Trotochaud, J. K. Ranney, K. N. Williams and S. W. Boettcher, *J. Am. Chem. Soc.*, 2012, **134**, 17253–17261.

3   R. Subbaraman, D. Tripkovic, K.-C. Chang, D. Strmcnik, A. P. Paulikas, P. Hirunsit, M. Chan, J. Greeley, V. Stamenkovic and N. M. Markovic, *Nature Materials*, 2012, **11**, 550–557.

4   D. K. Bediako, B. Lassalle-Kaiser, Y. Surendranath, J. Yano, V. K. Yachandra and D. G. Nocera, *J. Am. Chem. Soc.*, 2012, **134**, 6801–6809.

5   M. W. Kanan and D. G. Nocera, *Science*, 2008, **321**, 1072–1075.

6   N. S. McCool, D. M. Robinson, J. E. Sheats and G. C. Dismukes, *J. Am. Chem. Soc.*, 2011, **133**, 11446–11449.

7   S. Berardi, G. La Ganga, M. Natali, I. Bazzan, F. Puntoriero, A. Sartorel, F. Scandola, S. Campagna and M. Bonchio, *J. Am. Chem. Soc.*, 2012, **134**, 11104–11107.

8   P. F. Smith, C. Kaplan, J. E. Sheats, D. M. Robinson, N. S. McCool, N. Mezle and G. C. Dismukes, *Inorg. Chem.*, 2014, **53**, 2113–2121.

9   A. M. Ullman, Y. Liu, M. Huynh, D. K. Bediako, H. Wang, B. L. Anderson, D. C. Powers, J. J. Breen, H. D. Abruña and D. G. Nocera, *J. Am. Chem. Soc.*, 2014, **136**, 17681–17688.

10   A. I. Nguyen, M. S. Ziegler, P. Oña-Burgos, M. Sturzbecher-Hohne, W. Kim, D. E. Bellone and T. D. Tilley, *J. Am. Chem. Soc.*, 2015, **137**, 12865–12872.

11   M. D. Symes, Y. Surendranath, D. A. Lutterman and D. G. Nocera, *J. Am. Chem. Soc.*, 2011, **133**, 5174–5177.

12   R. Chakrabarty and B. K. Das, *J. Mol. Catal. A: Chemical*, 2004, **223**, 39–44.

13   R. Chakrabarty, P. Sarmah, B. Saha, S. Chakravorty and B. K. Das, *Inorg. Chem.*, 2009, **48**, 6371–6379.

14   K. Yoneda, K. Adachi, K. Nishio, M. Yamasaki, A. Fuyuhiro, M. Katada, S. Kaizaki and S. Kawata, *Angew. Chem. Int. Ed.*, 2006, **45**, 5459–5461.

15   M. Okamura, M. Kondo, R. Kuga, Y. Kurashige, T. Yanai, S. Hayami, V. K. K. Praneeth, M. Yoshida, K. Yoneda, S. Kawata and S. Masaoka, *Nature*, 2016, **530**, 1–4.

16   R. W. Saalfrank, N. Löw, S. Trummer, G. M. Sheldrick, M. Teichert and D. Stalke, *Eur. J. Inorg. Chem.*, 1998, 559–563.

17   R. W. Saalfrank, V. Seitz, F. W. Heinemann, C. Göbel and R. Herbst-Irmer, *J. Chem. Soc., Dalton Trans.*, 2001, 599–603.

18 T. Shiga, M. Noguchi, H. Sato, T. Matsumoto, G. N. Newton and H. Oshio, *Dalton Trans.*, 2013, **42**, 16185–16193.

19 H. Sato, M. Yamaguchi, T. Onuki, M. Noguchi, G. N. Newton, T. Shiga and H. Oshio, *Eur. J. Inorg. Chem.*, 2015, **2015**, 2193–2198.

20 V. Chandrasekhar, S. Das, A. Dey, S. Hossain and J.-P. Sutter, *Inorg. Chem.*, 2013, **52**, 11956–11965.

21 A.-L. Gassner, C. Duhot, J.-C. G Bünzli and A.-S. Chauvin, *Inorg. Chem.*, 2008, **47**, 7802–7812.

22 Y.-M. Luo, J. Li, L.-X. Xiao, R.-R. Tang and X.-C. Tang, *Spectrochimica Acta Part A*, 2009, **72**, 703–708.

23 O. V. Dolomanov, L. J. Bourhis, R. J. Gildea, J. A. K. Howard and H. Puschmann, *J Appl Crystallogr*, 2009, **42**, 339–341.

24 Q. Chen, M.-H. Zeng, Y.-L. Zhou, H. H. Zou and M. Kurmoo, *Chemistry of Materials*, 2010, **22**, 2114–2119.

25 S. Petit, P. Neugebauer, G. Pilet, G. Chastanet, A.-L. Barra, A. B. Antunes, W. Wernsdorfer and D. Luneau, *Inorg. Chem.*, 2012, **51**, 6645–6654.

26 N. E. Brese and M. O'Keeffe, *Acta Crystallogr., Sect. B: Struct. Sci.*, 1991, **47**, 192–197.

27 M. W. Kanan, J. Yano, Y. Surendranath, M. Dincă, V. K. Yachandra and D. G. Nocera, *J. Am. Chem. Soc.*, 2010, **132**, 13692–13701.

28 S. Shit, M. Nandy, G. Rosair, C. J. Gómez-García, J. J. Borras Almenar and S. Mitra, *Polyhedron*, 2013, **61**, 73–79.

29 S.-H. Zhang, N. Li, C.-M. Ge, C. Feng and L.-F. Ma, *Dalton Trans.*, 2011, **40**, 3000–3007.

Chapter 2

Synthesis and Electrochemical Property Control of Edge-sharing Hydroxyl-bridged Multinuclear Metal Complexes

Abstract

Hydroxyl-bridged heptanucler complex $[Fe^{III}Fe^{II}_6(Ln)_6(OH)_6](PF_6)_3$ (**Fe$_7$Ln**, n = 5, 6) were prepared via self-assemble reaction of HL5 (2-acetoacetyl pyridine), HL6 (1-phenyl-3-(pyridin-2-yl)propane-1,3-dione).   **Fe$_7$L5** has unique edge-sharing hydroxyl-bridged cluster structure that seven Fe ions on the same plane are bridged by the six hydroxyl anions and surrounded by six ligands.   **Fe$_7$L5** showed several redox waves in cyclic voltammetry, -1.05 V *vs.* Fc$^+$/Fc derived from Fe(III)/Fe(II) for central Fe(III), the two redox waves at -0.09 V and 0.20 V from Fe(III)/Fe(II) for two peripheral Fe(II), and small oxidation peaks at 0.4 V - 0.7 V.   We attempted to control the electrochemical property of the cluster by two method.   One method is introduction of substituent to ligand.   We newly synthesized edge-sharing hydroxyl-bridged cluster **Fe$_7$L6** with HL6.   The HL6 has longer π-conjugated system by introduction of phenyl group to terminal position of β-diketone. The other method is synthesis of heterometallic cluster.   We synthesized heterometallic cluster complexes, $[Fe^{III}M_6(L5)_6(OH)_6](PF_6)_3$ (**FeM$_6$L5**, M = Mn, Co, Ni, Zn) and $[Fe^{III}Fe_3Zn_3(L5)_6(OH)_6](PF_6)_3$ (**Fe$_4$Zn$_3$L5**) by one-pot reaction.   Herein, we investigated the effect of ligands and construction of heterometallic complex on electrochemical properties.

Introduction

   Controlling the redox property of Coordination clusters (CCs) is an indispensable task applied for various reactions such as water oxidation reaction, electron storage and electron mediator using their redox properties such as multi-electron transfer. High-nuclearity compound is attracted much attention because their unique electrochemical properties, e.g. high catalytic activity for water oxidation reaction (the pentanuclear iron cluster reported by S. Masaoka *et al.*[1]). Polyoxometalates (POMs) which are discrete anionic metal-oxygen clusters. It is assembly of the {MOx} polyhedra ($V^{IV,V}$, Mo^{VI}, or W^{VI} etc.), and have a wide range of functions utilizing its redox properties, such as being applied not only to catalysts but also to electron mediators.[2-4] Although POMs show various electrochemical properties, it is difficult to tune their redox potentials precisely for using in a targeted reaction. On the other hand, redox potentials of cluster complexes are tunable precisely by changing some of its constituent elements (ligand, bridging agent, metal ions). One of the strategy for controlling the potential is constructing a hetero metal cluster by introducing a redox inactive metal ions into a cluster composed of redox active metal ions. It is inspired by Mn_4CaO_5 clusters that works as oxygen evolution catalysts of Photosystem II (**Figure 1a**).[5] It forms cube structure composed of four manganese ions and a calcium ions bridged by five oxo anions. In the water oxidation reaction, it is considered that redox-active Mn ions work as reaction center and a redox-inactive Ca ions stabilizes the higher oxidation states for Mn ions by localizing the negative charge of bridging oxo ions to Mn ions, and adjusts redox potentials of Mn ions to catalyze reaction efficiently. Co-Zn Layered Double Hydroxide (**Co-Zn LDH**) also known as heterogeneous water and alcohol oxidation catalyst in electrochemical conditions consist of redox-active Co ions and inactive Zn ions (**Figure 1b**).[6,7] In this compound, it is also considered that redox-inactive Zn ions stabilize high oxidation state of redox-active Co ions to drive an oxidative reaction.
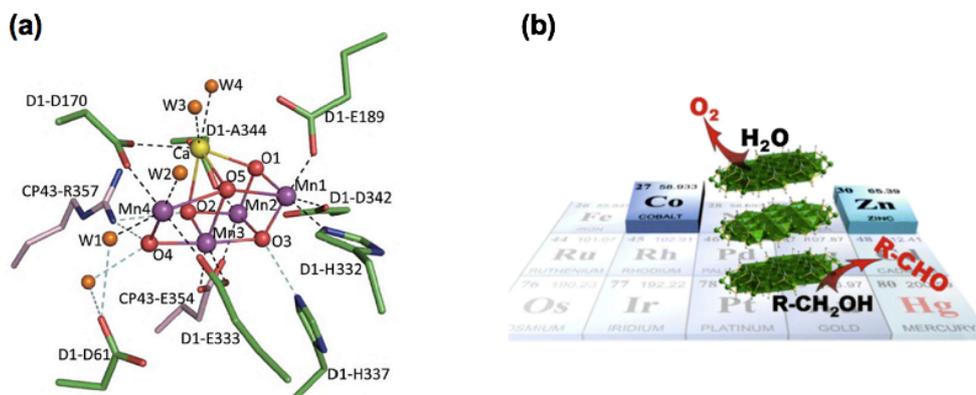
Figure 1. (a) Structure of the Mn_4CaO_5 cluster.[5] (b) Co-Zn LDH as an efficient catalyst for water and alcohol oxidation.[6,7]

This argument that redox-inactive metal ions is needed for accessing high oxidation state and efficient catalytic reaction has also been verified by other model compounds. T. Agapie *et al*. reported two complexes with the $[Mn_3CaO_4]$ and $[Mn_4O_4]$ cubane structure by a multinucleating ligand framework as a partial structural model of the Mn_4CaO_5 cluster in the Photosystem II (**Figure 2**).[8] Electrochemical study revealed that the calcium-containing $Mn^{IV}_3CaO_4$ cubane can be reduced at potential > 1 V more negative compared with the homometallic manganese $Mn^{IV}_3Mn^{III}O_4$ cubane. They also reported $[Mn_3MO_4]$ (M = Sr^{2+}, Zn^{2+}, Sc^{3+}, Y^{3+}) type cubane complex and a series of tetranuclear $[Mn_3M(\mu_4\text{-}O)(\mu_2\text{-}O)]$ (M = Na^+, Ca^{2+}, Sr^{2+}, Zn^{2+}, Y^{3+}) type heterometallic tri-manganese cluster complexes containing a redox-inactive metal ion by using the same ligand.[9] The redox potentials attributed to the $[Mn^{IV}_3MO_4]/[Mn^{IV}_2Mn^{III}MO_4]$ and $[Mn^{IV}Mn^{III}_2MO_2]/[Mn^{III}_3MO_2]$ redox couple of these complexes depend on the Lewis acidity of the redox-inactive metals. This result indicates possible role of the redox-inactive Ca^{2+} ion of the Mn-Ca cluster in modulating its redox potential. Similarly, Fukuzumi *et al*. reported that the redox inactive Ca^{2+} or Sc^{3+} ions binding to the oxo atom of non-heme oxo-iron complex stabilizes and improves ET pathways to high-valent Fe-oxo species.[10]
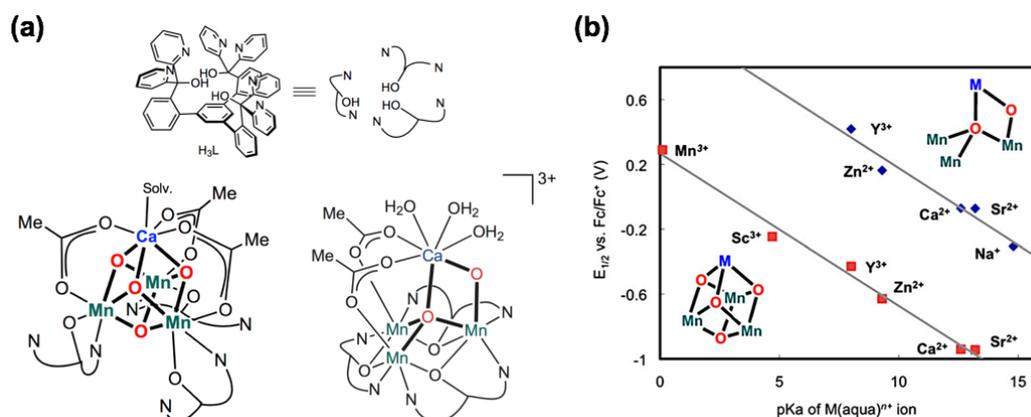
Figure 2. (a) Structures of [Mn$_3$CaO$_4$] cubane complex (left) and [Mn$_3$CaO$_2$] cluster (right). (b) Reduction potentials of [Mn$_3$MO$_4$] cubane type complexes (red squares) and [MMn$_3$O$_2$] complexes (blue diamonds) *vs*. pK_a of the corresponding M(aqua)$^{n+}$ ion as a measure of Lewis acidity.[8,9]

In chapter 1, we synthesized corner-sharing tetrahedra cluster, [M$_9$(L1)$_6$(OH)$_6$(sol.)$_6$] (**M$_9$L1**, M = Co^{II}, Ni^{II}) by using β-diketone based ligand. It was very rare structure and expected to induce multi-electron transfer due to multinuclear structure and hydroxyl-bridging structure similar to layered double hydroxide (LDH)[7] and cobalt oxide materials.[11-14] However, one electron (**Ni$_9$L1**) and three electron transfer (**Co$_9$L1**) was observed (**Figure 3**). Unfortunately, only one electron was observed from hydroxyl-bridged heptanuclear cluster core for **Co$_9$L1** and no redox properties was observed from the other six Co(II) coordinated to the tridentate coordination site of H$_2$L1. We attempted to synthesize analogs to improve the redox properties of these Co ions. However, despite the use of the ligand to which an electron-donating substituent had been introduced, the six Co(II) remained redox-inactive and the redox potential of the redox-active Co(II) changed slightly. As described in chapter 1, one of the reason for this is the lack of structural flexibility of coordination environment for redox-inactive six Co(II) ions and entire complex. Generally, 3d metal ions have large structural change such as bond distance and angles accompanying oxidation and reduction. For such reason, most of redox-active cluster complexes are constructed by simple ligands such as monodentate and bidentate ligands, or flexible ligands.
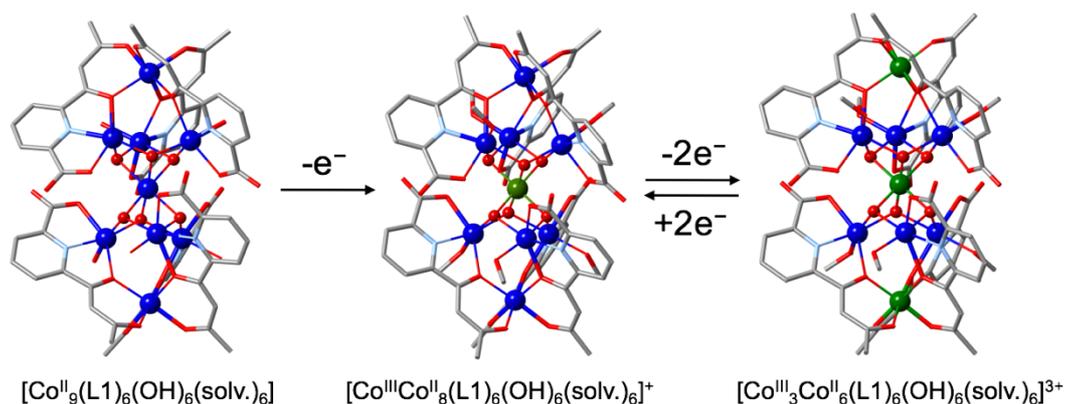
Figure 3. Three electron transfer process of **Co₉L1**. (Co^{III}: green; Co^{II}: blue; C: gray; O: red; and N: light blue)

In this work, to achieve the multi-electron transfer from hydroxyl-bridged cluster, we newly prepared HL5, which has a simplified structure of H$_2$L1, and attempted to synthesize a novel coordination cluster. By using HL5 which has two bidentate coordination site, it was expected that formation of a tetranuclear complex, which is half the structure of **M₉L1**. Unexpectedly, hydroxyl-bridged heptanucler complex [M$_7$(L5)$_6$(OH)$_6$](PF$_6$)n (**M₇L5**, M = Mn^{II}, Fe$^{II/III}$, Co^{II}, Ni^{II}, Zn^{II}; n = 2, 3) were formed by self-assembling reaction of HL5 with 3d metal ions (**Figure 4**). Although the structure of **M₇L5** was different from the structure what we expected, it had a cluster structure composed of seven metal ions and six hydroxyl ions which is the same composition but different structure as **M₉L1**. Such assembled structures were called "disk-shaped" cluster or "wheel-type" cluster, and it has been reported with several ligand or different bridging agent (e.g. OH⁻, OMe⁻, N$_3$⁻ and alkoxide)[15-47]. However, most of reported disk-like cluster was not focused on their electrochemical properties but magnetic properties. Therefore, there are relatively few reports on disk-like cluster complexes with iron ions that are expected to induce multi-electron transfer[19,25,28,41]. Particularly, there is no report on the electrochemical properties of disk-like iron clusters.
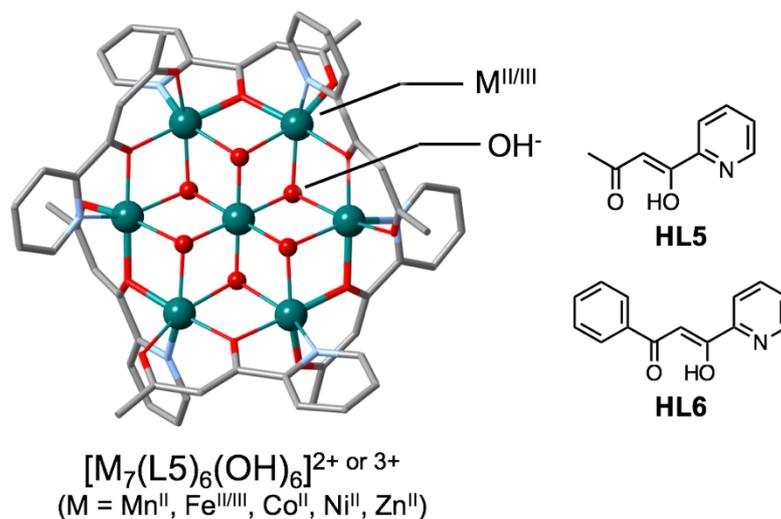
$$[M_7(L5)_6(OH)_6]^{2+ \text{ or } 3+}$$
(M = Mn^{II}, Fe$^{II/III}$, Co^{II}, Ni^{II}, Zn^{II})

Figure 4.   Structure of **M$_7$L5** and ligands (**HL5-HL6**).

For these reasons, here we focused on electrochemical property of disk-like iron cluster (**Fe$_7$L5**).   Furthermore, we attempted to control the electrochemistry for cluster by two method.   One is introduction of substituent to ligand and imparting structural flexibility.   We newly synthesized **HL6** (**Figure 4**).   **HL6** has longer π-conjugated system by introduction of phenyl group to terminal position of β-diketone.   The other method is synthesis of heterometallic cluster.   As described above, it is expected to control a redox property (redox potentials and number of electrons) by introduction of redox-inactive metal ions to cluster composed of redox-active metal ions.   In this work, we selected Zn ion as redox-inactive metal ion and tried to synthesize the FeZn heterometallic clusters, because we have prepared the disk-shaped heptanuclear cluster same structure as **Fe$_7$L5** by Zn ions.   And we tried to synthesize two kinds of complexes the Fe/Zn ratio of which is 1/6 and 4/3 considering structural features of clusters.   In **Fe$_7$L5**, there are two types of coordination environments.   One is the O6 coordination in central Fe(III), and the other is NO5 coordination in six peripheral Fe(II).   Therefore, by using the difference of coordination environments, it is expected to 1 to 6 type of heterometallic cluster shown in **Figure 5**.   In addition, this has three fold symmetry centering on a central Fe(III).   So, we considered that the half of peripheral Fe(II) can be replaced to Zn ions, and we can distinguish peripheral Zn from Fe(II).   Considering this structural features, we also tried to synthesize the 4 to 3 type heterometallic cluster.   Additionally, we also prepared 1 to 6 type heterometallic cluster by Mn(II), Co(II) to investigated the effect of construction of heterometallic cluster.   By construction of heterometallic complexes, it is expected that suppression of

increase of entire charge by decreasing the number of redox active metal ion and localize the negative charge of hydroxyl anion to Fe. By these effects, it is expected that stabilizing a high-oxidation state of Fe ions.

1. Two coordination environments (M_{O6} : M_{NO5} = 1 : 6)

M : M' = 1 : 6
heterometallic complex
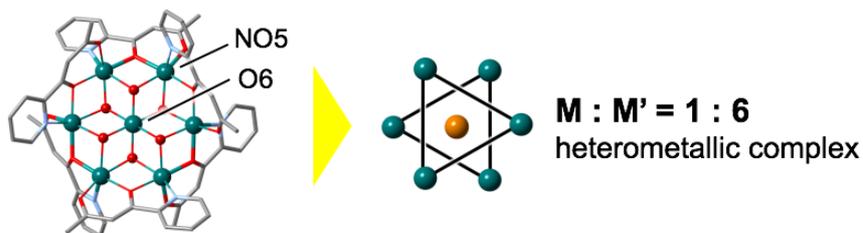
2. Two coordination environments + three-fold symmetry

M : M' = 4 : 3
heterometallic complex
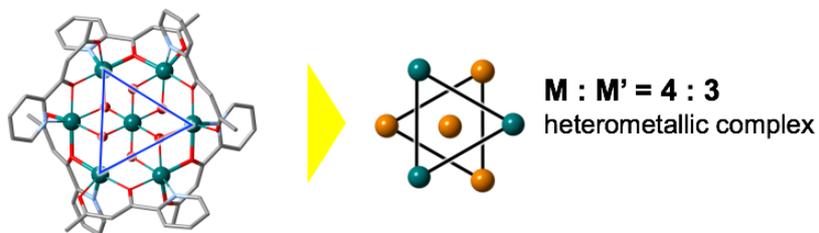
Figure 5. Strategy for synthesis of two types of heterometallic disk-like clusters.

Experimental

Physical measurements

Elemental analyses of carbon, hydrogen and nitrogen were carried out by the staff of technical support division graduate school of science, Kyushu University. UV-Vis absorption was measured by JASCO V-630. Infrared spectra were measured with a JASCO FT/IR-4200 using ATR method.   X-ray fluorescence analysis was carried out on a Rigaku EDX-70. ^{1}H NMR spectra were acquired on a JEOL JNM-ESA 600 spectrometer.   Cyclic voltammogram was recorded on an ALS 612D electrochemical analyzer in a degassed acetonitrile solution containing 0.1 M tetra(n-butyl)ammonium hexafluorophosphate (TBAPF$_6$) which was purified by recrystallization from ethanol. All electrodes used was purchased from BAS. Platinum electrode was used as counter electrode and glassy carbon electrode was used as working with electrode which was polished with 0.05 μm polishing alumina. As the reference electrode, RE-7 nonaqueous reference electrode (Ag^{+}/Ag) was used. Bulk electrolysis was carried on the platinum electrode as counter electrode, RE-7 nonaqueous electrode (Ag^{+}/Ag) as reference electrode (Ag^{+}/Ag) and porous carbon electrode as the working electrode.

Preparation

All chemicals were purchased from commercial sources and used without further purification. 2-acetoacetylpyridine (HL5) and 1-phenyl-3-(pyridin-2-yl)propane-1,3-dione (HL6) were prepared by Claisen condensation with reference to the literature method.[48]   Several complexes including Fe(II) were prepared under anaerobic condition.

2-acetoacetylpyridine (HL5)

2-methylpicolinate (13.71 g, 0.10 mol), acetone (11.62 g. 0.2 mol) and sodium methoxide methanoic solution (5 mol/l, 20 ml) was added to diethyl ether (200 ml). The mixture was stirred for a day.   The pale yellow precipitate was filtered and washed with diethyl ether and dried in vacuo.   After that, pale yellow powder was recrystallized from 30 ml of EtOH/H_2O (*v:v* = 1:1) containing acetic acid (6 ml). White crystals were collected by filtration and wash with water and dried in *vacuo*. Yield 7.317 g (44.9 %) ^{1}H NMR (600 MHz, CDCl$_3$ δ in ppm): 8.65 (d, 1H, J=4.8 Hz, py), 8.07 (d, 1H, J=7.8 Hz, py), 7.83 (t, 1H, J=7.8 Hz, py), 7.41 (d, 1H, J=6.0 Hz, py), 6.82 (s, 1H, –CH=), 2.23 (s, 3H, –CH$_3$).   Elemental analysis (%); Calcd. for $C_9H_9NO_2$: C 66.25, H 5.56, N 8.58; found: C 66.25, H 5.56, N 8.58. Formula weight 163.08 Formula weight 163.08   FT-IR (cm^{-1}); 1622, 1514, 1578, 1567, 1434, 1360, 1297, 1287, 1245, 1185, 1094, 1078, 984, 934, 847, 781, 741, 691

1-phenyl-3-(pyridin-2-yl)propane-1,3-dione (HL6)

2-methylpicolinate (2.742 g, 20 mmol), acetophenone (2.403 g 20 mol) and sodium methoxide methanoic solution (5 mol/l, 4.4 ml) was added to diethyl ether (40 ml). The mixture was stirred for 4 hours.   The pale yellow precipitate was filtered and washed with diethyl ether and dried in *vacuo*.   After that, pale yellow powder was dissolved in water (40 ml), and solution was acidified by acetic acid.   White precipitate of crude product was collected by filtration and wash with water.   White crystals of pure sample was obtained after recrystallization from hot EtOH, and dried in *vacuo*. Yield 2.00 g (44.4 %) ^{1}H NMR (600 MHz, CDCl$_3$ δ in ppm): 16.46 (s, 1H, –OH), 8.71 (d, 1H, J=4.2 Hz, py), 8.16 (d, 1H, J=7.8 Hz, py), 8.07 (d, 2H, J=7.8 Hz, Ph), 7.86 (t, 1H, J=7.8 Hz, py), 7.58 (s, 1H, –CH–), 7.55 (t, 1H, J=7.2 Hz, py), 7.48 (t, 2H, J=7.5 Hz, Ph), 7.436 (dd, 1H, J=7.2, 4.8 Hz, py) Elemental analysis (%);Calcd. for $C_{14}H_{11}NO_2$: C 74.65, H 4.92, N 6.22; Found: C 74.62, H 4.94, N 6.21. Formula weight 225.25   FT-IR (cm^{-1}); 1600, 1557, 1540, 1487, 1473, 1458, 1422, 1309, 1251, 1214, 1087, 1074, 1069, 1042, 1023, 994, 796, 774, 751, 710, 689, 668

[Fe^{III}Fe$^{II}_6$(L5)$_6$(OH)$_6$](PF$_6$)$_3$ (Fe$_7$L5)

FeSO$_4$·7H$_2$O (973 mg, 3.5 mmol) and ascorbic acid were dissolved in 5 ml of water. Then, Methanoic solution of HL5 (489 mg, 3.0 mmol) was added in the solution, followed by addition of Et$_3$N (623 µl). Dark purple solution was heated at 100 °C for 10 minutes by microwave reactor. After that, Methanoic solution of tetrabutylammonium hexafluorophosphate (1.161g, 2.5 mmol) was added to the dark purple solution. Black crystals formed after 1 day were collected by filtration and washed by diethyl ether. Crude sample were recrystallized from acetonitrile solution by ether diffusion. Black crystals formed within 2 weeks ware collected by filtration and washed with diethyl ether and dried *in vacuo*. Yield 100.2 mg (10.5 %), Elemental analysis (%); Calcd. for C$_{54}$H$_{54}$F$_{18}$Fe$_7$N$_6$O$_{18}$P$_3$ [Fe$_7$(L5)$_6$(OH)$_6$](PF$_6$)$_3$: C 34.12, H 2.86, N 4.42; found: C 34.77, H 2.85, N 4.42. Formula weight 1900.86 FT-IR (cm^{-1}); 1598, 1509, 1469, 1449, 1365, 1280, 1253, 1210, 1164, 1132, 1053, 1022, 1006, 940, 842, 783, 687

[Fe^{III}Fe$^{II}_6$(L6)$_6$(OH)$_6$](PF$_6$)$_3$ (Fe$_7$L6)

FeSO$_4$·7H$_2$O (389mg, 1.4 mmol) and ascorbic acid were dissolved in 2 ml of water. Then, Methanoic solution of HL6 (271 mg, 6.0 mmol) was added in the solution, followed by addition of Et$_3$N (250 µl). Dark purple solution was heated at 100 °C for 10 minutes by microwave reactor. After that, Methanoic solution of tetrabutylammonium hexafluorophosphate (387 mg, 1.0 mmol) was added to the dark purple solution. Black crystals formed after a day were collected by filtration and washed by diethyl ether. Crude sample were recrystallized from acetonitrile solution by ether diffusion. Black crystals formed within 2 weeks ware collected by filtration and washed with diethyl ether and dried *in vacuo*. Yield 100.0 mg (22.0 %), Elemental analysis (%); Calcd. for C$_{84}$H$_{66}$F$_{18}$Fe$_7$N$_6$O$_{18}$P$_3$ [Fe$_7$(L6)$_6$(OH)$_6$](PF$_6$)$_3$: C 44.38, H 2.93, N 3.70; found: C 44.64, H 3.07, N 3.56. Formula weight 2273.28 FT-IR (cm^{-1}); 1592, 1561, 1505, 1563, 1389, 1283, 1024, 839, 769, 708

[Fe^{III}Zn$_6$(L5)$_6$(OH)$_6$](PF$_6$)$_3$ (FeZn$_6$L5)

Fe(ClO$_4$)$_3$·6 H$_2$O (231 mg, 0.5 mmol) and Zn(ClO$_4$)$_2$·6 H$_2$O (1.127 g, 3.0 mmol), HL5 and Et$_3$N (623 µl) were dissolved in 20 ml of CH$_3$CN/H$_2$O (v:v = 3:1), and the solution was heated at 100 °C for 10 minutes by microwave reactor. Gray powder was collected by filtration and washed by acetone and diethyl ether. Counter anion (ClO$_4^-$) of complex was changed to PF$_6^-$ by addition of tetrabutylammonium hexafluorophosphate to acetonitrile solution of gray powder. After that, gray powder

of crude product was recrystallized from acetonitrile by ether diffusion. Pale blue crystals formed within 2 weeks ware collected by filtration and washed with diethyl ether and dried *in vacuo.* Yield 153.5 mg (15.7 %), Elemental analysis (%); Calcd. for $C_{54}H_{54}F_8N_6O_{18}P_3Zn_6$ [$FeZn_6(L5)_6(OH)$]$(PF_6)_3$: C 33.12, H 2.78, N 4.29; found: C 33.28, H 2.70, N 4.30. Formula weight 1958.07 FT-IR (cm^{-1}); 1620, 1597, 1515, 1465, 1456, 1423, 1365, 1279, 1261, 1210, 1160, 1143, 1050, 1026, 1003, 937, 746, 773, 685

[$Fe^{III}Mn_6(L5)_6(OH)_6$]$(PF_6)_3$ (FeMn$_6$L5)

Fe(ClO$_4$)$_3$·6H$_2$O (185 mg, 0.4 mmol) and Mn(ClO$_4$)$_2$·6H$_2$O (868 mg, 2.4 mmol) were mixed in 8 ml of MeOH/water (*v:v* = 3:1). HL5 (489 mg, 3.0 mmol) and Et$_3$N (499 µl) were added to the solution and stirred an hour. Formed orange powder of crude product were collected by filtration and washed by diethyl ether. The counter anion (ClO$_4^-$) of crude sample was changed to PF$_6^-$ by addition of tetrabutylammonium hexafluorophosphate to acetonitrile solution of sample. After that, crude sample was recrystallized by ether diffusion to the acetonitrile solution. The orange crystals formed within 2 days ware collected by filtration and washed with diethyl ether and dried *in vacuo.* Yield 60 mg (3.2 %), Elemental analysis (%); Calcd. for $C_{54}H_{54}F_{18}FeMn_6N_6O_{18}P_3$ [$FeMn_6(L5)_6(OH)_6$]$(PF_6)_3$: C 34.22, H 2.87, N 4.43; found: C 34.51, H 2.87, N 4.41. Formula weight 1895.42 FT-IR (cm^{-1}); 1617, 1510, 1454, 1419, 1363, 1277, 1211, 1162, 1137, 1017, 1002, 941, 846, 771, 738, 681

[$Fe^{III}Co_6(L5)_6(OH)_6$]$(PF_6)_3$ (FeCo$_6$L5)

Fe(ClO$_4$)$_3$·6H$_2$O (92 mg, 0.2 mmol) and Co(ClO$_4$)$_2$·6H$_2$O (439 mg, 1.2 mmol), and KPF$_6$ were mixed in 4 ml of water and stirred for 1 hour. 12 ml of acetonitrile are added to the solution, and formed KClO$_4$ were removed by filtration. HL5 (195 mg, 1.2 mmol) and Et$_3$N (250 µl) were added to the filtrate and stirred 12 hours. Brown powder of crude product were collected by filtration. Residual Counter anion (ClO$_4^-$) of complex was changed to PF$_6^-$ by addition of tetrabutylammonium hexafluorophosphate to acetonitrile solution of brown powder. Crude product was recrystallized by ether diffusion to acetonitrile solution. Crystals formed within 3 days ware collected by filtration and washed with diethyl ether and dried *in vacuo.* Yield 86.4 mg (22.5 %), Elemental analysis (%); Calcd. for $C_{54}H_{54}Co_6F_{18}FeN_6O_{18}P_3$ [$Fe^{III}Co_6(L5)_6(OH)_6$]: C 33.79, H 2.84, N 4.38; found: C 33.65, H 2.66, N 4.38. Formula weight 1919.39 FT-IR (cm^{-1}); 1619, 1600, 1512, 1464, 1454, 1365, 1280, 1258, 1209, 1163, 1140, 1050, 1022, 999, 935, 840, 774, 685

[Fe^{III}Ni$_6$(L5)$_6$(OH)$_6$](PF$_6$)$_3$ (FeNi$_6$L5)

Fe(ClO$_4$)$_3$·6H$_2$O (231 mg, 0.5 mmol) and Ni(ClO$_4$)$_2$·6H$_2$O (1.097 g, 3.0 mmol) were mixed in 10 ml of MeOH/water (*v:v* = 3:1). HL5 (489 mg, 3.0 mmol) and Et$_3$N (624 μl) were added to the solution and heated at 100 °C for 10 minutes by microwave reactor. Formed green powder of crude product were collected by filtration and washed by diethyl ether. The counter anion (ClO^{4-}) of complex was changed to PF$_6^-$ by addition of NH$_4$PF$_6$ aq. (1 M) to acetonitrile solution of crude sample. After that, powder sample was recrystallized by ether diffusion to the acetonitrile solution. The green crystals formed within 2 days ware collected by filtration and washed with diethyl ether and dried *in vacuo*. Yield 97.6 mg (8.9 %), Elemental analysis (%); Calcd. for C$_{54}$H$_{54}$F$_{18}$FeN$_6$Ni$_6$O$_{18}$P$_3$ [FeNi$_6$(L5)$_6$(OH)$_6$](PF$_6$)$_3$·CH$_3$CN: C 34.33, H 2.93, N 5.01; found: C 34.50, H 3.09, N 4.90. Formula weight 1959.00 FT-IR (cm^{-1}); 1621, 1517, 1456, 1422, 1362, 1282, 1211, 1160, 1142, 1053, 1024, 941, 841, 775, 686

[Fe^{III}Fe$_3$Zn$_3$(L5)$_6$(OH)$_6$](PF$_6$)$_3$ (Fe$_4$Zn$_3$L5)

FeSO$_4$·7H$_2$O (556 mg, 2.0 mmol) and ZnSO$_4$·7H$_2$O (431 mg, 1.5 mmol) and ascorbic acid were dissolved in 5 ml of water. Then, Methanoic solution of HL5 (489 mg, 3.0 mmol) was added in the solution, followed by addition of Et$_3$N (623 μl). Dark purple solution was heated at 100 °C for 10 minutes by microwave reactor. After that, Methanoic solution of tetrabutylammonium hexafluorophosphate (1.161g, 2.5 mmol) was added to the dark purple solution. After 2 day, black crystals formed after 2 days were collected by filtration and washed by diethyl ether. Dark blue crystals formed within 2 weeks ware collected by filtration and washed with diethyl ether and dried *in vacuo*. Yield 19.2 mg (4.8 %), Elemental analysis (%); Calcd. for C$_{56}$H$_{57}$F$_{18}$Fe$_4$N$_7$O$_{18}$P$_3$Zn$_3$ [Fe^{III}Fe$_3$Zn$_3$(L5)$_6$(OH)$_6$](PF$_6$)$_3$·CH$_3$CN: C 34.13, H 2.92, N 4.98; found: C 34.62, H 3.00, N 4.64. Formula weight 1970.52 FT-IR (cm^{-1}); 1617, 1599, 1508, 1465, 1449, 1416, 1366, 1279, 1258, 1210, 1158, 1140, 1156, 1017, 1000, 941, 846, 776, 687

X-ray Crystallography

All Single-crystal X-ray diffraction data were collected on a Bulker SMART APEX II ULTRA CCD-detector Diffractometer, a rotating-anode (Bruker Tourbo X-ray source) with graphite-monochromated $Mo_{K\alpha}$ radiation (λ = 0.71073 Å) was used. Computations were carried out on a APEX2 crystallographic software package and OLEX2 software. [49] A single crystal was mounted on a polymer film with liquid paraffin and the temperature kept –173°C under flowing N_2 gas. All of the structures were solved by direct method or intrinsic method. All the structures were expanded using Fourier techniques. Fullmatrixleast-squares refinements were carried out with anisotropic thermal parameters for all non-hydrogen atoms. The hydrogen atoms were attached based on the difference Fourier map and calculation geometrically. The SQUEEZE program was used to remove the contribution of the highly disordered solvent molecules from the structural calculations. Crystal parameters are summarized in **Table 1-3**.

Table 1. Crystallographic parameters of **Fe₇L5** and **Fe₇L6**

Complex	Fe₇L5	Fe₇L6
Formula	$C_{54}H_{54}N_6O_{18}F_{18}P_3Fe_7$	$C_{84}H_{66}F_{18}Fe_7N_6O_{18}P$
Formula weight	1900.89	2273.28
Temperature / K	100	100
Crystal size / mm	$0.211 \times 0.150 \times 0.046$	$1.095 \times 0.182 \times 0.066$
Crystal system	Monoclinic	Monoclinic
Space group	$P2_1/n$	C2/c
a / Å	18.906(3)	29.085(12)
b / Å	21.476(3)	27.816(12)
c / Å	24.105(4)	19.641(8)
α / °	90	90
β / °	105.671(2)	120.027(5)
γ / °	90	90
Volume / Å³	9424(2)	13758(10)
Z value	4	4
D (calcd.) / gcm⁻³	1.340	1.098
$R1$	0.0575	0.0969
$wR2$	0.1636	0.1408
Goodness of Fit	1.087	1.047

Table 2. Crystallographic parameters of **FeZn$_6$L5** and **FeMn$_6$L5**

Complex	FeZn$_6$L5	FeMn$_6$L5
Formula	C$_{54}$H$_{54}$N$_6$O$_{18}$F$_{18}$P$_3$FeZn$_6$	C$_{54}$H$_{54}$N$_6$O$_{18}$F$_{18}$P$_3$FeMn$_6$
Formula weight	1958.01	1895.43
Temperature / K	100	100
Crystal size / mm	$0.182 \times 0.075 \times 0.034$	$0.216 \times 0.162 \times 0.083$
Crystal system	monoclinic	monoclinic
Space group	$P2_1$/n	$P2$/c
a / Å	18.935(7)	16.374(18)
b / Å	21.296(8)	22.512(3)
c / Å	23.970(9)	13.4543(15)
α / °	90	90
β / °	105.804(5)	110.6780(10)
γ / °	90	90
Volume / Å^3	9301(6)	4544.5(9)
Z value	4	2
D (calcd.) / gcm^{-3}	1.398	1.385
R1	0.0780	0.1139
wR2	0.2227	0.3770
Goodness of Fit	0.910	1.338

Table 3. Crystallographic parameters of **FeCo$_6$L5** and **Fe$_4$Zn$_3$L5**

Complex	FeCo$_6$L5	Fe$_4$Zn$_3$L5
Formula	C$_{54}$H$_{54}$N$_6$O$_{18}$F$_{18}$P$_3$FeCo$_6$	C$_{54}$H$_{56}$F$_{18}$Fe$_4$N$_6$O$_{18}$P$_3$Zn$_3$
Formula weight	1919.37	1931.46
Temperature / K	100	100
Crystal size / mm	$0.562 \times 0.166 \times 0.110$	$0.056 \times 0.055 \times 0.074$
Crystal system	Monoclinic	Monoclinic
Space group	$P2_1$/n	$P2$/c
a / Å	19.062(2)	15.816(4)
b / Å	21.352(2)	22.497(6)
c / Å	24.021(3)	13.459(3)
α / °	90	90
β / °	105.9150(10)	110.583(3)
γ / °	90	90
Volume / Å^3	9402.2(18)	4483.(2)
Z value	4	2
D (calcd.) / gcm^{-3}	1.356	1.431
R1	0.0642	0.0902
wR2	0.1979	0.2741
Goodness of Fit	1.107	1.587

Result and Discussion

Crystal Structure of Heptanuclear Fe Cluster

The molecular structure of **Fe₇L5** and **Fe₇L6** are shown in **Figure 6-7**. All complexes formed almost the same structure that seven metal ions on the same plane are bridged by six hydroxyl anions and surrounded by six ligands. This assembled structures was typically called disk-like cluster or wheel-type cluster, and it has been reported with several ligand or different bridging agent (e.g. OH^-, OMe^-, N_3^- and alkoxide)[15-47]. Although several disk-like heptanuclear iron clusters have been reported[19,25,28,35,41], there is only one "hydroxyl bridged" iron clusters $\{(NH_4)[Fe_7^{III}(OH)(C_7H_{10}O_6)_6]\cdot(SO_4)_2\cdot18H_2O\}$ reported by A. Salifoglou.[41] Therefore, **Fe₇L5-Fe₇L6** were second example of hydroxyl-bridged disk-like iron heptanuclear cluster. Central Fe ion of each complexes were O6 coordination environment with six hydroxyl anion and peripheral Fe ions were NO6 coordination with a pyridine-enol site, β-diketonate site and two bridging hydroxyl anions. The average bond length of central Fe ions are 2.011 Å (**Fe₇L5**), 2.032 Å (**Fe₇L6**), which is shorter than that of peripheral Fe ions {(2.103 Å (**Fe₇L5**), 2.103 Å (**Fe₇L6**). Considering charge balance and bond valence sum (BVS) calculations, it was indicated that these complexes formed mixed valence state with Fe(III) in the central position of cluster and Fe(II) in peripheral site.[50] The results of the BVS calculations are summarized in **Table 8**.
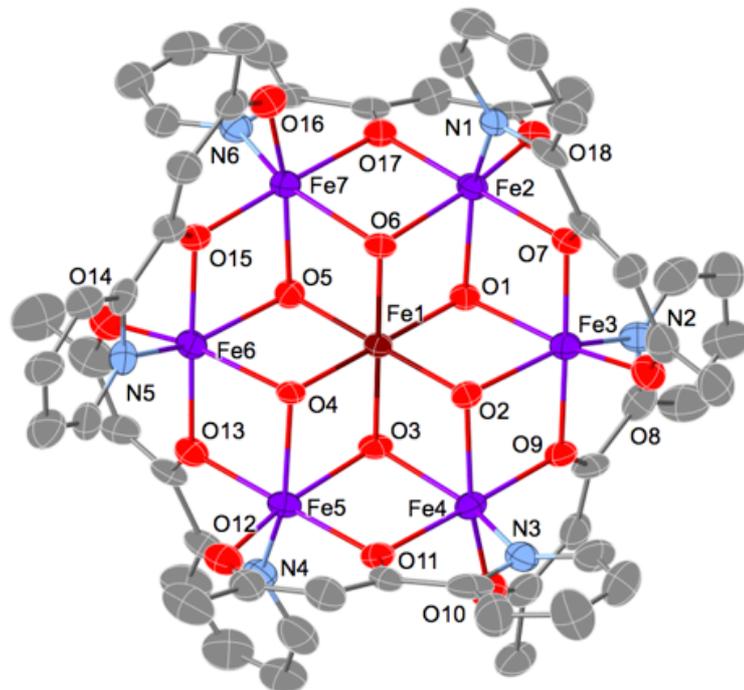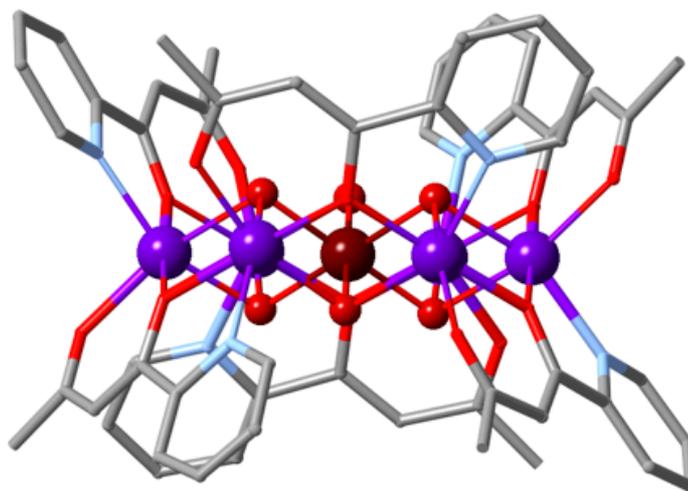
Figure 6. Molecular structure of **Fe₇L5**. **(a)** top view by ORTEP drawing with numbering scheme **(b)** side view by Ball and Stick drawing. H atoms, counter anions and solvent molecules are omitted for clarity. Fe^{II}: purple; Fe^{III}: dark red; C: gray; O: red; and N: light blue.

Table 4.   Selected bond distances for **Fe$_7$L5**.

Fe1–O1	2.004(4)	Fe1–O2	2.008(4)	Fe1–O3	2.020(4)
Fe1–O4	2.022(4)	Fe1–O5	2.013(4)	Fe1–O6	1.999(4)
Fe2–N1	2.145(6)	Fe2–O1	2.170(4)	Fe2–O6	2.156(4)
Fe2–O7	2.079(4)	Fe2–O17	2.032(5)	Fe2–O18	2.044(5)
Fe3–N2	2.150(6)	Fe3–O1	2.167(4)	Fe3–O2	2.169(4)
Fe3–O7	2.038(4)	Fe3–O8	2.049(5)	Fe3–O9	2.075(4)
Fe4–N3	2.117(6)	Fe4–O2	2.166(4)	Fe4–O3	2.161(4)
Fe4–O9	2.020(4)	Fe4–O10	2.040(5)	Fe4–O11	2.079(4)
Fe5–N4	2.130(6)	Fe5–O3	2.177(4)	Fe5–O4	2.159(4)
Fe5–O11	2.021(5)	Fe5–O12	2.053(5)	Fe5–O13	2.059(5)
Fe6–N5	2.124(6)	Fe6–O4	2.170(4)	Fe6–O5	2.152(4)
Fe6–O13	2.037(4)	Fe6–O14	2.055(5)	Fe6–O15	2.091(4)
Fe7–N6	2.123(6)	Fe7–O5	2.175(4)	Fe7–O6	2.162(4)
Fe7–O15	2.029(5)	Fe7–O16	2.055(5)	Fe7–O17	2.093(4)

Table 5. Selected bond angles for **Fe₇L5**.

|					
O1–Fe1–O2	82.36(17)	O1–Fe1–O3	97.39(17)	O1–Fe1–O4	179.42(17)
O1–Fe1–O5	97.49(18)	O2–Fe1–O3	82.75(17)	O2–Fe1–O4	97.53(17)
O2–Fe1–O5	179.46(18)	O3–Fe1–O4	83.15(17)	O5–Fe1–O3	97.79(17)
O5–Fe1–O4	82.61(17)	O6–Fe1–O1	83.49(17)	O6–Fe1–O2	96.81(17)
O6–Fe1–O3	178.94(18)	O6–Fe1–O4	95.96(17)	O6–Fe1–O5	82.65(17)
N1–Fe2–O1	149.3(2)	N1–Fe2–O6	88.62(18)	O6–Fe2–O1	76.05(16)
O7–Fe2–N1	75.4(2)	O7–Fe2–O1	80.83(16)	O7–Fe2–O6	99.01(17)
O17–Fe2–N1	104.3(2)	O17–Fe2–O1	99.53(17)	O17–Fe2–O6	81.09(17)
O17–Fe2–O7	179.64(19)	O17–Fe2–O18	83.98(19)	O18–Fe2–N1	107.0(2)
O18–Fe2–O1	94.47(17)	O18–Fe2–O6	160.65(18)	O18–Fe2–O7	96.00(19)
N2–Fe3–O1	93.98(19)	N2–Fe3–O2	150.7(2)	O1–Fe3–O2	75.07(16)
O7–Fe3–N2	106.9(2)	O7–Fe3–O1	81.84(17)	O7–Fe3–O2	98.52(17)
O7–Fe3–O8	83.89(19)	O7–Fe3–O9	177.99(18)	O8–Fe3–N2	99.4(2)
O8–Fe3–O1	162.74(19)	O8–Fe3–O2	97.60(17)	O8–Fe3–O9	96.29(19)
O9–Fe3–N2	75.1(2)	O9–Fe3–O1	97.64(16)	O9–Fe3–O2	79.47(17)
N3–Fe4–O2	91.03(19)	N3–Fe4–O3	151.1(2)	O3–Fe4–O2	75.95(16)
O9–Fe4–N3	103.6(2)	O9–Fe4–O2	80.75(17)	O9–Fe4–O3	99.67(17)
O9–Fe4–O10	83.83(19)	O9–Fe4–O11	178.14(18)	O10–Fe4–N3	100.3(2)
O10–Fe4–O2	162.66(19)	O10–Fe4–O3	99.01(18)	O10–Fe4–O11	98.03(19)
O11–Fe4–N3	76.1(2)	O11–Fe4–O2	97.40(16)	O11–Fe4–O3	80.06(18)
N4–Fe5–O3	89.55(19)	N4–Fe5–O4	149.9(2)	O4–Fe5–O3	76.46(15)
O11–Fe5–N4	103.7(2)	O11–Fe5–O3	80.97(17)	O11–Fe5–O4	100.26(17)
O11–Fe5–O12	84.4(2)	O11–Fe5–O13	177.91(19)	O12–Fe5–N4	102.6(2)
O12–Fe5–O3	162.9(2)	O12–Fe5–O4	97.60(17)	O12–Fe5–O13	97.5(2)
O13–Fe5–N4	75.1(2)	O13–Fe5–O3	97.21(17)	O13–Fe5–O4	80.25(17)
N5–Fe6–O4	90.13(19)	N5–Fe6–O5	149.7(2)	O5–Fe6–O4	76.07(16)
O13–Fe6–N5	103.2(2)	O13–Fe6–O4	80.47(17)	O13–Fe6–O5	100.91(17)
O13–Fe6–O14	84.10(19)	O13–Fe6–O15	175.95(19)	O14–Fe6–N5	101.3(2)
O14–Fe6–O4	162.56(19)	O14–Fe6–O5	99.10(18)	O14–Fe6–O15	99.72(19)
O15–Fe6–N5	74.8(2)	O15–Fe6–O4	95.94(16)	O15–Fe6–O5	79.91(17)
N6–Fe7–O5	92.37(18)	N6–Fe7–O6	150.5(2)	O6–Fe7–O5	75.29(16)
O15–Fe7–N6	105.2(2)	O15–Fe7–O5	80.74(17)	O15–Fe7–O6	99.17(17)
O15–Fe7–O16	83.82(19)	O15–Fe7–O17	177.99(18)	O16–Fe7–N6	100.0(2)
O16–Fe7–O5	162.29(19)	O16–Fe7–O6	98.82(17)	O16–Fe7–O17	97.90(19)
O17–Fe7–N6	75.6(2)	O17–Fe7–O5	97.40(16)	O17–Fe7–O6	79.57(17)
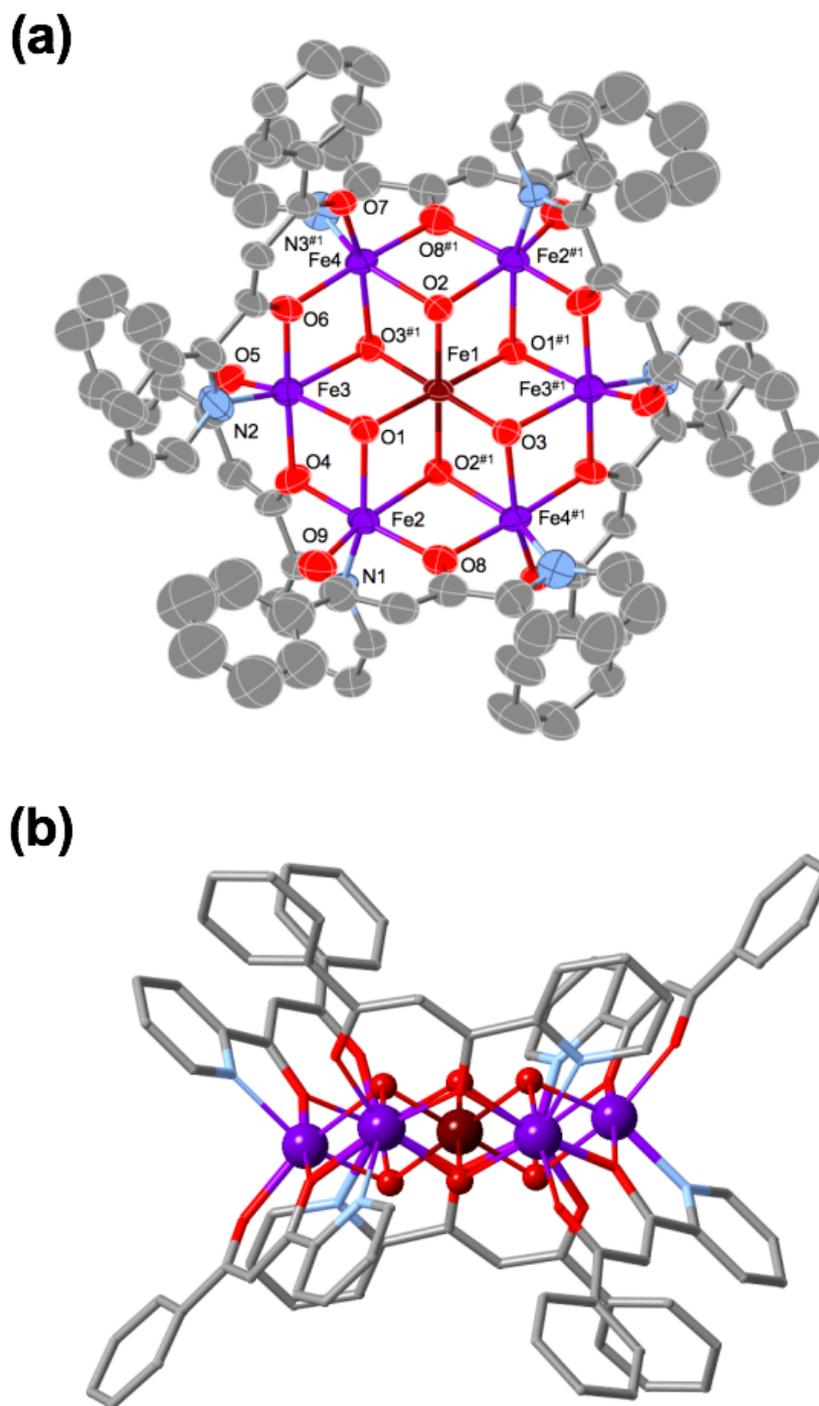
Figure 7. Molecular structure of **Fe₇L6**. **(a)** top view by ORTEP drawing with numbering scheme **(b)** side view by Ball and Stick drawing. H atoms, counter anions and solvent molecules are omitted for clarity. Fe^{II}: purple; Fe^{III}: dark red; C: gray; O: red; and N: light blue.

Table 6. Selected bond distances for **Fe₇L6**.

Fe1–O1$^{\#1}$	2.030(7)	Fe1–O1	2.030(7)	Fe1–O2	2.040(7)
Fe1–O2$^{\#1}$	2.040(7)	Fe1–O3$^{\#1}$	2.027(7)	Fe1–O3	2.027(7)
Fe2–N1	2.134(5)	Fe2–O1	2.157(7)	Fe2–O2$^{\#1}$	2.213(7)
Fe2–O4	2.076(8)	Fe2–O8	2.005(8)	Fe2–O9	2.049(9)
Fe3–N2	2.155(7)	Fe3–O1	2.224(8)	Fe3–O3$^{\#1}$	2.143(7)
Fe3–O4	2.030(8)	Fe3–O5	2.020(9)	Fe3–O6	2.078(7)
Fe4–N3$^{\#1}$	2.117(7)	Fe4–O2	2.147(7)	Fe4–O3$^{\#1}$	2.212(7)
Fe4–O6	2.009(8)	Fe4–O7	2.014(7)	Fe4–O8$^{\#1}$	2.077(8)

Symmetry operation (#1) 3/2-X, 1/2-Y, -Z

Table 7. Selected bond angles for **Fe₇L6**.

O1$^{\#1}$–Fe1–O1	180	O1–Fe1–O2$^{\#1}$	83.2(3)	O1$^{\#1}$–Fe1–O2$^{\#1}$	96.8(3)
O1$^{\#1}$–Fe1–O2	83.2(3)	O1–Fe1–O2	96.8(3)	O2–Fe1–O2$^{\#1}$	180
O3–Fe1–O1$^{\#1}$	83.0(3)	O3–Fe1–O1	97.0(3)	O3$^{\#1}$–Fe1–O1	83.0(3)
O3$^{\#1}$–Fe1–O1$^{\#1}$	97.0(3)	O3–Fe1–O2$^{\#1}$	83.5(3)	O3$^{\#1}$–Fe1–O2	83.5(3)
O3$^{\#1}$–Fe1–O2$^{\#1}$	96.5(3)	O3–Fe1–O2	96.5(3)	O3–Fe1–O3$^{\#1}$	180.0(4)
N1–Fe2–O1	153.5(3)	N1–Fe2–O2$^{\#1}$	95.5(3)	O1–Fe2–O2$^{\#1}$	76.4(3)
O4–Fe2–N1	74.6(3)	O4–Fe2–O1	80.5(3)	O4–Fe2–O2$^{\#1}$	92.8(3)
O8–Fe2–N1	100.4(3)	O8–Fe2–O1	102.7(3)	O8–Fe2–O2$^{\#1}$	79.3(3)
O8–Fe2–O4	170.3(3)	O8–Fe2–O9	84.1(3)	O9–Fe2–N1	97.2(3)
O9–Fe2–O1	97.9(3)	O9–Fe2–O2$^{\#1}$	160.6(3)	O9–Fe2–O4	104.7(4)
N2–Fe3–O1	94.5(3)	O3$^{\#1}$–Fe3–N2	152.1(3)	O3$^{\#1}$–Fe3–O1	76.0(3)
O4–Fe3–N2	100.8(3)	O4–Fe3–O1	80.0(3)	O4–Fe3–O3$^{\#1}$	103.2(3)
O4–Fe3–O6	170.2(3)	O5–Fe3–N2	96.4(4)	O5–Fe3–O1	161.3(3)
O5–Fe3–O3$^{\#1}$	100.4(3)	O5–Fe3–O4	83.1(3)	O5–Fe3–O6	105.8(3)
O6–Fe3–N2	74.6(3)	O6–Fe3–O1	91.7(3)	O6–Fe3–O3$^{\#1}$	79.5(3)
N3$^{\#1}$–Fe4–O2	152.7(17)	N3$^{\#1}$–Fe4–O3$^{\#1}$	93.9(16)	O2–Fe4–O3$^{\#1}$	76.8(3)
O6–Fe4–N3$^{\#1}$	100.3(18)	O6–Fe4–O2	103.1(3)	O6–Fe4–O3$^{\#1}$	79.4(3)
O6–Fe4–O7	84.7(3)	O6–Fe4–O8$^{\#1}$	171.1(3)	O7–Fe4–N3$^{\#1}$	98.6(16)
O7–Fe4–O2	97.6(3)	O7–Fe4–O3$^{\#1}$	161.3(3)	O7–Fe4–O8$^{\#1}$	103.6(3)
O8$^{\#1}$–Fe4–N3$^{\#1}$	75.6(18)	O8$^{\#1}$–Fe4–O2	79.3(3)	O8$^{\#1}$–Fe4–O3$^{\#1}$	93.0(3)

Symmetry operation (#1) 3/2-X, 1/2-Y, -Z

Table 8. Calculated value of valence (V_i)

	Fe1	Fe2	Fe3	Fe4	Fe5	Fe6	Fe7
Fe₇L5	3.03	2.36	2.34	2.42	2.40	2.36	2.36
	Fe1	Fe2	Fe3	Fe4	Fe5	Fe6	Fe7
Fe₇L6	2.87	2.37	2.35	2.44			

Electrochemical Properties of Heptanuclear Fe Cluster

Differential pulse voltammetry and cyclic voltammetry of **Fe₇L5-Fe₇L6** were measured in acetonitorile solution (**Figure 8, 9**). Anodic and cathodic potentials, $E_{1/2}$, and ΔE are summarized in **Table 9**. In the cyclic voltammogram of **Fe₇L5**, clear three quasi-reversible redox waves ($E_{1/2}$ = −1.05 V, −0.09 V, 0.19 V) and small three redox waves at 0.4 V - 0.7 V were observed. Bulk electrolysis measurement indicated the former three quasi-reversible redox waves were one electron transfer per molecule. Therefore, we assumed that the redox wave at −1.05 V *vs.* Fc⁺/Fc was derived from Fe(III)/Fe(II) for the central Fe(III) and the other two redox waves at −0.09 V and 0.19 V were from Fe(III)/Fe(II) for two peripheral Fe(II). It was unclear that which peripheral Fe(II) were oxidized in the redox process. Small three redox waves at 0.4 V - 0.7 V could be assigned to the Fe(III)/Fe(II) for the remaining peripheral Fe(II). **Fe₇L6** also showed redox behavior similar **Fe₇L5**. The potentials for three redox waves were −0.95 V, 0.01 V and 0.31 V, which shifted to the positive potential side by 0.1 V compared to the redox potential of **Fe₇L5**. This result indicates that oxidation state is unstabilized by introduction of the phenyl group. For the central Fe(III), the average bond distance of **Fe₇L6** (2.032 Å) is longer than that of **Fe₇L5** (2.011 Å), indicating that the central Fe(III) of **Fe₇L6** has less electron density from bridging hydroxyl anion. This structural change induced the positive shift of central Fe(III). The shift of peripheral Fe(II) may be induced by destabilized the oxidized state due to the steric hindrance of the phenyl group.

Table 9. Electrochemical data (V *vs.* Fc⁺/Fc) for **Fe₇L5** and **Fe₇L6**.

Complex	E_{pa} / V E_{pc} / V	$E_{1/2}$ / V (ΔE / V)	E_{pa} / V E_{pc} / V	$E_{1/2}$ / V (ΔE / V)	E_{pa} / V E_{pc} / V	$E_{1/2}$ / V (ΔE / V)
Fe₇L5	−1.00 −1.10	−1.05 (0.10)	−0.05 −0.13	−0.09 (0.09)	0.24 0.15	0.19 (0.09)
Fe₇L6	−0.89 −0.100	−0.95 (0.11)	0.09 −0.08	0.01 (0.17)	0.37 0.24	0.31 (0.13)

Figure 8. The DPV (**a**) and CV (**b**) curves for **Fe$_7$L5**. (Complex 0.2 mM in 0.1 M TBAPF$_6$ acetonitrile solution. Scan rate 0.1 V/s)
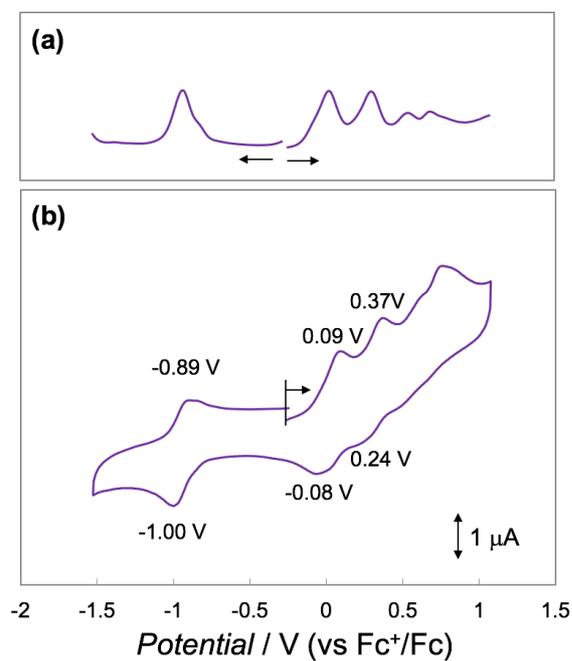

Figure 9. The DPV (a) and CV (b) curves for **Fe$_7$L6**. (Complex 0.2 mM in 0.1 M TBAPF$_6$ acetonitrile solution. Scan rate 0.05 V/s)

Crystal Structure of FeM Heterometallic Cluster

The molecular structure of FeM heterometallic clusters are shown in **Figure 10-13**. The **FeZn$_6$L5** and **FeCo$_6$L5** formed almost the same structure as **Fe$_7$L5** that seven metal ions are bridged by six hydroxyl anions and surrounded by six ligands. The central Fe(III) adopted an O6 coordination geometry with six hydroxyl anion and peripheral metal ions adopted a NO6 coordination geometry with a pyridine-enol site, β-diketonate site and two bridging hydroxyl anions. The average bond length of central metal ion is 2.011 and 2.014 Å for the **FeZn$_6$L5** and **FeCo$_6$L5** respectively, which is consistent with average bond length of central Fe(III) in **Fe$_7$L5** (2.011 Å) and typical of Fe(III). The average bond length of peripheral metal ions of 2.093 and 2.085 Å are shorter than that of central Fe(II), indicating that peripheral metal ions are Zn(II) and Co(II) respectively. This result is supported by the BVS calculations, XRF analysis (**Table 18**, **19**).

Fe$_4$Zn$_3$L5 and **FeMn$_6$L5** formed a slightly different structure from the other heterometallic clusters described above. In the peripheral coordination site, there are two types of coordination environment alternately due to the difference of orientation of the ligands. One is O6 coordination geometry with two β-diketone site and two bridging hydroxyl anions, and the other is N2O4 coordination geometry with two pyridine-enolate site and two bridging hydroxyl anions. The average bond length of central metal ion is 2.009 Å, which is typical of Fe(III). The average bond distances of **Fe$_4$Zn$_3$L5** are 2.100 Å for O6 coordinated metal ions and 2.083 Å for N2O4 coordinated metal ions. Considering this structural features, we estimated that Fe(II) and Zn(II) are located in the O6 and N2O4 coordination site respectively, because ionic radius of Fe(II) are larger than that of Zn(II). In the **FeMn$_6$L5**, although only Mn(II) was located in the peripheral, it formed the same structure as **Fe$_4$Zn$_3$L5** that has two types of coordination environment. One of the reason for this might be because of weaker coordination bond for Mn(II) with large ionic radius. The average bond length is 2.009 Å for central Fe(III), and 2.175 Å and 2.151 Å for O6 N2O4- and O6-coordinated peripheral Mn(II). These results are supported by the BVS calculations, XRF analysis (**Table 18, 19**).

Although there are many reports for disk-like heptanuclear cluster, MM'$_6$ type heterometallic clusters are very few (NaFe$_6$, LiFe$_6$[15-17] or FeCu$_6$[47]). Especially, M$_4$M'$_3$ type heterometallic clusters are very rare (Mn$_4$Fe$_3$, Mn$_4$In$_3$, In$_4$Mn$_3$,[22] and Mn$_4$Na$_3$[27]).
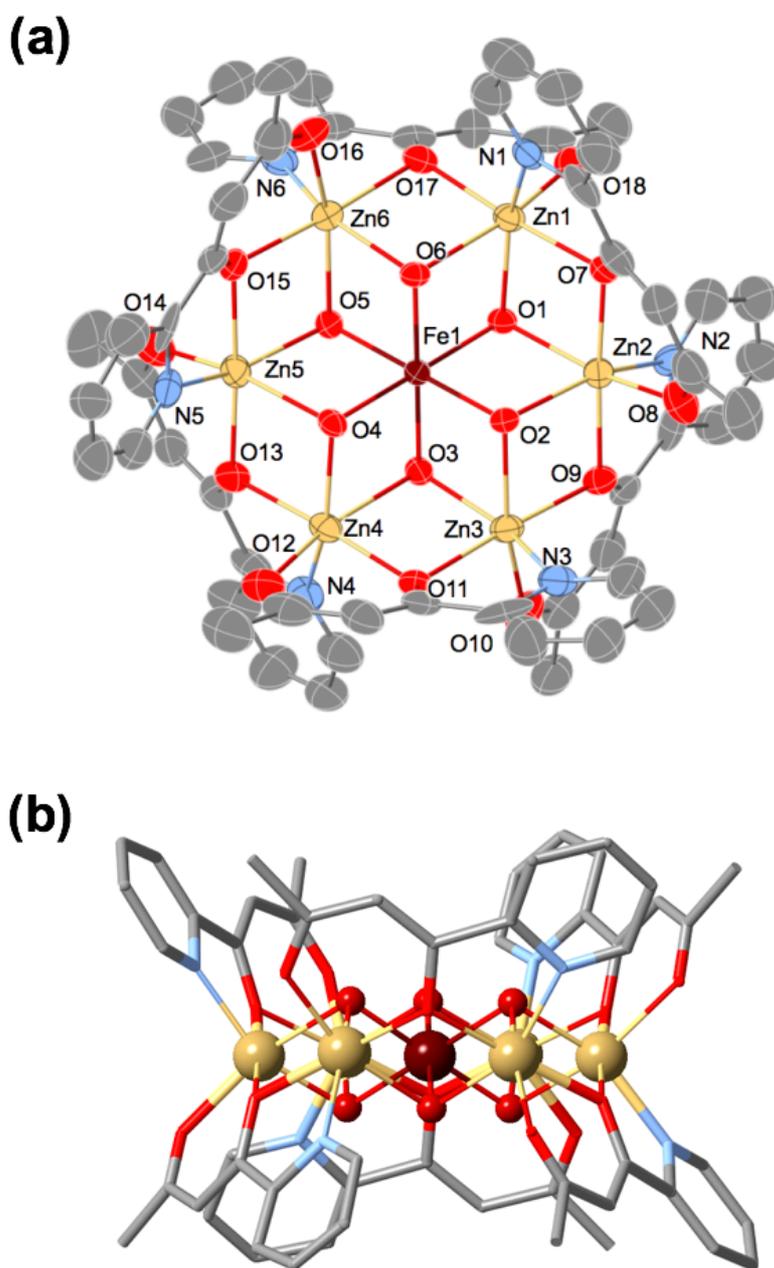
Figure 10. Molecular structure of **FeZn₆L5**. **(a)** top view by ORTEP drawing with numbering scheme **(b)** side view by Ball and Stick drawing. H atoms, counter anions and solvent molecules are omitted for clarity. Fe^{III}: dark red; Zn: pale yellow; C: gray; O: red; and N: light blue.

Table 10.   Selected bond distances for **FeZn₆L5**.

Fe1–O1	2.013(4)	Fe1– O2	2.011(4)	Fe1–O3	2.009(4)
Fe1–O4	2.015(4)	Fe1–O5	2.016(4)	Fe1–O6	2.002(4)
Zn1–N1	2.107(5)	Zn1–O1	2.092(4)	Zn1–O6	2.171(4)
Zn1–O7	2.070(4)	Zn1–O17	2.037(4)	Zn1–O18	2.081(4)
Zn2–N2	2.111(5)	Zn2–O1	2.161(4)	Zn2–O2	2.108(4)
Zn2–O7	2.020(4)	Zn2–O8	2.086(5)	Zn2–O9	2.067(4)
Zn3–N3	2.107(5)	Zn3–O2	2.164(4)	Zn3–O3	2.091(4)
Zn3–O9	2.023(4)	Zn3–O10	2.059(5)	Zn3–O11	2.073(4)
Zn4–N4	2.089(5)	Zn4–O3	2.192(4)	Zn4–O4	2.082(4)
Zn4–O11	2.020(4)	Zn4–O12	2.095(5)	Zn4–O13	2.060(4)
Zn5–N5	2.086(5)	Zn5–O4	2.189(4)	Zn5–O5	2.085(4)
Zn5–O13	2.022(4)	Zn5–O14	2.077(5)	Zn5–O15	2.082(4)
Zn6–N6	2.079(5)	Zn6–O5	2.182(4)	Zn6–O6	2.077(4)
Zn6–O15	2.032(4)	Zn6–O16	2.100(4)	Zn6–O17	2.081(4)

Table 11. Selected bond angles for **FeZn₆L5**.

O1–Fe1–O4	179.08(14)	O1–Fe1–O5	97.74(16)	O2–Fe1–O1	82.36(15)
O2–Fe1–O4	97.31(15)	O2–Fe1–O5	179.68(16)	O3–Fe1–O1	97.90(15)
O3–Fe1–O2	82.37(15)	O3–Fe1–O4	82.90(14)	O3–Fe1–O5	97.92(15)
O4–Fe1–O5	82.58(16)	O6–Fe1–O1	82.62(15)	O6–Fe1–O2	97.58(14)
O6–Fe1–O3	179.46(16)	O6–Fe1–O4	96.58(15)	O6–Fe1–O5	82.13(15)
N1–Zn1–O6	89.44(16)	O1–Zn1–N1	151.43(19)	O1–Zn1–O6	76.88(13)
O7–Zn1–N1	77.46(19)	O7–Zn1–O1	81.43(14)	O7–Zn1–O6	103.34(15)
O7–Zn1–O18	93.03(17)	O17–Zn1–N1	100.12(19)	O17–Zn1–O1	101.94(15)
O17–Zn1–O6	79.89(15)	O17–Zn1–O7	175.86(15)	O17–Zn1–O18	84.33(17)
O18–Zn1–N1	105.32(18)	O18–Zn1–O1	94.74(15)	O18–Zn1–O6	160.09(16)
N2–Zn2–O1	93.73(16)	O2–Zn2–N2	153.07(19)	O2–Zn2–O1	76.74(14)
O7–Zn2–N2	102.30(19)	O7–Zn2–O1	80.90(14)	O7–Zn2–O2	100.97(14)
O7–Zn2–O8	84.51(17)	O7–Zn2–O9	176.37(15)	O8–Zn2–N2	98.51(19)
O8–Zn2–O1	162.66(17)	O8–Zn2–O2	97.03(16)	O9–Zn2–N2	76.95(19)
O9–Zn2–O1	102.67(15)	O9–Zn2–O2	80.65(14)	O9–Zn2–O8	92.08(18)
N3–Zn3–O2	91.45(17)	O3–Zn3–N3	153.74(19)	O3–Zn3–O2	76.93(14)
O9–Zn3–N3	99.59(19)	O9–Zn3–O2	80.30(14)	O9–Zn3–O3	101.48(15)
O9–Zn3–O10	84.30(18)	O9–Zn3–O11	176.63(16)	O10–Zn3–N3	99.6(2)
O10–Zn3–O2	162.34(18)	O10–Zn3–O3	97.90(16)	O10–Zn3–O11	93.99(18)
O11–Zn3–N3	77.81(19)	O11–Zn3–O2	101.82(14)	O11–Zn3–O3	81.61(15)
N4–Zn4–O3	89.82(17)	N4–Zn4–O12	101.3(2)	O4–Zn4–N4	151.8(2)
O4–Zn4–O3	77.06(14)	O4–Zn4–O12	98.23(16)	O11–Zn4–N4	99.9(2)
O11–Zn4–O3	80.39(15)	O11–Zn4–O4	102.31(15)	O11–Zn4–O12	83.83(18)
O11–Zn4–O13	176.39(16)	O12–Zn4–O3	162.08(17)	O13–Zn4–N4	76.9(2)
O13–Zn4–O3	101.13(15)	O13–Zn4–O4	81.25(15)	O13–Zn4–O12	95.13(18)
N5–Zn5–O4	89.92(17)	N5–Zn5–O5	152.17(19)	O5–Zn5–O4	76.95(14)
O13–Zn5–N5	99.2(2)	O13–Zn5–O4	79.57(14)	O13–Zn5–O5	102.29(16)
O13–Zn5–O14	84.72(17)	O13–Zn5–O15	176.30(16)	O14–Zn5–N5	101.7(2)
O14–Zn5–O4	161.80(17)	O14–Zn5–O5	97.67(17)	O14–Zn5–O15	95.21(18)
O15–Zn5–N5	77.1(2)	O15–Zn5–O4	101.06(15)	O15–Zn5–O5	81.40(15)
N6–Zn6–O5	92.40(17)	N6–Zn6–O16	100.09(18)	N6–Zn6–O17	76.93(19)
O6–Zn6–N6	152.62(18)	O6–Zn6–O5	76.56(14)	O6–Zn6–O16	97.56(16)
O6–Zn6–O17	81.11(16)	O15–Zn6–N6	100.78(19)	O15–Zn6–O5	80.23(15)
O15–Zn6–O6	101.86(16)	O15–Zn6–O16	83.53(17)	O15–Zn6–O17	176.39(16)
O16–Zn6–O5	161.11(17)	O17–Zn6–O5	102.56(15)	O17–Zn6–O16	94.09(17)

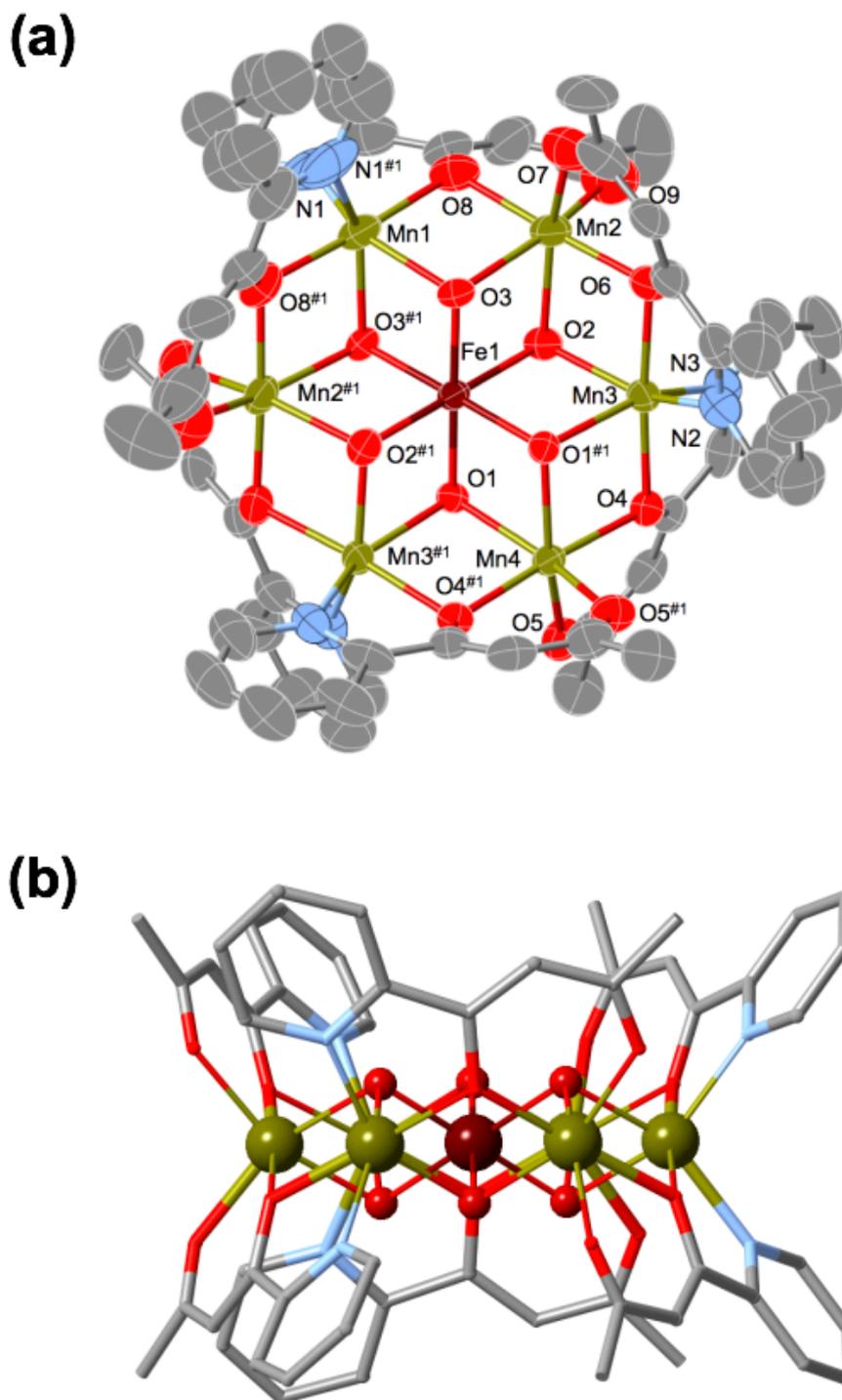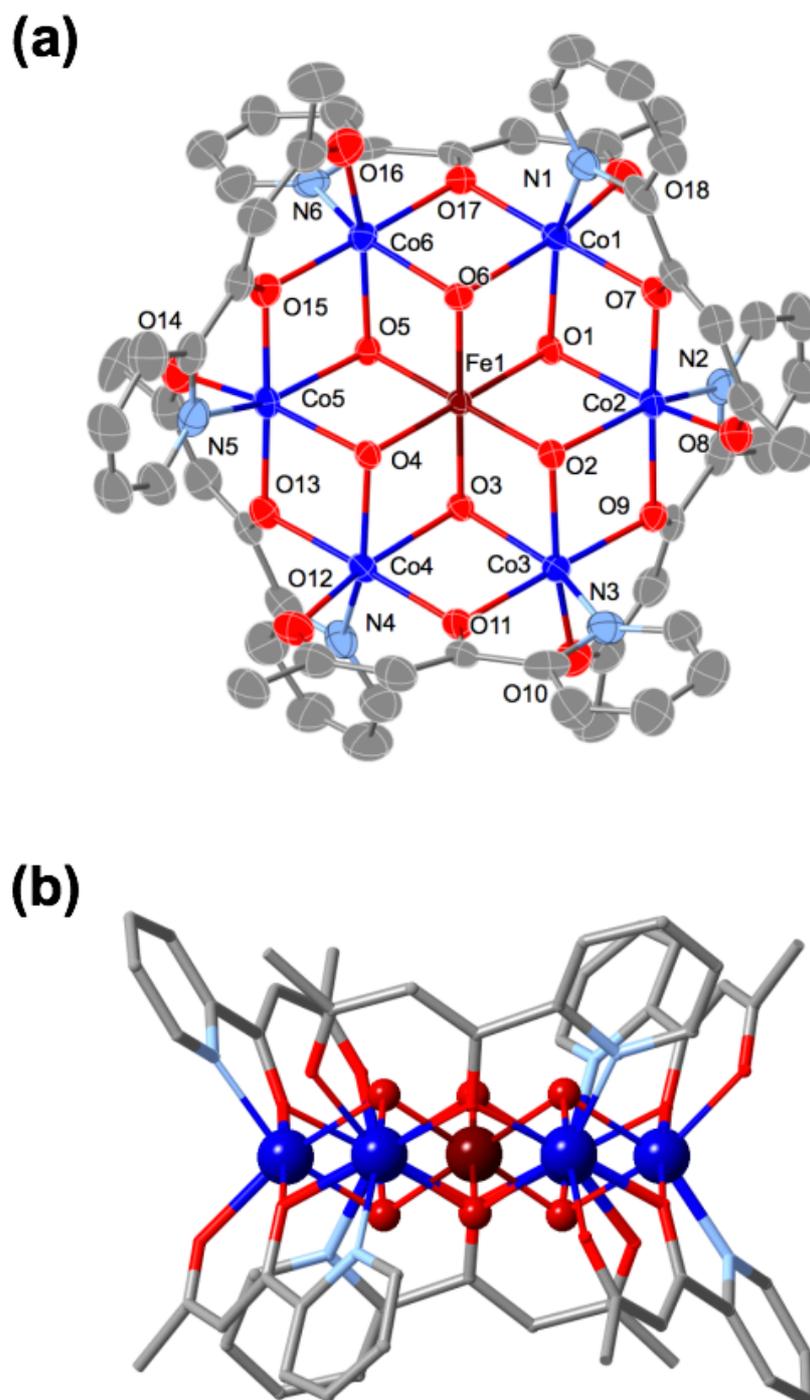**Figure 11.** The Molecular structure of **FeMn₆L5**. **(a)** top view by ORTEP drawing with numbering scheme **(b)** side view by Ball and Stick drawing. H atoms, counter anions and solvent molecules are omitted for clarity. Fe^{II}: purple; Fe^{III}: dark red; C: gray; O: red; and N: light blue.

Table 12.   Selected bond distances for **FeMn₆L5**.

Fe1–O1	2.034(4)	Fe1–O1$^{\#1}$	2.034(4)	Fe1–O2$^{\#1}$	2.044(5)
Fe1–O2	2.044(5)	Fe1–O3	2.031(4)	Fe1–O3$^{\#1}$	2.031(4)
Mn1–N1	2.205(4)	Mn1–N1$^{\#1}$	2.205(4)	Mn1–O3$^{\#1}$	2.180(4)
Mn1–O3	2.180(4)	Mn1–O8	2.144(5)	Mn1–O8$^{\#1}$	2.144(5)
Mn2–O2	2.193(4)	Mn2–O3	2.203(4)	Mn2–O6	2.114(5)
Mn2–O7	2.134(6)	Mn2–O8	2.115(5)	Mn2–O9	2.150(7)
Mn3–N2	2.185(4)	Mn3–N3	2.210(3)	Mn3–O1$^{\#1}$	2.178(4)
Mn3–O2	2.166(4)	Mn3–O4	2.156(4)	Mn3–O6	2.150(4)
Mn4–O1$^{\#1}$	2.196(4)	Mn4–O1	2.196(4)	Mn4–O4	2.117(4)
Mn4–O4$^{\#1}$	2.117(4)	Mn4–O5	2.137(4)	Mn4–O5$^{\#1}$	2.137(4)

Symmetry operation (#1) 1-X, +Y, 3/2-Z

Table 13. Selected bond distances for **FeMn$_6$L5**.

O1–Fe1–O1$^{#1}$	81.8(2)	O1–Fe1–O2$^{#1}$	82.04(16)	O1–Fe1–O2	97.92(16)
O1$^{#1}$–Fe1–O2	82.04(16)	O1$^{#1}$–Fe1–O2$^{#1}$	97.92(16)	O2–Fe1–O2$^{#1}$	179.94(18)
O3–Fe1–O1	179.31(13)	O3–Fe1–O1$^{#1}$	97.79(18)	O3$^{#1}$–Fe1–O1$^{#1}$	179.31(12)
O3$^{#1}$–Fe1–O1	97.79(18)	O3–Fe1–O2$^{#1}$	98.60(17)	O3–Fe1–O2	81.45(16)
O3$^{#1}$–Fe1–O2	98.60(17)	O3$^{#1}$–Fe1–O2$^{#1}$	81.45(16)	O3–Fe1–O3$^{#1}$	82.6(2)
N1$^{#1}$–Mn1–N1	106.6(5)	O3–Mn1–N1$^{#1}$	94.9(4)	O3–Mn1–N1	149.0(2)
O3$^{#1}$–Mn1–N1	94.94(16)	O3$^{#1}$–Mn1–N1$^{#1}$	149.0(5)	O3$^{#1}$–Mn1–O3	75.9(2)
O8$^{#1}$–Mn1–N1	106.3(2)	O8–Mn1–N1	71.5(2)	O8–Mn1–N1$^{#1}$	106.3(5)
O8$^{#1}$–Mn1–N1$^{#1}$	71.5(5)	O8$^{#1}$–Mn1–O3$^{#1}$	81.23(17)	O8–Mn1–O3	81.23(17)
O8–Mn1–O3$^{#1}$	101.56(17)	O8$^{#1}$–Mn1–O3	101.56(17)	O8–Mn1–O8$^{#1}$	176.5(2)
O2–Mn2–O3	74.43(16)	O6–Mn2–O2	81.73(18)	O6–Mn2–O3	100.46(17)
O6–Mn2–O7	82.0(2)	O6–Mn2–O8	177.41(17)	O6–Mn2–O9	97.6(3)
O7–Mn2–O2	158.4(2)	O7–Mn2–O3	94.78(18)	O7–Mn2–O9	102.9(2)
O8–Mn2–O2	100.60(18)	O8–Mn2–O3	81.33(16)	O8–Mn2–O7	96.0(2)
O8–Mn2–O9	81.2(2)	O9–Mn2–O2	93.2(2)	O9–Mn2–O3	156.2(2)
N2–Mn3–N3	105.10(17)	O1$^{#1}$–Mn3–N3	151.27(16)	O1$^{#1}$–Mn3–N2	93.48(16)
O2–Mn3–N3	96.28(16)	O2–Mn3–N2	150.26(18)	O2–Mn3–O1$^{#1}$	76.07(16)
O4–Mn3–N3	73.01(16)	O4–Mn3–N2	103.88(16)	O4–Mn3–O1$^{#1}$	81.45(14)
O4–Mn3–O2	101.99(16)	O6–Mn3–N3	104.15(18)	O6–Mn3–N2	73.40(19)
O6–Mn3–O1$^{#1}$	102.05(17)	O6–Mn3–O2	81.57(18)	O6–Mn3–O4	175.59(16)
O1–Mn4–O1$^{#1}$	74.7(2)	O4$^{#1}$–Mn4–O1	81.93(15)	O4–Mn4–O1	101.23(15)
O4$^{#1}$–Mn4–O1$^{#1}$	101.23(15)	O4–Mn4–O1$^{#1}$	81.93(15)	O4$^{#1}$–Mn4–O4	176.1(2)
O4$^{#1}$–Mn4–O5	96.05(16)	O4–Mn4–O5	81.50(16)	O4–Mn4–O5$^{#1}$	96.05(16)
O4$^{#1}$–Mn4–O5$^{#1}$	81.50(16)	O5$^{#1}$–Mn4–O1	157.29(18)	O5$^{#1}$–Mn4–O1$^{#1}$	93.49(15)
O5–Mn4–O1	93.49(15)	O5–Mn4–O1$^{#1}$	157.29(18)	O5–Mn4–O5$^{#1}$	103.6(2)

Symmetry operation (#1) 1-X, +Y, 3/2-Z

Figure 12. The molecular structure of **FeCo₆L5**. **(a)** top view by ORTEP drawing with numbering scheme **(b)** side view by Ball and Stick drawing. H atoms, counter anions and solvent molecules are omitted for clarity. Fe^{III}: dark red; Co: blue; C: gray; O: red; N: light blue.

Table 14.   Selected bond distances for **FeCo₆L5**.

Fe1–O1	2.007(2)	Fe1–O2	2.019(2)	Fe1–O3	2.012(2)
Fe1–O4	2.008(2)	Fe1–O5	2.021(2)	Fe1–O6	2.014(2)
Co1–N1	2.100(3)	Co1–O1	2.121(2)	Co1–O6	2.156(2)
Co1–O7	2.074(3)	Co1–O17	2.014(3)	Co1–O18	2.077(3)
Co2–N2	2.093(3)	Co2–O1	2.146(2)	Co2–O2	2.133(2)
Co2–O7	2.015(2)	Co2–O8	2.068(3)	Co2–O9	2.052(2)
Co3–N3	2.124(3)	Co3–O2	2.139(2)	Co3–O3	2.133(2)
Co3–O9	2.014(2)	Co3–O10	2.075(3)	Co3–O11	2.045(2)
Co4–N4	2.095(3)	Co4–O3	2.147(2)	Co4–O4	2.127(2)
Co4–O11	2.012(3)	Co4–O12	2.063(3)	Co4–O13	2.059(3)
Co5–N6	2.094(3)	Co5–O5	2.151(2)	Co5–O6	2.120(2)
Co5–O15	2.007(2)	Co5–O16	2.058(3)	Co5–O17	2.059(2)
Co6–N5	2.092(3)	Co6–O4	2.151(2)	Co6–O5	2.120(2)
Co6–O13	2.014(3)	Co6–O14	2.086(3)	Co6–O15	2.048(3)

Table 15. Selected bond angles for **FeCo$_6$L5**.

O1–Fe1–O2	83.51(10)	O1–Fe1–O3	96.68(9)	O1–Fe1–O4	179.00(10)
O1–Fe1–O5	96.09(9)	O1–Fe1–O6	82.63(10)	O2–Fe1–O5	179.29(9)
O3–Fe1–O2	82.51(10)	O3–Fe1–O5	96.96(10)	O3–Fe1–O6	179.25(10)
O4–Fe1–O2	97.33(10)	O4–Fe1–O3	82.92(9)	O4–Fe1–O5	83.06(9)
O4–Fe1–O6	97.76(10)	O6–Fe1–O2	97.70(10)	O6–Fe1–O5	82.82(10)
N1–Co1–O1	151.96(11)	N1–Co1–O6	92.46(10)	O1–Co1–O6	76.73(9)
O7–Co1–N1	76.70(11)	O7–Co1–O1	79.99(9)	O7–Co1–O6	100.73(10)
O7–Co1–O18	94.13(11)	O17–Co1–N1	103.00(12)	O17–Co1–O1	100.59(10)
O17–Co1–O6	80.34(9)	O17–Co1–O7	178.89(11)	O17–Co1–O18	84.85(11)
O18–Co1–N1	99.18(12)	O18–Co1–O1	97.82(10)	O18–Co1–O6	162.91(11)
N2–Co2–O1	89.34(11)	N2–Co2–O2	151.63(12)	O2–Co2–O1	77.59(9)
O7–Co2–N2	101.41(12)	O7–Co2–O1	80.71(10)	O7–Co2–O2	101.16(10)
O7–Co2–O8	85.56(11)	O7–Co2–O9	177.27(10)	O8–Co2–N2	104.40(12)
O8–Co2–O1	162.28(10)	O8–Co2–O2	94.27(10)	O9–Co2–N2	77.45(12)
O9–Co2–O1	101.71(9)	O9–Co2–O2	80.68(9)	O9–Co2–O8	92.31(10)
N3–Co3–O2	93.22(11)	N3–Co3–O3	152.50(12)	O3–Co3–O2	76.94(9)
O9–Co3–N3	103.91(12)	O9–Co3–O2	81.40(9)	O9–Co3–O3	99.96(10)
O9–Co3–O10	84.86(11)	O9–Co3–O11	177.79(10)	O10–Co3–N3	98.94(13)
O10–Co3–O2	163.50(11)	O10–Co3–O3	96.60(10)	O11–Co3–N3	76.72(12)
O11–Co3–O2	100.70(10)	O11–Co3–O3	79.95(9)	O11–Co3–O10	92.96(11)
N4–Co4–O3	91.28(11)	N4–Co4–O4	152.53(12)	O4–Co4–O3	77.03(9)
O11–Co4–N4	101.81(12)	O11–Co4–O3	80.38(9)	O11–Co4–O4	100.60(10)
O11–Co4–O12	85.13(11)	O11–Co4–O13	178.63(10)	O12–Co4–N4	99.70(13)
O12–Co4–O3	163.36(11)	O12–Co4–O4	97.82(10)	O13–Co4–N4	77.16(12)
O13–Co4–O3	100.52(9)	O13–Co4–O4	80.63(10)	O13–Co4–O12	94.14(11)
N6–Co5–O5	90.54(11)	N6–Co5–O6	152.02(12)	O6–Co5–O5	77.34(9)
O15–Co5–N6	101.17(12)	O15–Co5–O5	80.45(9)	O15–Co5–O6	101.51(10)
O15–Co5–O16	85.88(11)	O15–Co5–O17	178.28(11)	O16–Co5–N6	100.24(13)
O16–Co5–O5	164.02(11)	O16–Co5–O6	97.51(11)	O16–Co5–O17	94.03(11)
O17–Co5–N6	77.15(12)	O17–Co5–O5	99.88(9)	O17–Co5–O6	80.20(10)
N5–Co6–O4	90.46(11)	N5–Co6–O5	151.53(12)	O5–Co6–O4	77.41(9)
O13–Co6–N5	102.45(13)	O13–Co6–O4	81.07(10)	O13–Co6–O5	100.98(10)
O13–Co6–O14	84.72(12)	O13–Co6–O15	178.25(10)	O14–Co6–N5	100.99(12)
O14–Co6–O4	163.40(11)	O14–Co6–O5	97.05(10)	O15–Co6–N5	76.69(12)
O15–Co6–O4	100.43(10)	O15–Co6–O5	80.28(9)	O15–Co6–O14	93.93(12)
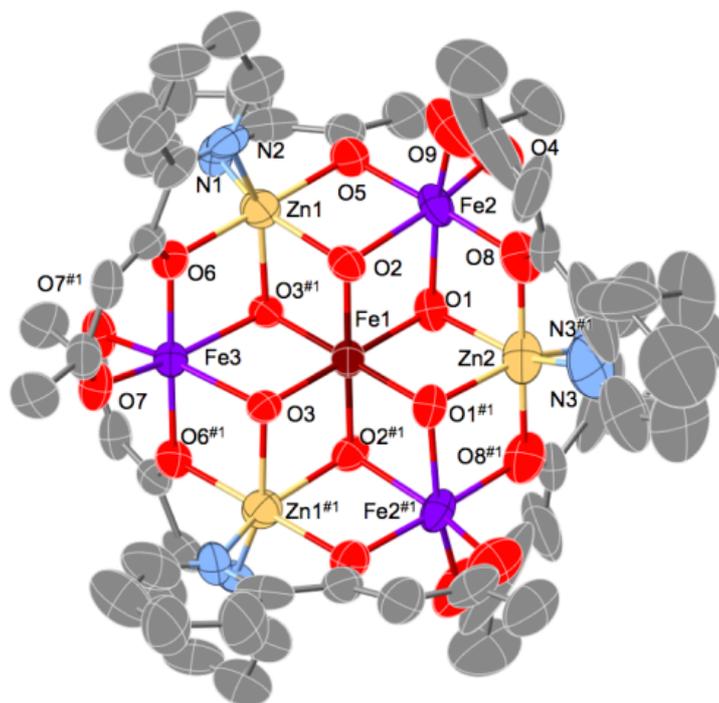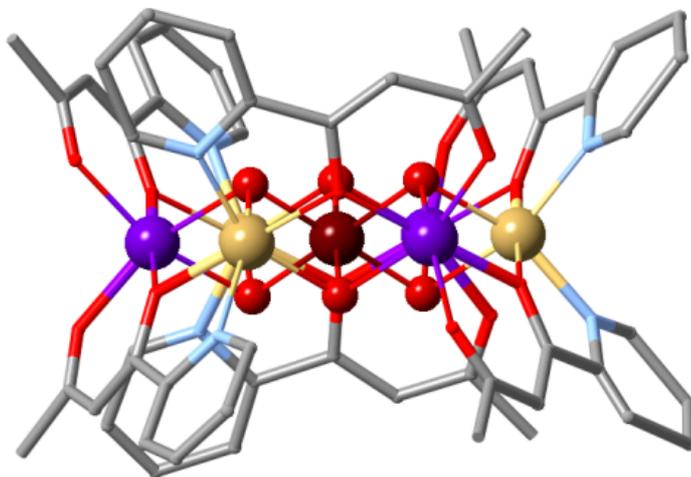
Figure 13. Molecular structure of **Fe₄Zn₃L5**. **(a)** top view by ORTEP drawing with numbering scheme **(b)** side view by Ball and Stick drawing. H atoms, counter anions and solvent molecules are omitted for clarity. Fe^{II}: purple; Fe^{III}: dark red; Zn: pale yellow; C: gray; O: red; and N: light blue.

Table 16. Selected bond distances for **Fe₄Zn₃L5**.

Fe1–O1	2.011(6)	Fe1–O1	2.011(6)	Fe1–O3	2.004(6)
Fe1–O3$^{\#1}$	2.004(6)	Fe1–O2$^{\#1}$	2.013(6)	Fe1–O2$^{\#1}$	2.013(6)
Fe2–O1	2.206(7)	Fe2–O2	2.174(6)	Fe2–O4	2.049(8)
Fe2–O5	2.021(7)	Fe2–O8	2.035(7)	Fe2–O9	2.140(10)
Fe3–O3	2.169(5)	Fe3–O3$^{\#1}$	2.169(5)	Fe3–O6	2.030(6)
Fe3–O6$^{\#1}$	2.030(6)	Fe3–O7	2.079(6)	Fe3–O7	2.079(6)
Zn1–N1	2.075(9)	Zn1–N2	2.112(8)	Zn1–O2	2.130(6)
Zn1–O3$^{\#1}$	2.146(6)	Zn1–O5	2.060(7)	Zn1–O6	2.068(6)
Zn2–N3	2.017(10)	Zn2–N3$^{\#1}$	2.017(10)	Zn2–O1	2.163(6)
Zn2–O1$^{\#1}$	2.163(6)	Zn2–O8	2.046(7)	Zn2–O8$^{\#1}$	2.046(7)

Symmetry operation (#1) 1-X, +Y, 1/2-Z

Table 17. Selected bond angles for **Fe₄Zn₃L5**.

O1$^{\#1}$–Fe1–O1	84.4(3)	O1$^{\#1}$–Fe1–O2	96.7(3)	O1–Fe1–O2	83.0(2)
O3–Fe1–O1	178.8(2)	O3$^{\#1}$–Fe1–O1	96.6(3)	O3$^{\#1}$–Fe1–O2	82.9(2)
O3–Fe1–O2	97.4(2)	O2–Fe2–O1	75.0(2)	O4–Fe2–O1	95.7(3)
O4–Fe2–O2	160.6(3)	O4–Fe2–O9	97.8(3)	O5–Fe2–O1	97.6(2)
O5–Fe2–O2	80.0(3)	O5–Fe2–O4	84.5(4)	O5–Fe2–O8	177.8(3)
O5–Fe2–O9	98.4(4)	O8–Fe2–O1	80.4(2)	O8–Fe2–O2	98.5(3)
O8–Fe2–O4	96.6(3)	O8–Fe2–O9	83.3(4)	O9–Fe2–O1	160.0(3)
O9–Fe2–O2	95.9(3)	O3$^{\#1}$–Fe3–O3	74.9(3)	O6$^{\#1}$–Fe3–O3	80.4(2)
O6–Fe3–O3	98.9(2)	O6$^{\#1}$–Fe3–O6	179.1(3)	O6$^{\#1}$–Fe3–O7	96.4(3)
O6–Fe3–O7	84.2(3)	O7–Fe3–O3	95.1(2)	O7$^{\#1}$–Fe3–O3	159.9(3)
N1–Zn1–N2	102.9(3)	N1–Zn1–O2	153.1(3)	N2–Zn1–O2	96.2(3)
O5–Zn1–N1	76.7(3)	O5–Zn1–N2	105.3(4)	O5–Zn1–O2	80.2(3)
O5–Zn1–O6	179.5(3)	O6–Zn1–N1	102.8(3)	O6–Zn1–N2	74.7(3)
O6–Zn1–O2	100.3(2)	N3–Zn2–O1	155.1(5)	N3$^{\#1}$–Zn2–O1	96.0(4)
N3–Zn2–O8	76.2(5)	N3$^{\#1}$–Zn2–O8	103.3(5)	O8–Zn2–O1	81.2(3)
O8$^{\#1}$–Zn2–O1	99.3(3)				

Symmetry operation (#1) 1-X, +Y, 1/2-Z

Table 18.   The result of XRF analysis

	Fe	Zn
FeZn₆L	1.05	6
	Fe	Ni
FeNi₆L	0.93	6
	Fe	Mn
FeMn₆L	0.83	6
	Fe	Co
FeCo₆L	1.25	6
	Fe	Zn
Fe₃Zn₄L	3.07	4

Table 19.   Calculated value of valence for **FeM₆L5** (V_i)

	Fe1	Mn1	Mn2	Mn3	Mn4	Co5	Co6
FeZn₆L	3.04						
	Fe1	Mn1	Mn2	Mn3	Mn4		
FeMn₆L	2.83	2.27	2.26	2.29	2.28		
	Fe1	Co1	Co2	Co3	Co4	Co5	Co6
FeCo₆L	3.02	2.22	2.26	2.23	2.26	2.28	2.26
	Fe1	Fe2	Fe3				
Fe₄Zn₃L	3.05	2.25	2.30				

Electrochemical Property of FeM Heterometallic Cluster

Differential pulse voltammetry and cyclic voltammetry of heterometallic complexes were shown in **Figure 16-20**, and anodic and cathodic potentials, $E_{1/2}$, and ΔE are summarized in **Table 20** and **21**. **FeZn$_6$L** showed only a couple of quasi-reversible redox waves (E_{pa} = –0.91 V, E_{pc} = –0.98 V) which is derived from Fe(III)/Fe(II) of central Fe(III). The redox potential ($E_{1/2}$) is –0.94 V which is shifted to the positive potential side compared with that of **Fe$_7$L5** ($E_{1/2}$ = –1.05 V). There are no peaks in the positive potential region. It also supported that all peripheral metal ions in **FeZn$_6$L** were redox-inactive Zn ions. **Fe$_4$Zn$_3$L5** showed three redox waves at –1.10 V, –0.05 V and 0.22 V. This redox behavior is similar to that of **Fe$_7$L5**. These redox waves are also considered to be derived from the central Fe(III) and two peripheral Fe(II). In **Fe$_4$Zn$_3$L5**, three peaks observed at 0.4 V - 0.7 V in **Fe$_7$L** were reduced to one. This result supported that decrease of the number of Fe(II) in peripheral coordination site, and **Fe$_4$Zn$_3$L** was not a mixture of **Fe$_7$L5** and **Zn$_7$L5**. Redox potentials of peripheral Fe(II) were shifted positively compere to **Fe$_7$L5**. This is due to the difference of coordination environments of peripheral Fe(II) (NO5 coordination in **Fe$_7$L** and O6 coordination in **Fe$_4$Zn$_3$L5**).

Table 20.   Electrochemical data for **Fe$_7$L5**, **FeZn$_6$L** and **Fe$_4$Zn$_3$L5**.

Complex	E_{pa} / V E_{pc} / V	$E_{1/2}$ / V (ΔE / V)	E_{pa} / V E_{pc} / V	$E_{1/2}$ / V (ΔE / V)	E_{pa} / V E_{pc} / V	$E_{1/2}$ / V (ΔE / V)
Fe$_7$L5	–1.00 –1.10	–1.05 (0.10)	–0.05 –0.13	–0.09 (0.09)	0.24 0.15	0.19 (0.09)
Fe$_4$Zn$_3$L5	–0.92 –1.10	–1.01 (0.18)	0.02 –0.12	–0.05 (0.14)	0.30 0.13	0.22 (0.17)
FeZn$_6$L5	–0.91 –0.98	–0.95 (0.07)				

Comparing the redox potentials from central Fe(III) of each complex, as the number of Zn was increased, the redox potential from central Fe(III) shifted positively. It indicates that oxidation state of central Fe(III) was unstabilized with Zn(II) ions, and those results were completely the opposite from what we expected. To elucidate the reason for this, we investigated the electrochemical properties of the other heterometallic cluster, **FeM$_6$L** (M = Mn, Co, Ni, **Figure 18-20**). **FeMn$_6$L5**, **FeCo$_6$L5** and **FeNi$_6$L5** also showed redox wave from central Fe(III) at –0.77 V, –1.02 V and –

1.06 V respectively, which also shifted to the positive potential side compared with that of **Fe$_7$L5**.   Electrochemical and structural data for central Fe(III) of each complex were summarized in **Table 21**.   The average bond distance of **FeMn$_6$L** (2.032 Å) is longer than the other complexes' ones, indicating that the central Fe(III) has less electron density from bridging hydroxyl anion and easy to be reduced.   In the case of [Mn$_3$MO$_4$] (M = Sr^{2+}, Zn^{2+}, Sc^{3+}, Y^{3+}) type cubane complex and tetranuclear [Mn$_3$M(μ_4-O)(μ_2-O)] (M = Na$^+$, Ca^{2+}, Sr^{2+}, Zn^{2+}, Y^{3+}) type heterometallic tri-manganese complexes reported by T. Agapie *et al.*, The redox potentials attributed to the [Mn$^{IV}_3$MO$_4$]/[Mn$^{IV}_2$Mn^{III}MO$_4$] and [Mn^{IV}Mn$^{III}_2$MO$_2$]/[Mn$^{III}_3$MO$_2$] redox couple of these complexes depend on the Lewis acidity of the redox-inactive metals.[9]   However, in heptanuclear complexes, redox potential of central Fe(III) is not correlated with pKa of the corresponding [M(H$_2$O)$_6$]$^{2+}$ ion as a measure of Lewis acidity (**Table 21**, **Figure 14**).[51]   We investigated average octahedral distortion parameter which is average values of deviation from 90 degrees for the twelve cis-O-Fe-O angles in the octahedron (**Table 21**).   In this case, distortion of central Fe(III) roughly correlates with redox potential rather than bond length.   Redox potential sifted positively as the distortion parameter increased.   A large distortion parameter suggests that the Fe(III) has structural stress.   It is considered that more distorted Fe(III) is more readily reduced to Fe (II) having a large ionic radius and a longer bond distance in order to alleviate such structural stress.   Therefore, although it is necessary to consider in more detail, it is indicated that distortion of metal ion is one of the factors that change the redox potential.

Table 21.   Structural and electrochemical data of central Fe(III) for each complex.

Complex	$E_{1/2}$ / V	$d_{(M-OH)}$[a]/ Å	|90-θ|ave.[b]/ °	pK_a value [c]
Fe$_7$L5	−1.05	2.011	7.16	9.3
FeZn$_6$L5	−0.94	2.011	7.505	9.0
FeMn$_6$L5	−0.77	2.043	8.1	10.6
FeCo$_6$L5	−1.02	2.013	7.08	9.7
FeNi$_6$L5	−1.06	-	-	9.86

[a] Average Fe-OH distance.   [b] Octahedral distortion parameter calculated by average of |90–θ| for the twelve cis-O-Fe-O angles in the octahedron. [c] pKa value of Metal/H$_2$O complexes, [M(OH)$_6$]$^{2+}$ (Metal is peripheral metal ions of each complexes.)
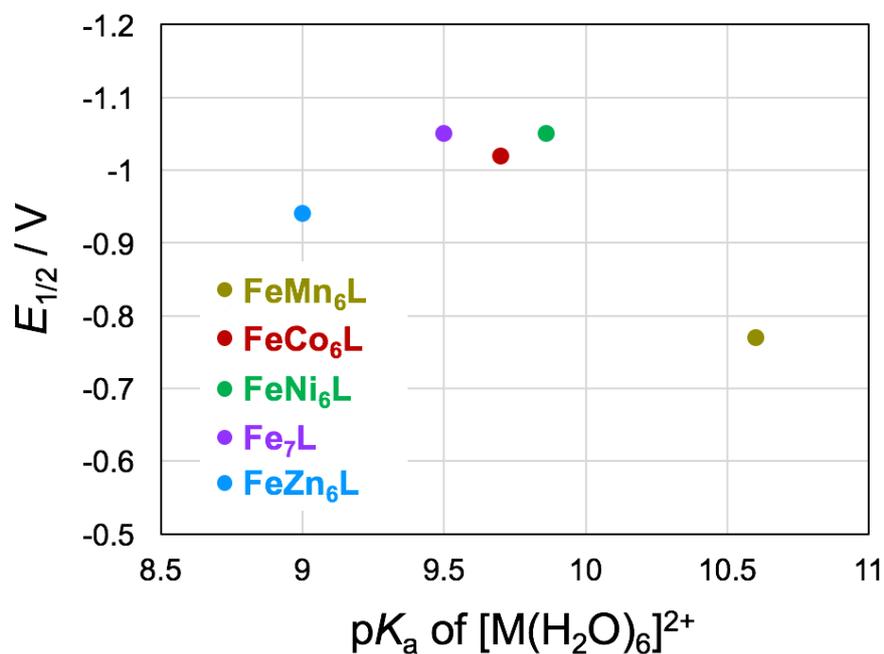
Figure 14. Redox potentials, $E_{1/2}$ (V *vs.* Fc$^+$/Fc) of central Fe(III) for each complexes *vs.* pKa of the corresponding $[M(H_2O)_6]^{2+}$ ion as a measure of Lewis acidity.
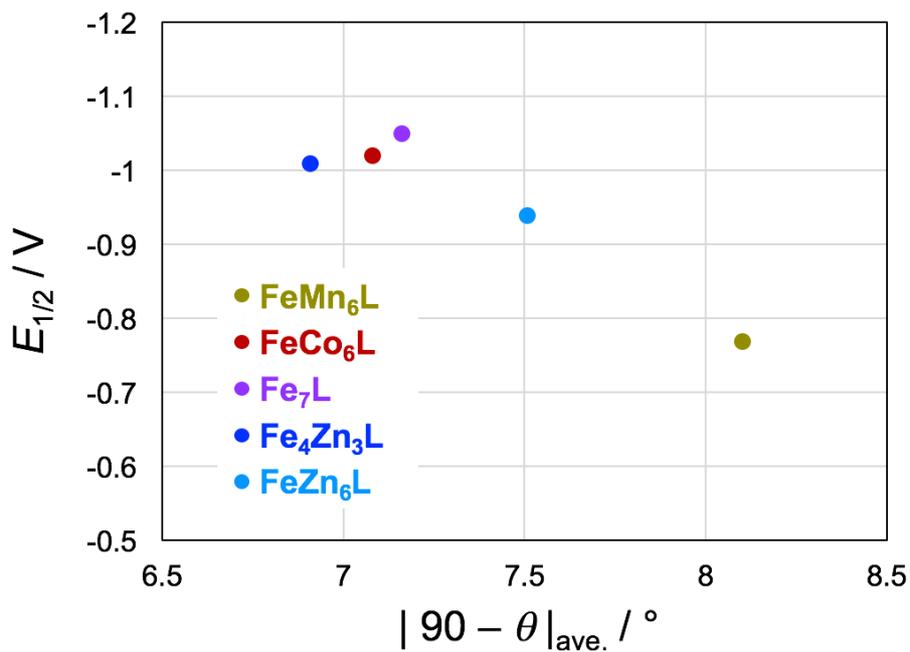
Figure 15. Redox potentials, $E_{1/2}$ (V *vs.* Fc$^+$/Fc) of central Fe(III) *vs.* average distortion parameter, $|90-\theta|_{ave.}$ (°) of central Fe(III) for each complex.
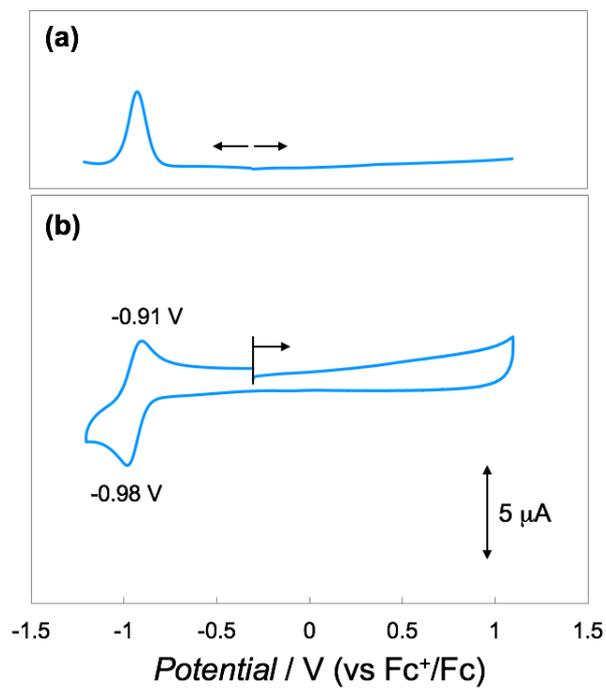
Figure 16. DPV (**a**) and CV (**b**) curves for **FeZn₆L5**. (Complex 0.2 mM in 0.1 M TBAPF₆ acetonitrile solution. Scan rate 0.1 V/s)
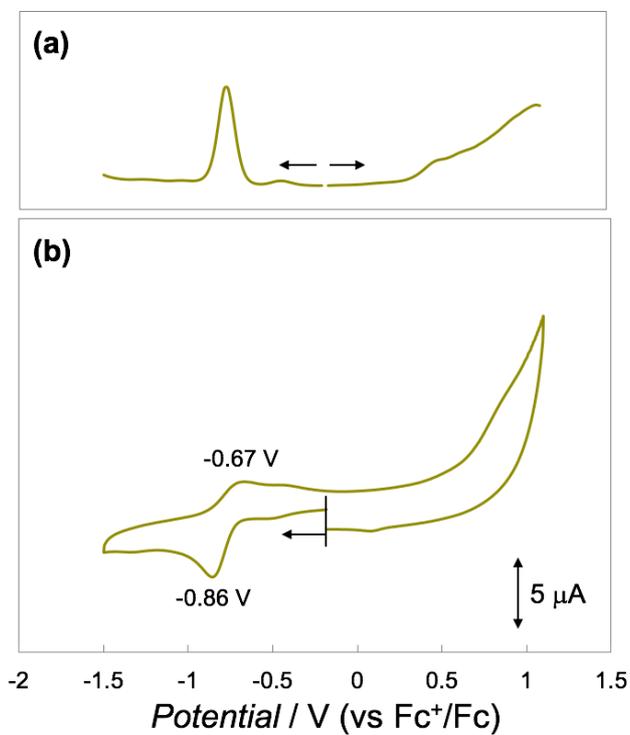
Figure 17. DPV (**a**) and CV (**b**) curves for **FeMn₆L5**. (Complex 0.2 mM in 0.1 M TBAPF₆ acetonitrile solution. Scan rate 0.1 V/s).
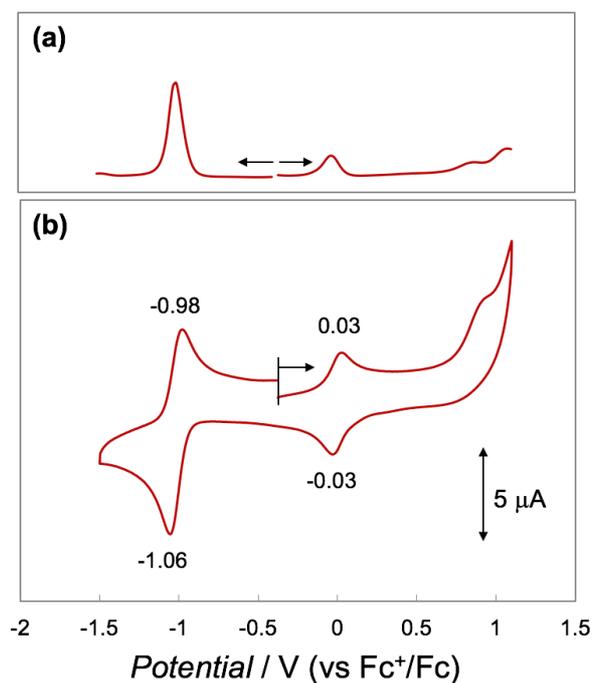
Figure 18. DPV (**a**) and CV (**b**) curves for **FeCo₆L5**. (Complex 0.2 mM in 0.1 M TBAPF₆ acetonitrile solution. Scan rate 0.1 V/s)
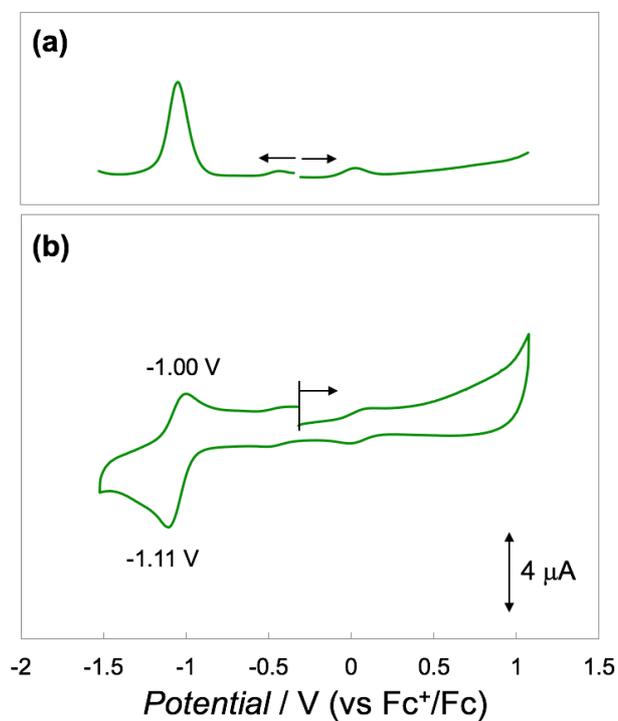
Figure 19. DPV (**a**) and CV (**b**) curves for **FeNi₆L5**. (Complex 0.2 mM in 0.1 M TBAPF₆ acetonitrile solution. Scan rate 0.1 V/s)
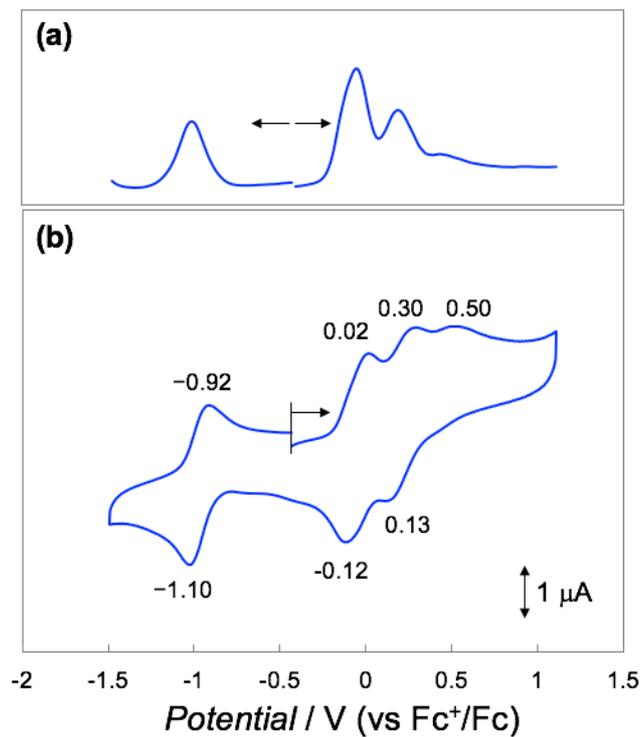
Figure 20. DPV (**a**) and CV (**b**) curves for **Fe₃Zn₄L5**. (Complex 0.2 mM in 0.1 M TBAPF₆ acetonitrile solution. Scan rate 0.1 V/s)

Conclusion

We prepared, hydroxyl-bridged heptanucler complex $[Fe^{III}Fe^{II}_7(Ln)_6(OH)_6](PF_6)_3$ (**Fe$_7$Ln**, n = 5, 6) and heterometallic complexes, $[Fe^{III}M^{II}_7(L5)_6(OH)_6](PF_6)_3$ (**FeM$_6$L5**, M = Mn, Co, Ni, Zn) and $[Fe^{III}Fe_3Zn_3(L5)_6(OH)_6](PF_6)_3$ (**Fe$_4$Zn$_3$L5**) via self-assemble reaction. The all complexes have unique edge-sharing hydroxyl-bridged cluster structure that seven metal ions on the same plane are bridged by the six hydroxyl anions and surrounded by six ligands. In the **FeM$_6$L5**, Fe(III) was located selectively at the central of the cluster and second metal ions are located in the peripheral coordination site. In the **Fe$_4$Zn$_3$L5**, a Fe(III) was located at the central of the cluster, and Fe(II) and Zn(II) is located alternately in peripheral coordination site. **Fe$_7$L5** showed multi-electron transfer derived from a central Fe(III) and peripheral Fe(II). These redox waves of **Fe$_7$L6** showed the similar redox behavior as **Fe$_7$L5**, and the redox potentials are more positive compared to the **Fe$_7$L5** due to the slight structural changes. In heterometallic complexes with redox-inactive Zn ions, the number of redox peaks decreased to one as the number of replaced Zn ions increased. It strongly supported that the formation of **FeZn$_6$L5** and **Fe$_4$Zn$_3$L5** and they are not a mixture of **Fe$_7$L5** and **Zn$_7$L5**. The redox waves are more positive compared to the **Fe$_7$L5** due to the difference of coordination environment for peripheral Fe(II). The other heterometallic complexes, **FeM$_6$L5**, also showed clear quasi-reversible redox wave of Fe(III)/Fe(II) from central Fe(III). Although these redox potentials are not correlated with Lewis acidity of peripheral metal ions, they roughly correlate with the distortion parameter of central Fe(III) ion. It is considered that more distorted Fe(III) is more readily reduced to Fe (II) having a large ionic radius and a longer bond distance in order to alleviate such structural stress. Therefore, although it is necessary to consider in more detail, it is indicated that distortion of metal ion is one of the factors that change the redox potential. Considering this results, we have to modify the ligand design to construct structurally flexible cluster complex to induce multi-electron transfer to achieve high oxidation state, e.g. Co(IV), Fe(IV) and Mn(IV). In addition, investigation of the effect of the other redox-inactive metal ions such as Ca^+, Cd^{2+} to the redox potential is needed. Rational synthesis and investigation of electrochemical properties of heterometallic complex provides a rational strategy for tuning the redox properties of heterometallic clusters for new effective catalyst.

References

1   M. Okamura, M. Kondo, R. Kuga, Y. Kurashige, T. Yanai, S. Hayami, V. K. K. Praneeth, M. Yoshida, K. Yoneda, S. Kawata and S. Masaoka, *Nature*, 2016, **530**, 1–4.

2   A. Dolbecq, E. Dumas, C. R. Mayer and P. Mialane, *Chem. Rev.*, 2010, **110**, 6009–6048.

3   H. Lv, Y. V. Geletii, C. Zhao, J. W. Vickers, G. Zhu, Z. Luo, J. Song, T. Lian, D. G. Musaev and C. L. Hill, *Chem. Soc. Rev.*, 2012, **41**, 7572.

4   S.-S. Wang and G.-Y. Yang, *Chem. Rev.*, 2015, **115**, 4893–4962.

5   Y. Umena, K. Kawakami, J.-R. Shen and N. Kamiya, *Nature*, 2011, **473**, 55–60.

6   X. Zou, A. Goswami and T. Asefa, *J. Am. Chem. Soc.*, 2013, **135**, 17242–17245.

7   C. Li, M. Wei, D. G. Evans and X. Duan, *Small*, 2014, **10**, 4469–4486.

8   J. S. Kanady, E. Y. Tsui, M. W. Day and T. Agapie, *Science*, 2011, **333**, 733–736.

9   E. Y. Tsui and T. Agapie, *Proceedings of the National Academy of Sciences*, 2013, **110**, 10084–10088.

10   S. Fukuzumi, Y. Morimoto, H. Kotani, P. Naumov, Y.-M. Lee and W. Nam, *Nature Chemistry*, 2010, **2**, 756–759.

11   M. W. Kanan and D. G. Nocera, *Science*, 2008, **321**, 1072–1075.

12   M. W. Kanan, J. Yano, Y. Surendranath, M. Dincă, V. K. Yachandra and D. G. Nocera, *J. Am. Chem. Soc.*, 2010, **132**, 13692–13701.

13   X. L. Hu, S. Piccinin, A. Laio and S. Fabris, *ACS Nano*, 2012, **6**, 10497–10504.

14   G. Mattioli, P. Giannozzi, A. Amore Bonapasta and L. Guidoni, *J. Am. Chem. Soc.*, 2013, **135**, 15353–15363.

15   A. Caneschi, A. Cornia and S. J. Lippard, *Angew. Chem. Int. Ed. Engl.*, 1995, **34**, 467–469.

16   A. Caneschi, A. Cornia, A. C. Fabretti, S. Foner, D. Gatteschi, R. Grandi and L. Schenetti, *Chem. Eur. J.*, 1996, **2**, 1379–1387.

17   G. L. Abbati, A. Cornia, A. C. Fabretti, A. Caneschi and D. Gatteschi, *Inorg. Chem.*, 1998, **37**, 1430–1431.

18   G. L. Abbati, A. Cornia, A. C. Fabretti, A. Caneschi and D. Gatteschi, *Inorg. Chem.*, 1998, **37**, 3759–3766.

19   H. Oshio, N. Hoshino, T. Ito, M. Nakano, F. Renz and P. Gütlich, *Angew. Chem. Int. Ed.*, 2003, **42**, 223–225.

20   N. C. Harden, M. A. Bolcar, W. Wernsdorfer, K. A. Abboud, W. E. Streib and G. Christou, *Inorg. Chem.*, 2003, **42**, 7067–7076.

21   Y.-Z. Zhang, F. Pan, Z.-M. Wang and S. Gao, *Chem. Commun.*, 2006, 3302.

22 R. W. Saalfrank, R. Prakash, H. Maid, F. Hampel, F. W. Heinemann, A. X. Trautwein and L. H. Böttger, *Chem. Eur. J.*, 2006, **12**, 2428–2433.

23 R. W. Saalfrank, A. Scheurer, R. Prakash, F. W. Heinemann, T. Nakajima, F. Hampel, R. Leppin, B. Pilawa, H. Rupp and P. Müller, *Inorg. Chem.*, 2007, **46**, 1586–1592.

24 S. Koizumi, M. Nihei, T. Shiga, H. Nojiri, R. Bircher, O. Waldmann and F. Fernandez-Alonso, *Chem. Eur. J.*, 2007, **13**, 8445–8453.

25 T. Liu, B.-W. Wang, Y.-H. Chen, Z.-M. Wang and S. Gao, *Zeitschrift für anorganische und allgemeine Chemie*, 2008, **634**, 778–783.

26 X.-T. Wang, B.-W. Wang, Z.-M. Wang, W. Zhang and S. Gao, *Inorg. Chim. Acta*, 2008, **361**, 3895–3902.

27 C.-M. Liu, D.-Q. Zhang and D.-B. Zhu, *Inorg. Chem.*, 2009, **48**, 792–794.

28 N. Hoshino, A. M. Ako, A. K. Powell and H. Oshio, *Inorg. Chem.*, 2009, **48**, 3396–3407.

29 S. T. Meally, G. Karotsis, E. K. Brechin, G. S. Papaefstathiou, P. W. Dunne, P. McArdle and L. F. Jones, *CrystEngComm*, 2010, **12**, 59–63.

30 S. Hill, S. Datta, J. Liu, R. Inglis, C. J. Milios, P. L. Feng, J. J. Henderson, E. del Barco, E. K. Brechin and D. N. Hendrickson, *Dalton Trans.*, 2010, **39**, 4693.

31 S. K. Langley, N. F. Chilton, M. Massi, B. Moubaraki, K. J. Berry and K. S. Murray, *Dalton Trans.*, 2010, **39**, 7236.

32 Y.-L. Zhou, M.-H. Zeng, L.-Q. Wei, B.-W. Li and M. Kurmoo, *Chemistry of Materials*, 2010, **22**, 4295–4303.

33 S.-H. Zhang and C. Feng, *Journal of Molecular Structure*, 2010, **977**, 62–66.

34 S.-H. Zhang, N. Li, C.-M. Ge, C. Feng and L.-F. Ma, *Dalton Trans.*, 2011, **40**, 3000–3007.

35 S. Mukherjee, R. Bagai, K. A. Abboud and G. Christou, *Inorg. Chem.*, 2011, **50**, 3849–3851.

36 A. A. Kitos, C. G. Efthymiou, C. Papatriantafyllopoulou, V. Nastopoulos, A. J. Tasiopoulos, M. J. Manos, W. Wernsdorfer, G. Christou and S. P. Perlepes, *Polyhedron*, 2011, **30**, 2987–2996.

37 S. T. Meally, C. McDonald, P. Kealy, S. M. Taylor, E. K. Brechin and L. F. Jones, *Dalton Trans.*, 2012, **41**, 5610.

38 S.-Y. Chen, C. C. Beedle, P.-R. Gan, G.-H. Lee, S. Hill and E.-C. Yang, *Inorg. Chem.*, 2012, **51**, 4448–4457.

39 A. M. Ullman and D. G. Nocera, *J. Am. Chem. Soc.*, 2013, **135**, 15053–15061.

40 J. A. Przyojski, N. N. Myers, H. D. Arman, A. Prosvirin, K. R. Dunbar, M. Natarajan, M. Krishnan, S. Mohan and J. A. Walmsley, *Journal of Inorganic Biochemistry*, 2013, **127**, 175–181.

41 M. Menelaou, E. Vournari, V. Psycharis, C. P. Raptopoulou, A. Terzis, V. Tangoulis, Y. Sanakis, C. Mateescu and A. Salifoglou, *Inorg. Chem.*, 2013, **52**, 13849–13860.

42 R. X. Zhao, Q. P. Huang, G. Li, S.-H. Zhang, H. Y. Zhang and L. Yang, *J Clust Sci*, 2014, **25**, 1099–1108.

43 Q. P. Huang, S.-H. Zhang, H. Y. Zhang, G. Li and M. C. Wu, *J Clust Sci*, 2014, **25**, 1489–1499.

44 K. R. Vignesh, S. K. Langley, K. S. Murray and G. Rajaraman, *Chem. Eur. J.*, 2014, **21**, 2881–2892.

45 F. Kobayashi, R. Ohtani, S. Teraoka, W. Kosaka, H. Miyasaka, Y. Zhang, L. F. Lindoy, S. Hayami and M. Nakamura, *Dalton Trans.*, 2017, **46**, 8555–8561.

46 J.-H. Xu, L.-Y. Guo, H.-F. Su, X. Gao, X.-F. Wu, W.-G. Wang, C.-H. Tung and D. Sun, *Inorg. Chem.*, 2017, **56**, 1591–1598.

47 R. Saiki, N. Yoshida, N. Hoshino, G. N. Newton, T. Shiga and H. Oshio, *Chem. Lett.*, 2017, **46**, 1197–1199.

48 Y.-M. Luo, J. Li, L.-X. Xiao, R.-R. Tang and X.-C. Tang, *Spectrochimica Acta Part A*, 2009, **72**, 703–708.

49 O. V. Dolomanov, L. J. Bourhis, R. J. Gildea, J. A. K. Howard and H. Puschmann, *J Appl Crystallogr*, 2009, **42**, 339–341.

50 N. E. Brese and M. O'Keeffe, *Acta Crystallogr., Sect. B: Struct. Sci.*, 1991, **47**, 192–197.

51 V. E. Jackson, A. R. Felmy and D. A. Dixon, *J. Phys. Chem. A*, 2015, **119**, 2926–2939.

Chapter 3

Magnetic Properties of [3M-M-3M] and

[M-6M] Type Coordination Clusters

Abstract

Systematic synthesis of Coordination Clusters (CCs) and elucidation of the correlation between magnetism and structure of it would lead to new useful single-molecule magnet SMMs. Here, we prepared two types of coordination cluster, nonanuclear complexes (M_9Ln, M = Co, Ni; n = 1–4; H_2Ln = 6-acetoacetyl-2-pyridinecarboxylic acid derivatives) and heptanuclear cluster (Ni_7L5_X, HL5 = 2-acetoacetylpyridine; X = OH^-, OMe^- and N_3^-) and investigated their magnetic properties. M_9Ln has a unique hydroxyl-bridged heptanuclear M(II) core, $[M_7(\mu_3\text{-}OH)_6]^{8+}$, which is [3M-M-3M] type structure that two trinuclear core is connected via a central M(II) by six hydroxyl anions. On the other hand, Ni_7L5_X has the disk-shaped structure that seven metal ions are arranged by bridging with six anions (OH^-, OMe^- and N_3^-) in a [M-6M] formation and surrounded by six ligands. All nonanuclear complexes (M_9Ln) showed similar overall antiferromagnetic behavior including spin-frustrated state with the antiferromagnetically coupled triangles ferromagnetically interact with the central M(II) ion through hydroxyl-bridges and weakly antiferromagnetically interact with the terminal M(II) ions. The magnitude of interactions μ_3-hydroxyl-bridge for Ni_9Ln was consistent with the magneto-structural correlation for reported Ni_4O_4 cubane type complexes. In disk-shaped heptanuclear cluster, only $Ni_7L5\_N_3$ showed overall ferromagnetic behavior derived from ferromagnetic interaction through N_3-bridging between the central Ni(II) and the peripheral Ni(II). It also showed the slight frequency-dependent in phase and out-of-phase ac signal in an applied dc field of 3 kOe at 2 K, suggesting that very small energy barriers are exist in such condition.

Introduction

The magnetic properties of Coordination clusters (CCs) have attracted much attention because of their inherent properties such as large spin ground states, high magnetic anisotropy and single-molecule magnet (SMM) behavior, which is expected to be applied in data storage and memory devices. One of the most famous example of single-molecule magnets is oxo-bridged dodecanuclear manganese cluster, $[Mn_{12}O_{12}(OAc)_{16}(H_2O)_4]$, which is the first example of single molecule magnets. (**Figure 1**). [1,2] This manganese cluster contains a central oxo-bridged cubane $Mn^{IV}_4O_4$ core surrounded by outer eight Mn^{III} ions with eight μ_3-O^{2-} bridges. This cluster showed hysteresis loops including several steps and a long magnetization relaxation time below a temperature of 4 K due to the large spin grand state of $S = 10$ derived from magnetic coupling of eight Mn^{III} ions and four Mn^{IV} ions and a negative axial anisotropy. Since the discovery of SMM behavior of dodecanuclear manganese cluster, the magnetic properties of multinuclear clusters have been actively studied so far. Development of rational synthetic strategy and systematic synthesis of coordination cluster and elucidation of the correlation between magnetism and structure of it would lead to new useful SMMs which can be used higher temperature. Most of coordination cluster are synthesized by using a spontaneous self-assembling reaction of metal ions and simple ligand such as acetate-based ligands described above. However, it is difficult to obtain the target structure with such method, because there are so many possible structures in the self-assembly process. It is useful to use a rigidity ligand with some coordination site to minimize the variability of structures. Using a self-assembly reaction of such ligand is more rational than using simple ligands described above and easier than making complicated huge multidentate ligands by complicated organic synthesis.
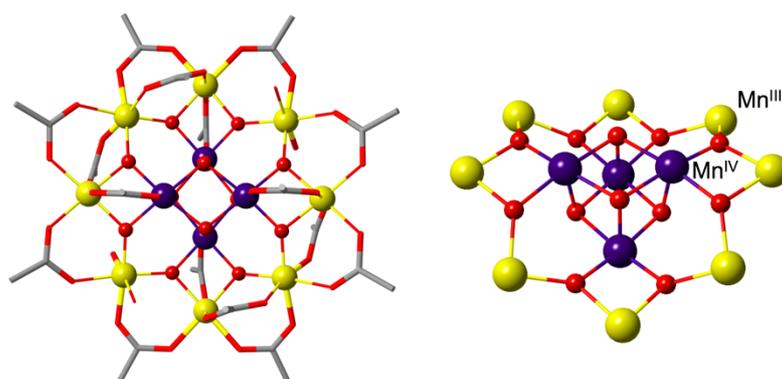
Figure 1. Entire Structure (left) and oxo-bridged core structure (right) of oxo-bridged dodecanuclear manganese cluster, $[Mn_{12}O_{12}(OAc)_{16}(H_2O)_4]$.

We have synthesized nonanuclear and heptanuclear complexes including two types of hydroxyl-bridged heptad cluster core by using β-diketone based ligands, H_2L1 (6-acetoacetyl-2-pyridinecarboxylic acid) and HL5 (2-acetoacetylpyridine) (**Figure 2**). Nonanuclear complexes, $[M_9(L1)_6(OH)_6(sol.)_6]$ (**M₉L1**, M = Co, Ni) including [3M-M-3M] type heptad cluster core that two trinuclear core is connected via a central M(II) ions by six hydroxyl anions. On the other hand, heptanuclear complex, $[Ni_7(L5)_6(OH)_6](ClO_4)_2$ (**Ni₇L5_OH**) has [M-6M] type structure that a central Ni(II) ion is surrounded by six Ni(II) ions on the same plane six hydroxyl bridging. In this study, we focused on the magnetic properties of these two types of coordination clusters. We investigated the effect of their bridging angle and type of bridging anion on magnetic properties by systematically changing them. In the case of **Ni₉L1**, examined substituent effects of ligands (H_2Ln) on the structure, and magnetic properties. In the **Ni₇L5_OH**, we synthesized derivative complexes with different bridging agents (OMe⁻ and N_3^-) because end on bridges induce ferromagnetic coupling and azido-bridged clusters have been reported as new SMMs.
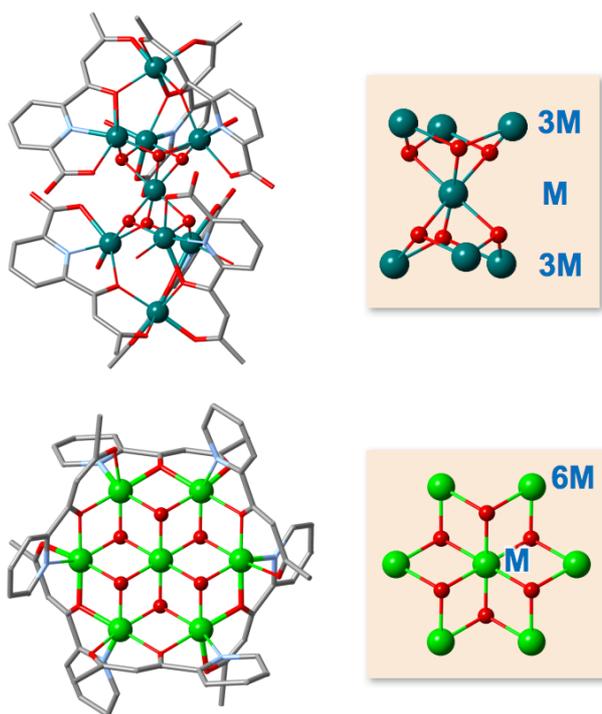
Figure 2. Entire Structure (left) and oxo-bridged core structure (right) of nonanuclear complexes (**M₉L1**) and heptanuclear complex (**Ni₇L5_OH**).

Experimental Section

Physical measurements

Elemental analyses of carbon, hydrogen and nitrogen were carried out by the staff of technical support division graduate school of science, Kyushu University. X-ray fluorescence analysis was carried out on a Rigaku EDX-70. ^{1}H NMR spectra were acquired on a JEOL JNM-ESA 600 spectrometer. The magnetic susceptibilities of all samples were measured on Quantum Design MPMS-XL5R SQUID susceptometer in the temperature range of 2-300 K in an applied DC field of 1000 Oe. The samples were put into a gelatin capsule, placed in a plastic straw, and then fixed to the end of the sample transport rod. Diamagnetic correction was calculated by using Pascal constant. The molar magnetic susceptibility, χ_M, was corrected for the diamagnetism of the constituent atoms and the sample tube.

Preparations

All chemicals were purchased from commercial sources and used without further purification. Dimethyl pyridine 2,6-carboxylate (**a**) and dimethyl 4-methoxypyridine-2,6-dicarboxylate (**b**) were prepared according to literature procedures.[3,4] The preparation of the 6-acetoacetyl-2-pyridinecarboxylic acid (H$_2$L1) and its derivatives were carried out in three steps including a Claisen condensation with reference to the literature method.[5] Synthetic scheme of the ligand is shown in **scheme 1**. 2-acetoacetylpyridine (HL5) were prepared by Claisen condensation. Synthesis of H$_2$Ln (n = 1-4) and heptanuclear complexes are described in Chapter 1, and synthesis of HL5 is described in Chapter 2.
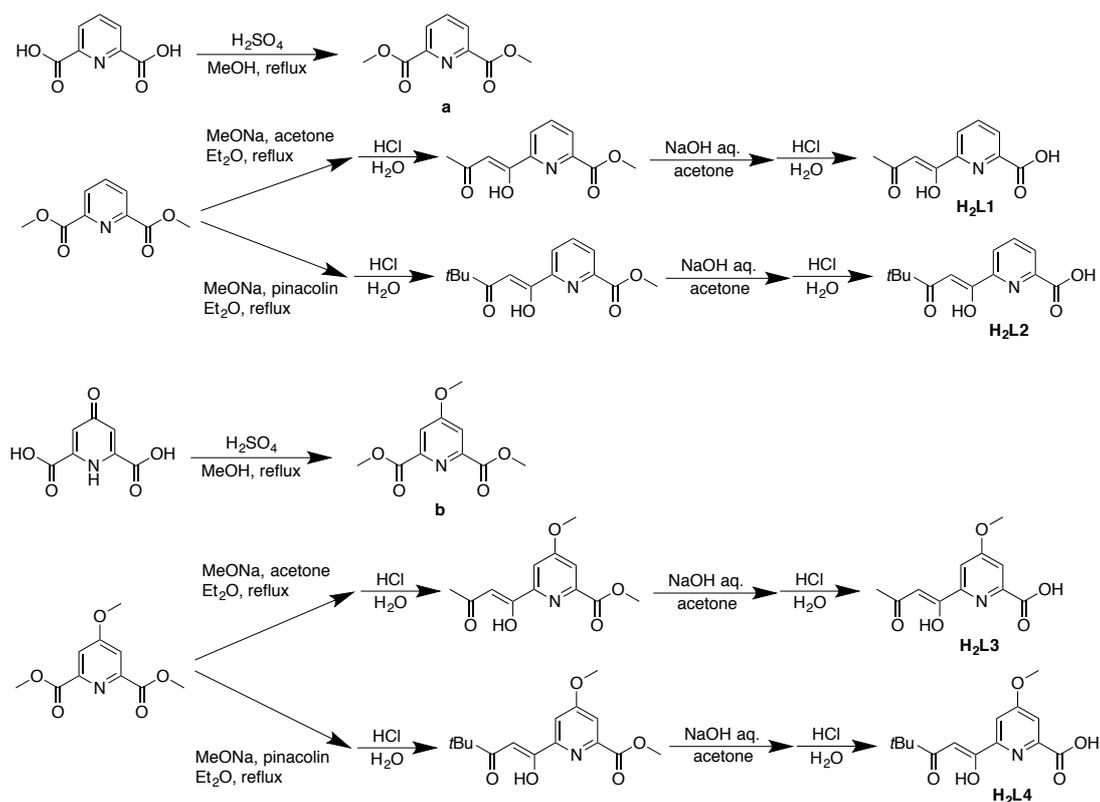
Scheme 1. Synthetic scheme of 6-acetoacetyl-2-pyridinecarboxylic acid and its derivatives.

[Ni$_7$(L5)$_6$(OH)$_6$](ClO$_4$)$_2$·4H$_2$O **(Ni$_7$L5_OH)**

HL5 (98 mg, 0.6 mmol), Ni(ClO$_4$)$_2$·6(H$_2$O) (256 mg, 0.7 mmol) and Et$_3$N (124 ml) were dissolved in 4 ml of acetonitrile/H$_2$O (*v:v*=3:1). The mixed solution was heated with microwave for 5 minutes at 100 ºC. Green powder formed was collected by filtration and washed with diethyl ether. Crude product was dissolved in acetonitrile and recrystallized by ether diffusion. Green crystals were collected by filtration and washed with diethyl ether and dried in vacuo. Yield 59 mg (33.6 %). Elemental analysis (%); Calcd. for C$_{54}$H$_{62}$Cl$_2$N$_6$Ni$_7$O$_{30}$ [Ni$_7$(L5)$_6$(OH)$_6$](ClO$_4$)$_2$·4H$_2$O: C 36.92, H 3.56, N 4.78; found: C 36.99, H 3.33, N 4.79. Formula weight 1756.86 FT-IR (cm^{-1}); 1619, 1599, 1510, 1455, 1282, 1092, 941, 767, 687

[Ni$_7$(L5)$_6$(OMe)$_6$](ClO$_4$)$_2$·7H$_2$O **(Ni$_7$L5_OMe)**

HL5 (98 mg, 0.6 mmol), Ni(ClO$_4$)$_2$·6(H$_2$O) (256 mg, 0.7 mmol) and Et$_3$N (124 ml) were dissolved in 2 ml of MeOH. The mixed solution was heated with microwave for 5 minutes at 100 ºC. Green powder formed was collected by filtration and washed with diethyl ether. Crude product was dissolved in acetonitrile and recrystallized by ether diffusion. green crystals were collected by filtration and washed with diethyl ether and dried in vacuo. Yield 47.0 mg (24.8 %). Elemental analysis (%); Calcd. for C$_{60}$H$_{80}$Cl$_2$N$_6$Ni$_7$O$_{33}$ [Ni$_7$(L5)$_6$(OMe)$_6$](ClO$_4$)$_2$·7H$_2$O: C 38.03, H 4.26, N 4.43; found: C 37.67, H 3.74, N 4.68. Formula weight 1895.06 FT-IR (cm^{-1}); 1619, 1599, 1510, 1455, 1281, 1099, 941, 766, 687

[Ni$_7$(L5)$_6$(N$_3$)$_6$](ClO$_4$)$_2$·3H$_2$O **(Ni$_7$L5_N$_3$)**

HL5 (98 mg, 0.6 mmol) and Ni(ClO$_4$)$_2$·6(H$_2$O) (256 mg, 0.7 mmol) in 3 ml of acetonitrile were added to the 1 ml of NaN$_3$ (58 mg, 0.9 mmol) aqueous solution. Mixed solution was heated with microwave for 5 minutes at 100 ºC. Green powder formed was collected by filtration and washed with diethyl ether. Crude product was dissolved in acetonitrile/DMF (*v:v* = 2:1) and recrystallized by ether diffusion. Green crystals were collected by filtration and washed with diethyl ether and dried in vacuo. Yield 40 mg (21.2 %). Elemental analysis (%); Calcd. for C$_{54}$H$_{54}$Cl$_2$N$_{24}$Ni$_7$O$_{23}$ [Ni$_7$(L5)$_6$(N$_3$)$_6$](ClO$_4$)$_2$·3H$_2$O: C 34.34, H 2.88, N 17.80; found: C 34.83, H 2.98, N 17.19. Formula weight 1888.92 FT-IR (cm^{-1}); 2090, 1600, 1517, 1467, 1454, 1282, 1102, 1089, 941, 783, 718, 687

X-ray Crystallography

All Single-crystal X-ray diffraction data were collected on a Bulker SMART APEX II ULTRA CCD-detector Diffractometer, a rotating-anode (Bruker Tourbo X-ray source) with graphite-monochromated $Mo_{K\alpha}$ radiation (λ = 0.71073 Å) was used. Computations were carried out on a APEX2 crystallographic software package and OLEX2 software.[6]   A single crystal was mounted on a polymer film with liquid paraffin and the temperature kept -173 ºC under flowing N_2 gas.   All of the structures were solved by direct method or intrinsic method.   All the structures were expanded using Fourier techniques.   Fullmatrixleast-squares refinements were carried out with anisotropic thermal parameters for all non-hydrogen atoms.   The hydrogen atoms were attached based on the difference Fourier map and calculation geometrically.   The SQUEEZE program was used to remove the contribution of the highly disordered solvent molecules from the structural calculations.   Crystal parameters for heptanuclear complexes (**Ni₇L5_OH**, **Ni₇L5_OMe**, **Ni₇L5_N₃**) are summarized in **Table 1**.   (Crystal parameters for nonanuclear complexes shown in Chapter 1)

Table 1. Crystallographic parameters of **Ni₇L5_OH** and **Ni₇L5_OMe**

Complex	Ni₇L5_OH	Ni₇L5_OMe
Formula	$C_{56}H_6Cl_2N_6Ni_7O_{28}$	$C_{60}H_{16}Cl_2N_6Ni_7O_{26}$
Formula weight	1692.54	1708.66
Temperature / K	100	100
Crystal size / mm	$0.036 \times 0.148 \times 0.452$	$0.092 \times 0.047 \times 0.046$
Crystal system	monoclinic	Monoclinic
Space group	$C2/m$	$C2/m$
a / Å	27.572(6)	13.080(2)
b / Å	20.987(5)	22.845(4)
c / Å	13.173(3)	15.314(3)
α / °	90	90
β / °	94.597(3)	111.450(2)
γ / °	90	90
Volume / Å³	7598(3)	4259.2(12)
Z value	4	2
D (calcd.) / gcm⁻³	1.480	1.340
$R1$	0.1027	0.0902
$wR2$	0.1452	0.3132
Goodness of Fit	1.265	1.102

Table 2. Crystallographic parameters of **Ni₇L5_N₃**

Complex	**Ni₇L5_N₃**
Formula	$C_{54}H_{48}Cl_2N_{24}Ni_7O_{20}$
Formula weight	1835.03
Temperature / K	100
Crystal size / mm	$0.217 \times 0.189 \times 0.076$
Crystal system	Triclinic
Space group	$P\bar{1}$
a / Å	12.8411(12)
b / Å	13.2969(13)
c / Å	13.9873(13)
α / °	65.8620(10)
β / °	87.7830(10)
γ / °	64.8360(10)
Volume / Å^3	1946.0(3)
Z value	1
D (calcd.) / gcm^{-3}	1.566
$R1$	0.0493
$wR2$	0.1653
Goodness of Fit	1.112

Results and Discussion

Crystal Structure of [3M-M-3M] type Cluster

The molecular structure of **Co$_9$L1** is shown in **Figure 3**. **Co$_9$L1** has a unique nonanuclear structure with central heptad core and terminal mononuclear units in a [1-7-1] formation that a hydroxyl-bridged heptanuclear Co(II) core, [Co$_7$(μ_3-OH)$_6$]$^{8+}$, was flanked by mononuclear Co(II) units, [Co(Ln)$_3$]$^{4-}$. The heptad core of **Co$_9$L1** is [3M-M-3M] type structure that two trinuclear core is combined with a central Co(II) by six hydroxyl anions. This is quite different structure form oxygen-bridged cluster sandwiched between triplicated mononuclear unit reported so far which include [M$_3$(μ_3-O)] or [M$_3$(μ_3-OH)] type and it can be described [3M] [7-11] and [3M-3M] [9,12] type cluster structure respectively. This assembled structure is corner-sharing tetrahedra-type and similar to a "double-cubane structure" which can be vied as two M$_4$O$_4$ cubane cores sharing the one metal corner. Cluster complexes having such structures are reported by Mohamedally K. *et al.* and Dominique, L. *et al.* with Cobalt and Nickel ions respectively, and they showed SMM behavior. [13,14] In the terminal mononuclear units, Co(II) ion (Co1, Co9 for **Co$_9$L1**) was in an O6 octahedral coordination geometry with three β-diketonate sites of Ln^{2-}. In the heptad core, six Co(II) ions of triad (Co2-Co4, Co6-Co8) were in an O5N1 octahedral coordination environment with a tridentate site of Ln^{2-}, two hydroxyl ions and solvent. The central Co(II) ion (Co5) was octahedrally surrounded by six hydroxyl ions and linked with six Co(II) ions of triad by μ_3-hydroxyl bridges. The average bond distances of Co-L that are in the range 2.0-2.3 Å, which is typical for Co(II) ion. The valence of Co is also supported by bond valence sum (BVS) calculation (**Table 6**).[15] The Co-O-Co angles between terminal Co(II) and Co(II) of triad in heptad core through enolate-bridge are 118° - 123° and Co···Co distances are about 3.7 - 3.8 Å. In the heptad core, Co-O-Co angles between central Co(II) ions and the other Co(II) of triad in the heptad are around 93° - 98°, which are smaller than that of Co(II) of triad in the heptad (121° - 125°). Furthermore, Co···Co distances between central Co(II) and the other Co(II) of triad in the heptad are also shorter than that of Co(II) of triad in the heptad (3.0 - 3.1 Å and 3.5 - 3.7 Å).

Co$_9$L1$^+$_ClO$_4$ which synthesized by oxidation of **Co$_9$L1** with *t*-butyl hydroperoxide, formed almost the same as **Co$_9$L1** (**Figure 3**) and included a counter anion (ClO$_4^-$) in the crystal structure. Only the average bond distance of Co ions (Co5, Co14) to O is in the range of 1.9 Å - 2.0 Å which is typical for Co(III) ion. The valence of Co is also supported by BVS calculation (**Table 6**). The Co···Co distances between central

Co(III) and the other Co(II) ions in heptad slightly shortened and Co-O-Co angles slightly increased compared with that of **Co₉L1**. **Co₉L1⁺_Ce** which synthesized by oxidation of **Co₉L1** with strong oxidant $(NH_3)_2[Ce^{IV}(NO)_6]$ also formed almost the same structure as **Co₉L1** and included $[Ce(NO_3)_6]^{3-}$ as counter anion in the crystal structure (**Figure 3**). Average bond distance of terminal and Co ions to O is in the range of 1.8 Å - 2.0 Å which is typical for Co(III) ion. This result is supported by BVS calculation (**Table 6**). Therefore, three cobalt ions with O6 coordination by β-diketonate site and bridging hydroxyl anion was oxidized. As in **Co₉L1⁺_ClO₄**, The Co⋯Co distances between central Co(III) and the other cobalt ions in heptad also slightly shortened and Co-O-Co angles slightly increased compared with that of **Co₉L1**. There is a trigonal axis passes through the three Co ions (Co1, Co3, Co1#8) and C_2 axis passes though the Co3. This highly symmetric structure is attributed to high symmetric d electron configuration (t_{2g}^6) of trivalent cobalt ion and three-fold symmetry of $[Ce(NO_3)_6]^{3-}$.

Ni₉L*n* also formed the same [1-7-1] structure as **Co₉L1** that a hydroxyl-bridged heptanuclear Ni(II) core, $[Ni_7(\mu_3-OH)_6]^{8+}$, was flanked by mononuclear Ni(II) units, $[Ni(L*n*)_3]^{4-}$. The heptad core of **Ni₉L*n*** is [3M-M-3M] type structure that two trinuclear core is combined with a central Ni(II) by six hydroxyl anions. The average bond distances of Ni-L that are in the range 2.0-2.2 Å, which is typical for Ni(II) ion. The valence of Ni is also supported by bond valence sum (BVS) calculation (**Table 11**). The Ni-O-Ni angles between terminal Ni(II) ions and Ni(II) ions of triad in the heptad core with enolate-bridge are 121° - 125° and distances of two metals are about 3.7 - 3.8 Å. In the heptad core, Ni-O-Ni angles between central Ni(II) and the other Ni(II) ions of triad are around 94° - 96°, which are smaller than that of Ni(II) of triad in the heptad (123° - 127°). Furthermore, Ni⋯Ni distances between central Ni(II) and the other Ni(II) of triad in the heptad are also shorter than that of Ni(II) ions of triad in the heptad (3.0 - 3.1 Å and 3.5 - 3.7 Å).
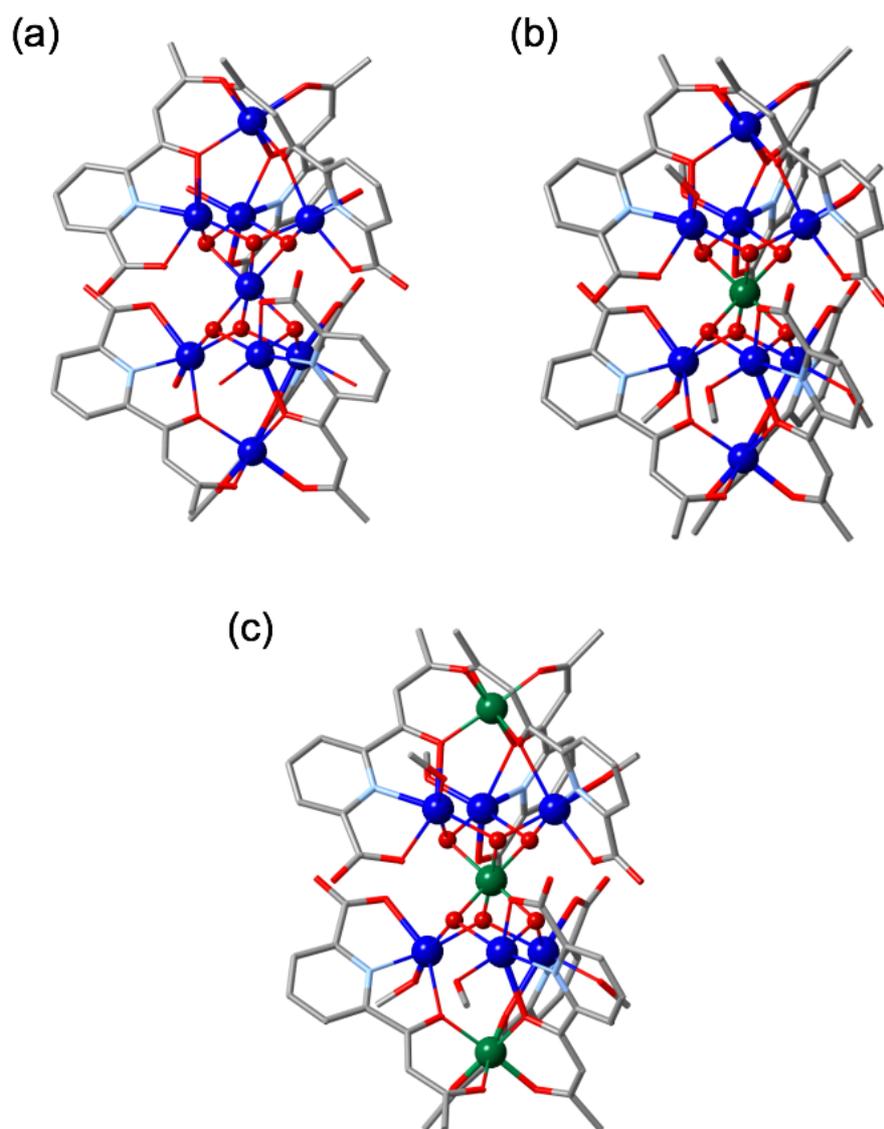
Figure 3.   Molecular structure of **Co$_9$L1** (a), **Co$_9$L1$^+$** (b) and **Co$_9$L1^{3+}** (c).   H atoms and solvent molecules are omitted for clarity. (Co^{II}: blue; Co^{III}: green; C: gray; O: red; N: light blue)

Table 3. Selected bond angles (°) and Co···Co distances (Å) for **Co₉L1**.

Co1–O2–Co2	122.31(10)	Co1–O6–Co3	118.84(10)	Co1–O10–Co4	121.55(10)
Co9–O14–Co6	120.36(10)	Co9–O18–Co7	120.76(10)	Co9–O22–Co8	122.07(10)
Co3–O25–Co2	124.55(11)	Co4–O26–Co3	121.33(11)	Co2–O27–Co4	124.51(12)
Co7–O28–Co6	123.68(11)	Co8–O29–Co7	121.12(11)	Co6–O30–Co8	123.61(11)
Co2–O25–Co5	93.54(9)	Co2–O27–Co5	95.48(9)	Co3–O25–Co5	96.64(9)
Co5–O26–Co3	95.13(9)	Co4–O26–Co5	97.96(10)	Co5–O27–Co4	94.74(9)
Co5–O28–Co6	93.71(9)	Co6–O30–Co5	96.39(9)	Co7–O28–Co5	97.29(9)
Co5–O29–Co7	95.05(9)	Co8–O29–Co5	97.17(9)	Co5–O30–Co8	94.25(9)
Co1···Co2	3.768(1)	Co1···Co3	3.722(1)	Co1···Co4	3.790(1)
Co2···Co3	3.629(2)	Co3···Co4	3.553(1)	Co4···Co2	3.632(1)
Co2···Co5	3.036(1)	Co3···Co5	3.070(1)	Co4···Co5	3.070(1)
Co6···Co5	3.056(1)	Co7···Co5	3.072(1)	Co8···Co5	3.069(1)
Co6···Co7	3.644(1)	Co7···Co8	3.579(2)	Co8···Co9	3.630(1)
Co6···Co9	3.724(1)	Co7···Co9	3.746(1)	Co8···Co9	3.771(1)

Table 4. Selected bond angles (°) and Co···Co distances (Å) for **Co₉L1⁺_ClO₄** (°).

Co1–O10–Co4	121.9(2)	Co1–O2–Co2	121.8(2)	Co1–O6–Co3	121.6(2)
Co9–O22–Co8	121.2(2)	Co9–O18–Co7	121.4(2)	Co6–O14–Co9	120.9(2)
Co4–O27–Co2	121.3(2)	Co2–O25–Co3	119.8(2)	Co3–O26–Co4	120.3(2)
Co8–O29–Co7	120.9(2)	Co7–O28–Co6	121.1(2)	Co6–O30–Co8	119.2(2)
Co4–O27–Co5	98.8(2)	Co4–O26–Co5	97.3(2)	Co3–O26–Co5	99.7(2)
Co3–O25–Co5	98.8(1)	Co2–O25–Co5	99.1(2)	Co2–O27–Co5	97.2(1)
Co5–O30–Co8	99.6(2)	Co8–O29–Co5	97.6(1)	Co5–O29–Co7	99.2(1)
Co7–O28–Co5	98.2(2)	Co5–O28–Co6	98.7(2)	Co6–O30–Co5	97.5(2)
Co10–O38–Co11	117.46(17)	Co10–O42–Co12	121.40(19)	Co10–O46–Co13	121.94(17)
Co18–O50–Co15	119.98(19)	Co18–O54–Co16	120.22(18)	Co18–O58–Co17	120.59(18)
Co12–O61–Co11	119.96(17)	Co13–O62–Co12	120.00(17)	Co11–O63–Co13	121.04(16)
Co16–O64–Co15	120.81(17)	Co17–O65–Co16	119.34(16)	Co15–O66–Co17	119.64(17)
Co14–O61–Co11	97.42(15)	Co14–O61–Co12	99.73(16)	Co14–O62–Co12	97.26(15)
Co14–O62–Co13	99.14(16)	Co14–O63–Co11	99.07(15)	Co14–O63–Co13	98.01(16)
Co14–O64–Co15	96.99(16)	Co14–O64–Co16	99.20(15)	Co14–O65–Co16	97.42(16)
Co14–O65–Co17	99.61(16)	Co14–O66–Co15	99.42(16)	Co14–O66–Co17	98.21(14)
Co1···Co2	3.716(2)	Co1···Co3	3.581(1)	Co1···Co4	3.714(1)
Co2···Co3	3.581(1)	Co3···Co4	3.597(1)	Co4···Co2	3.597(1)
Co2···Co5	3.009(1)	Co3···Co5	3.044(1)	Co4···Co5	2.999(1)

Co6⋯Co5	3.013(1)	Co7⋯Co5	3.029(1)	Co8⋯Co5	3.024(1)
Co6⋯Co7	3.610(1)	Co7⋯Co8	3.628(1)	Co8⋯Co6	3.577(1)
Co6⋯Co9	3.706(1)	Co7⋯Co9	3.709(1)	Co8⋯Co9	3.681(2)
Co10⋯Co11	3.610(1)	Co10⋯Co12	3.729(1)	Co10⋯Co13	3.715(1)
Co11⋯Co12	3.571(1)	Co12⋯Co13	3.593(1)	Co11⋯Co13	3.608(1)
Co11⋯Co14	3.006(1)	Co12⋯Co14	3.006(1)	Co13⋯Co14	3.016(1)
Co14⋯Co15	3.004(1)	Co14⋯Co16	3.012(1)	Co14⋯Co17	3.019(1)
Co15⋯Co16	3.618(1)	Co16⋯Co17	3.585(1)	Co15⋯Co17	3.573(1)
Co15⋯Co18	3.665(1)	Co16⋯Co18	3.667(1)	Co17⋯Co18	3.673(1)

Table 5. Selected bond angles (°) and Co⋯Co distances (Å) for **Co₉L1³⁺_Ce** (°).

Co1-O2-Co2	123.7	Co2-O5-Co2$^{\#1}$	119.4(1)	Co2-O5-Co3	98.52
Co2-O5$^{\#1}$-Co3	97.8				
Co1⋯Co2	3.726	Co2⋯Co2	3.5921(9)	Co2⋯Co3	3.018

Symmetry Operation: (#1) +Y-X, 1-X, +Z; (#2) 1-Y, 1+X-Y, +Z; (#3) 4/3-X, 2/3-Y, 5/3-Z; (#4) 1/3+Y, 2/3-X+Y, 5/3-Z; (#5) 1+Y-X, 1-X, +Z; (#6) 1-Y, +X-Y, +Z; (#7) 1/3-Y+X, -1/3+X, 5/3-Z; (#8) 2/3-Y+X, 4/3-Y, 11/6-Z; (#9) 2/3-X, 1/3-X+Y, 11/6-Z; (#10) -1/3+Y, 1/3+X, 11/6-Z

Table 6. Calculated value of valence (V_i)

Complex	Co1	Co2	Co3	Co4	Co5	Co6	Co7	Co8	Co9
Co₉L1	2.16	2.12	2.13	2.11	2.10	2.10	2.11	2.12	2.15
Co₉L1⁺_ClO₄	2.24	2.22	2.21	2.23	3.32	2.20	2.20	2.22	2.28
Co₉L1³⁺_Ce	3.60	2.16	3.38						
	Co10	**Co11**	**Co12**	**Co13**	**Co14**	**Co15**	**Co16**	**Co17**	**Co18**
Co₉L1⁺_ClO₄	2.27	2.23	2.28	2.23	3.49	2.25	2.23	2.23	2.31
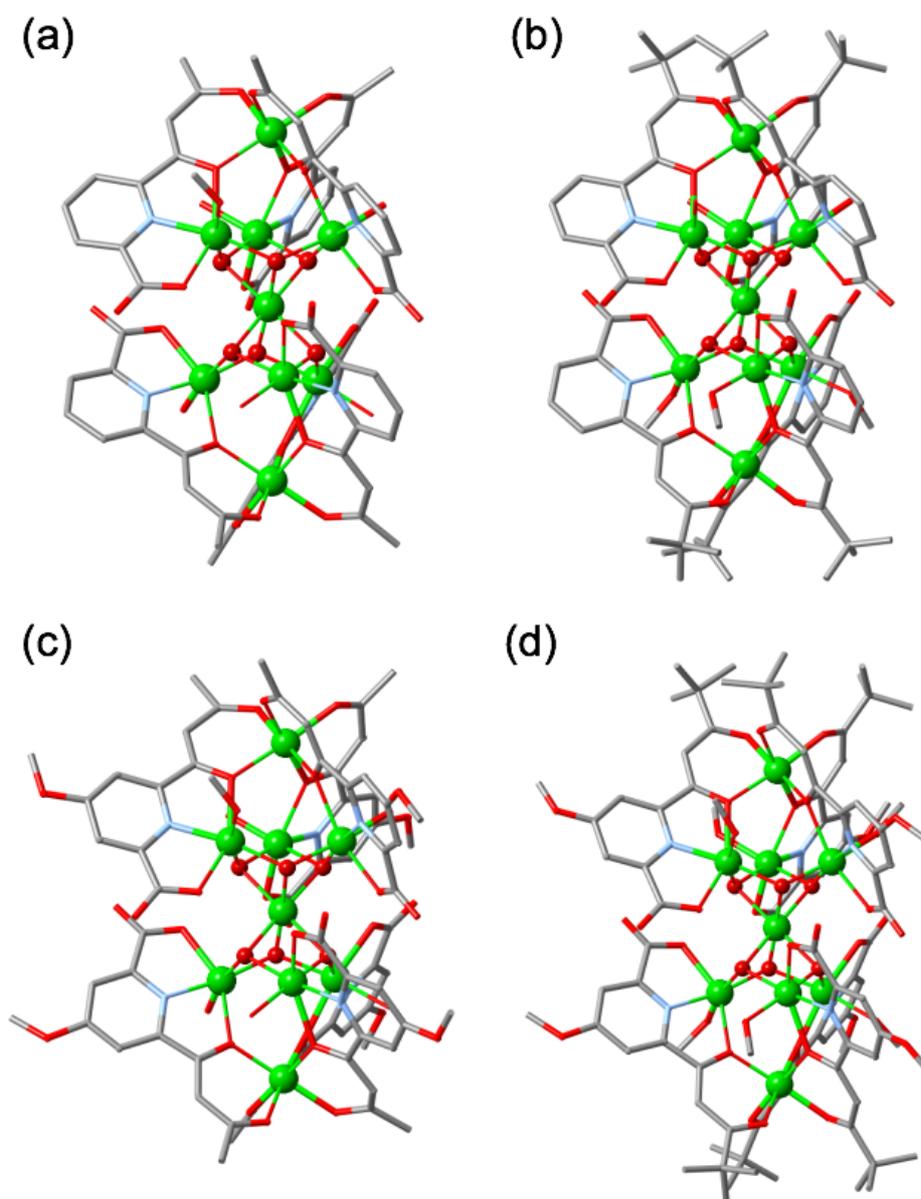
Figure 4.   Molecular structure of **Ni$_9$L1** (a), **Ni$_9$L2** (b), **Ni$_9$L3** (c) and **Ni$_9$L4** (d).   H atoms and solvent molecules are omitted for clarity. (Ni: light green; C: gray; O: red; N: light blue)

Table 7.   Selected bond angles (°) and Ni···Ni distances (Å) for **Ni₉L1** (°).

Ni1–O2–Ni2	123.10(6)	Ni1–O6–Ni3	124.67(6)	Ni1–O10–Ni4	123.70(6)
Ni6–O14–Ni9	124.66(6)	Ni7–O18–Ni9	121.62(6)	Ni8–O22–Ni9	123.96(6)
Ni2–O25–Ni3	125.75(6)	Ni3–O26–Ni4	123.09(6)	Ni4–O27–Ni2	125.52(6)
Ni6–O28–Ni7	126.25(6)	Ni7–O29–Ni8	123.24(7)	Ni8–O30–Ni6	125.96(7)
Ni2–O27–Ni5	94.93(5)	Ni2–O25–Ni5	94.75(5)	Ni3–O25–Ni5	95.10(5)
Ni3–O26–Ni5	95.83(5)	Ni4–O26–Ni5	96.06(5)	Ni4–O27–Ni5	95.71(5)
Ni5–O28–Ni6	94.53(5)	Ni5–O30–Ni6	94.64(6)	Ni5–O28–Ni7	95.02(5)
Ni5–O29–Ni7	95.63(6)	Ni5–O29–Ni8	95.90(6)	Ni5–O30–Ni8	95.32(6)
Ni1···Ni2	3.7599(7)	Ni1···Ni3	3.7963(7)	Ni1···Ni4	3.7668(7)
Ni2···Ni3	3.6145(6)	Ni3···Ni4	3.5523(8)	Ni4···Ni2	3.6109(7)
Ni2···Ni5	3.0195(6)	Ni3···Ni5	3.0329(7)	Ni4···Ni5	3.0320(7)
Ni5···Ni6	3.0137(7)	Ni5···Ni7	3.0297(7)	Ni5···Ni8	3.0268(6)
N6···Ni7	3.6148(8)	Ni7···Ni8	3.5455(7)	Ni8···Ni6	3.5968(6)
Ni6···Ni9	3.7633(7)	Ni7···Ni9	3.7398(7)	Ni8···Ni9	3.8179(7)

Table 8.   Selected bond angles (°) and Ni···Ni distances (Å) for **Ni₉L2** (°).

Ni1–O2–Ni2	122.6(2)	Ni5–O6–Ni4	124.1(2)	Ni2–O9–Ni2#2	124.7(2)
Ni4–O10–Ni4#2	125.7(2)	Ni2–O9–Ni3	95.9(2)	Ni2–O9#2–Ni3	95.2(2)
Ni3–O10–Ni4	95.1(2)	Ni3–O10#2–Ni4	95.5(2)		
Ni1···Ni2	3.732(1)	Ni2···Ni2#2	3.574(1)	Ni2···Ni3	3.019(1)
Ni3···Ni4	3.023(1)	Ni4···Ni4#2	3.594(1)	Ni4···Ni5	3.763(1)

Symmetry operation (#1) 1/2+Z, 3/2-X, 1-Y; (#2) 3/2-Y, 1-Z, -1/2+X

Table 9.   Selected bond angles (°) and Ni···Ni distances (Å) for **Ni₉L3** (°).

Ni1–O2–Ni2	123.4(3)	Ni1–O7–Ni3	122.9(5)	Ni1–O12–Ni4	124.5(4)
Ni9–O17–Ni6	124.4(3)	Ni9–O22–Ni7	123.2(3)	Ni9–O27–Ni8	122.4(3)
Ni2–O31–Ni3	126.3(4)	Ni4–O32–Ni3	125.6(3)	Ni4–O33–Ni2	122.5(3)
Ni6–O34–Ni7	125.7(3)	Ni7–O35–Ni8	127.5(3)	Ni8–O36–Ni6	123.2(3)
Ni2–O31–Ni5	95.9(3)	Ni2–O33–Ni5	96.5(2)	Ni3–O31–Ni5	94.4(3)
Ni3–O32–Ni5	94.0(3)	Ni4–O32–Ni5	95.2(2)	Ni4–O33–Ni5	96.1(2)
Ni6–O34–Ni5	95.0(3)	Ni6–O36–Ni5	94.9(2)	Ni7–O34–Ni5	94.8(3)
Ni7–O35–Ni5	95.1(2)	Ni8–O35–Ni5	95.3(2)	Ni8–O36–Ni5	96.2(2)
Ni10–O44–Ni11	123.2(3)	Ni10–O49–Ni12#1	123.7(3)	Ni10–O54–Ni13#1	124.2(3)
Ni12–O58–Ni11#1	126.7(3)	Ni13–O59–Ni12	123.2(3)	Ni11–O60–Ni13#1	124.2(3)

Ni11#1–O58–Ni14	94.5(2)	Ni11–O60–Ni14	95.3(2)	Ni12–O58–Ni14	95.0(2)
Ni12–O59–Ni14	95.5(2)	Ni13–O59–Ni14	96.2(2)	Ni13#1–O60–Ni14	95.7(2)
Ni1···Ni2	3.761(3)	Ni1···Ni3	3.744(3)	Ni1···Ni4	3.843(2)
Ni6···Ni9	3.841(2)	Ni7···Ni9	3.747(2)	Ni8···Ni9	3.729(2)
Ni2···Ni3	3.606(2)	Ni3···Ni4	3.604(3)	Ni2···Ni4	3.527(2)
Ni6···Ni7	3.579(3)	Ni7···Ni8	3.644(2)	Ni6···Ni8	3.542(1)
Ni2···Ni5	3.042(2)	Ni3···Ni5	3.008(2)	Ni4···Ni5	3.017(3)
Ni5···Ni6	3.005(2)	Ni5···Ni7	3.013(3)	Ni5···Ni8	3.028(1)
Ni10···Ni11	3.732(1)	Ni10···Ni12	3.815(2)	Ni10···Ni13	3.808(1)
Ni11···Ni12	3.623(2)	Ni12···Ni13	3.543(2)	Ni11···Ni13	3.577(2)
Ni11···Ni14	3.019	Ni12···Ni14	3.017	Ni13···Ni14	3.033

Symmetry operation (#1) 1-X, +Y, -1/2-Z

Table 10. Selected bond angles (°) and Ni···Ni distances (Å) for **Ni₉L4** (°).

Ni1–O2–Ni2	122.8(1)	Ni1–O7–Ni3	122.4(1)	Ni1–O12–Ni4	124.0(1)
Ni2–O16–Ni3	125.4(1)	Ni3–O17–Ni4	125.2(1)	Ni4–O18–Ni2	122.5(1)
Ni2–O16–Ni5	95.6	Ni2–O18–Ni5	96	Ni3–O16–Ni5	95.3
Ni3–O17–Ni5	94.9	Ni4–O17–Ni5	95.7	Ni4–O18–Ni5	95.9
Ni1···Ni2	3.7488(6)	Ni1···Ni3	3.7322(7)	Ni1···Ni4	3.8165(7)
Ni2···Ni3	3.6000(7)	Ni3···Ni4	3.5857(8)	Ni2···Ni4	3.5419(7)
Ni2···Ni5	3.0309	Ni3···Ni5	3.0253	Ni4···Ni5	3.0356

Symmetry operation (#1) 1-X, +Y, 1/2-Z

Table 11. Calculated value of valence (V_i)

Complex	Ni1	Ni2	Ni3	Ni4	Ni5	Ni6	Ni7	Ni8	Ni9
Ni₉L1	2.15	2.01	2.04	2.04	1.94	2.02	2.05	2.02	2.14
Ni₉L2	2.19	2.04	1.98	2.03	2.15				
Ni₉L3	2.17	2.06	2.03	2.04	1.97	2.02	2.02	2.06	2.18
Ni₉L4	2.17	2.04	2.02	2.02	1.95				
	Ni10	**Ni11**	**Ni12**	**Ni13**	**Ni14**				
Ni₉L3	2.16	2.03	2.04	1.91	1.97				

Crystal Structure of [M-6] type Cluster

The molecular structure of **Ni₇L5_OH**, **Ni₇L5_OMe and Ni₇L5_N₃** are shown in **Figure 5-10**. All complexes formed almost the same structure that seven Ni ions are arranged on the same plane by bridging with six anions (OH⁻, OMe⁻ and N₃⁻) and surrounded by six ligands. This assembled structures was called "disk-shaped cluster" or "wheel-type cluster", and it has been reported with several ligand or different bridging agent (e.g. OH⁻, OMe⁻, N₃⁻ and alkoxide).[16-47] In **Ni₇L5_OH, Ni₇L5_OMe,** central Ni ions were in an O6 octahedral coordination environment with six hydroxyl anions. Peripheral Ni ions were in an NO6 octahedral coordination environment with a pyridine-enolate site of L5⁻, β-diketonate site and two bridging hydroxyl anions. On the other hand, in **Ni₇L5_N3**, central Ni ion is N6 octahedral coordination environment with six azide anions, and peripheral Ni ions were N3O3 octahedral coordination environment with a pyridine-enolate site, β-diketonate site and two bridging azide anions. The average bond distances of Ni-L that are in the range 2.0-2.2 Å, which is typical for Ni(II) ion. The valence of Ni is also supported by bond valence sum (BVS) calculations (**Table 11**).[15] In **Ni₇L5_OH**, and **Ni₇L5_OMe**, the Ni···Ni distances between peripheral Ni(II) ions are *ca.* 3.1 Å, and Ni-O-Ni angles are 102° - 103° and 97° - 99° for enolate bridging and hydroxyl bridging respectively. The Ni···Ni distances between a central Ni(II) ion and peripheral Ni(II) ions are *ca.* 3.1 Å, and Ni-N-Ni angles are 97° - 99°. In **Ni₇L5_N₃**, the Ni···Ni distances between peripheral Ni(II) ions are *ca.* 3.2 Å, and Ni-N-Ni angles are 106° - 108° and 94° - 96° for enolate bridging and azide bridging respectively. The Ni···Ni distances between a central Ni(II) ion and peripheral Ni(II) ions are 3.1 Å - 3.2 Å, and Ni-O-Ni angles are 96° - 98°. The Ni-N-Ni angles of **Ni₇L5_N3** are smaller than that of oxygen bridged complexes (**Ni₇L5_OH**, and **Ni₇L5_OMe).**
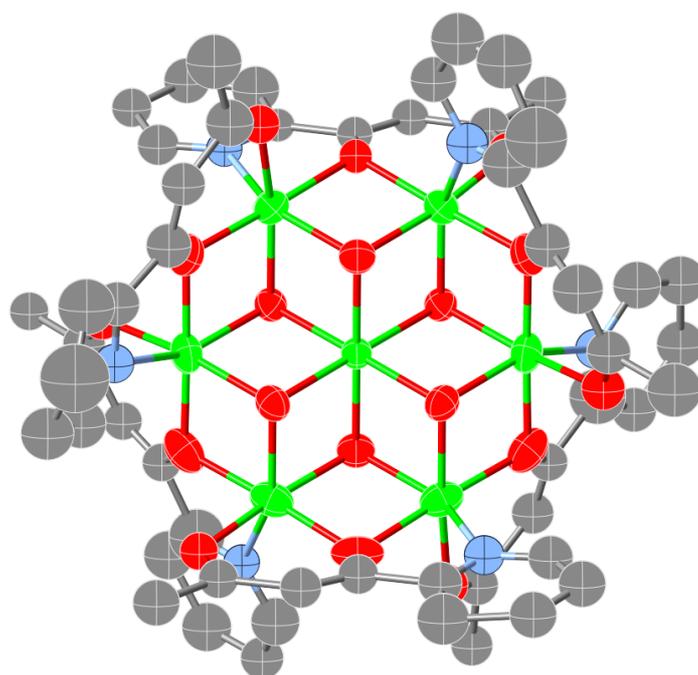
Figure 5. An ORTEP view of **Ni₇L5_OH**. H atoms, solvent molecules and counter anions are omitted for clarity (Ni: light green; C: gray; O: red; and N: light blue)
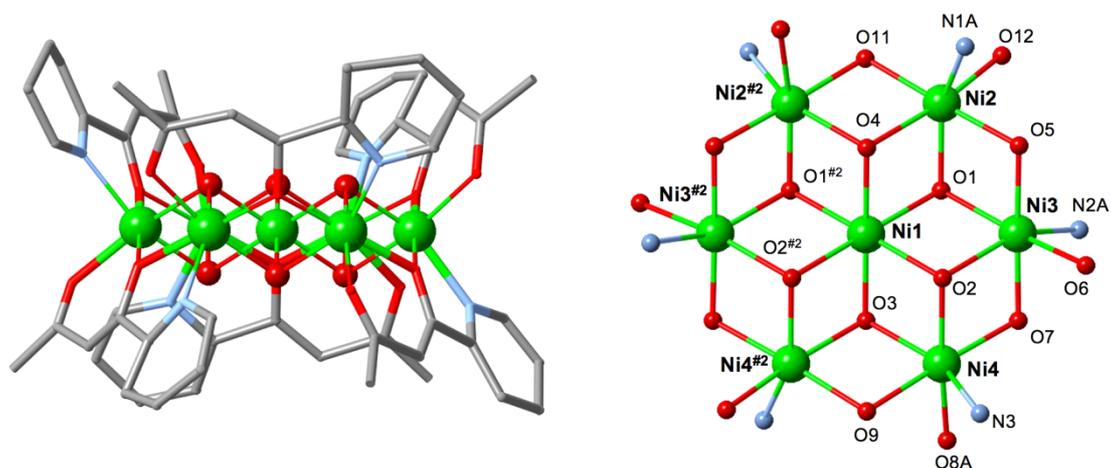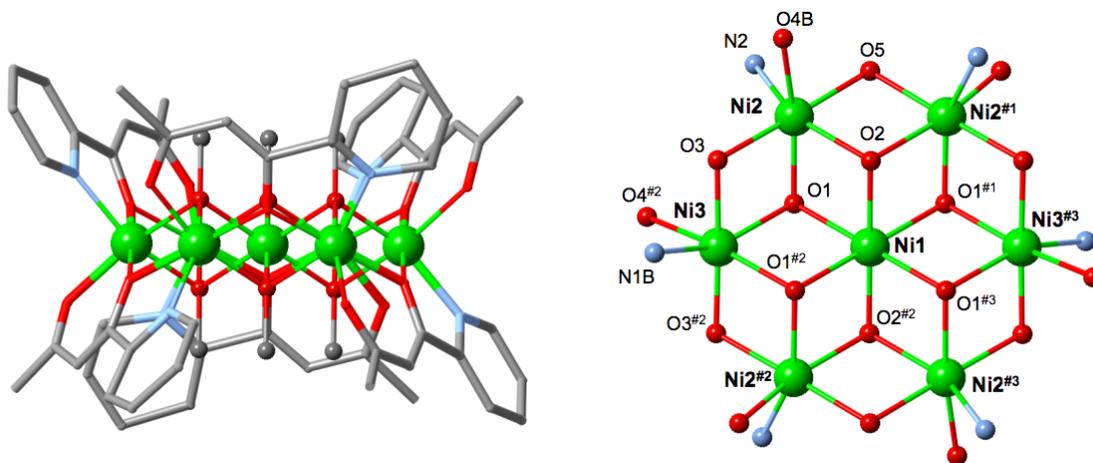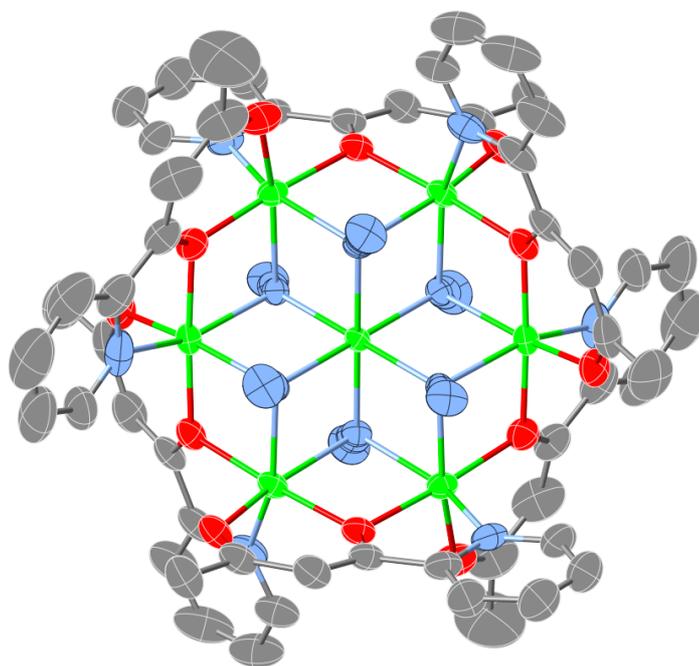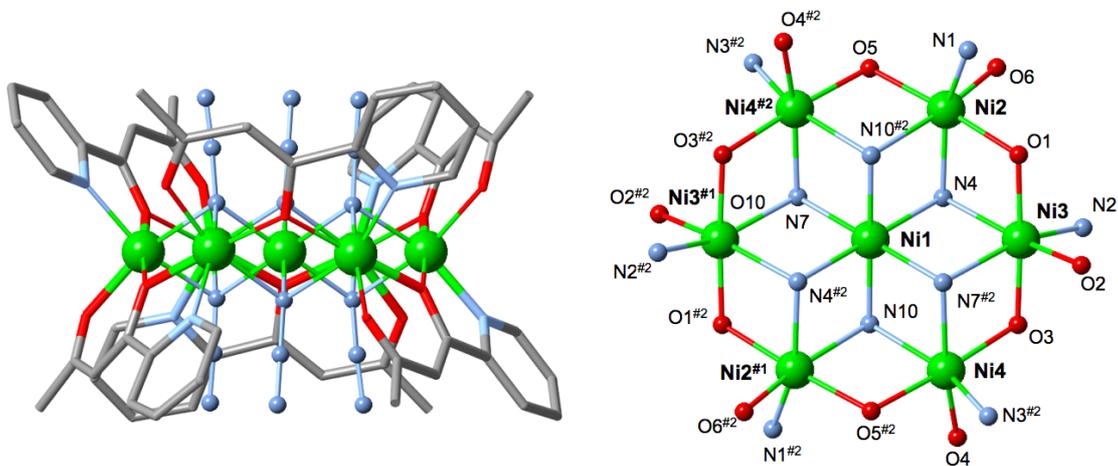

Figure 6. Molecular structure of **Ni₇L5_OH** (left) and the core (right). H atoms, solvent molecules and counter anions are omitted for clarity.

Table 12. Selected bond distances for **Ni₇L5_OH** (Å).

Ni1–O1[#2]	2.062(4)	Ni1–O1	2.062(4)	Ni1–O2[#2]	2.056(4)
Ni1–O2	2.056(4)	Ni1–O3	2.067(6)	Ni1–O4	2.043(6)
Ni2–N1A	2.076(18)	Ni2–O1	2.070(5)	Ni2–O4	2.059(4)
Ni2–O5	1.985(5)	Ni2–O11	1.993(4)	Ni2–O12[#2]	2.038(12)
Ni3–N2A	2.132	Ni3–O1	2.063(4)	Ni3–O2	2.063(5)
Ni3–O5	1.996(5)	Ni3–O6A	2.025(13)	Ni3–O7	1.999(5)
Ni4–N3	2.054	Ni4–O2	2.045(5)	Ni4–O3	2.059(5)
Ni4–O7	2.014(5)	Ni4–O8A	2.068(13)	Ni4–O9	2.010(5)
Ni1···Ni2	3.109	Ni1···Ni3	3.104	Ni1···Ni4	3.105
Ni2···Ni2	3.105	Ni2···Ni3	3.105	Ni3···Ni4	3.112
Ni4···Ni4	3.098				

Symmetry Operation: (#1) 1/2-X, 1/2-Y, 1-Z; (#2) +X, 1-Y, +Z

Table 13. Selected bond angles for **Ni₇L5_OH** (°).

Ni1–O1–Ni2	97.60(19)	Ni1–O4–Ni2	98.6(2)
Ni1–O1–Ni3	97.6(2)	Ni1–O2–Ni3	97.8(2)
Ni4–O2–Ni1	98.40(19)	Ni4–O3–Ni1	97.6(2)
Ni2–O4–Ni2[#2]	97.9(3)	Ni2–O11–Ni2[#2]	102.3(3)
Ni2–O1–Ni3	97.38(19)	Ni2–O5–Ni3	102.5(2)
Ni3–O2–Ni4	98.5(2)	Ni3–O7–Ni4	101.7(2)
Ni4–O3–Ni4[#2]	97.6(3)	Ni4–O9–Ni4[#2]	100.8(3)

Symmetry Operation: (#1) 1/2-X, 1/2-Y, 1-Z; (#2) +X, 1-Y, +Z
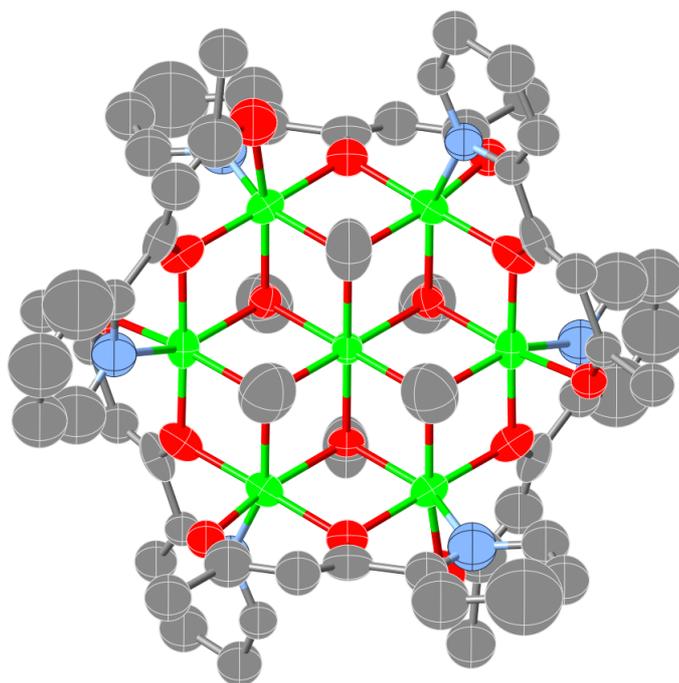
Figure 7. An ORTEP view of **Ni₇L5_OMe**. H atoms, solvent molecules and counter anions are omitted for clarity (Ni: light green; C: gray; O: red; and N: light blue)

Figure 8. Molecular structure of **Ni₇L5_OMe** (left) and the core (right). H atoms, solvent molecules and counter anions are omitted for clarity.

Table 14. Selected bond distances for **Ni₇L5_OMe** (Å).

Ni1–O1[#1]	2.059(4)	Ni1–O1[#2]	2.059(4)	Ni1–O1[#3]	2.059(4)
Ni1–O1	2.059(4)	Ni1–O2	2.052(5)	Ni1–O2[#3]	2.052(5)
Ni2–N2	2.144(2)	Ni2–O4B	2.108(2)	Ni2–O1	2.077(4)
Ni2–O2	2.064(4)	Ni2–O3	2.003(5)	Ni2–O5	1.997(4)
Ni3–N1B	2.079(10)	Ni3–O1	2.070(4)	Ni3–O1[#2]	2.070(4)
Ni3–O3	1.983(4)	Ni3–O3[#2]	1.983(4)	Ni3–O4[#2]	2.097(8)
Ni1···Ni2	3.118	Ni1···Ni3	3.106	Ni2···Ni3	3.113
Ni2···Ni2[#1]	3.117(1)				

Symmetry Operation: (#1) 1+X, 1-Y, +Z; (#2) 1-X, +Y, 1-Z; (#3) 1-X, 1-Y, 1-Z

Table 15. Selected bond angles for **Ni₇L5_OMe** (°).

Ni1–O1–Ni2	97.85(18)	Ni1–O2–Ni2	98.5(2)
Ni1–O1–Ni3	97.57(18)	Ni1–O1[#2]–Ni3	97.57(18)
Ni2–O5–Ni2[#1]	102.6(3)	Ni2–O2–Ni2[#1]	98.1(2)
Ni2–O1–Ni3	97.27(17)	Ni2–O3–Ni3	102.70(19)

Symmetry Operation: (#1) 1+X, 1-Y, +Z

Figure 9. An ORTEP view of **Ni₇L5_N₃**. H atoms, solvent molecules and counter anions are omitted for clarity (Ni: light green; C: gray; O: red; and N: light blue)

Figure 10. Molecular structure of **Ni₇L5_ N₃** (left) and the core (right). H atoms, solvent molecules and counter anions are omitted for clarity.

Table 16. Selected bond distances for **Ni₇L5_ N₃** (Å).

Ni1–N4	2.090(3)	Ni1–N7	2.076(3)	Ni1–N10	2.102(3)
Ni2$^{\#2}$–N10	2.184(3)	Ni2–N1	2.063(3)	Ni2–N4	2.151(3)
Ni2–O1	1.996(3)	Ni2–O5	1.983(3)	Ni2–O6	2.019(3)
Ni3–N2	2.035(4)	Ni3–N4	2.171(3)	Ni3$^{\#2}$–N7	2.146(3)
Ni3–O1	1.974(3)	Ni3–O2	2.015(3)	Ni3–O3	1.996(3)
Ni4$^{\#2}$–N3	2.037(3)	Ni4$^{\#2}$–N7	2.187(3)	N10–Ni4	2.153(3)
Ni4–O3	1.972(3)	Ni4–O4	2.013(3)	Ni4–O5$^{\#2}$	2.000(3)
Ni1···Ni2	3.15	Ni1···Ni3	3.177	Ni1···Ni4	3.208
Ni2···Ni3	3.197	Ni2···Ni4	3.195	Ni3···Ni4	3.193

Symmetry operation (#1) -X, 2-Y, -Z; (#2) 1-X, 2-Y, 1-Z

Table 17. Selected bond angles for **Ni₇L5_ N₃** (°).

Ni1–N4–Ni2	97.87(12)	Ni1–N10–Ni2$^{\#2}$	96.47(12)
Ni1–N4–Ni3	96.41(12)	Ni1–N7–Ni3$^{\#2}$	97.61(12)
Ni1–N7–Ni4$^{\#2}$	97.59(11)	Ni1–N10–Ni4	97.87(12)
Ni2–N4–Ni3	95.41(11)	Ni3–O1–Ni2	107.29(11)
Ni3$^{\#2}$–N7–Ni4$^{\#2}$	95.03(12)	Ni4–O3–Ni3	107.28(12)
Ni4–N10–Ni2$^{\#2}$	94.84(12)	Ni2–O5–Ni4$^{\#2}$	106.58(11)

Symmetry operation (#1) -X, 2-Y, -Z; (#2) 1-X, 2-Y, 1-Z

Table 18. Calculated value of valence (V_i)

Complex	Ni1	Ni2	Ni3	Ni4
Ni₇L5_OH	2.01	2.01	2.09	2.11
Ni₇L5_OMe	2.02	2.07	2.18	
Ni₇L5_N₃	2.40	2.26	2.32	2.30

Magnetic Properties of [3M-M-3M] type Cobalt Cluster

Magnetic behaviors of **Co₉Ln** and its oxidized species (**Co₉L1**, **Co₉L1⁺_ClO₄**, **Co₉L1³⁺_ClO₄**) are shown in the form of $\chi_M T$ vs. T plots and M vs. H plots (**Figure 12, 13, 14**). All complexes show similar antiferromagnetic behavior. The $\chi_M T$ value of **Co₉L1** at 300 K (23.7 emu mol⁻¹ K) are much larger than the spin-only value of nine high-spin Co(II) ions (16.9 emu mol⁻¹ K). This is commonly for the Co^{II} complexes (ground term is $^4T_{1g}$) due to the unquenched orbital momentum. In the low temperature, $\chi_M T$ value decreases due to the week antiferromagnetic interaction, spin-orbit coupling and zero-field splitting (ZFS) of Co(II) ions. In the magnetization studies, no saturation was seen for any cobalt complexes up to 50 kG at 2 K (**Figure 14**). This is because of the high anisotropy of the Co(II) ions and the high nuclearity of the complexes. The magnetic behaviors in the range of 300 K-20 K were simulated using the isotropic exchange Hamiltonian by the PHI program.[48] To avoid over fitting, we used a simple model ignoring the ZFS of Co(II) ions and intermolecular interaction. Spin model for the simulation is shown in **Figure 11**. **Co₉Ln** has a pseudo-c_3 symmetry with a rotation axis extending thorough Co1 and Co9, so we consider the three type of interaction, J1 through enolate-bridge with the bridging angle of $ca.$ 121°, J2 through μ₃-hydroxyl-bridge between triad Co(II) in the heptad core with $ca.$ 123°, J3 through μ₃-hydroxyl-bridge between central Co5 and the other six triad Co(II) in the heptad core with $ca.$ 95°. It should be noted that this simulation by considering J and g as isotropic are quite rough because the two factors are typically anisotropic in cobalt complexes. Calculated J values and average Co-O-Co bond angles and Co⋯Co distances are summarized in **Table 19**. In **Co₉L³⁺_ClO₄**, only the interaction between triad Co(II) in the heptad (J2) operates because terminal Co(III) and central Co(III) are diamagnetic. In addition that, the interaction between terminal Co(II) and triad Co(II) in the heptad (J1) operates in **Co₉L⁺_ClO₄.**

In the oxidized species, the magnitude of J1 and J2 values are in the range of –2.34 to –5.46 cm⁻¹, indicating weak antiferromagnetic interaction operates between corresponding Co(II) ions. The sign of J1 and J2 of negative are consistent with the result of the nonananuclear nickel complexes described later. We attempted to simulate the magnetic susceptibility data of **Co₉L1**, however, a satisfactory result could not be achieved. The magnitude of J3 for **Co₉L1** was estimated by subtraction of $\chi_M T$ values of **Co9L1³⁺_ClO₄** from **Co₉L1** (**Figure 15**). The difference of $\chi_M T$ value ($\varDelta\chi_M T$) gradually decreased to around 50 K and increased below 30 K, indicating ferromagnetic interaction is operative between central Co(II) and the other six triad Co(II) in the

heptad core. Increase of ΔM value also indicates such ferromagnetic interaction (**Figure 16**). This result is also consistent with the result of nonanuclear nickel complexes, and smaller bridging angle of 95° than the other corresponding angles.
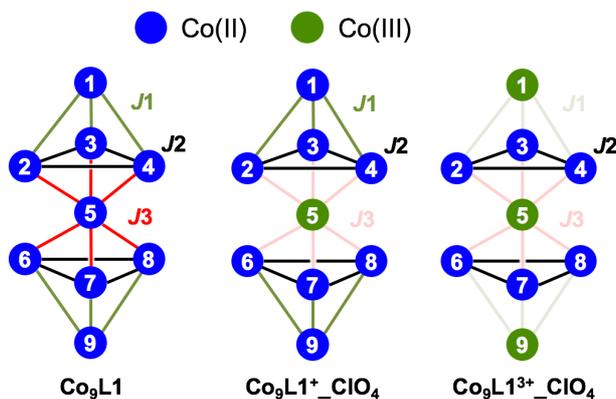
(Co₉L1)
$$H = -2J_1(S_1S_2 + S_1S_3 + S_1S_4 + S_6S_9 + S_7S_9 + S_8S_9)$$
$$\quad -2J_2(S_2S_3 + S_3S_4 + S_2S_4 + S_6S_7 + S_7S_8 + S_6S_8)$$
$$\quad -2J_3(S_2S_5 + S_3S_5 + S_4S_5 + S_5S_6 + S_5S_7 + S_5S_8)$$

(Co₉L1⁺_ClO₄)
$$H = -2J_1(S_1S_2 + S_1S_3 + S_1S_4 + S_6S_9 + S_7S_9 + S_8S_9)$$
$$\quad -2J_2(S_2S_3 + S_3S_4 + S_2S_4 + S_6S_7 + S_7S_8 + S_6S_8)$$

(Co₉L1³⁺_ClO₄)
$$H = -2J_2(S_2S_3 + S_3S_4 + S_2S_4 + S_6S_7 + S_7S_8 + S_6S_8)$$

Figure 11. Spin model and Hamiltonian used in the fitting procedure.

Table 19. Calculated J values (cm^{-1}), average Co-O-Co angles (°) and Co$\cdots$Co distances (Å).

	g value	J	Interaction	Co-O-Co$_{(ave.)}$ / °	Co$\cdots$Co$_{(ave.)}$ / Å
Co₉L1		$J1$	AF	121.0	3.74
		$J2$	AF	123.1	3.61
		$J3$	F	95.6	3.06
Co₉L1⁺_ClO₄	2.49	$J1$	AF (−2.34)	120.7	3.69
		$J2$	AF (−5.46)	120.3	3.60
Co₉L1³⁺_ClO₄	2.52	$J2$	AF (−4.67)	119.6[a]	3.59[a]

[a] Structural information is obtained from **Co₉L1³⁺_Ce**
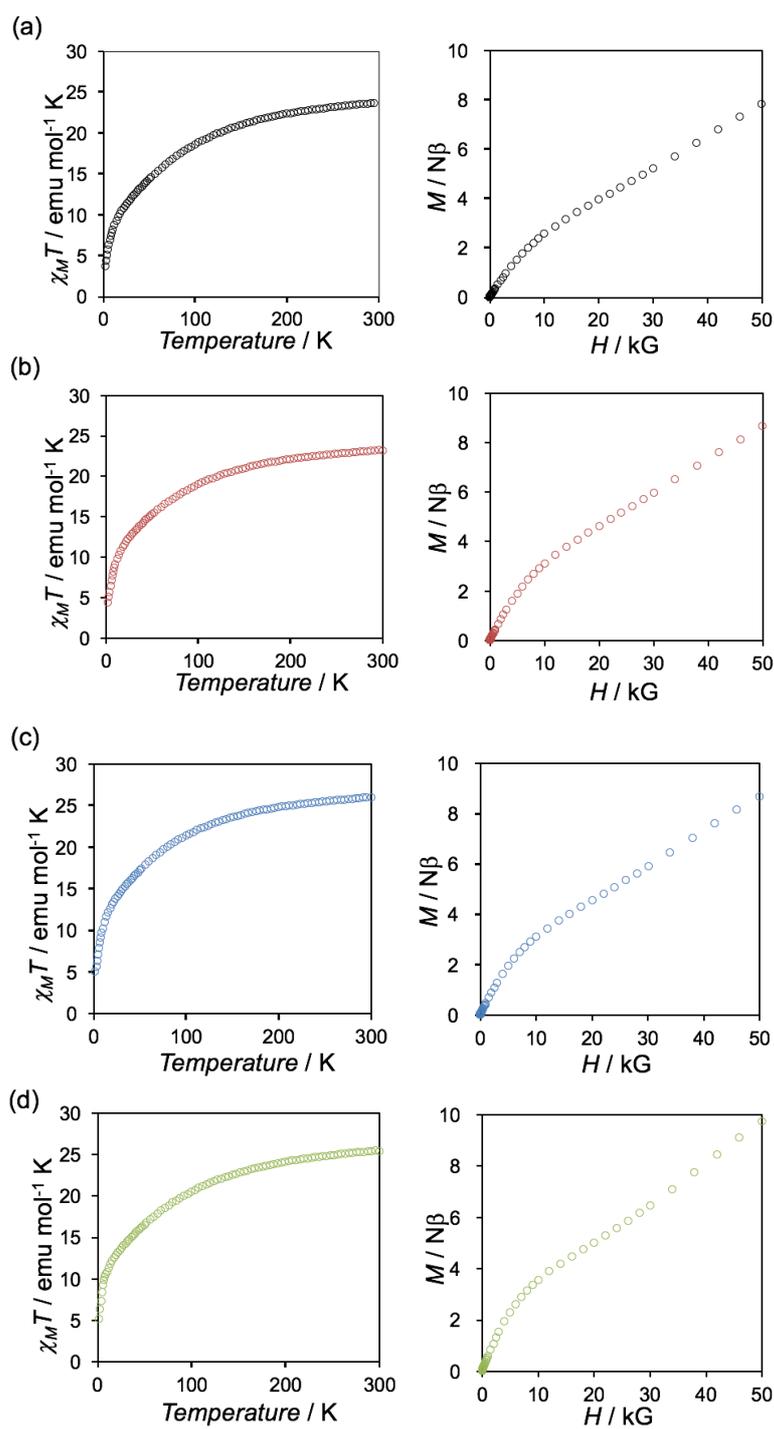
Figure 12. $\chi_M T$ vs. T curve at applied field (H) of 1 kOe and magnetization curve at 2 K for **Co₉L1** (a), **Co₉L2** (b), **Co₉L3** (c), **Co₉L4** (d)
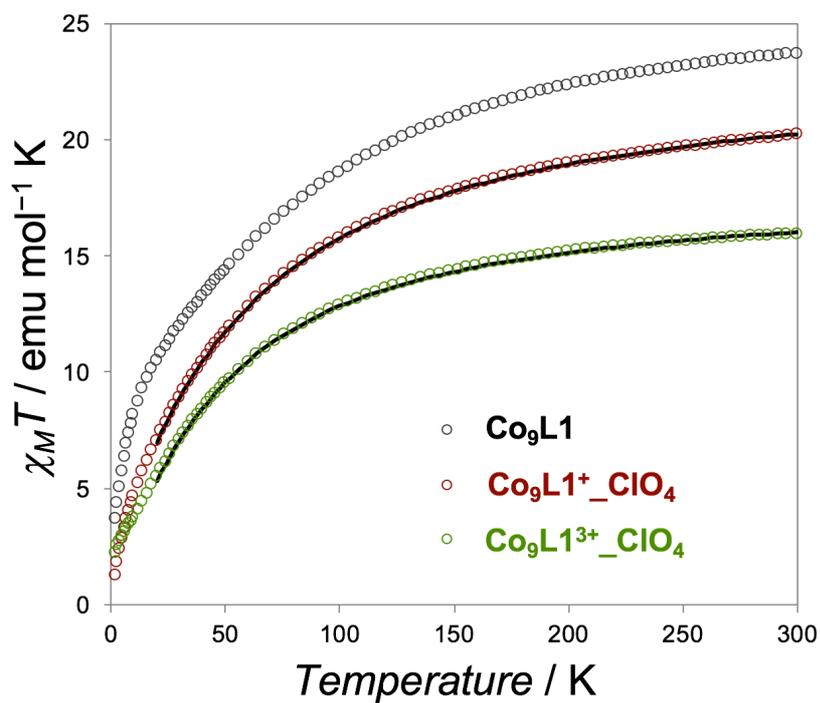
Figure 13. Temperature dependence of $\chi_M T$ at an applied field (H) of 1 kOe (The solid lines represent theoretical curve.)
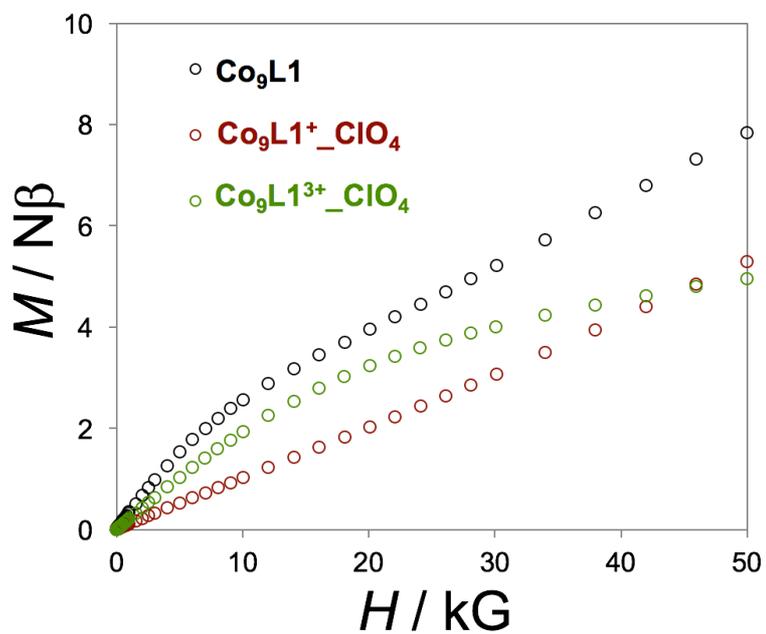
Figure 14. Field-dependence of magnetization of cobalt complexes at 2 K.
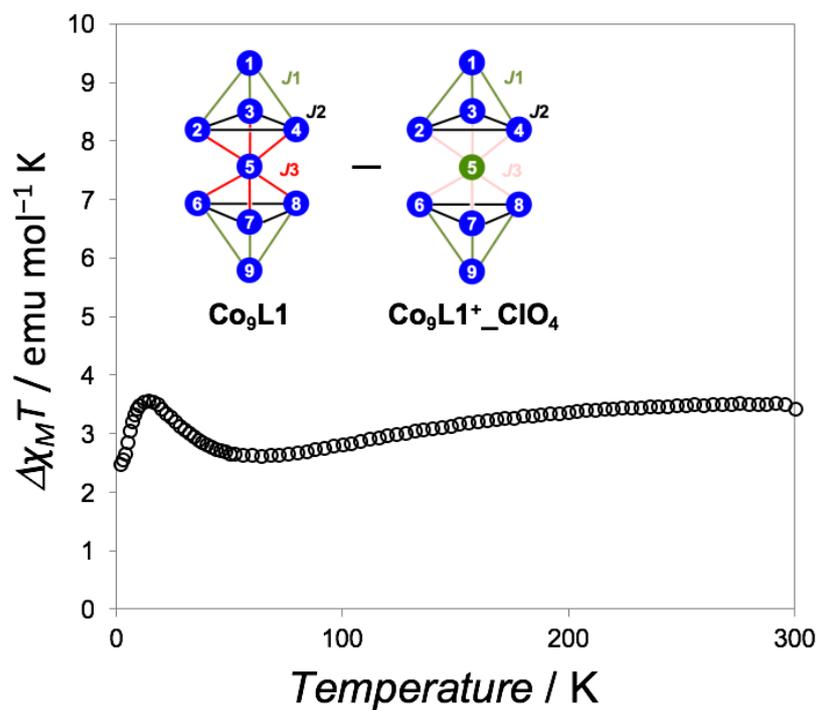
Figure 15. The difference of $\chi_M T$ value ($\Delta\chi_M T$) obtained by subtracting $\chi_M T$ value of **Co₉L1⁺_ClO₄** from **Co₉L1.**
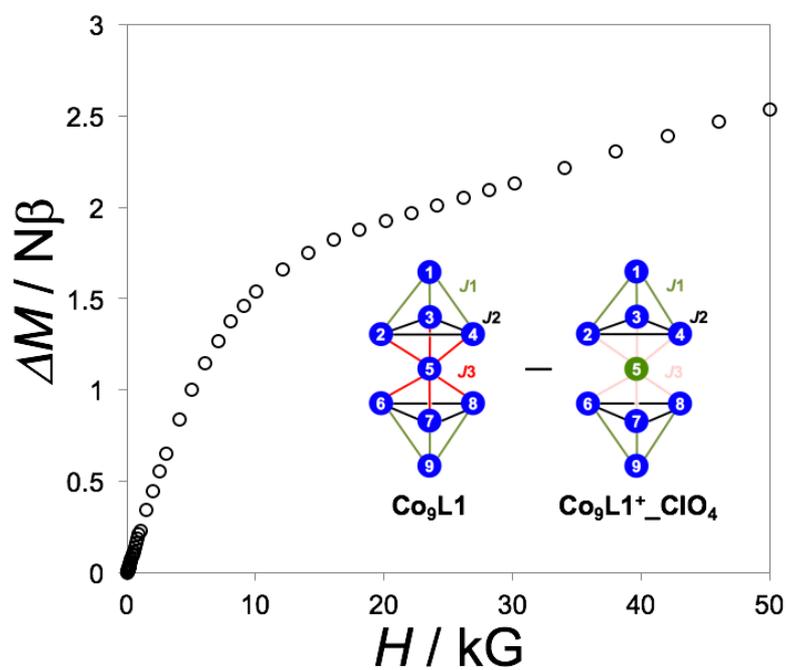
Figure 16. ΔM value obtained by subtracting M value of **Co₉L1⁺_ClO₄** from **Co₉L1.**

Magnetic Properties of [3M-M-3M] type Nickel Cluster

Magnetic behavior of each nickel complexes is measured and shown in the form of $\chi_M T$ vs. T plots and M vs. H plots (**Figure 19**). The $\chi_M T$ values of two complexes at 300 K are 9.4 - 10.7 emu mol^{-1} K, which is slightly higher than the expected spin-only value of seven non-interacting high-spin Ni^{II} ions (9.0 emu mol^{-1} K, g = 2.0) due to the orbital contribution. All complexes showed similar antiferromagnetic behavior. In the low temperature, $\chi_M T$ values decrease due to the week antiferromagnetic interaction and zero-field splitting (ZFS) of Ni(II) ions. The magnetic behaviors were simulated using to the isotropic exchange Hamiltonian by the PHI program.[48] Hamiltonian and the spin model used for the simulation is shown in **Figure 17**. To avoid over fitting, we used a simple model ignoring the ZFS of Ni(II) ions and intermolecular interaction. As in **Co₉L1**, **Ni₉Ln** has a pseudo-c_3 symmetry with a rotation axis extending through Ni1 and Ni9, so we consider the three type of interaction, J1 through enolate-bridge with the bridge angle of $ca.$ 123°, J2 through μ_3-hydroxyl-bridge between triad Ni(II) in the heptad core with ca. 125°, J3 thorough μ_3-hydroxyl-bridge between central Ni(II) and the other six triad Ni(II) in the heptad core with $ca.$ 95°. Calculated J values and average Ni-O-Ni bond angles of each nickel complexes are summarized in **Table 20**. J1 values are in the range of −0.59 to −0.95 cm^{-1} and these values are roughly consistent with the reported values for enolate-bridged six-coordinated Ni(II) ions with β-diketonate (Ni-O-Ni angles of 123.9 - 127.5°).[49] In the hydroxyl-bridged heptad core, The sign of J2 and J3 are negative and positive, respectively. Correlation between the Ni-O-Ni angles bridged by μ_3-OR (R = H, Me) and magnitude of magnetic interaction have been reported for the different Ni$_4$O$_4$ cubane type complexes (**Figure 18**).[50-58] The ferromagnetic interaction operates when Ni-O-Ni angle α is below 99°, and crossovers to the antiferromagnetic one in α > 99°. The ferromagnetic interaction J3 values of 15.02 to 23.12 cm^{-1} between the Ni5 and the other Ni(II) centers in the heptad core is consistent with the magneto-structural correlation with bridging angle. The J2 values of −15.02 to −25.21 cm^{-1} are weaker than the expected valued from the magneto-structural correlation, which is explained by the longer Ni⋯Ni distance than that of the reported cubane complexes. The combination of magnetic interactions is expected to form a unique spin structure based on spin-frustration, but these compounds showed no dynamic magnetic behavior above 2 K.

Table 20. Calculated J values (cm^{-1}), average Ni-O-Ni angles (°) and average Ni···Ni distances (Å).

	Ni$_9$L1	Ni$_9$L2	Ni$_9$L3	Ni$_9$L4
g **value**	2.14	2.11	2.11	2.06
*J*1	−0.95	−0.64	−0.69	−0.59
Ni-O-Ni angle	123.62	123.35	123.58	123.06
Ni···Ni distance	3.77	3.75	3.78	3.77
*J*2	−25.21	−24.46	−19.31	−16.15
Ni-O-Ni angle	124.97	125.24	124.92	123.36
Ni···Ni distance	3.59	3.59	3.59	3.58
*J*3	23.12	22.26	17.40	15.02
Ni-O-Ni angle	95.29	95.44	95.33	95.56
Ni···Ni distance	3.03	3.02	3.02	3.03
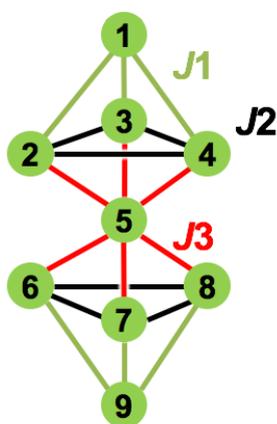
$$H = -2J_1(S_1S_2 + S_1S_3 + S_1S_4 + S_6S_9 + S_7S_9 + S_8S_9)$$
$$-2J_2(S_2S_3 + S_3S_4 + S_2S_4 + S_6S_7 + S_7S_8 + S_6S_8)$$
$$-2J_3(S_2S_5 + S_3S_5 + S_4S_5 + S_5S_6 + S_5S_7 + S_5S_8)$$

$$R = \left[\sum(\chi_M T_{exp} - \chi_M T_{calc})^2 \Big/ \sum(\chi_M T_{exp})^2\right]^{1/2}$$

Figure 17. Spin model and Hamiltonian equation used in the fitting procedure.

Table 21. Literature structural and magnetic data for complexes with a $[Ni_4(\mu_3\text{-}OR)_4]$ cubane core. [50-58]

	$\mu_3\text{-}OR$	Ni-O-Ni (°)	$J\,(cm^{-1})$
$[Ni_4(\mu\text{-}OMe)_4(sal)_4(EtOH)_4]$	methoxido	97.73	7.46
$[Ni_4(\mu\text{-}OMe)_4(chta)_4(NO_3)_4]$	methoxido	99	-0.57
$[Ni_4(\mu\text{-}OCH_3)_4(TMB)_4(OAc)_2]$	methoxido	100.9	-9.1
	methoxido	93	18
$[Ni_4(\mu\text{-}OH)_4(tzdt)_4(py)_4]$	hydroxido	95.85	17.5
	hydroxido	103.2	-22
$[Ni_4(\mu\text{-}OMe)_4(dbm)_4(MeOH)_4]$	methoxido	96.7	12.2
	methoxido	99.6	-3.4
$[Ni_4Cl_4(HL)_4]$	alkoxido	97.26	7.29
	alkoxido	100.4	-2.08
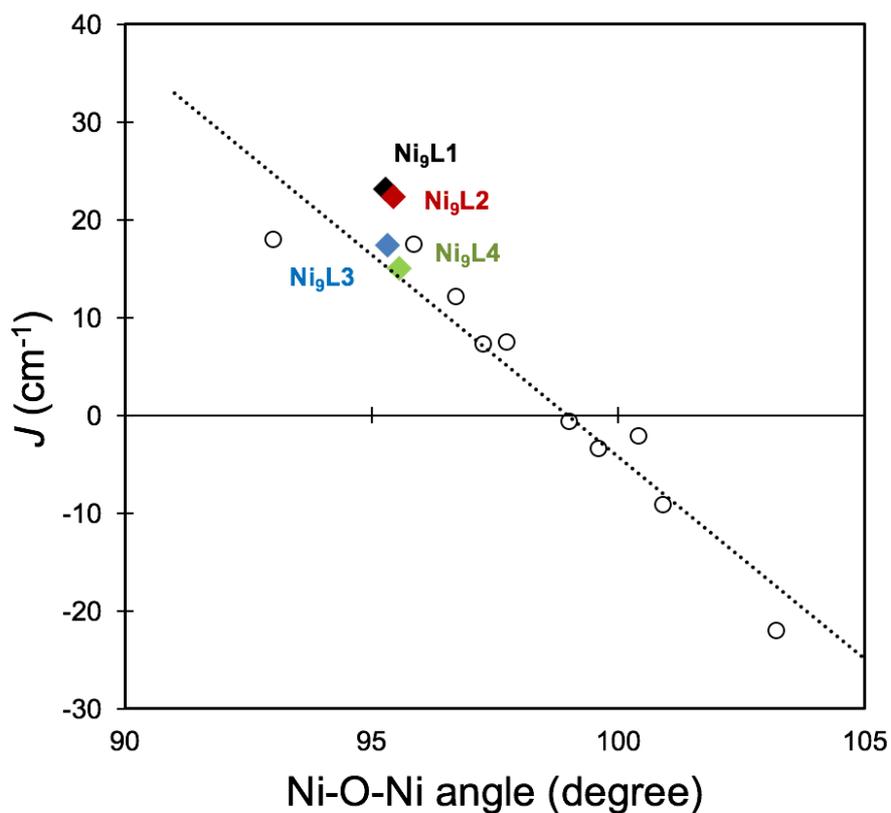
Figure 18. Correlation of Ni-O-Ni angles (degree) and magnetic interactions (J) for complexes with a $[Ni_4(\mu_3\text{-}OR)_4]$ cubane core.
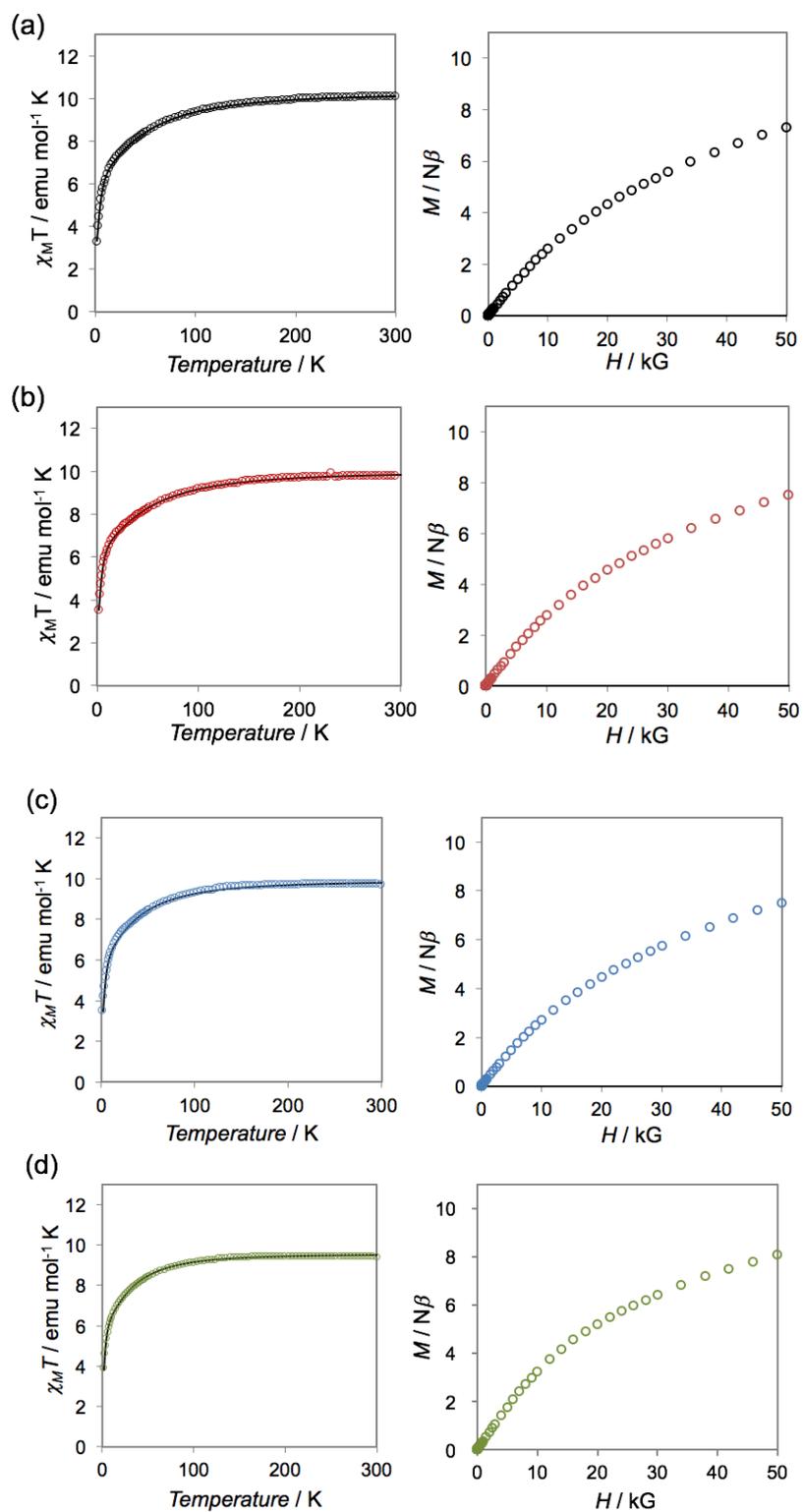
Figure 19. $\chi_M T$ vs. T curve at applied field (H) of 1 kOe and magnetization curve at 2 K for **Ni₉L1** (a), **Ni₉L2** (b), **Ni₉L3** (c), **Ni₉L4** (d) (The solid lines represent theoretical curve.)

Magnetic Properties of [M-6M] Type Nickel Cluster

Magnetic behavior of edge-sharing heptanuclear nickel complexes were measured and shown in the form of $\chi_M T$ *vs.* *T* plots and *M* *vs.* *H* plots (**Figure 22-25**). Oxygen-bridged complexes (**Ni₇L5_OH**, **Ni₇L5_OMe**) showed similar magnetic behavior.   The $\chi_M T$ values of two complexes at 300 K are 7.69 and 7.32 emu mol^{-1} K, which is higher than the expected spin-only value of seven non-interacting high-spin Ni^{II} ions (7.0 emu mol^{-1} K, g = 2.0) due to the orbital contribution.   The $\chi_M T$ values slowly increase to a maximum (8.87 emu mol^{-1} K at 52 K and 8.53 emu mol^{-1} K at 72 K), indicating the very weak ferromagnetic coupling between Ni^{II} ions.   In the low temperature, $\chi_M T$ values decrease due to the week antiferromagnetic interaction and zero-field splitting (ZFS) of Ni(II) ions.   The magnetic behaviors were simulated using the isotropic exchange Hamiltonian by the PHI program,[48] and spin model used for the simulation is shown in **Figure 20**.   To avoid over fitting, we used a simple model ignoring the ZFS of Ni(II) ions and intermolecular interaction.   We consider the two type of interaction, *J*1 through μ₃-oxygen-bridge between central Ni(II) and six peripheral Ni(II) ions with *ca.* 98°, *J*2 through μ₃-oxygen and enolate-bridge between peripheral Ni(II) ions with ca. 102°.   Calculated *J* values and average Ni-O-Ni bond angles of each complexes are summarized in **Table 22**.   In **Ni₇L5_OH** and **Ni₇L5_OMe**, *J*1 values are 4.90 and 4.52 cm^{-1} and *J*2 values are –4.49 and –4.48 cm^{-1} respectively.   As in the cases of **Ni₉L*n***, *J* values and corresponding bridging-angles of **Ni₇L5_OH** and **Ni₇L5_OMe** are also consistent with the magneto-structural correlation of the Ni₄O₄ cubane type complexes (**Figure 21**).

On the other hand, **Ni₇L5_N₃** showed a different ferromagnetic behavior form the oxygen-bridged cluster (**Figure 24**).   The $\chi_M T$ value at 300 K of 8.07 emu mol^{-1} K is also higher than the expected spin-only value of seven non-interacting high-spin Ni^{II} ions (7.0 emu mol^{-1} K, g = 2.0) due to the orbital contribution.   The $\chi_M T$ values sharply increase to a maximum (30.09 emu mol^{-1} K at 7 K), indicating the strong ferromagnetic coupling between Ni^{II} ions.   In the low temperature, $\chi_M T$ values decrease due to the zero-field splitting (ZFS).   The *J*1 and *J*2 values are 14.03 cm^{-1} and 0.33 cm^{-1} respectively, indicating ferromagnetic interaction operates between central Ni(II) and peripheral six Ni(II) ions through N₃ bridging.   In the measurement of magnetization *M* with the applied field *H* at 2 K, the magnetization M was saturated at 14.35 Nβ which is consistent saturation value of seven Ni(II) ions (**Figure 25**).

AC susceptibility measured with no applied dc field were performed in the range of 1-1000 Hz was shown in **Figure 26**.   The frequency-dependent in-phase and out-of-phase ac signals were not observed.

The relaxation time of SMMs can be tuned by applying dc field and tuning the energy gap.[13,22,27,32]   In the temperature dependence of the ac susceptibility in an applied dc field of 3000 Oe, the slight frequency-dependent in phase and out-of-phase ac signal were observed below 7 K (**Figure 27**).   However no maximum was observed, indicating that energy barrier is very small even though it was measured in an applied dc field.

Table 22.   Calculated J values (cm^{-1}), average Ni-X-Ni angles (°) and average Ni···Ni distances (Å). (X = O or N)

	Ni$_7$L5_OH	Ni$_7$L5_OMe	Ni$_7$L5_N$_3$
g value	2.25	2.27	2.09
$J1$ / cm^{-1}	4.90	4.52	14.03
Ni-X-Ni$_{(ave.)}$ / °	97.9	98.0	97.3
Ni···Ni$_{(ave.)}$ / Å	3.11	3.11	3.18
$J2$ / cm^{-1}	−4.49	−4.81	0.33
Ni-X-Ni$_{(ave.)}$ / °	99.8	100.1	101.1
Ni···Ni$_{(ave.)}$ / Å	3.11	3.11	3.20

$$H = -2J_1\left(\sum_{j=2}^{7} S_1 S_j\right) - 2J_2\left(\sum_{j=2}^{6} S_j S_{j+1} + S_2 S_7\right)$$

$$R = \left[\sum\left(\chi_M T_{exp} - \chi_M T_{calc}\right)^2 \middle/ \sum\left(\chi_M T_{exp}\right)^2\right]^{1/2}$$
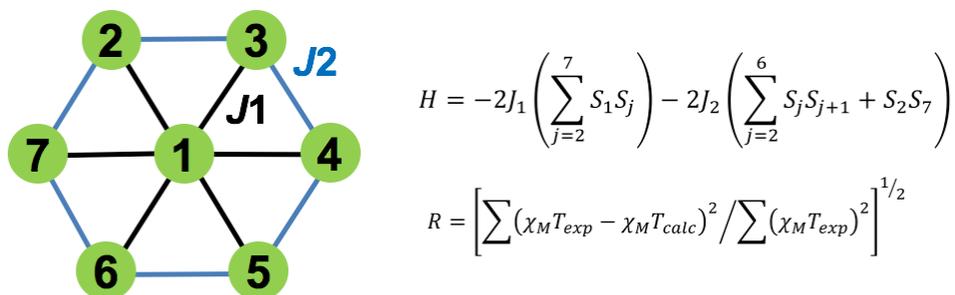
Figure 20.   Spin model and Hamiltonian equation used in the fitting procedure.
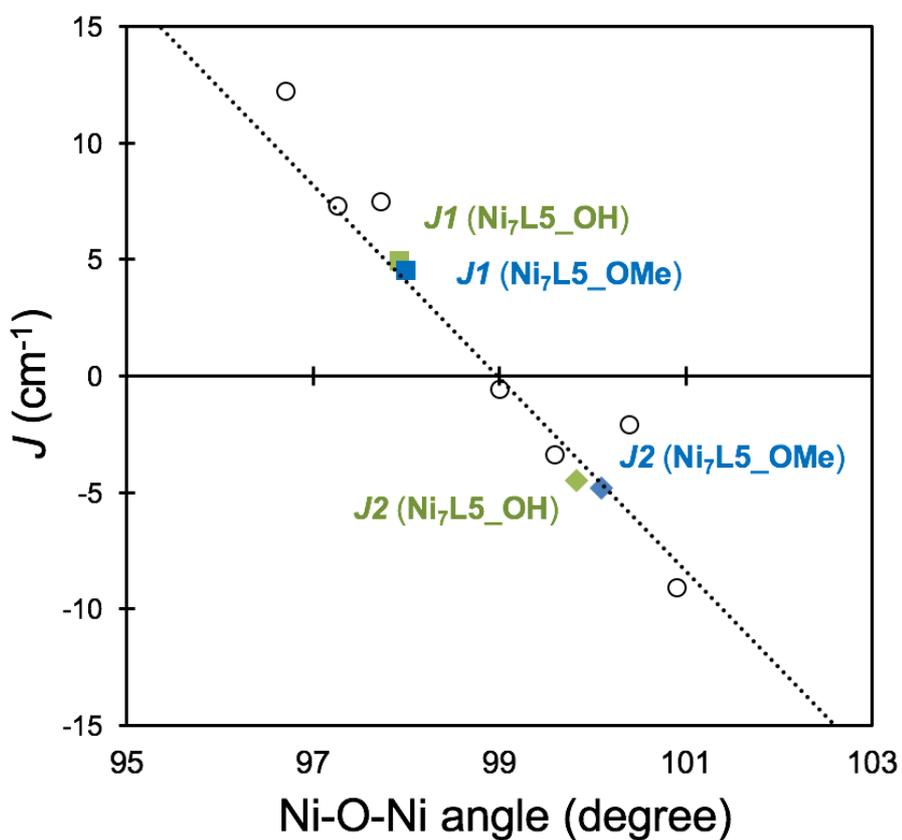
Figure 21.   Correlation of Ni-O-Ni angles (degree) and magnetic interactions (J) for complexes with a $[Ni_4(\mu_3\text{-}OR)_4]$ cubane core.
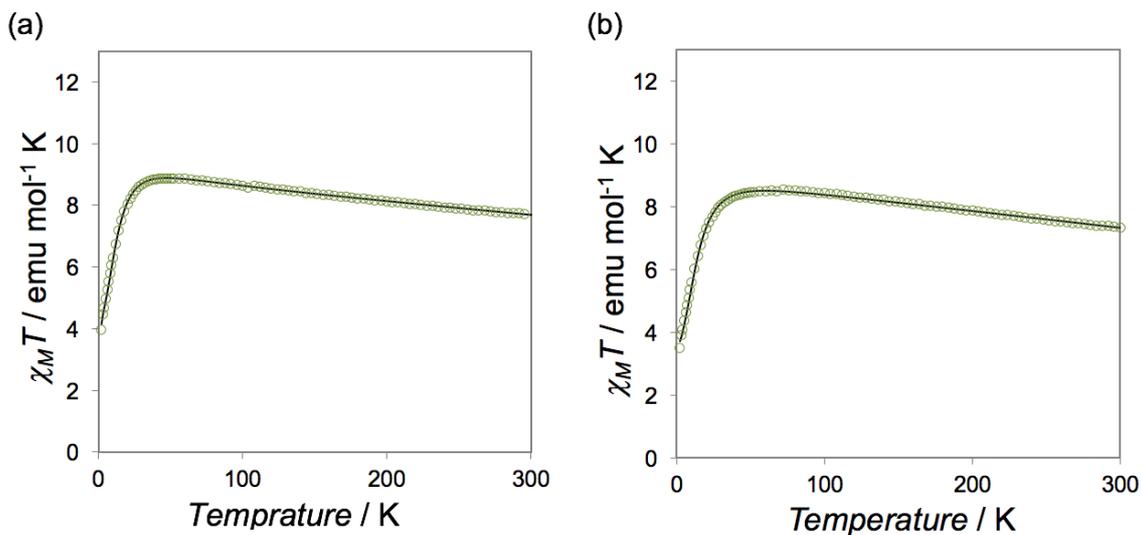
Figure 22. Temperature dependence of $\chi_M T$ at an applied field (H) of 1 kOe for **Ni₇L5_OH** (a), **Ni₇L5_OMe** (b). (The solid lines represent theoretical curve.)
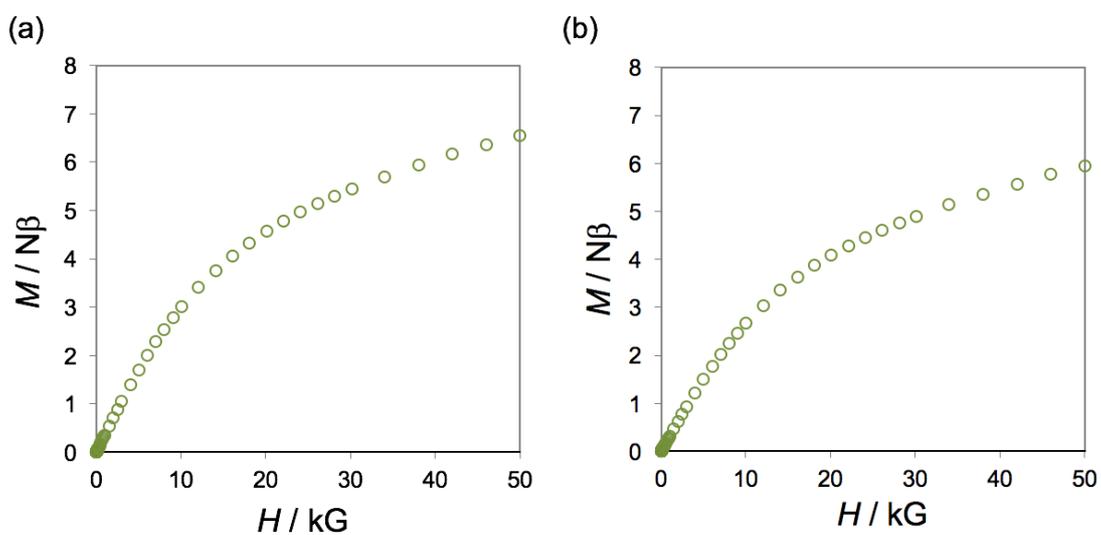
Figure 23. Field-dependence of magnetization of cobalt complexes at 2 K for for **Ni₇L5_OH** (a), **Ni₇L5_OMe** (b).
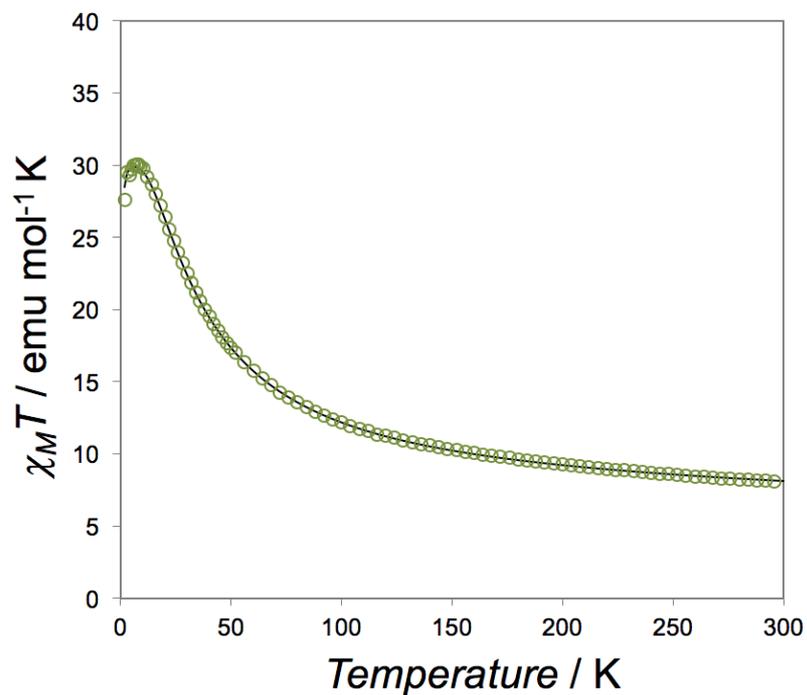
Figure 24. Temperature dependence of $\chi_M T$ at an applied field (H) of 1 kOe for **Ni₇L5_N₃**. (The solid lines represent theoretical curve.)
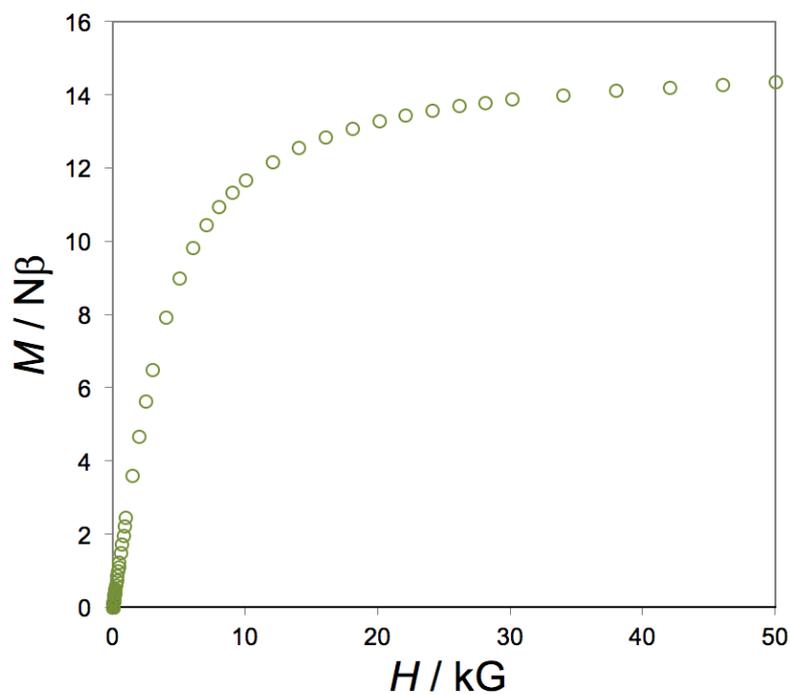
Figure 25. Field-dependence of magnetization of cobalt complexes at 2 K for **Ni₇L5_N₃**.
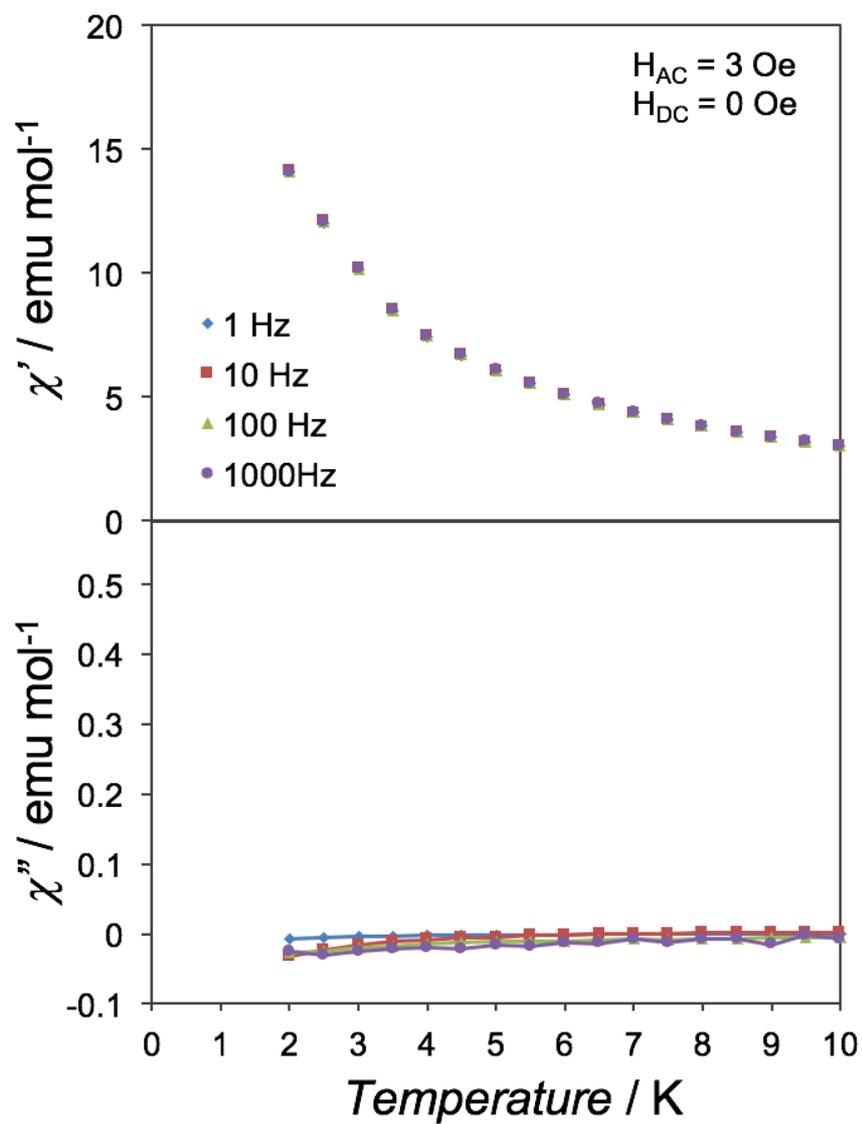
Figure 26.   Temperature dependence of the ac susceptibility for **Ni₇L5_N₃** in zero applied field with an oscillating field of 3 Oe.
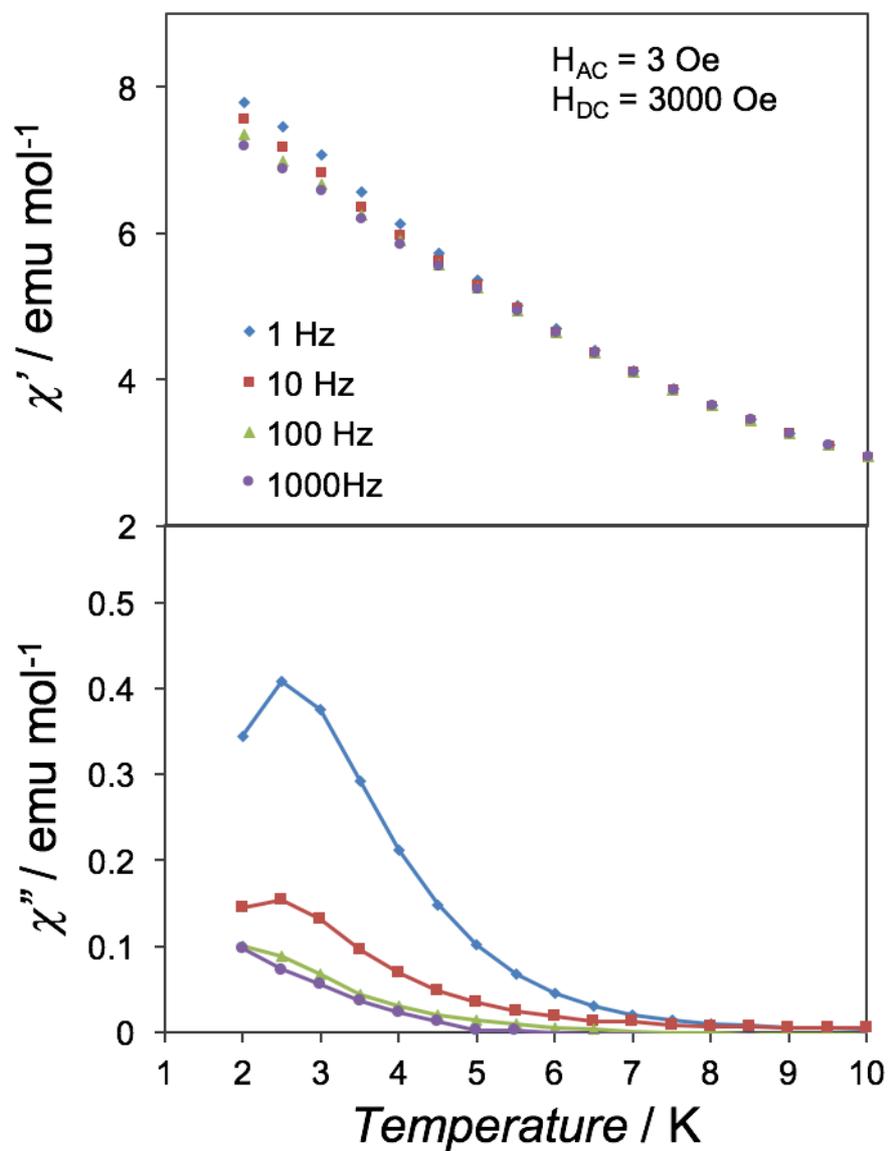
Figure 27. Temperature dependence of the ac susceptibility for **Ni₇L5_N₃** in an applied field H_{dc} = 3000 Oe with an oscillating field of 3 Oe.

Conclusion

We synthesized two types of CCs, nonanuclear complexes (**M₉Ln**) including unique [3M-M-3M] type μ_3-hydroxyl-bridged heptad cluster core and disk-shaped heptanuclear cluster including [M-6M] type μ_3-anion-bridged heptad cluster by self-assembling reaction, and investigated their magnetic properties. All nonanuclear complexes showed similar antiferromagnetic behavior.

We estimated the exchange interaction for **Co₉L1** by synthesis and investigation of magnetic properties for its oxidized species in which several diamagnetic Co(III) are exist. In the **Ni₉Ln**, all exchange interaction was estimated in detail by simulation. In all nonanuclear complexes, the antiferromagnetically coupled triangles ferromagnetically interact with the central M(II) ion and weakly antiferromagnetically interact with the terminal M(II) ions. Particularly in **Ni₉Ln**, the calculated J value though μ_3-bridging between the central Ni(II) and the other triad Ni(II) in the heptad core is consistent with the magneto-structural correlation for different Ni_4O_4 cubane type complexes. In disk-shaped heptanuclear cluster, **Ni₇L5_OH** and **Ni₇L5_OMe** showed similar weak ferromagnetic magnetic behavior. As in the cases of **Ni₉Ln**, J values though μ_3-bridging between the central Ni(II) and the peripheral Ni(II) for oxygen-bridged complexes are also consistent with the magneto-structural correlation for Ni_4O_4 cubane type complexes. On the other hand, **Ni₇L5_N₃** showed ferromagnetic behavior derived from ferromagnetic interaction through N_3-bridging between the central Ni(II) and the peripheral Ni(II). It also showed the slight frequency-dependent in phase and out-of-phase ac signal in an applied dc field of 1 kOe at 2 K, suggesting that very low energy barriers are exist in such condition. Therefore, as next step, construction of azido-bridged disk-shaped cluster with other metal ion such as Mn, Fe and Co is needed to achieve high energy barriers for coordination cluster usable as SMM at high temperature. In addition, preparation of heterometallic cluster complex is also one of the targets that we should try. Development of rational and systematic synthesis of coordination clusters are expected to lead new useful SMMs.

References

1   R. Sessoli, H. L. Tsai, A. R. Schake, S. Wang, J. B. Vincent, K. Folting, D. Gatteschi, G. Christou and D. N. Hendrickson, *J. Am. Chem. Soc.*, 1993, **115**, 1804–1816.

2   R. Sessoli, D. Gatteschi, A. Caneschi and M. A. Novak, *Nature*, 1993, **365**, 141–143.

3   A.-L. Gassner, C. Duhot, J.-C. G Bünzli and A.-S. Chauvin, *Inorg. Chem.*, 2008, **47**, 7802–7812.

4   V. Chandrasekhar, S. Das, A. Dey, S. Hossain and J.-P. Sutter, *Inorg. Chem.*, 2013, **52**, 11956–11965.

5   Y.-M. Luo, J. Li, L.-X. Xiao, R.-R. Tang and X.-C. Tang, *Spectrochimica Acta Part A*, 2009, **72**, 703–708.

6   O. V. Dolomanov, L. J. Bourhis, R. J. Gildea, J. A. K. Howard and H. Puschmann, *J Appl Crystallogr*, 2009, **42**, 339–341.

7   K. Yoneda, K. Adachi, K. Nishio, M. Yamasaki, A. Fuyuhiro, M. Katada, S. Kaizaki and S. Kawata, *Angew. Chem. Int. Ed.*, 2006, **45**, 5459–5461.

8   R. Ishikawa, M. Nakano, A. Fuyuhiro, T. Takeuchi, S. Kimura, T. Kashiwagi, M. Hagiwara, K. Kindo, S. Kaizaki and S. Kawata, *Chem. Eur. J.*, 2010, **16**, 11139–11144.

9   T. Shiga, M. Noguchi, H. Sato, T. Matsumoto, G. N. Newton and H. Oshio, *Dalton Trans.*, 2013, **42**, 16185–16193.

10   H. Sato, M. Yamaguchi, T. Onuki, M. Noguchi, G. N. Newton, T. Shiga and H. Oshio, *Eur. J. Inorg. Chem.*, 2015, **2015**, 2193–2198.

11   M. Okamura, M. Kondo, R. Kuga, Y. Kurashige, T. Yanai, S. Hayami, V. K. K. Praneeth, M. Yoshida, K. Yoneda, S. Kawata and S. Masaoka, *Nature*, 2016, **530**, 1–4.

12   R. W. Saalfrank, V. Seitz, F. W. Heinemann, C. Göbel and R. Herbst-Irmer, *J. Chem. Soc., Dalton Trans.*, 2001, 599–603.

13   Q. Chen, M.-H. Zeng, Y.-L. Zhou, H. H. Zou and M. Kurmoo, *Chemistry of Materials*, 2010, **22**, 2114–2119.

14   S. Petit, P. Neugebauer, G. Pilet, G. Chastanet, A.-L. Barra, A. B. Antunes, W. Wernsdorfer and D. Luneau, *Inorg. Chem.*, 2012, **51**, 6645–6654.

15   N. E. Brese and M. O'Keeffe, *Acta Crystallogr., Sect. B: Struct. Sci.*, 1991, **47**, 192–197.

16   A. Caneschi, A. Cornia and S. J. Lippard, *Angew. Chem. Int. Ed. Engl.*, 1995, **34**, 467–469.

17   A. Caneschi, A. Cornia, A. C. Fabretti, S. Foner, D. Gatteschi, R. Grandi and L. Schenetti, *Chem. Eur. J.*, 1996, **2**, 1379–1387.

18   G. L. Abbati, A. Cornia, A. C. Fabretti, A. Caneschi and D. Gatteschi, *Inorg. Chem.*, 1998, **37**, 1430–1431.

19   G. L. Abbati, A. Cornia, A. C. Fabretti, A. Caneschi and D. Gatteschi, *Inorg. Chem.*, 1998, **37**, 3759–3766.

20   H. Oshio, N. Hoshino, T. Ito, M. Nakano, F. Renz and P. Gütlich, *Angew. Chem. Int. Ed.*, 2003, **42**, 223–225.

21   N. C. Harden, M. A. Bolcar, W. Wernsdorfer, K. A. Abboud, W. E. Streib and G. Christou, *Inorg. Chem.*, 2003, **42**, 7067–7076.

22   Y.-Z. Zhang, F. Pan, Z.-M. Wang and S. Gao, *Chem. Commun.*, 2006, 3302.

23   R. W. Saalfrank, R. Prakash, H. Maid, F. Hampel, F. W. Heinemann, A. X. Trautwein and L. H. Böttger, *Chem. Eur. J.*, 2006, **12**, 2428–2433.

24   R. W. Saalfrank, A. Scheurer, R. Prakash, F. W. Heinemann, T. Nakajima, F. Hampel, R. Leppin, B. Pilawa, H. Rupp and P. Müller, *Inorg. Chem.*, 2007, **46**, 1586–1592.

25   S. Koizumi, M. Nihei, T. Shiga, M. Nakano, H. Nojiri, R. Bircher, O. Waldmann, S. T. Ochsenbein, H. U. Güdel, F. Fernandez-Alonso and H. Oshio, *Chem. Eur. J.*, 2007, **13**, 8445–8453.

26   T. Liu, B.-W. Wang, Y.-H. Chen, Z.-M. Wang and S. Gao, *Zeitschrift für anorganische und allgemeine Chemie*, 2008, **634**, 778–783.

27   X.-T. Wang, B.-W. Wang, Z.-M. Wang, W. Zhang and S. Gao, *Inorg. Chim. Acta*, 2008, **361**, 3895–3902.

28   C.-M. Liu, D.-Q. Zhang and D.-B. Zhu, *Inorg. Chem.*, 2009, **48**, 792–794.

29   S. Hill, S. Datta, J. Liu, R. Inglis, C. J. Milios, P. L. Feng, J. J. Henderson, E. del Barco, E. K. Brechin and D. N. Hendrickson, *Dalton Trans.*, 2010, **39**, 4693.

30   S. T. Meally, G. Karotsis, E. K. Brechin, G. S. Papaefstathiou, P. W. Dunne, P. McArdle and L. F. Jones, *CrystEngComm*, 2010, **12**, 59–63.

31   S. K. Langley, N. F. Chilton, M. Massi, B. Moubaraki, K. J. Berry and K. S. Murray, *Dalton Trans.*, 2010, **39**, 7236.

32   Y.-L. Zhou, M.-H. Zeng, L.-Q. Wei, B.-W. Li and M. Kurmoo, *Chemistry of Materials*, 2010, **22**, 4295–4303.

33   S.-H. Zhang and C. Feng, *Journal of Molecular Structure*, 2010, **977**, 62–66.

34   S.-H. Zhang, N. Li, C.-M. Ge, C. Feng and L.-F. Ma, *Dalton Trans.*, 2011, **40**, 3000–3007.

35   S. Mukherjee, R. Bagai, K. A. Abboud and G. Christou, *Inorg. Chem.*, 2011, **50**, 3849–3851.

36   A. A. Kitos, C. G. Efthymiou, C. Papatriantafyllopoulou, V. Nastopoulos, A. J. Tasiopoulos, M. J. Manos, W. Wernsdorfer, G. Christou and S. P. Perlepes, *Polyhedron*, 2011, **30**, 2987–2996.

37   S. T. Meally, C. McDonald, P. Kealy, S. M. Taylor, E. K. Brechin and L. F. Jones, *Dalton Trans.*, 2012, **41**, 5610.

38   S.-Y. Chen, C. C. Beedle, P.-R. Gan, G.-H. Lee, S. Hill and E.-C. Yang, *Inorg. Chem.*, 2012, **51**, 4448–4457.

39   A. M. Ullman and D. G. Nocera, *J. Am. Chem. Soc.*, 2013, **135**, 15053–15061.

40   J. A. Przyojski, N. N. Myers, H. D. Arman, A. Prosvirin, K. R. Dunbar, M. Natarajan, M. Krishnan, S. Mohan and J. A. Walmsley, *Journal of Inorganic Biochemistry*, 2013, **127**, 175–181.

41   M. Menelaou, E. Vournari, V. Psycharis, C. P. Raptopoulou, A. Terzis, V. Tangoulis, Y. Sanakis, C. Mateescu and A. Salifoglou, *Inorg. Chem.*, 2013, **52**, 13849–13860.

42   R. X. Zhao, Q. P. Huang, G. Li, S.-H. Zhang, H. Y. Zhang and L. Yang, *J Clust Sci*, 2014, **25**, 1099–1108.

43   Q. P. Huang, S.-H. Zhang, H. Y. Zhang, G. Li and M. C. Wu, *J Clust Sci*, 2014, **25**, 1489–1499.

44   K. R. Vignesh, S. K. Langley, K. S. Murray and G. Rajaraman, *Chem. Eur. J.*, 2014, **21**, 2881–2892.

45   F. Kobayashi, R. Ohtani, S. Teraoka, W. Kosaka, H. Miyasaka, Y. Zhang, L. F. Lindoy, S. Hayami and M. Nakamura, *Dalton Trans.*, 2017, **46**, 8555–8561.

46   J.-H. Xu, L.-Y. Guo, H.-F. Su, X. Gao, X.-F. Wu, W.-G. Wang, C.-H. Tung and D. Sun, *Inorg. Chem.*, 2017, **56**, 1591–1598.

47   R. Saiki, N. Yoshida, N. Hoshino, G. N. Newton, T. Shiga and H. Oshio, *Chem. Lett.*, 2017, **46**, 1197–1199.

48   N. F. Chilton, R. P. Anderson, L. D. Turner, A. Soncini and K. S. Murray, *J. Comput. Chem.*, 2013, **34**, 1164–1175.

49   Y.-Y. Hui, H.-M. Shu, H.-M. Hu, J. Song, H.-L. Yao, X.-L. Yang, Q.-R. Wu, M.-L. Yang and G.-L. Xue, *Inorg. Chim. Acta*, 2010, **363**, 3238–3243.

50   J. E. Andrew and A. B. Blake, *J. Chem. Soc. A*, 1969, **0**, 1456–1461.

51   J. A. Barnes and W. E. Hatfield, *Inorg. Chem.*, 1971, **10**, 2355–2357.

52   B. Aurivillius, H. Kvande, P. G. Wahlbeck and E. Näsäkkälä, *Acta Chem. Scand.*, 1977, **31a**, 501–508.

53 W. L. Gladfelter, M. W. Lynch, W. P. Schaefer, D. N. Hendrickson and H. B. Gray, *Inorg. Chem.*, 1981, **20**, 2390–2397.

54 P. Boyd, R. L. Martin and G. Schwarzenbach, *Aust. J. Chem.*, 1988, **41**, 1449–1456.

55 L. Ballester, E. Coronado, A. Gutierrez, A. Monge, M. F. Perpinan, E. Pinilla and T. Rico, *Inorg. Chem.*, 1992, **31**, 2053–2056.

56 M. A. Halcrow, J.-S. Sun, J. C. Huffman and G. Christou, *Inorg. Chem.*, 1995, **34**, 4167–4177.

57 A. Ferguson, J. Lawrence, A. Parkin, J. Sanchez-Benitez, K. V. Kamenev, E. K. Brechin, W. Wernsdorfer, S. Hill and M. Murrie, *Dalton Trans.*, 2008, **115**, 6409.

58 A. Das, F. J. Klinke, S. Demeshko, S. Meyer, S. Dechert and F. Meyer, *Inorg. Chem.*, 2012, **51**, 8141–8149.

Concluding Remarks

In this thesis, the author systematically studied on the electrochemical and redox properties of two types of coordination clusters (CCs).   In chapter 1, the author succeeded in synthesizing novel nonanuclear complexes, $[M_9(OH)_6(Ln)_6(sol.)]$ (**M_9Ln**, M = Co, Ni; n = 1-4).   **M_9Ln** formed a unique corner-sharing tetrahedra-type structure with a central hydroxyl-bridged heptanuclear core, $[M_7(\mu_3\text{-}OH)_6]^{8+}$, and terminal mononuclear units, $[M^{II}(L1)_3]^{4-}$, constitute the nonanuclear structure in a [1-7-1] formation.   The author investigated the electrochemical properties of **M_9L1** in detail, and elucidated redox process of **Co_9Ln** by structural analysis of oxidized species.   The redox properties are regulated by introducing the electron-donating substituent.   In chapter 2, the author succeeded in preparing disk-shaped heptanucler complex $[Fe^{III}Fe^{II}_6(Ln)_6(OH)_6](PF_6)_3$ (**Fe_7Ln**, n = 5, 6) and heterometallic complexes, $[Fe^{III}M^{II}_6(L5)_6(OH)_6](PF_6)_3$ (**FeM_6L5**, M = Mn, Co, Ni, Zn) and $[Fe^{III}Fe_3Zn_3(L5)_6(OH)_6](PF_6)_3$ (**Fe_4Zn_3L5**) by one-pot reaction.   The all complexes have unique edge-sharing hydroxyl-bridged cluster structure that seven metal ions on the same plane are bridged by the six hydroxyl anions and surrounded by six ligands. Although the magnetic properties of disk-shaped heptanuclear complexes has been already reported by several groups, we prepared homo- and heterometallic complexes and investigated their redox properties systematically.   The **Fe_7L5** showed multi-electron transfer derived from a central Fe(III) and peripheral Fe(II) and these redox waves are regulated by introducing the substituent (**Fe_7L6**) and replacing the several peripheral Fe(II) to redox-inactive Zn ion and the other 3D metal ions.   In the heterometallic complexes, redox wave is more positive compared to the **Fe_7L5**.   In these complexes, the redox potentials are and roughly correlate with the distortion parameter of central Fe(III) ion.   Therefore, in this study, the author demonstrated that distortion of metal ion is one of the factors that change the redox potential.   In chapter 3, the author investigated magnetic properties of synthesized two types of CCs, nonanuclear complexes (**M_9Ln**) and disk-shaped heptanuclear nickel cluster $[Ni_7(X)_6(L5)_6]$ (**M_7L5_X**, X = OH, OMe, N_3).   The author estimated the exchange interaction for **Co_9L1** by synthesis and investigation of magnetic properties for its oxidized species.   In the **Ni_9Ln**, all exchange interactions were estimated in detail by simulation.   In the all nonanuclear complexes, the antiferromagnetically coupled triangles ferromagnetically interact with the central Ni(II) ion and weakly antiferromagnetically interact with the terminal Ni(II) ions.   Particularly in **Ni_9Ln**, the calculated J value though μ_3-bridging between the central Ni(II) and the other triad

Ni(II) in the heptad core is consistent with the magneto-structural correlation for different Ni_4O_4 cubane type complexes.   As in the cases of **Ni$_9$Ln**, J values though μ_3-bridging between the central Ni(II) and the peripheral Ni(II) for oxygen-bridged complexes are also consistent with the magneto-structural correlation in **Ni$_7$L5_OH** and **Ni$_7$L5_OMe**.   **Ni$_7$L5_N$_3$** showed overall ferromagnetic behavior derived from ferromagnetic interaction through N$_3$-bridging.   It also showed the slight frequency-dependent in phase and out-of-phase ac signal in an applied dc field of 1 kOe at 2 K, suggesting that very low energy barriers are exist in such condition.   These works elucidate the effect of structural changes to electrochemical and magnetic properties.   These rational and systematic synthesis and investigation of their physical properties of homo and heterometallic CCs provides a rational strategy for tuning the such properties toward realization of new effective catalyst and useful SMMs.

Acknowledgement

Yasuhiro Tsuji
Department of Chemistry
Graduate School of Science
Kyushu University
March 2018

List of Publication

1. Nonanuclear Ni(II) Complexes in a [1-7-1] Formation Derived from Asymmetric Multidentate Ligands: Magnetic and Electrochemical Properties
   Y. Tsuji, T. Togo, A. Mishima, T. Koshiyama, M. Ohba
   Dalton Transactions, accepted (2018) DOI: 10.1039/C8DT00161H

2. Magnetic and Electrochemical Properties of Nonanuclear Co(II) Complexes Including Corner-Sharing Tetrahedra Type Cluster
   Y. Tsuji, T. Togo, A. Mishima, T. Koshiyama, M. Ohba
   (*to be submitted*)

3. Magnetic Properties of Disk-Shaped Edge-sharing Heptanuclear Nickel Clusters
   Y. Tsuji, A. Mishima, T. Koshiyama, M. Ohba
   (*to be submitted*)

4. Rational Synthesis and Multi-Electron Transfer of Hydroxyl-Bridged Heterometallic Multinuclear Complexes
   Y. Tsuji, T. Koshiyama, M. Ohba
   (*to be submitted*)

Other Publication

1. T. Koshiyama, N. Kanda, K. Iwata, M. Honjo, S. Asada, T. Hatae, Y. Tsuji, M. Okamura, R. Kuga, S. Masaoka, M. Ohba,
   Regulation of a cerium(IV)-driven O_2 evolution reaction using composites of liposome and lipophilic ruthenium complexes,
   Dalton Trans., 2015, **44**, 15126-15129

2. M. Honjo, T. Koshiyama, Y. Fukunaga, Y. Tsuji, M. Tanaka, M. Ohba,
   Sensing of fluoride ions in aqueous media using a luminescent coordination polymer and liposome composite,
   Dalton Trans., 2017, **46**, 7141-7144

3. T. Togo, Y. Tsuji, A. Mishima, T. Koshiyama, M. Ohba,
   Selective Synthesis and Structural Conversion of Di- and Octa-nuclear Mn(II), Co(II), and Zn(II) Complexes,
   Chem. Lett. (accepted on Feb. 2018)